Fractional Order Ubriaco Entropy and its Generalizations: New Paradigms for Decision-Making, Flow Dynamics and Survival Analysis

विधारत्नम् महद्धनम्

Thesis submitted in partial fulfilment

for the Award of Degree

Doctor of Philosophy

by

Poulami Paul

RAJIV GANDHI INSTITUTE OF PETROLEUM TECHNOLOGY
JAIS, INDIA - 229304

21MA0001 **2026**

CERTIFICATE

It is to be certified that the work contained in the thesis titled "***Fractional Order Ubriaco Entropy and its Generalizations: New Paradigms for Decision-Making, Flow Dynamics and Survival Analysis*** " by ***Poulami Paul*** has been carried out under my supervision and that this work has not been submitted elsewhere for a degree.

It is further certified that the student has fulfilled all the requirements of Comprehensive, Candidacy and SOTA.

Prof. Chanchal Kundu
(Supervisor)

DECLARATION BY THE CANDIDATE

I, **Poulami Paul**, certify that the work embodied in this thesis is my own bona fide work and carried out by me under the supervision of **Prof. Chanchal Kundu** from **August, 2021** to **January, 2026** at the Rajiv Gandhi Institute of Petroleum Technology, Jais, India. The matter embodied in this thesis has not been submitted for the award of any other degree. I declare that I have faithfully acknowledged and given credits to the research workers wherever their works have been cited in my work in this thesis. I further declare that I have not willfully copied any other's work, paragraphs, text, data, results, etc., reported in journals, books, magazines, reports dissertations, theses, etc., or available at websites and have not included them in this thesis and have not cited as my own work.

Date: **Poulami Paul**

Place: (Roll No.: 21MA0001)

CERTIFICATE BY THE SUPERVISOR

It is certified that the above statement made by the student is correct to the best of our knowledge.

Prof. Chanchal Kundu **Head of Department**

(Supervisor) **(Mathematical Sciences)**

CERTIFICATE

CERTIFIED that the work contained in the thesis titled ***Fractional Order Ubriaco Entropy and its Generalizations: New Paradigms for Decision-Making, Flow Dynamics and Survival Analysis*** by **Poulami Paul** has been carried out under my supervision. It is also certified that she fulfilled the mandatory requirement of TWO quality publications arose out of her thesis work.

It is further certified that the two publications (copies enclosed) of the aforesaid **Ms. Poulami Paul** have been published in the Journals indexed by:

(a) SCI

(b) SCI Extended

(c) SCOPUS

(Prof. Chanchal Kundu)
Supervisor

(Dr. Sudeep Kundu)
Convener, DPGC

COPYRIGHT TRANSFER CERTIFICATE

Title of the Thesis: Fractional Order Ubriaco Entropy and its Generalizations: New Paradigms for Decision-Making, Flow Dynamics and Survival Analysis

Name of the Student: Poulami Paul

Copyright Transfer

The undersigned hereby assigns to the Rajiv Gandhi Institute of Petroleum Technology, Jais, India, all rights under copyright that may exist in and for the above thesis submitted for the award of the "***DOCTOR OF PHILOSOPHY***".

Date: **POULAMI PAUL**
Place: Roll No.: 21MA0001

NOTE: However, the author may reproduce or authorize others to reproduce material extracted verbatim from the thesis or derivative of the thesis for author's personal use provided that the source and the Institute's copyright notice are indicated.

Acknowledgements

This journey of my PhD has felt like a roller coaster ride, which brought both uplifting moments of immense happiness and difficult periods of profound emotional turmoil and mental stress. I would like to specially thank all those people who have supported me throughout this journey as this is not my journey alone. First, I would like to express my deepest gratitude to my supervisor, *Prof. Chanchal Kundu*, for his continuous support and encouragement throughout this journey. His dedication and inspiring guidance have consistently given me the strength and determination to move forward and do what is right without loosing hope, even in the face of repeated failures. The process of writing this thesis has been profoundly overwhelming, following a long period of challenges and multiple rejections. This work is a reflection of those experiences, and whatever achievements I have made are the result of his unwavering support and belief in my abilities. I am truly grateful to the institute RGIPT for providing me the opportunity to carry out my research under his esteemed guidance.

I am forever grateful to my parents for their constant support and faith in me. Their blessings and motivation gave me the strength to continue with this amazing and memorable journey. I would like to thank my eternal souls, especially my Gannu dada, Buri Maa, Hanumanji, Rama Krishna Paramahansji and Lord Jagannath, and my late grandparents, whose invisible protective hand and blessings gave me the strength to stay positive even when the odds were all against me and never let me give up even at my lowest moment.

I would also like to express my deep appreciation to the Head of our department, Dr. Manoj Kumar Rajpoot for his assistance in taking care of all the departmental needs to improve its quality, Dr. Pradeep Das, our former DPGC and Dr. Sudeep Kundu, our present DPGC for their cooperation in maintaining harmony and efficiency of the department. I would specially like to acknowledge Dr. Dhrubasish Bhattacharyya from my research progress evaluation comittee for his valuable suggestions and inputs. I would also like to express my deepest gratitude to my external thesis reviewers for their valuable feedback, which helped strengthen the credibility and quality of my thesis. In addition, I would also like to extend my hearfelt gratitude to all the faculties who have taught me during my Ph.D. coursework, Dr. Gobinda Rakshit, Dr. Alpesh Kumar, Dr. Shivanshu Shrivastava, Dr. Saroj Kumar Mishra, Dr. Kavita Srivastava and Dr. Anirban Mukherhjee, for their valuable teachings and motivation to perform well in their respective subjects.

I would like to thank my senior, Dr. Deepak Kumar Yadav, who was a source of inspiration for me and set good examples of hardwork and discipline in this journey, thereby teaching me some important lessons of survival in difficult times and motivating me to rise silently and independently, even when no one is noticing. I am deeply grateful for his constant encouragement and invaluable motivation throughout this journey.

Another important and unforgettable part of my life are my friends who made this journey interesting and happening. I would like to acknowledge the company and support of my friends in RGIPT – Vidit and Swati, and my friends outside this institute – Pallavi, Mousumi and Shilpa, who always cheered me up at difficult times and kept my spirits high. I would like to thank my other labmates - Shishupal, Sashank and Heera for their spirited and joyful company throughout this journey. I would also like to thank my dear friends from the department, Rajesh and Puja, who became like family to me. I fondly remember the wonderful times we shared during the early days of my doctoral journey, memories that I will cherish throughout my life.

There are many people other than them who pushed me beyond my limits and helped me experience the light of this day that once seemed impossible, including my seniors, labmates, and my friends from other departments, especially, Swapna, Ekta, Puja and Sikha. Most importantly, this journey taught me to fight back hard and never quit or give up on myself even when all the odds were against me. So I also want to extend my heartiest thanks to those people who made this journey more challenging and never believed that I could accomplish my tasks without quitting.

Lastly, I would like to thank my most dearest members of my life, my little fur baby Jerry, and my paw friend Jacky whom I lost in 2022. They were my constant stress busters and lightened my mood whenever it felt heavy. This journey would be incomplete without acknowledging their presence in my life.

Poulami Paul

Dedicated to

My Parents

Pradip Kumar Paul and *Swapna Paul*

&

My Best Friend

Dr. Deepak Kumar Yadav

&

My Furry Friends

Jerry and *Lt. Jacky*

Contents

List of Notations and Abbreviations

$\mathbb{R}$:	Set of all real numbers
$\mathcal{Z}^+$:	Set of positive real numbers
ρ:	Pearson correlation coefficient
σ:	Standard deviation
μ:	Mean
$Var(X)$:	Variance of X
s^2:	Sample variance
R^2:	Coefficient of regression
Cov:	Covariance
$p(\cdot)$:	Probability mass function (pmf)
$f(\cdot)$:	Probability density function (pdf)
$F(\cdot)$:	Cumulative distribution function (cdf)
$S(\cdot)$:	Survival function (sf)
$Q(v)$:	Quantile function (QF)
$q(p)$:	Quantile density function (qdf)
$\hat{\mathcal{V}}$:	Normalized vertical flow velocity variable
$\mathcal{V}$:	Non-normal vertical flow velocity variable
$\hat{\nu}$:	Normalized vertical flow velocity
$\hat{\nu}_m$:	Mean normalized vertical flow velocity
$\hat{c}_m$:	Mean suspended sediment concentration (SSC)
$\hat{c}$:	Normalized SSC
$\hat{c}_h$:	Maximum SSC at channel surface
$\hat{\mathcal{C}}$:	Normalized SSC variable
${}_aD_x^{\alpha}$:	R-L derivative
$\psi(\cdot)$:	Digamma function
$\Gamma(\cdot)$:	Complete gamma function
$I_S(p)$:	Shannon information gain function

I_U^α:	Ubriaco information gain function
I_M^q:	Machado information gain function
$H_S(p)$:	Shannon entropy
$H_S(f)$:	Differential entropy
$H_{M,q}(p)$:	Machado entropy
$H_{M,q}(f)$:	Machado fractional differential entropy
$H_U^\alpha(p)$ or $S_\alpha(p)$:	Ubriaco entropy
$H_U^\alpha(f)$ or $H^\alpha(f)$:	Fractional differential entropy (FDE)
$CR\xi_\alpha(X)$:	Fractional cumulative residual entropy (FCRE)
$CP\xi_\eta(X)$:	Fractional generalized cumulative past entropy (FGCCPE)
$CR\xi_Q(X)$:	Quantile-based cumulative residual entropy (QCRE)
$CP\xi_Q(X)$:	Quantile-based cumulative past entropy (QCPE)
$\mathcal{C}R\xi_Q^\alpha(X)$:	Quantile-based fractional cumulative residual entropy (QFCRE)
$\mathcal{C}P\xi_Q^\eta(X)$:	Quantile-based fractional generalized cumulative past entropy (QFGCPE)
$\mathcal{C}P\xi_Q^\eta(X,v)$:	Dynamic quantile-based fractional generalized cumulative past entropy (DQFGCPE)
α:	Fractional order of Ubriaco entropy
q:	Fractional order of Machado entropy
η:	Fractional order of QFGCPE
$E[u(X(A,\theta))]$:	Expected utility of action A with state space θ
$\mathcal{G}=(\Theta,\mathcal{A},\vartheta)$:	General decision analysis model
$u(\cdot)$:	Utility function
$X=X(a,\theta)$:	Payoff
Θ:	State space
$\mathcal{A}$:	Action space
$R(A)$:	Risk measure
λ:	Risk-return trade-off parameter
$NH_S(p)$:	Normalized Shannon entropy
$h(\cdot)$:	Hazard function
$r(\cdot)$:	Reversed hazard function
$\mathcal{R}(v)$:	Reversed hazard quantile function
$\mathcal{E}$:	Elasticity
h_U^α or s_x:	Ubriaco entropy function

NS_α:	Normalized Ubriaco entropy
$\bar{H}^\alpha(f;t)$:	Past FDE
$H^\alpha(f;t)$:	Residual FDE
$\Gamma(n,x)$:	Incomplete gamma integral
$E_m(n)$:	Generalized exponential integral
$L(f,\hat{\nu})$:	Lagrangian function
FC:	Fractional calculus
R-L:	Riemann-Liouville
r.v.:	Random variable
CRE:	Cumulative residual entropy
CPE:	Cumulative past entropy
FE:	Fractional entropy
NFE:	Normalized fractional entropy
EU-E:	Expected utility-entropy
EU-EV:	Expected utility-entropy-variance
EU-FE:	Expected utility- fractional entropy
EU-FEV:	Expected utility-fractional entropy-variance
NEU-FE:	Expected utility-fractional entropy
NEU-FEV:	Expected utility-fractional entropy-variance
MSE:	Mean square error
RMSE:	Root mean square error
NVar:	Normalized variance
NEU:	Normalized expected utility
PDP:	Partial dependence plot
ANN:	Artificial neural network
RF:	Random forest
SSC:	Suspended sediment concentration
KM:	Kaplan-Meier
hr:	Hazard rate
rhr:	Reversed hazard rate
disp:	order of dispersion
HQ:	Hazard quantile
RHQ:	Reversed hazard quantile
Jack:	Jackknife estimate
CI:	Bootstrap confidence interval

List of Figures

List of Tables

Abstract

"Entropy is a measure of our ignorance about the detailed state of a system."
— E. T. Jaynes

Classical information-theoretic measures, particularly Shannon entropy, form the foundation of modern information theory by quantifying uncertainty as the expected information gain associated with probabilistic outcomes. While Shannon entropy is mathematically elegant and well suited to extensive systems due to its additive nature, this same property limits its applicability to non-extensive systems characterized by long-range interactions, memory effects, multiscale heterogeneity, and nonlinear dynamics. Such features are inherent in financial markets, turbulent hydraulic flows and sediment transport in open channels, and survival data, thereby creating a significant gap between entropy theory and its practical deployment in these complex real-world settings. Although several generalizations of Shannon entropy have been proposed to overcome these limitations, many of them remain either system-specific or lack a unified framework for interpretation and application across diverse disciplines.

Among the parametric generalizations of Shannon entropy, the entropy proposed by Ubriaco represents a fractional order extension grounded in the principles of fractional calculus. By replacing the logarithmic information measure with a fractional order formulation, Ubriaco entropy introduces controlled non-extensivity through a fractional parameter. This construction relaxes the strict additivity property while preserving key axiomatic properties of Shannon entropy, including continuity and concavity, recovering Shannon entropy as a limiting case. This theoretical structure enables adaptive sensitivity to uncertainty in systems where correlations, long-range dependence, and nonlinear interactions play a dominant role. Despite these advantages, the application of Ubriaco entropy has remained largely theoretical. In particular, the fractional order parameter has lacked a clear physical or behavioral interpretation, and issues related to scale dependence, numerical stability, and the limitations of continuous and non-parametric formulations have restricted its adoption in applied settings.

The central motivation of this thesis is to bridge this long-standing gap between theory and practice by transforming Ubriaco entropy into a meaningful, interpretable, and application-oriented uncertainty measure. The primary aim is to develop a unified entropy-based framework that integrates parametric, normalized, differential, and non-parametric extensions of entropy to model uncertainty in non-extensive systems across finance, hydraulics, and survival analysis.

The thesis begins with a rigorous theoretical analysis of Ubriaco entropy, establishing the fractional order parameter $\alpha \in [0, 1]$ as a sensitivity index that governs the response of entropy to uncertainty. In financial decision-making, this parameter admits a natural behavioral interpretation as an indicator of investor risk tolerance, with lower values corresponding to conservative (risk-averse) behavior and higher values reflecting adventurous (risk-seeking) tendencies. Four types of real-time portfolio datasets, namely, diversified, large-cap, mid-cap and hypothetical, are used to numerically validate the theoretical results. Building on this insight, two novel fractional entropy-based risk measures are proposed, and corresponding decision-making models are formulated that explicitly incorporate investor-specific behavioral biases through the parameter α. The proposed models are validated using real data from the Portuguese stock market (PSI20) with the help of artificial neural network (ANN), demonstrating their practical relevance and interpretability (Chapter 2).

To address scale dependence and numerical instability inherent in fractional entropy measures, a normalized form of Ubriaco entropy for discrete random variables is introduced, leading to a normalized fractional entropy (NFE)-based decision-making framework. Normalization preserves the underlying fractional structure while ensuring comparability across datasets. Empirical studies using NIFTY50 data from the Indian stock market show that NFE-based risk measures, when combined with machine-learning techniques such as ANNs and random forests, yield robust and stable predictions and superior stock selection models. Regularized linear models, including Lasso and Ridge regression, are shown to outperform the FE-based models, developed previously, due to improved stability and reduced error dispersion (Chapter 3).

The applicability of Ubriaco entropy is further extended to physical systems through the development of fractional differential entropy (FDE), a continuous formulation suit-

able for modeling turbulent hydraulic flow velocity and suspended sediment concentration (SSC) in open channels. The FDE-based models is shown to perform well even in unsteady turbulent sediment-laden flows through wide open channels. Comparative analyses demonstrate that the proposed models outperform existing one-dimensional formulations for most experimental and field datasets. The framework is further generalized using fractional entropy formulated by Machado, a parametric generalization of Ubriaco entropy, highlighting that the proposed methodology is principle-driven rather than restricted to a specific entropy form (Chapters 4 – 6).

Finally, to complement parametric entropy models and address situations where density estimation is unreliable, particularly in survival analysis, the thesis develops a non-parametric generalization of Ubriaco entropy termed as the quantile-based fractional generalized cumulative past entropy. This entropy measure enables robust quantification of mortality uncertainty and temporal variability in age-at-death distributions without restrictive distributional assumptions (Chapter 7) .

Overall, this thesis attempts to systematically bridge the gap between fractional entropy theory and practical application by providing a coherent, interpretable, and empirically validated entropy-based framework for uncertainty quantification across finance, hydraulics, and survival studies. By integrating parametric flexibility, normalization, continuous formulations, and non-parametric robustness, the work elevates Ubriaco entropy from a largely theoretical generalization of Shannon entropy to a unifying and versatile tool for modeling uncertainty in complex non-extensive systems (Chapter 8).

Key Words and Phrases: Decision model, flow velocity, fractional order entropy, risk measure, survival data analysis, suspended sediment concentration, Ubriaco entropy.

Chapter 1

Introduction and State-of-the-Art Review

"Information is information, not matter or energy."
— Norbert Wiener

1.1 Introduction

The development of information theory transformed the notions of *information* and *uncertainty* into precise mathematical concepts. In the classical framework, Shannon entropy quantifies the average uncertainty associated with a probability distribution and provides the foundation for data compression, communication theory, statistical inference, and decision-making (Cover and Thomas, 2006; Shannon, 1948). The concept also reflects a broader interdisciplinary link with thermodynamics (Clausius, 1865), probability theory and statistics (Kullback, 1959), where entropy serves as a measure of uncertainty, disorder, or information content.

Despite its fundamental role, classical Shannon entropy may not fully capture the uncertainty structure of complex real-world systems. Financial markets, turbulent hydraulic flows, sediment transport, and survival data often exhibit nonlinearity, heterogeneity, memory-like effects, long-range dependence, and heavy-tailed behaviour. Such features motivate the use of generalized entropy measures that can represent richer and more flexible forms of uncertainty.

Several generalizations of Shannon entropy have therefore been proposed. Rényi entropy (Rényi, 1961) and Tsallis entropy (Tsallis, 1988) introduce parametric generalizations to describe systems that deviate from classical extensive assumptions. One mathematical framework particularly suited to this task is *fractional calculus (FC)*, which extends differentiation and integration to non-integer orders. Its origins date back to an early correspondence between L'Hospital and Leibniz, concerning the interpretation of a derivative of fractional order, such as $n = \frac{1}{2}$, in the symbolic form $D^n y = \frac{d^n y}{dx^n}$. This foundational question subsequently motivated systematic investigations, leading to the formulation of several widely used fractional derivative operators (see Debnath, 2004; Butzer and Westphal, 2000, for further reference). Fractional operators inherently incorporate memory and hereditary effects, making them highly effective for characterizing systems whose present state depends not only on current conditions but also on the entire history of the process (see Dalir and Bashour, 2010, and references therein). Among its commonly used definitions are the Riemann-Liouville, Caputo, and Grünwald-Letnikov derivatives (Oliveira and Machado, 2014). While the Riemann-Liouville derivative is favored in theoretical formulations, the Caputo derivative is often preferred in applications due to its compatibility with classical initial conditions, and the Grünwald-Letnikov approach provides a natural link to numerical discretization.

Motivated by the ability of fractional operators to encode history dependence, Ubriaco (2009) introduced a fractional generalization of Shannon entropy by applying FC concepts to the logarithmic information kernel. By replacing the classical derivative with a fractional *Riemann-Liouville (R-L)* derivative, this formulation allows the entropy measure to tune sensitivity to probabilities, particularly amplifying or attenuating the influence of rare events. The resulting fractional entropy is shown to be Lesche stable and more sensitive towards temporal evolution of signals, thereby providing a flexible, mathematically grounded framework for modeling complex non-extensive systems.

By linking information theory with FC, this approach enables entropy measures that capture both local probabilistic structure and global, memory-dependent behavior. This synergy forms a central methodological foundation of the present thesis, which employs fractional order entropy to develop adaptive risk measures, model hydraulic processes in open-channel flows, and analyze survival data to study uncertainty in human mortality. Fractional order entropy measures enrich this framework by introducing a fractional parameter that can regulate the sensitivity of the entropy measure to probability variations, rare events, and distributional heterogeneity. This thesis builds on this direction by focusing on fractional order Ubriaco entropy and its generalizations, with applications to financial decision-making, hydraulic flow and sediment transport, and survival analysis.

Throughout this thesis, 'log(·)' denotes the natural logarithm, unless stated otherwise.

1.2 State-of-the-art review and mathematical preliminaries

From an information-theoretic viewpoint, the limitations of Shannon entropy in describing complex and heterogeneous non-extensive systems have motivated researchers to develop *parametric* generalizations (Rényi, 1961; Tsallis, 1988) and *non-parametric* formulations (Rao et al., 2004; Di Crescenzo and Longobardi, 2009). While parametric entropies introduce tunable parameters to regulate uncertainty sensitivity and non-extensive behavior, non-parametric approaches emphasize robustness through structural and distribution-free representations.

FC, once regarded as a mathematical curiosity, has emerged as a powerful analytical framework across applied sciences and engineering, finance, economics, and social sciences, enabling the modeling of long-range correlations, complexity, and anomalous behavior in real-world systems (see Machado et al., 2011; Sun et al., 2018; Lopes and Machado, 2020, and references therein). These developments naturally led to the formulation of *fractional order entropy* measures, which combines classical information measures with fractional dynamics to capture richer structural properties of data. In this section, we review the fractional order entropy measures studied in the present work. Before providing a brief discussion on the entropy definitions used in this study, we provide a brief summary table for some of the existing entropy measures motivating this study (see Table 1.2.1). This will help in comparing the features, utilities, and limitations of Shannon entropy and other generalized entropy formulations in studying complex systems. The comparison in Table 1.2.1 shows that no single entropy measure is universally suitable for all data structures. Shannon entropy provides the classical foundation, while generalized entropy measures introduce additional flexibility through parameters, non-additivity, fractional order, or quantile-based representations. The present thesis builds on this development by using fractional entropy as a unifying principle, while selecting the specific entropy form according to the structure of the data: discrete financial risk data, continuous hydraulic profiles, and quantile-based survival data.

Table 1.2.1: Brief comparison of entropy measures relevant to the thesis.

Entropy measure	**Main feature**	**Limitation**	**Relevance to thesis**
Shannon entropy	Classical measure of average uncertainty	Limited flexibility for non-extensive or memory-dependent systems	Provides the baseline entropy framework.
Rényi entropy	Parametric generalization emphasizing different probability regions	Interpretation of the order parameter may be problem-dependent	Used for comparison with generalized entropy approaches.
Tsallis entropy	Non-additive entropy for non-extensive systems	Parameter selection and interpretation may be difficult	Motivates the need for flexible non-extensive entropy measures.
Ubriaco entropy	Fractional order entropy based on fractional calculus	Fractional parameter requires clearer practical interpretation	Forms the main theoretical foundation of the thesis.
Machado entropy	Extends fractional entropy to a broader real-order framework	May be analytically more involved	Used for generalized SSC profile modelling.
Cumulative entropy	Uses distribution or survival functions instead of density alone	May still depend on distributional form	Motivates survival and lifetime uncertainty measures.
Quantile-based entropy	Uses quantile functions and ordered data	Requires careful quantile estimation	Useful for survival data and censored observations.

1.2.1 Fractional order Ubriaco entropy

The classical Shannon entropy of a discrete r.v. X with probability mass function $p = (p(1), \ldots, p(N))$ is defined as

$$H_S(p) = -\sum_{x=1}^{N} p(x) \log p(x). \tag{1.2.1}$$

Although Shannon entropy is a fundamental measure of uncertainty, many complex systems exhibit nonlocal interactions, memory-like effects, long-range dependence, and heterogeneous uncertainty structures. These features have motivated several generalized entropy measures, including fractional entropy formulations.

Using ideas from FC, Ubriaco (2009) introduced a fractional order generalization of Shannon entropy, now commonly known as *Ubriaco entropy*. It is motivated by the representation of Shannon entropy

$$H_S = \lim_{t\to -1} \frac{d}{dt} \sum_{x} p(x)^{-t}, \tag{1.2.2}$$

where the ordinary derivative is replaced by a fractional Riemann–Liouville derivative (see Valério et al., 2013, and references therein for an overview on fractional derivatives). This construction leads to the following closed-form expression for a discrete r.v. with n possible outcomes:

$$H_U^{\alpha}(p) = \sum_{x=1}^{n} p(x) \left[-\log p(x)\right]^{\alpha}, \quad \alpha \in [0,1]. \tag{1.2.3}$$

The parameter α controls the sensitivity of the entropy measure to the information gain term $-\log p(x)$. When $\alpha = 1$, Ubriaco entropy reduces to the classical Shannon entropy. For $\alpha \neq 1$, it provides a non-additive fractional generalization that can represent heterogeneous and non-extensive uncertainty structures. Ubriaco entropy also satisfies the Lesche stability condition (Ubriaco, 2009), which supports its robustness under small perturbations of the probability distribution.

For an absolutely continuous r.v. X with positive support $[0, c]$, $c > 0$, the continuous analogue of (1.2.3) is defined as (Foroghi et al., 2022)

$$H_U^{\alpha}(f) = \int_0^c f(x)[-\log f(x)]^{\alpha} dx, \quad \alpha \in [0,1], \tag{1.2.4}$$

where $f(x)$ is the probability density function of X. This measure is called *fractional differential entropy (FDE)* and reduces to the Shannon differential entropy

$$H_S(f) = -\int_0^c f(x) \log f(x)\, dx, \tag{1.2.5}$$

when $\alpha = 1$.

1.2.2 Fractional Machado entropy

While Ubriaco entropy introduces a fractional order parameter $\alpha \in [0, 1]$, its sensitivity range is restricted to the unit interval. To provide greater flexibility, Machado proposed a real-order fractional generalization in which the order parameter is allowed to vary over $q \in \mathbb{R}$ (Machado, 2014). This extension gives the entropy measure a broader sensitivity range and makes it useful for modelling more heterogeneous or dynamically varying uncertainty structures.

Machado's construction is based on the Shannon information gain function $I_S(p) = -\log p(x)$. Using fractional calculus, the corresponding real-order fractional information gain is defined as:

$$I_M^q(p) = -\frac{p(x)^{-q}}{\Gamma(q+1)}\big(\log p(x) + \tilde{\psi}\big), \quad q \in \mathbb{R}, \tag{1.2.6}$$

where $\tilde{\psi} = \psi(1) - \psi(1-q)$, $\Gamma(\cdot)$ is the gamma function, and $\psi(\cdot) = \frac{d}{dx} \log \Gamma(\cdot)$ is the digamma function.

Using (1.2.6), the Machado fractional entropy of order $q \in \mathbb{R}$ for a discrete r.v. X with n possible outcomes is given by

$$H_{M,q}(p) = \sum_{x=1}^{n} p(x) \left[-\frac{p(x)^{-q}}{\Gamma(q+1)}\big(\log p(x) + \tilde{\psi}\big)\right], \quad q \in \mathbb{R}. \tag{1.2.7}$$

For an absolutely continuous r.v. X with pdf $f(x)$, the corresponding Machado fractional differential entropy is

$$H_{M,q}(f) = \int_0^c f(x) \left[-\frac{f(x)^{-q}}{\Gamma(q+1)}\big(\log f(x) + \tilde{\psi}\big)\right] dx, \quad q \in \mathbb{R}. \tag{1.2.8}$$

When $q = 0$, Machado entropy reduces to the classical Shannon entropy in the discrete case and to Shannon differential entropy in the continuous case. Thus, Machado entropy extends the fractional entropy framework by allowing real-order sensitivity control. This additional flexibility is useful in the present thesis for deriving a more general fractional entropy-based formulation of suspended sediment concentration profiles.

1.2.3 Fractional order cumulative entropy measures

Although Shannon entropy has a clear interpretation for discrete random variables, its continuous analogue, differential entropy, may be negative and depends strongly on the underlying pdf. This makes its empirical estimation difficult in many applied problems. Cumulative entropy measures address this limitation by using distribution or survival functions instead of the pdf.

The cumulative residual entropy (CRE) proposed by Rao et al. (2004) measures uncertainty in the remaining lifetime of a system using the survival function. Its dual version, cumulative past entropy (CPE), introduced by Di Crescenzo and Longobardi (2009), uses the cumulative distribution function and measures uncertainty associated with past lifetime or inactivity time (see Navarro et al., 2010, for more details). Fractional extensions of these measures introduce additional sensitivity parameters and lead to fractional cumulative residual entropy (FCRE) and fractional generalized cumulative past entropy (FGCPE).

For a continuous r.v. X with cdf $F(x)$ and survival function $S(x) = 1 - F(x)$, the fractional cumulative residual entropy is defined as (Xiong et al., 2019):

$$CR\xi_\alpha(X) = \int_0^c S(x)\big[-\log S(x)\big]^\alpha\, dx, \quad \alpha \in [0,1]. \tag{1.2.9}$$

This measure extends CRE by allowing the parameter α to adjust the sensitivity of the entropy measure to residual-lifetime uncertainty.

The corresponding fractional generalized cumulative past entropy is defined as (Di Crescenzo et al., 2021):

$$CP\xi_\eta(X) = \frac{1}{\Gamma(\eta+1)} \int_0^c F(x)\big[-\log F(x)\big]^\eta\, dx, \quad \eta > 0. \tag{1.2.10}$$

Here, η controls the sensitivity of the measure to cumulative past uncertainty, while the factor $\Gamma(\eta+1)^{-1}$ provides normalization across fractional orders.

These fractional cumulative measures are useful in reliability and survival analysis because they avoid direct dependence on the pdf and provide flexible tools for modelling residual and past lifetime uncertainty. They also motivate the quantile-based cumulative entropy framework developed later in the thesis.

1.2.4 Quantile-based cumulative entropy measures

Fractional cumulative entropy measures such as FCRE and FGCPE are useful for lifetime and reliability analysis, but they still depend on distribution or survival functions. In many practical settings, especially with censored, truncated, incomplete, or analytically intractable data, this dependence can make estimation difficult. Quantile-based entropy measures address this issue by representing uncertainty through quantile functions rather than direct density or distribution estimation.

For a continuous r.v. X with cdf F and pdf f, the quantile function is defined as:

$$Q(v) = F^{-1}(v) = \inf\{x : F(x) \geq v\}, \qquad 0 \leq v \leq 1, \tag{1.2.11}$$

with quantile density $q(v) = Q'(v)$, whenever it exists. The quantile density satisfies

$$q(v)f(Q(v)) = 1, \tag{1.2.12}$$

which links the quantile and density representations.

Using this representation, Sankaran and Sunoj (2016) introduced quantile-based versions of cumulative residual entropy and cumulative past entropy. The quantile-based CRE is given by

$$CR\xi_Q(X) = -\int_0^1 (1-p)\log(1-p)\, q(p)\, dp, \tag{1.2.13}$$

and the quantile-based CPE is

$$CP\xi_Q(X) = -\int_0^1 p\log(p)\, q(p)\, dp. \tag{1.2.14}$$

A fractional extension, known as quantile-based fractional cumulative residual entropy (QFCRE), was proposed by Sunoj and Sebastian (2025) and is defined as:

$$\mathcal{C}R\xi_Q^{\alpha}(X) = \int_0^1 (1-p)\big[-\log(1-p)\big]^{\alpha} q(p)\, dp, \quad 0 \leq \alpha \leq 1. \tag{1.2.15}$$

Quantile-based cumulative entropy measures are useful because they avoid direct density estimation and are naturally connected with ordered data, percentiles, and survival probabilities. The fractional parameter provides additional sensitivity control over different regions of the distribution. These features make quantile-based fractional entropy particularly suitable for survival data, censored observations, and other applications where density-based formulations may be unstable or difficult to apply.

1.3 Inspiration and rationale for the current study

The notion of information and its quantification lie at the heart of modern science and engineering. The earliest information measure proposed by Shannon (1948) is mathematically elegant and optimally suited for extensive systems in which components interact weakly and additivity holds. However, many real-world systems violate these assumptions. Financial markets exhibit long-range dependence, heavy-tailed fluctuations, and behavioral feedback; hydraulic flows and sediment transport are governed by turbulence, memory effects, and multiscale interactions; survival and reliability data are influenced by censoring, heterogeneity, and temporal dependence. In such non-extensive systems, classical entropy measures often fail to capture the intrinsic structure of uncertainty.

Since the formulation of Shannon entropy as an information measure, a growing interest has emerged to develop parametric generalizations of Shannon entropy and investigate the consequences of applying these new entropies to various fields, especially physics. Among these generalized formulations, Rényi and Tsallis entropies are mostly used to study the complex behaviors of physical processes and special features such as fractal patterns and scale-dependent dynamics exhibited by physical systems (see Rényi, 1961; Tsallis, 1988). These entropy measures introduce tunable parameters that modify sensitivity to probability distributions and allow departures from strict additivity, making them efficient uncertainty quantifiers to characterize variability and disorder in natural and socio-economic systems, thereby addressing some of the limitations of Shannon entropy.

However, these formulations exhibit inherent structural limitations that restrict their effectiveness in modeling systems characterized by memory, nonlocal interactions, and long-range dependence. Rényi entropy retains additivity only for statistically independent systems and loses this property under dependence, without offering a clear or continuous interpretation of intermediate regimes between extensivity and non-extensivity. Tsallis entropy is expressed as an explicit algebraic identity between entropies of subsystems and replaces the additivity with a pseudo-additivity rule through the local Jackson $q-$derivative operator. This modifies scaling properties but not history dependence since the pseudo-additivity emerges as an algebraic identity, not as a convolution, memory kernel, or operator acting over a domain. As a result, the transition from extensive to non-extensive behavior in these formulations is governed by prescribed composition rules, rather than emerging naturally from the structure of the entropy measure itself. Furthermore, although the parameters in Rényi (Rényi, 1961) and Tsallis (Tsallis, 1988) entropies control sensitivity to probability distributions, particularly tail behavior, their interpretation is often context-dependent and lacks behavioral interpretations or direct connection to the intrinsic memory or nonlocal characteristics of the underlying system. Therefore, these parameters are unable to explicitly encode long-range dependence, hereditary effects, or cumulative influence of past states, which are central features of many real-world physical processes.

Driven by these limitations, Ubriaco (2009) proposed a fractional order generalization of Shannon entropy for non-integer order between 0 and 1 by incorporating fractional calculus directly at the level of the information gain (see Eq. (1.2.3)). Instead of deforming the entropy through algebraic scaling alone, Ubriaco's formulation employs a fractional R-L derivative operator that relaxes strict additivity in a continuous manner while naturally accounting for nonlocal and memory effects. The resulting entropy for discrete r.vs remains positive and concave, preserves the probabilistic foundation of Shannon entropy, and recovers it as a limiting case when the fractional parameter is unity. The bounded parameter space confines information gain values and relaxes strict additivity by introducing controlled non-extensivity through the fractional parameter, making fractional order Ubriaco entropy particularly suitable for optimization and decision-making problems, frequently encountered in real world. The corresponding continuous analogue given by (1.2.4) pose analytical and computational challenges because of direct continuous extension, often limiting practical interpretation and inference. As a result, despite strong theoretical foundations, Ubriaco entropy has largely remained confined to abstract mathematical studies, with limited empirical validation and systematic application beyond physics and statistical mechanics. Thus, this leaves its potential largely unexplored in other scientific and engineering domains, such as hydrology, hydraulics, financial decision theory, and survival analysis. Identifying meaningful application domains and practical interpretations of this entropy therefore remains an open and important problem. Moreover, clear behavioral and application-specific interpretations of the fractional parameter remain underexplored. A generalized formulation of Ubriaco entropy (1.2.3) proposed later by Machado (2014) extends the fractional parameter space to the real line, enhancing sensitivity to signal evolution, and reinforcing the principle-driven nature of entropy-based complexity modeling of random systems, which is defined by (1.2.8).

In addition, normalized forms of Shannon entropy have demonstrated notable advantages over their non-normalized counterparts, including improved comparability, numerical stability, and interpretability across heterogeneous systems without altering the underlying uncertainty structure. Normalization maps entropy values to the bounded interval $[0, 1]$, enabling meaningful comparison across datasets with different supports, reducing sensitivity to sample size, resolution, and discretization, and enhancing stability in optimization and machine-learning algorithms. Motivated by these advantages, this study proposes a normalized version of fractional order Ubriaco entropy.

Parallel to parametric generalizations, non-parametric extensions of Shannon entropy, most notably CRE introduced by Rao et al. (2004) and CPE proposed by Di Crescenzo and Longobardi (2009), have emerged as robust alternatives for uncertainty quantification of residual life and past life, respectively. Unlike classical entropy measures that rely on probability density estimation, cumulative entropies are defined in terms of distribution or survival functions, making them particularly suitable for reliability and survival analysis and ensuring consistency across discrete and continuous settings. Extending the idea of CPE to non-extensive systems, fractional cumulative past entropy measure has been introduced. In particular, the FGCPE is defined by Di Crescenzo et al. (2021), as given in (1.2.10), which is a normalized form of FCPE, extending the parameter space to positive real numbers.

Inspired by cumulative entropy frameworks, alternative quantile-based cumulative representations are developed by Sankaran and Sunoj (2016) to provide robust and non-parametric, distribution-free measures of uncertainty for situations when distribution or survival functions are analytically intractable or difficult to estimate. This helps in avoiding explicit density estimation and distribution assumptions. This leads to significant reduction in computational challenges, thereby offering enhanced robustness and interpretability, especially in cases of truncation, censoring, or incomplete data.

To incorporate fractional dynamics into these representations, quantile-based fractional cumulative residual entropy measures have been proposed by Sunoj and Sebastian (2025), as defined in (1.2.15). This formulation mitigates sensitivity to tail misspecification and strong modeling assumptions while providing localized and interpretable uncertainty assessment in financial data showing long-range correlations and anomalous variations (see Sunoj and Sebastian, 2025). However, to the best of our knowledge, no work seems to have been done based on quantile-based representation of FGCPE as defined in Eq. (1.2.10).

The above discussion leads to the following unanswered questions that motivate the present thesis:

1. How can the fractional order parameter in Ubriaco entropy be given a clear behavioural, physical, or probabilistic interpretation in real-data applications?

2. Can fractional entropy be incorporated into decision-theoretic risk measures that

combine expected utility, entropy-based uncertainty, and variance for stock selection and portfolio decision-making?

3. Can normalization reduce scale dependence and improve comparability and numerical stability of fractional entropy-based risk measures across heterogeneous financial datasets?

4. Can fractional differential entropy provide a physically interpretable and empirically accurate framework for modeling continuous vertical velocity and suspended sediment concentration profiles in open-channel flows?

5. Can Machado-type fractional entropy yield a more general analytical formulation for normalized suspended sediment concentration profiles?

6. Can a quantile-based fractional generalized cumulative past entropy measure be developed to quantify lifetime uncertainty when density estimation is unreliable or censoring is present?

Overall, the primary motivation of the present work is to address this long-standing gap by transforming fractional order entropy measures due to Ubriaco from predominantly theoretical constructs into practically meaningful, interpretable, and empirically validated tools for uncertainty quantification in non-extensive systems across finance, flow dynamics, and survival analysis. Specifically, the objectives are to:
(i) assign clear behavioral interpretations to the fractional parameter of (1.2.3) in financial decision-making and develop entropy-based risk measures for stock selection and portfolio optimization;
(ii) enhance numerical stability and comparability in the proposed decision-models under risk through normalization and machine learning techniques;
(iii) apply continuous extensions of fractional entropies (1.2.4) and (1.2.8) to model vertical velocity and suspended sediment concentration profiles in open-channel flows; and
(iv) propose robust, distribution-free quantile-based FGCPE (QFGCPE), explore some of its properties and applications in survival analysis, where data involves censoring and density estimation is unreliable.

Through rigorous theoretical development and extensive empirical validation using real data sets, the thesis attempts exemplary connections between fractional entropy theory and real-world application, establishing fractional order entropy-based methods as versatile and unifying tools for modeling uncertainty in random systems.

1.4 Synopsis of principal domains and concepts explored in the present study

In this section, we outline the principal application domains of the fractional order entropy measure proposed by Ubriaco (2009), focusing on the key ideas underlying financial decision theory, flow dynamics, and survival analysis. These domains represent the primary contexts in which information-theoretic concepts are applied throughout this study.

1.4.1 Decision-making under risk

Decision-making under risk is central to economics, finance, operations research, and statistics, where choices must be made under uncertainty while accounting for preferences. The relevant literature includes utility-based normative models, behavioural theories of risk perception, and information-theoretic approaches to uncertainty quantification. These perspectives motivate decision-making frameworks that remain mathematically tractable, flexible under distributional complexity, and capable of accommodating heterogeneous attitudes toward risk.

Prospect theory

Prospect Theory, introduced by Kahneman and Tversky (1979), provides a descriptive framework for decision-making under risk. It evaluates outcomes as gains and losses relative to a reference point and replaces objective probabilities with nonlinear decision weights. For a risky prospect with outcomes x_i and probabilities p_i, preferences are represented by

$$V = \sum_i \pi(p_i) v(x_i),$$

where $v(\cdot)$ is the value function and $\pi(\cdot)$ is the probability weighting function. This framework captures behavioural features such as loss aversion, risk aversion for gains, risk seeking for losses, and nonlinear probability weighting.

Expected utility theory and general decision analysis model

Expected utility theory provides a normative framework for rational choice under risk (von Neumann and Morgenstern, 1947). A decision problem may be represented as $\mathcal{G} = (\Theta, \mathcal{A}, u)$, where Θ is the state space, $\mathcal{A}$ is the action space, and $u(\cdot)$ is a utility function encoding preferences. For an action A, the expected utility is

$$EU(A) = \sum_{o \in O} P_A(o)U(o),$$

where $P_A(o)$ is the probability of outcome o conditional on A, and $U(o)$ is the utility of the outcome. More generally, for finite action and state spaces, an action A_i can be written as

$$A_i = \begin{pmatrix} x_{i1} & x_{i2} & \dots & x_{im_i} \\ p_{i1} & p_{i2} & \dots & p_{im_i} \end{pmatrix},$$

where x_{ij} is the payoff and p_{ij} its probability of occurrence (Yang and Qiu, 2005). Although expected utility theory is mathematically elegant, it may assign identical values to actions having different uncertainty structures. This limitation motivates the incorporation of entropy into decision-making models.

Expected utility-entropy theory

Entropy-based decision models incorporate information-theoretic uncertainty into expected utility. Unlike variance or higher-order moments, entropy captures global distributional uncertainty without relying on symmetry assumptions. The expected utility-entropy model of Yang and Qiu (2005) defines the risk of an action $A \in \mathcal{A}$ as

$$R(A) = \begin{cases} \lambda H_S(A,\theta) - (1-\lambda)\dfrac{E[u(X(A,\theta))]}{\max\limits_{A\in\mathcal{A}}\{|E[u(X(A,\theta))]|\}}, & \text{if } \max\limits_{A\in\mathcal{A}}\{|E[u(X(A,\theta))]|\} \neq 0, \\ \lambda H_S(A,\theta), & \text{otherwise,} \end{cases} \tag{1.4.1}$$

where $H_S(A,\theta)$ is the Shannon entropy of the state distribution and $0 \le \lambda \le 1$ is the risk–return trade-off parameter. This framework combines subjective utility with objective distributional uncertainty and has been used to explain decision problems such as the Lévy problem (Lévy, 1992), the Allais paradox (Allais, 1953), and the common ratio effect (Machina, 1987).

Normalized expected utility-entropy theory

To improve comparability and address scale dependence, Yang and Qiu (2014) proposed the normalized expected utility-entropy model. The normalized Shannon entropy is

$$NH_S(p) = \begin{cases} -\dfrac{\sum_{x=1}^{n} p(x)\log p(x)}{\log n}, & n > 1, \\ 0, & n = 1, \end{cases} \tag{1.4.2}$$

so that $NH_S(p) \in [0,1]$. The corresponding normalized risk measure is

$$R(A) = \begin{cases} \lambda NH_S(A,\theta) - (1-\lambda)\dfrac{E[u(X(A,\theta))]}{\max\limits_{A\in\mathcal{A}}\{|E[u(X(A,\theta))]|\}}, & \text{if } \max\limits_{A\in\mathcal{A}}\{|E[u(X(A,\theta))]|\} \neq 0, \\ \lambda NH_S(A,\theta), & \text{otherwise,} \end{cases} \tag{1.4.3}$$

where $0 \leq \lambda \leq 1$. This model was motivated by the need to represent heterogeneous risk attitudes more consistently (Fischer and Kleine, 2007) and has been linked to behavioural phenomena such as certainty effects, the common ratio effect, and the common consequence effect (Machina, 1987; Kahneman and Tversky, 1979).

Expected utility-entropy-variance theory

Entropy and variance capture complementary aspects of uncertainty. Variance measures spread around the mean, while entropy measures distributional dispersion more globally (Ebrahimi et al., 1999; Cover and Thomas, 2006). Entropy also reflects broader distributional characteristics and has been used as a risk measure in decision and financial analysis (see Brachinger and Weber, 1997, and references therein). Motivated by these distinctions, Brito (2020) proposed the expected utility-entropy-variance risk measure

$$R(A) = \frac{\lambda}{2}\left[H_S(A,\theta) + \frac{\text{Var}[X(A,\theta)]}{\max\limits_{A\in\mathcal{A}}\{\text{Var}[X(A,\theta)]\}}\right] - (1-\lambda)\frac{E[u(X(A,\theta))]}{\max\limits_{A\in\mathcal{A}}\{|E[u(X(A,\theta))]|\}}, \tag{1.4.4}$$

where $0 \leq \lambda \leq 1$. This framework combines utility, entropy, and variance, and can distinguish actions that share identical expected utility and entropy but differ in payoff dispersion. It has also been used to address Allais-type and Lévy-type decision problems (Brito, 2020).

Normalized expected utility-entropy-variance theory

A further normalized extension was proposed by Brito (2022), combining normalized Shannon entropy and normalized variance with expected utility. The normalized expected utility-entropy-variance measure is

$$R(A) = \frac{\lambda}{2}\left[NH_S(A,\theta) + \frac{\text{Var}[X(A,\theta)]}{\max\limits_{A\in\mathcal{A}}\{\text{Var}[X(A,\theta)]\}}\right] - (1-\lambda)\frac{E[u(X(A,\theta))]}{\max\limits_{A\in\mathcal{A}}\{|E[u(X(A,\theta))]|\}}. \tag{1.4.5}$$

Normalization places entropy and variance on comparable scales and improves their coherent integration with expected utility. This framework has been used to explain decision scenarios inadequately addressed by expected utility alone, including certainty effects and the common ratio effect (Brito, 2022).

The above models show that entropy enriches classical decision-making by capturing distributional uncertainty beyond expected utility and variance. However, these formulations are based on Shannon entropy, whose uncertainty response is fixed. This motivates the fractional entropy-based decision models developed in this thesis, where the fractional order parameter introduces an additional mechanism for representing heterogeneous risk sensitivity.

1.4.2 Portfolio optimization: evolution of models and stock selection approaches

Stock markets are complex adaptive systems with nonlinear interactions and evolving dependence structures (Bonanno et al., 2001). Portfolio optimization therefore aims to balance expected return and risk under uncertainty. The classical foundation is the mean–variance (MV) framework of Markowitz, which formalizes portfolio choice through the trade-off between expected return and variance-based risk (Markowitz, 1952). The MV model introduced the ideas of efficient portfolios and the efficient frontier, and remains a central reference point in portfolio theory.

Despite its importance, the MV framework has limitations. Variance captures only second-order dispersion around the mean and may fail to represent asymmetry, tail risk, higher-order effects, and distributional uncertainty in financial returns (Markowitz, 1959; Philippe, 1996; Markowitz, 2000). Moreover, MV theory does not directly address stock preselection, which becomes important in high-dimensional markets where large asset universes increase estimation error, instability, and computational burden (Brito, 2023).

Cardinality-constrained portfolio optimization attempts to control portfolio size and practical trading restrictions, but it introduces combinatorial complexity (Gao and Li, 2013). Asset preselection provides a related strategy by identifying a smaller subset of stocks before portfolio optimization, thereby reducing dimensionality while preserving much of the efficiency of the full portfolio (Chang et al., 2000; Yam et al., 2016; Zhu et al,, 2017). However, both cardinality constraints and preselection procedures may require additional algorithmic effort (Chang et al., 2000; Fieldsend et al., 2004; Gao and Li, 2013).

The adequacy of variance as the only risk measure has also been questioned, especially because it does not distinguish upside and downside risk and may be sensitive to distributional assumptions (Soofi et al., 1997; Dionisio et al., 2007). Entropy provides an alternative uncertainty measure that captures distributional dispersion without relying only on second moments. It was introduced into financial risk measurement by Philippatos and Wilson (1972) and has since been widely used in finance for uncertainty, diversification, and portfolio optimization (Buchen and Kelly, 1996; Zellner, 1996; Stutzer, 2000; Molgedey and Ebeling, 2000; London et al., 2001; Dionisio et al., 2006; Zhou, 2013). Mean-entropy portfolio models show that entropy can complement variance and provide a richer description of return distributions and investor preferences (Philippatos and Gressis, 1975; Usta and Kantar, 2011; Aksarayli and Pala, 2018). Since entropy is concave and variance is convex, their joint use can provide a more balanced description of portfolio risk (see Bonami, 2009; Gao and Li, 2013, and references therein).

Expected utility-entropy (EU-E) based stock selection models further use entropy as an asset preselection tool (Yang et al., 2017). By combining expected utility with entropy-based uncertainty, these models rank assets and identify informative subsets for portfolio construction. Empirical studies show that EU-E selected subsets can approximate the efficient frontier of the full market while using fewer assets (see Yang et al., 2017; Mercurio et al., 2020, and references therein). Extensions that include variance, such as expected utility–entropy–variance (EU-EV) models, improve the asset-ranking framework while maintaining portfolio efficiency (Brito, 2023).

Other extensions include fuzzy and possibilistic portfolio optimization, uncertainty theory, entropy-based fuzzy portfolio models, and multi-criteria decision frameworks (Huang, 2007; Huang, X., 2008a; Huang, 2008b; Jana et al., 2009; Qin et al., 2009; Bhattacharyya et al., 2013; Li et al., 2019; Galankashi et al., 2020; Mehralizade et al., 2020; Li and Zhang, 2021). Machine learning methods have also been integrated into stock selection and portfolio optimization, showing that carefully selected asset subsets can reduce dimensionality and estimation error while maintaining or improving portfolio performance (Huang, 2012; Qu et al., 2017; Liu and Yeh, 2017; Paiva et al., 2019; Wang et al., 2020; Chen et al., 2021).

Overall, the literature shows a progression from classical MV analysis toward hybrid, entropy-based, multi-criteria, and data-driven portfolio frameworks. This progression motivates the present thesis, where fractional entropy-based risk measures are used for stock selection and portfolio decision-making under uncertainty.

1.4.3 Vertical distribution of streamwise velocity in open channels

The vertical distribution of streamwise velocity is fundamental in open-channel hydraulics because it influences discharge estimation, energy and momentum correction factors, sediment entrainment, suspended sediment transport, and near-bed erosion processes (Chow, 1959). In turbulent open-channel flows, velocity generally increases from the bed toward the free surface, although the maximum velocity may occur below the free surface depending on channel geometry, secondary currents, and flow conditions (Nakagawa, 1993; Dey, 2024). Hence, accurate representation of the vertical velocity profile is important for both hydraulic analysis and practical computations.

Deterministic velocity models

Classical velocity-profile models are mainly deterministic and are derived from conservation principles together with turbulence closure assumptions. Important examples include power-law formulations and the Prandtl–von Kármán logarithmic law (Prandtl, 1925; von Kármán, 1930), with outer-layer corrections such as wake functions introduced to improve representation near the free surface (Coles, 1956). These models are simple and physically interpretable, but often depend on empirical constants, flow-region assumptions, and separate near-bed or outer-layer descriptions. Their accuracy may deteriorate in flows with velocity-dip phenomena, strong secondary currents, or complex boundary effects (Nakagawa, 1993).

Probabilistic and entropy-based velocity models

Because turbulent open-channel flow is stochastic, probabilistic models provide an alternative way to represent velocity distributions. Entropy-based approaches treat the time-averaged velocity as a random variable and use the maximum entropy principle to determine the least-biased distribution consistent with known constraints (Jaynes, 1957a,b). Shannon entropy was first used in open-channel hydraulics by Chiu and co-workers to derive unified exponential-type velocity profiles (Chiu, 1987). Although such models often perform better than classical piecewise laws, the absence of an additional sensitivity parameter can limit their flexibility.

Generalized entropy measures address this limitation. Tsallis entropy introduces a non-extensive parameter and has been used to derive power-law-type velocity distributions for turbulent open-channel flows (Tsallis, 1988; Singh and Luo, 2011; Luo, 2009; Singh, 2014). Rényi entropy provides another adjustable-order framework and has been used to develop closed-form one-dimensional velocity profiles with improved predictive accuracy over classical and Shannon-entropy-based models (Rényi, 1961; Kumbhakar and Ghoshal, 2016). More recently, fractional entropy has been used to account for incomplete or partially known information in turbulent flows (Kumbhakar and Tsai, 2023). In such models, the entropy index and Lagrange multipliers are determined through constraint systems, often including momentum conservation, leading to analytical velocity expressions valid across the flow depth (Kumbhakar et al., 2020; Ahamed and Kundu, 2024).

These developments show a shift from purely deterministic velocity laws toward uncertainty aware entropy-based descriptions. Deterministic models provide physical simplicity, while entropy-based models offer unified probabilistic formulations capable of representing complex turbulent velocity structures. This motivates the present thesis to use fractional differential entropy for modeling vertical velocity profiles and to connect the resulting formulation with suspended sediment transport analysis.

1.4.4 Vertical profile of suspended sediment concentration and its significance

Sediment transport in open channels occurs mainly as bed load and suspended load, with the present study focusing on the suspended component (Dey, 2012, 2014). Suspended sediment concentration (SSC) is important for estimating sediment fluxes, reservoir sedimentation, fluvial morphology, pollutant transport, and water-quality impacts. In turbulent open-channel flows, suspended particles are maintained by the balance between gravitational settling and upward turbulent diffusion. As a result, SSC is generally highest near the bed and decreases toward the free surface, making accurate near-bed modeling essential.

Experimental studies show that vertical SSC profiles may be classified into Type I and Type II profiles. Type I profiles decrease monotonically from the bed to the free surface, whereas Type II profiles exhibit non-monotonic behaviour with an interior maximum. Type II behaviour is associated with complex turbulence-particle interactions, lift forces, and nonlocal transport effects, and remains difficult to represent using classical models (Ahamed and Kundu, 2023).

Classical deterministic descriptions of SSC are mainly based on advection–diffusion theory, with the Rouse equation serving as the standard benchmark (Rouse, 1937). Although widely used, the Rouse model relies on simplifying assumptions such as logarithmic velocity distribution and idealized diffusivity. These assumptions may fail near the bed and free surface, particularly in sediment-laden turbulent flows and in cases involving velocity-dip effects. Moreover, deterministic diffusion-based models are generally limited in their ability to represent non-monotonic SSC profiles.

Entropy-based probabilistic models provide an alternative by treating SSC as a random variable and deriving its distribution through the maximum entropy principle. Shannon entropy-based models yielded exponential-type SSC profiles and improved near-bed predictions compared with classical Rouse-type models (Chiu et al., 2000; Choo, 2000). However, their flexibility is limited because Shannon entropy does not contain a tunable sensitivity parameter. Generalized entropy models were therefore introduced. Tsallis entropy produces power-law-type SSC distributions and improves the representation of nonlinear concentration profiles (Cui and Singh, 2014). Rényi entropy further improves flexibility and can represent physically meaningful nonzero concentrations near the free surface (Ghoshal et. al, 2018). Nevertheless, these generalized entropy models are still mainly suited to monotonic Type I profiles.

Fractional entropy provides a more flexible framework by incorporating an entropy index associated with incomplete or partially known information, which is common in sediment-laden turbulent flows (Ahamed and Kundu, 2023). Existing studies show that fractional entropy-based SSC models can outperform Shannon-, Tsallis-, and Rényi-based models for Type I profiles and can also represent both Type I and Type II SSC profiles within a unified framework.

The key research gap is therefore the need for an entropy-based SSC formulation that is flexible enough to capture strong near-bed gradients, nonlinear vertical decay, and possible non-monotonic concentration behaviour, while remaining physically interpretable and applicable with limited observational data. This motivates the present thesis to develop fractional entropy-based SSC models that connect probabilistic uncertainty modeling with the physical structure of sediment transport in open-channel turbulent flows.

1.4.5 Survival analysis

Survival analysis consists of statistical methods for modeling the time until the occurrence of an event of interest, such as death, disease recurrence, recovery, or system failure. It is widely used in clinical research to evaluate treatment effectiveness through patient survival times over a follow-up period (Kartsonaki, 2016). Although originally developed in medical and cancer studies, survival analysis is now used in epidemiology, public health, demography, reliability engineering, and health economics because it accounts for both the timing and occurrence of events.

The two fundamental quantities in survival analysis are the survival and hazard functions. For a survival time T with cdf $F(t)$, the survival function is

$$S(t) = \mathbb{P}(T > t) = 1 - F(t),$$

which gives the probability of surviving beyond time t. The hazard function describes the instantaneous event risk at time t, conditional on survival up to that time:

$$h(t) = \lim_{\Delta t \to 0} \frac{\mathbb{P}(t \leq T < t + \Delta t \mid T \geq t)}{\Delta t} = \lim_{\Delta t \to 0} \frac{S(t) - S(t + \Delta t)}{\Delta t \, S(t)}.$$

These functions describe the distributional behaviour of lifetime data and are central to clinical, demographic, and reliability applications.

Survival analysis methods are commonly classified as non-parametric, semi-parametric, and parametric. Non-parametric methods make no distributional assumption. The Kaplan–Meier estimator is the most widely used method for estimating the survival function in the presence of right-censored data (Kaplan and Meier, 1958; Goel et al., 2010). If $t_1 < t_2 < \cdots < t_K$ are the ordered event times, with d_k events among n_k individuals at risk just before t_k, then

$$\widehat{S}(t) = \prod_{t_k \leq t} \left(1 - \frac{d_k}{n_k}\right).$$

The estimator is a step function that changes only at observed event times and is useful for descriptive survival analysis and group comparison.

Semi-parametric methods specify the effect of covariates while leaving the baseline hazard unspecified. The Cox proportional hazards model is the most common example and relates covariates to survival through hazard ratios (Cox, 1972; Kalbfleisch and Schaubel, 2023). Parametric methods assume a specific lifetime distribution, such as exponential, Weibull, log-normal, or log-logistic, and are useful for direct estimation, prediction, extrapolation, and reliability analysis.

These classical survival tools provide the statistical foundation for the quantile-based entropy measures developed later in the thesis. In particular, the presence of censoring and the difficulty of reliable density estimation motivate the use of quantile-based entropy formulations for measuring lifetime and death-time uncertainty.

1.4.6 Survival analysis for human mortality and death-time uncertainty

Survival and mortality analysis is central to demography, actuarial science, and biostatistics. Traditional demographic tools such as life tables and life expectancy summarize population health, but they do not fully describe the distribution of ages at death or the uncertainty associated with lifetime variation. Survival analysis addresses this by treating age at death as a r.v. and studying mortality through survival functions, hazard functions, and lifetime distributions.

In demographic studies, the survival function $S(t)$ gives the probability of surviving beyond age t. Its shape reflects the degree of dispersion in ages at death. The concept of *rectangularization of the survival curve* describes the concentration of deaths at older ages and the compression of mortality into a narrower age interval. A more rectangular survival curve indicates lower lifespan uncertainty, whereas a less rectangular curve reflects greater heterogeneity in survival outcomes.

Entropy-based measures provide a useful way to quantify this death-time uncertainty. Keyfitz (1977) introduced the Keyfitz entropy index to measure the sensitivity of life expectancy to proportional mortality changes across ages. This index links the shape of the survival curve with lifespan variability: lower entropy corresponds to stronger rectangularization, while higher entropy indicates greater uncertainty in age at death. Empirical work by Nagnur (1986) further showed that mortality change involves both increasing mean survival and decreasing dispersion in ages at death.

Information-theoretic approaches to population dynamics and aging were further developed by Demetrius (1974, 1975, 1976), establishing a formal link between Shannon-type entropy and demographic survival analysis. More recent studies have applied Shannon entropy, cumulative residual entropy, and related measures to life tables and survival functions (Machado and Lopes, 2021). These measures help compare mortality regimes, lifespan inequality, rectangularization, and structural shifts caused by socioeconomic change, medical progress, or external shocks.

The remaining research gap is that many existing entropy-based survival measures rely on density, distribution, or survival-function representations that may be difficult to estimate reliably for censored, incomplete, or irregular lifetime data. This motivates the quantile-based fractional generalized cumulative past entropy framework developed in this thesis, which uses quantile representations to provide a more flexible and robust measure of death-time uncertainty, especially in the presence of censored survival data.

1.5 Overview of the major outcomes

The present work highlights the versatility and unifying potential of fractional order entropy measures in addressing complex challenges across finance, environmental hydraulics, and medical survival data analysis. The thesis comprises six major research contributions, which are summarized below.

Chapter 1 introduces the principal concepts and provides a summary of the major ideas from the domains explored in the study.

Chapter 2 introduces a novel decision-making framework for stock selection based on fractional order entropy due to Ubriaco. By tuning the fractional parameter α, the model captures varying attitudes of individuals toward risk. Values of α near 1 indicate high risk tolerance (adventurous attitude), while those near 0 reflect risk aversion (conservative attitude). The sensitivity of the fractional order entropy to changing risk preferences of decision-makers is demonstrated through four real-world portfolio models, namely, large-cap, mid-cap, diversified, and hypothetical. Furthermore, two new risk measures, termed as expected utility–fractional entropy (EU-FE) and expected utility-fractional entropy and variance (EU-FEV), are introduced to develop decision models aligned with investors' risk preferences. The performance of the developed models are compared with existing decision-making approaches, thereby demonstrating its superiority and consistency. The effectiveness of the decision model is further tested with financial stock market data of Portuguese stock market (PSI 20) by finding efficient frontiers of portfolio with the aid of *Artificial Neural Network* (ANN).

Inspired by the developments in Chapter 2, we introduce the notion of normalized fractional order entropy aligned with investors' risk preferences in **Chapter 3**. Here, we propose two novel risk measures, termed normalized expected utility–fractional entropy (NEU-FE) and normalized expected utility–fractional entropy–variance (NEU-FEV), which combine normalized fractional entropy with expected utility and variance. The risk sensitivity is controlled by the fractional parameter α, interpolating between conservative or risk aversion ($\alpha \to 0$) and adventurous or high-risk tolerance ($\alpha \to 1$) attitudes. The proposed risk measures form the basis of two decision making frameworks applied to the Indian stock market data (NIFTY 50) to identify an optimal low-risk set of five stocks from a broader list. Comparative analyses with existing fractional entropy-based models, supported by machine learning techniques (Random Forest, Ridge Regression, Lasso Regression, and Artificial Neural Networks), demonstrate the robustness of the proposed measures. Statistical significance tests further validate model reliability and identify the most effective approach for ranking stocks in accordance with investors' preferences.

In the preceding chapters, Ubriaco entropy is studied for discrete r.vs. In **Chapter 4**, this framework is extended to the continuous domain through a detailed investigation of its continuous analogue, termed fractional differential entropy (FDE). Several analytical and numerical properties of FDE are established, highlighting its distinctive features and advantages over existing entropy measures. This entropy is evaluated for some well-known continuous distributions, illustrating its relevance to reliability analysis and statistical modeling of complex systems. Since the vertical variation of velocity governs momentum transfer and turbulence structure, the flow velocity and its vertical distribution in open-channel hydraulics is studied within the FDE framework. We model the one-dimensional vertical velocity profile of turbulent flows in wide open channels by using FDE and the principle of maximum entropy. A one-parameter spatial distribution function is introduced to improve velocity estimation. The proposed model is validated using experimental and field data through regression analysis, and a comparative study demonstrates its superior performance over existing entropy-based hydraulic models.

Open channel flow often carries toxic wastes and non-degradable materials as sediments, which negatively impact marine life and water quality. Regular monitoring of the distribution of suspended sediment concentration (SSC) in open channel flows is critically important for effective water resource management. In **Chapter 5**, we introduce a simplified yet robust model for estimation, grounded in FDE theory to accurately characterizing the vertical distribution of SSC in open-channel flows. The normalized SSC is modeled as a continuous r.v, subject to a physical boundary condition of zero concentration at the water surface. Using a leading-order approximation approach, the problem is then expressed in terms of a power series solution within a maximum entropy optimization framework. The resulting closed-form solution for the SSC profile is rigorously validated against both experimental data and real-world field measurements. Comparative analyses demonstrate that the proposed FDE-based model not only achieves higher predictive accuracy but also offers substantial computational efficiency relative to conventional deterministic and classical entropy-based methods. Further the sensitivity of the parameters of the proposed model is investigated through resampling methods such as bootstrap and Jackknife empirical likelihood methods. These findings suggest that the FDE approach provides an effective and practical tool for sediment transport modeling in natural and engineered waterways.

In **Chapter 6**, an alternative extension of the SSC model is proposed using the fractional order entropy due to Machado. The Lambert W function is employed to derive the pdf under a specified convergence criterion, which is then used to obtain the vertical concentration distribution. To address the computational complexity of determining the Lagrange multipliers and the entropy index in the fractional entropy-based concentration model, a new minimization problem is formulated that incorporates the convergence condition. The proposed model is validated using both experimental and field data sets. Additionally, regression and error analyses are conducted to demonstrate the model's advantages over extant entropy-based probabilistic and classical deterministic models.

Understanding uncertainty in human mortality is a central problem in survival analysis, particularly for life-threatening diseases such as lung cancer. Classical survival analysis tools, including survival and hazard functions, primarily provide pointwise or instantaneous descriptions of mortality risk and therefore offer limited insight into the evolving uncertainty associated with survival times at the population level. Information-theoretic measures provide a natural complementary framework by quantifying the dispersion and unpredictability of lifetimes in a distributional sense. In this context, in **Chapter 7**, a *quantile-based fractional generalized cumulative past entropy* (QFGCPE), along with its dynamic extension (DQFGCPE), is proposed to analyze uncertainty in mortality using life-table data and to study the temporal evolution of uncertainty in lung cancer survival. By integrating quantile-based representations with fractional order entropy, the proposed framework enables tunable sensitivity across survival horizons while avoiding distributional assumptions. Key analytical properties, including bounds, monotonicity, and stochastic ordering relations, are established, and nonparametric estimators based on empirical and Kaplan–Meier methods are developed to accommodate both uncensored and right-censored data. Overall, the proposed approach offers a unified and interpretable measure of mortality uncertainty that complements classical survival analysis tools.

In **Chapter 8**, this thesis presents the concluding remarks, which justify our claim that fractional order Ubriaco entropy and its generalizations due to Machado and the proposed quantile-based representation present a versatile and powerful extension of classical information theory. Through new formulations, modeling frameworks, and extensive empirical validation across finance, hydrodynamics and biomedical survival analysis, the work establishes fractional entropy as a unifying paradigm for uncertainty quantification and complex system modeling. Thereafter, this chapter presents some future scopes and unaccomplished extensions of this work. This chapter is followed by a comprehensive list of references. In addition, a list of publications arising from this thesis is provided at the end.

To maintain self-containment, key concepts and foundational results are intentionally reiterated across chapters, with selected entropy definitions and application-specific details reproduced where necessary.

Chapter 2

Fractional Order Entropy-Based Decision-Making Models under Risk [1]

"A good decision is based on knowledge and not on numbers."
— Plato

Building on the decision analysis frameworks and financial applications reviewed in the previous chapter, this chapter examines the fractional order entropy for discrete random variables, introduced by Ubriaco (2009), as a behavioral measure of uncertainty for representing investor risk preferences under varying probability structures. By analyzing how the fractional parameter reflects conservative (low risk tolerance) to adventurous (high risk tolerance) risk attitudes, this study establishes a flexible framework for quantifying risk-return trade-offs in financial portfolio decision-making. Building on the behavioral insights of Ubriaco entropy, two novel entropy-based decision-making models are proposed to support rational and profit-seeking investment decisions. Thereafter, the models are integrated with artificial neural networks (ANNs) to identify optimal asset combinations and construct efficient portfolio frontiers, demonstrating the practical relevance of fractional order entropy in modern financial optimization problems.

[1] The work presented in this chapter has been published in *Communications in Nonlinear Science and Numerical Simulation*, 152, 109106 (2026), https://doi.org/10.1016/j.cnsns.2025.109106.

2.1 Introduction

The introduction of statistical moments as a measure to quantify financial returns and risk has been recorded as one of the biggest milestones in modern portfolio theory. A systematic approach to decision-making in the context of portfolio selection was first introduced by Markowitz (1952) through the formulation of the mean-variance criterion for identifying optimal portfolios. In this framework, an optimal portfolio is achieved by maximizing expected returns represented by the first-order moment (mean) of the return distribution of the stocks, while minimizing the risk quantified by the second-order moment about the mean (variance). However, since variance works only for symmetric distributions, relying on it as a risk measure can sometimes lead to misleading results. To address this issue, Philippatos and Wilson (1972) introduced the mean-entropy framework, establishing entropy as a more general and competent risk measure, since it depends on the probability distribution of outcomes rather than directly on the numerical values of the underlying data and does not require restrictive distributional assumptions. The mean-entropy model was shown to be equally efficient as the mean-variance model. Thereafter, entropy-based approaches have gained prominence in portfolio selection as alternatives to traditional risk measures. This line of work was further extended by Philippatos and Gressis (1975) for evaluating the behavior of entropy-based measures under a variety of return distributions, including uniform, normal, and lognormal models. Their findings demonstrated that entropy remains a robust and informative measure of uncertainty even when the underlying data deviate from classical assumptions. In particular, they highlighted a key advantage of entropy, noting that unlike variance-based measures, it does not rely on any specific distributional form. This makes entropy especially suitable for modelling financial returns that often exhibit asymmetry, heavy tails, and other non-Gaussian characteristics. Furthermore, Usta and Kantar (2011) and Aksarayli and Pala (2018) incorporated higher order statistical moments in their entropy-based models to develop the mean-variance-skewness-entropy (MVSE) and the mean-variance-skewness-kurtosis-entropy (MVSKE) models, respectively. Recently, Mercurio et al. (2020) introduced a return-entropy-based portfolio optimization model that outperformed several existing approaches. Collectively, these studies indicate that integrating entropy with other decision-making criteria improves model performance (cf. Yang et al., 2017; Brito, 2023, and references therein).

However, all these studies just focused on constructing efficient portfolios from a preselected set of stocks. But real-world investment begins with identifying the ideal set of stock options. Increasing the number of stocks in a portfolio helps in lowering the variance of a portfolio. This will lead to reduction in risk. Consequently, diversifying a portfolio lowers the perceived risk associated with return uncertainty. However, the degree of diversification of a portfolio depends on the investors' risk attitudes towards return uncertainty and the expected utility of the stocks. It is considered that investors with high risk tolerance will prefer actions or investment decisions with higher returns while those with low risk tolerance will prefer decisions with moderate returns so as to avoid risk. Therefore, an effective decision-making framework must account for both utility-based risk aversion and sensitivity to uncertainty in returns. Thus, the balance between risk and return can be achieved by monitoring the number of stocks prior to constructing an efficient frontier for portfolios. A variety of stock selection models are developed in literature. Among them some noteworthy contributions include the use of some machine learning methods designed to help with stock selection and construction of efficient portfolios. Liu and Yeh (2017) used artificial neural networks to develop stock selection models tailored to investors' risk preferences. Various other machine learning methods, such as long short-term memory (LSTM), eXtreme Gradient Boosting (XGBoost), support vector regression, genetic algorithms, random forests, and support vector machines (SVM), have also been applied to evaluate stock quality and rank them based on predicted risks and returns (see Brito, 2023, and references therein). These ranked stocks are then used to construct optimal portfolios using techniques discussed earlier, like the mean-variance and mean-entropy methods. Furthermore, Yang et al. (2017) utilized the expected utility–entropy model, originally developed by Yang and Qiu (2005), for stock selection prior to portfolio optimization. More recently, Brito (2020, 2023) extended this model by incorporating variance into the decision-making criteria for stock selection.

Nevertheless, existing decision-making models remain limited in their ability to capture the dynamic nature of investors' risk tolerance in relation to the uncertainty embedded in stock return distributions. In particular, these models often fail to integrate machine learning techniques, such as artificial neural networks (ANNs), which are well suited for analyzing the complex and nonlinear relationships between input variables and output responses. Moreover, they need behaviorally grounded extensions, such as incorporating fractional or other generalized entropies into modeling decision-making under risk influenced by heterogeneous risk attitudes of individuals. Besides, the choice of utility functions and associated trade-off parameters in current models is frequently ad hoc, with limited empirical calibration or behavioral justification. Furthermore, existing entropy-based stock selection models formulated by Yang et al. (2017) and Brito (2023) do not adequately capture the interaction between investors' sensitivity to return uncertainty and the expected utility derived from investment outcomes.

In response to these limitations, machine learning (ML)-driven approaches have emerged as powerful tools in modern financial decision-making, significantly influencing trading and investment strategies. Leveraging the predictive capabilities of ML techniques, particularly ANNs, this study introduces novel fractional order entropy-based risk measures that explicitly account for individual preferences and evolving risk tolerance levels in decision-making under uncertainty. The resulting frameworks integrate expected utility, variance, and fractional order entropy within a unified decision-making structure. This integration provides an enhanced, risk-aware methodology for stock selection and portfolio optimization, effectively bridging behavioral risk modeling with data-driven learning techniques. These new risk measures demonstrate how integrating conventional decision-making frameworks with artificial neural networks (ANNs) produces a robust and adaptive framework for precise and insightful stock selection in dynamic market environments, while explicitly accounting for heterogeneous investor behavior under risk. By embedding behavioral sensitivity to uncertainty within the learning architecture, the proposed framework addresses key limitations of existing models and enables more effective portfolio management in the presence of risk. In particular, individual risk sensitivity arising from return uncertainty is behaviorally modeled through the fractional parameter of Ubriaco entropy (Ubriaco, 2009), which provides a flexible mechanism for representing varying degrees of risk aversion and risk-seeking behavior.

To facilitate clarity, the remainder of the chapter is organized into the following sections: Section 2.2 presents a brief review of the existing literature relevant to the present study and identifies the research gaps that motivate its objectives. In Section 2.3, the behavior of the fractional order information gain and entropy functions due to Ubriaco is studied in the human decision-making context, with the results further illustrated using real-world portfolio datasets (diversified, large-cap, mid-cap and hypothetical). In Section 2.4, we introduce two risk measures based on Ubriaco fractional entropy for modeling decision-making under risk. The section examines their theoretical properties as risk measures and analyzes their behavior across different values of the fractional parameter. In addition, the proposed decision-analysis models are compared with existing Shannon entropy-based models to solve some important investment decision problems and paradoxes. Their relative advantages over traditional entropy-based approaches are further demonstrated using real market data from the Portuguese stock market index (PSI20), complemented by a detailed statistical analysis of the proposed risk measures using ANN. Section 2.5 presents stock selection methodologies based on the proposed decision models and constructs efficient portfolio frontiers using the mean-variance optimization framework applied to the PSI20 data. Finally, Section 2.6 concludes the chapter with a summary of the main findings and implications.

2.2 Information gain function, entropy and decision models under risk: Review

Building on the motivation and objectives outlined in the previous section, this study adopts fractional entropy as a central tool for formulating decision-making models under risk arising from uncertainty. The proposed framework explicitly incorporates individual risk attitudes through the fractional parameter α, which enables a flexible representation of heterogeneous behavioral responses to uncertainty. Accordingly, this section provides a concise review of the information gain and fractional entropy measures employed in the present study, emphasizing their effectiveness in quantifying uncertainty and modeling risk sensitivity. In addition, it surveys relevant literature on entropy-based decision-making and portfolio selection, highlighting prior efforts to integrate investor risk preferences into optimal decision frameworks and identifying the gaps addressed in this work.

The Shannon entropy is one of the most popular information measure quantifying the uncertainty of a random action having multiple possible states of nature or outcomes pioneered by Shannon (1948). The uncertainty associated with a specific state can be represented in terms of information gain function. Then the entropy can be considered as the expected value of the information gain. High values of information gain (or the level of surprise) on the actual occurrence of an outcome is associated with higher uncertainty. The Shannon information gain function is defined as:

$$I_S(p) = -\log p(x), \tag{2.2.1}$$

where $p(x) = P(X = x)$ is the probability mass function (pmf) describing the distribution of a discrete random variable X corresponding to an action. The least biased representation of an action's uncertainty is determined by the pmf with maximum Shannon entropy. This interesting feature of Shannon entropy evoked interest in researchers to design alternative entropy formulations for a wide variety of applications, especially in decision-making. Among these generalized entropy measures, one of the most popular and useful ones are those proposed by Rényi (1961) and Tsallis (1988).

In the context of human decision-making, individuals' differing levels of risk tolerance have a significant impact on the perceived uncertainty of an outcome. This accounts for the diverse behavioral patterns reflected in the information gain function. Aggarwal (2021b) formulated a new form of probabilistic entropy that offers a holistic representation of the perceived uncertainty. This formulation introduces a positive real-valued parameter to capture an individual's attitude towards uncertainty. However, these entropy formulas are based on probabilistic uncertainty. Therefore, to account for fuzzy uncertainties or the uncertainties owing to incompleteness, randomness and vagueness along with the individual attitudes in human decision-making framework, some other variations of fuzzy entropy functions have been developed in literature (see Aggarwal, 2021a, and references therein). Despite all the modifications in the entropy formulation, the interval of entropy values between minimum and maximum information gain is too wide for most of the existing generalized entropy formulations. Intuitively, this will affect the prediction accuracy and consistency of the decision models. Hence, the Shannon entropy is predominantly used in the decision models under risk and uncertainty.

von Neumann and Morgenstern (1947) pioneered the use of expected utility as a criterion for making optimal decisions among risky alternatives in their expected utility model. This model is based on the assumption that individuals tend to choose a risky option to achieve maximum expected utility. Nonetheless, the model falls short in both normative and descriptive aspects when addressing well-known decision paradoxes like those of Allais (1953) and Lévy (1992). Later, Yang and Qiu (2005) developed a normative decision-making model under risk, namely, the expected utility-entropy (EU-E) model. It incorporated both the decision-maker's subjective preferences through a utility function and objective uncertainty quantified by Shannon entropy. They used the weighted linear average of the expected utility function and the entropy function to quantify the risk associated with an action. Yet, the EU-E model lacked mathematical generality and failed to satisfy certain behavioral axioms related to the ordering of preferences among uncertain prospects and their combinations. To address this, Luce et al. (2005) introduced a linear weighted utility function combined with an entropy term as a numerical representation. Yang and Qiu (2014) later improved the EU-E model by introducing a normalized entropy function, resulting in the normalized expected utility-entropy (NEU-E) model, designed to address decision problems involving highly distinct states of nature. This decision approach provides a logical framework to anticipate the certainty effect described in prospect theory (see Kahneman and Tversky, 1979). Dong et al. (2016) further explored the expected utility and entropy-based decision-making model, highlighting the pivotal role of Shannon entropy in risk-based decision analysis. Further refinements were introduced by Brito (2020, 2022) through the incorporation of variance as an additional risk measure. These models have successfully resolved several decision paradoxes and investment problems, offering a better explanation for anomalies in individual decisions. They also provided deeper insights to the mean-variance criterion introduced by Markowitz (1952) and Pollatsek and Tversky (1970). Overall, these decision models provide substantial evidence that incorporating entropy enhances decision robustness, particularly in highly uncertain environments. However, most existing decision-analysis frameworks remain confined to Shannon entropy and do not explore fractional order generalizations or mechanisms for real-time adaptability.

Motivated by these observations, this chapter rigorously examines the potential of the fractional order entropy proposed by Ubriaco (2009) to characterize the influence of human risk attitudes on information gain associated with outcome uncertainty. The fractional Ubriaco entropy is particularly significant, as it represents a generalized fractional extension of Shannon entropy. By incorporating a fractional parameter $\alpha \in (0,1)$, the formulation given by Ubriaco provides enhanced flexibility for characterizing complex systems with diverse statistical properties at a finer level of granularity (see Machado, 2014). Moreover, the fractional framework has been further extended to construct a broad class of fractional order entropy measures by replacing the pmf with sf and cdf, as demonstrated by Xiong et al. (2019) and Di Crescenzo et al. (2021), respectively. If $p(x) = P(X = x)$ is the pmf for x^{th} outcome of an action, then the fractional order entropy for a n-state discrete system is defined by Ubriaco (2009) as:

$$H_U^{\alpha}(p) = \sum_{x=1}^{n} p(x)(-\log p(x))^{\alpha};\ \alpha \in [0,1]. \tag{2.2.2}$$

Clearly, when $\alpha = 1$, the fractional order entropy (2.2.2) is equivalent to the Shannon entropy.

Here, the parameter α allows the Ubriaco entropy function (2.2.2) to customize itself so as to accommodate the unique attitudes of decision-makers towards the likelihood of an outcome. Risk-seeking individuals are more affirmative about the occurrence of low probable outcomes. Such people have an adventurous attitude while making decisions. And the ones who are more averse to risks are more doubtful about low probable outcomes. Such individuals are said to have a conservative attitude towards certainty of an outcome (see Aggarwal, 2021a,b). However, Shannon entropy lacks the flexibility to reflect such subjective perceptions of uncertainty that arise from heterogeneity in individual risk attitudes. This limitation is naturally overcome by the fractional order entropy (2.2.2), where the fractional parameter α provides a mechanism to adapt the entropy measure to varying behavioral responses toward uncertainty.

This influenced us to adopt the fractional order entropy due to Ubriaco in modeling risky decisions. The general decision analysis model is framed as: Let K be a finite action space comprising actions k_i for $i = 1, 2, \ldots, l$. Each risky action k_i is associated with a state space $\Theta_i = \{\theta_{i_1}, \theta_{i_2}, \ldots, \theta_{i_{l_i}}\}$, where the overall state space is denoted by $\Theta = \{\theta_1, \theta_2, \ldots, \theta_l\}$. The probability distribution over states given action k_i is represented by $p_{ij} = P(\theta = \theta_{ij} \mid k = k_i)$, subject to the conditions $\sum_{j=1}^{l_i} p_{ij} = 1$ and $p_{ij} \geq 0$. The expected payoff resulting from state θ_{ij} under action a_i is given by $X = X(k_i, \theta_{ij}) = x_{ij}, \quad (i = 1, 2, \ldots, l;\ j = 1, 2, \ldots, l_i)$. The utility function, capturing an individual's risk attitude, is denoted by $u = u(X)$. A detailed tabulated form of this generalized decision model is given in Yang and Qiu (2005). To advance the decision models proposed by Yang and Qiu (2005) and Brito (2020), we introduce the use of Ubriaco fractional entropy (2.2.2) in place of Shannon entropy to capture the perceived uncertainty of outcomes due to varying risk attitudes of individuals alongside the risk preferences or risk aversion tendency represented by the expected utility of the outcome. This leads us to formulate two novel risk measures:

1. Expected Utility–Fractional Entropy (EU-FE) risk measure, and
2. Expected Utility–Fractional Entropy–Variance (EU-FEV) risk measure.

2.3 Information gain and entropy functions

2.3.1 Ubriaco information gain function

In decision-making, individuals exhibit either adventurous or conservative attitudes, reflecting high or low risk tolerance, respectively. An adventurous person tends to trust the occurrence of an outcome even when it is uncertain or unlikely. In contrast, a conservative individual remains doubtful about an outcome's occurrence, even as its probability increases. To capture these nuances in human behavior, we use the Ubriaco information

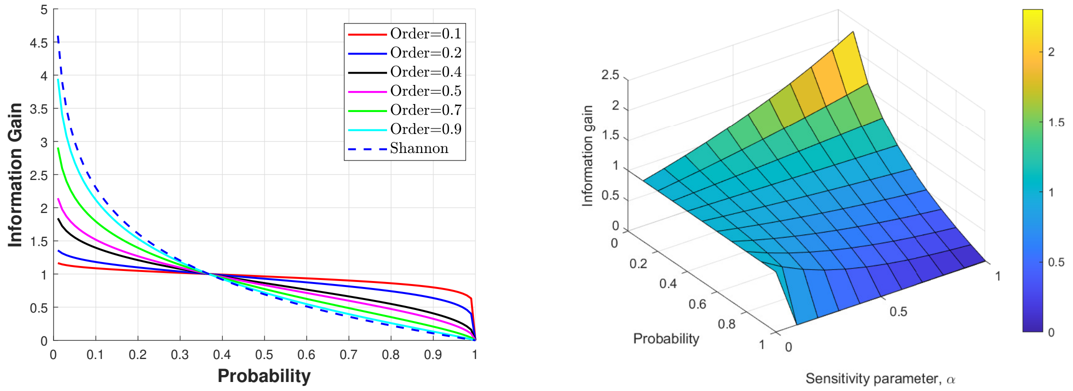

Figure 2.3.1: Information gain function for Ubriaco entropy w.r.t probability.

gain function, expressed as follows:

$$I_U^{\alpha}(p) = (-\log p(x))^{\alpha}, \alpha \in [0, 1], \tag{2.3.1}$$

where $p(x) \in (0, 1]$ denotes probability of the x^{th} likely outcome of a random event.

From (2.3.1), we observe that the information gained from an outcome is inversely proportional to its likelihood $p(x)$. However, the rate at which information decreases with increasing $p(x)$ varies with different values of α. Therefore, it is important to examine the behavior of function (2.3.1) with respect to both varying probabilities and changing α values.

Fig. 2.3.1 illustrates that for higher values of $\alpha \geq 0.5$, the information gain exhibits a sharper decline at low probability values, reflecting a more adventurous risk attitude. Individuals with such preferences derive substantial information from low-probability events; however, as p approaches unity, their perception of uncertainty stabilizes, resulting in only marginal changes in perceived outcome uncertainty. Conversely, for $\alpha < 0.5$, the information gain curve flattens, indicating a slower decline in the information gained, particularly at lower probability levels ($p < 0.5$). As p increases beyond 0.5, the information gain decreases more rapidly, approaching zero near $p = 1$, where the decision-maker attains complete confidence in the outcome. In this regime, the occurrence of the outcome generates little to no surprise or informational content. Consequently, lower values of α correspond to a more conservative attitude toward uncertainty. Moreover, as an individual's inclination toward adventurous behavior increases, the subjective range of low-probability outcomes narrows with increasing α (from 0.5 to 1) and widens as conservative preferences dominate. This behavior indicates that higher values of α exert a stronger influence on reducing information gain at low probability levels, whereas lower values of α (close to zero) have a more pronounced effect at higher probability values p.

Thus, the fractional parameter α in the Ubriaco information gain and entropy framework admits a clear behavioral interpretation in the context of decision-making under uncertainty. It acts as a sensitivity parameter that regulates how strongly a decision-maker responds to variations in outcome probabilities. Larger values of α amplify the informational impact of low-probability events, thereby modeling optimistic or risk-seeking behavior, whereas smaller values attenuate this sensitivity and emphasize caution toward unlikely outcomes, reflecting conservative or risk-averse preferences. In the limiting case $\alpha \to 1$, the measure reduces to Shannon entropy, corresponding to a neutral, distribution-driven assessment of uncertainty. Conversely, as $\alpha \to 0$, the entropy becomes increasingly dominated by high-probability outcomes, capturing heightened aversion to uncertainty. Thus, the fractional parameter α provides a continuous and interpretable mechanism for embedding heterogeneous behavioral risk attitudes within an information-theoretic decision framework. Consequently, the deviations in individual risk-taking tendencies, particularly, the conservative behavioral responses to uncertainty, that couldnot not captured by Shannon entropy can be effectively represented using the fractional order Ubriaco information gain function (2.3.1). By adjusting the fractional parameter $\alpha \in [0, 1]$, the function characterizes how decision-makers with differing risk tolerance levels perceive information gain or uncertainty across varying probability values.

2.3.2 Sensitivity of Ubriaco information gain function

Since variations in human attitudes toward uncertainty substantially affect the rate at which information about outcome certainty diminishes, the response of the information gain function to changes in probability displays distinct patterns across different values of α, particularly at low and high probability levels. This response behavior is referred to as the elasticity, or sensitivity, of the information gain function.

The sensitivity can be quantified by taking the modulus of the ratio of the function's slope with respect to probability to the information gain per unit probability. Mathematically, this elasticity measure is defined as:

$$\mathcal{E} = \left| \frac{dI_U^\alpha(p)/dp}{I_U^\alpha(p)/p} \right| = \frac{\alpha}{-\log p}, \tag{2.3.2}$$

where $|\cdot|$ denotes the absolute value. The quantity $\mathcal{E}$ represents the degree of responsiveness of the information gain function to variations in likelihood values, thereby providing a measure of its sensitivity to changes in probability.

From the sensitivity plot shown in Fig. 2.3.2, the elasticity function defined in (2.3.2) is observed to be increasing and convex for all $\alpha \in [0, 1]$. The information gain exhibits greater sensitivity at higher probability levels ($p > 0.5$) and relatively weaker responsiveness at lower values of p. As α decreases, the probability values at which sensitivity increases sharply shift progressively closer to unity. This behavior indicates that smaller values of α are associated with reduced responsiveness over a broader range of probabilities, reflecting a more conservative attitude toward uncertainty. In particular, for sufficiently small α, substantial variations in information gain occur only when p approaches one. Equivalently, as $\alpha \to 0$, noticeable changes in sensitivity are confined to a narrow region of high-probability values (with p shifting toward 1).

Consequently, the fractional parameter α may be tuned to represent varying levels of sensitivity consistent with individual attitudes toward uncertainty. In this sense, α functions as a behavioral sensitivity parameter for the Ubriaco information gain function, effectively capturing heterogeneity in risk attitudes, especially among decision-makers with low risk tolerance.

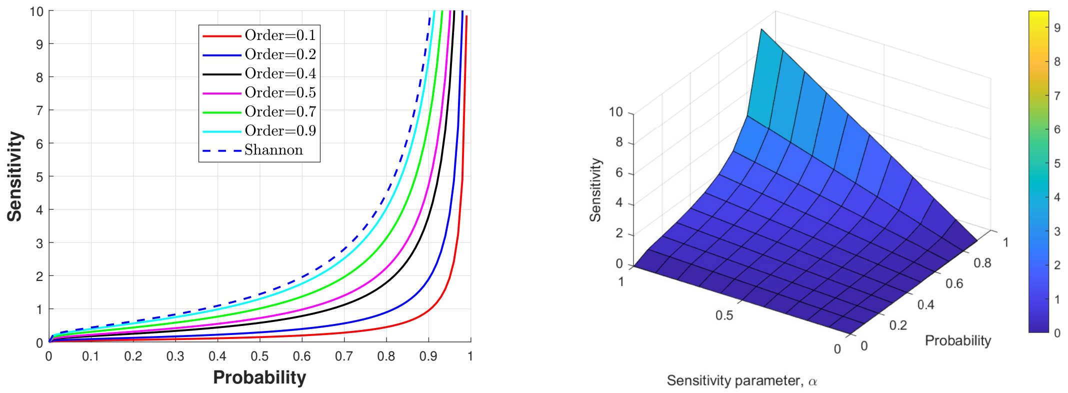

Figure 2.3.2: Sensitivity of information gain function for Ubriaco entropy.

2.3.3 Ubriaco entropy function

Entropy can be interpreted as the area under the curve of an entropy function. Comparing these areas helps evaluate the effectiveness of an entropy measure in representing uncertainty. Intuitively, an entropy function that covers a larger area is considered a more efficient measure of information for a given random variable with finite support (see Karci, 2016). Therefore, we analyze the Ubriaco entropy function $h_U^\alpha(p) = p(x)[-\log(p(x))]^\alpha$ for different values of α and compare its performance with the Shannon entropy $h_S(p) =$

$-p(x)\log p(x)$. The following theorem presents the monotonic behavior of $h_U^\alpha(p)$ as the order α varies. The proof is straightforward and hence omitted.

Theorem 2.3.1. *The entropy function h_U^α decreases as α decreases from 1 to 0 when $0 < p(x) \leq \frac{1}{e}(= 0.368)$. However, when $0.368 < p(x) < 1$, the entropy function shows an increasing behavior with decrease in α.*

Proof. The result is obtained by equating the derivative of the entropy function $h_U^\alpha(p)$ to zero and assuming the fractional order information gain to be non-zero. □

Remark 2.3.1. *From Theorem 2.3.1, we can conclude that when $\frac{1}{e} < p(x) < 1$, fractional-order entropy measures with $\alpha < 1$ are more suitable for representing system uncertainty, as they capture a higher level of informational content than Shannon entropy. Nevertheless, when $0 < p(x) \leq \frac{1}{e}$, Shannon entropy dominates the corresponding Ubriaco fractional order entropy measures for all $\alpha < 1$.*

This behavior is further elucidated by the illustration shown in Fig. 2.3.3 for a n-state system. The figure also demonstrates that the entropy function $h_U^\alpha(p)$ is non-negative and concave for all admissible values of p.

Thus, for events whose outcome probabilities exceed 0.368, the fractional parameter α can be appropriately tuned to extract maximum information about uncertainty, thereby supporting more informed and effective decision-making.

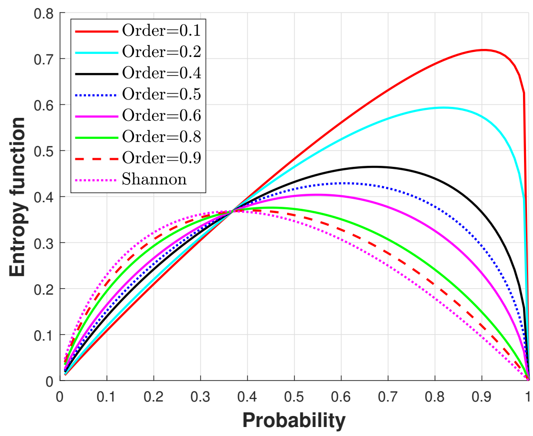

Figure 2.3.3: Ubriaco entropy function of a n -state system for different α.

This claim is further supported by analyzing the behavior of Ubriaco entropy across varying probability values and fractional orders α for a binomial system with two micro-

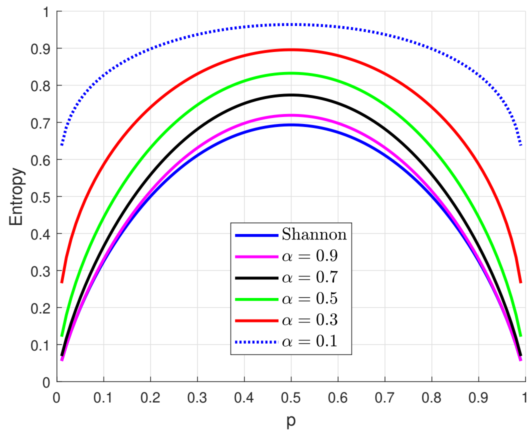

Figure 2.3.4: Ubriaco entropy of a binomial system for different α.

scopic states, as illustrated in Fig. 2.3.4. For such a system, the fractional order entropy is given by:

$$H_U^\alpha(p) = p[-\log p]^\alpha + q[-\log q]^\alpha, \tag{2.3.3}$$

where p =probability of success of an outcome and $q = 1 - p$ is the probability of its failure.

From Fig. 2.3.4, it is evident that the fractional order entropy yields higher values, i.e., more information about uncertainty, when $\alpha = 0.1$, and the least information when $\alpha = 1$ (corresponding to Shannon entropy). This indicates that the information content of Ubriaco entropy increases as α decreases in a binomial system. The figure also shows that, for all $\alpha \in (0, 1]$, Ubriaco entropy attains its peak when the outcomes are equally likely, i.e., when $p = 0.5$.

2.3.4 Validation through portfolio data

The previous section provided a rigorous analysis of the monotonicity of Ubriaco information gain function with respect to probabilities through graphical representations. It was observed that for individuals with higher risk tolerance ($\alpha > 0.5$), the effect of α is more pronounced in reducing uncertainty for low-probability outcomes as their likelihood increases. Consequently, entropy reaches its maximum when $\alpha \to 1$ at low probability values (specifically, below 0.368, as stated in Theorem 2.3.1).

In this subsection, we examine four portfolio models, namely, diversified, large-cap, mid-cap, and hypothetical, as reported in Tables 2.3.1, 2.3.2, 2.3.3, and 2.3.4, respectively, to empirically validate the theoretical findings regarding the behavior of fractional order Ubriaco entropy under varying risk attitudes. The diversified portfolio consists of stocks selected across multiple sectors to reduce concentration risk, whereas the large-cap and mid-cap portfolios are composed of equities classified based on their market capitalization, representing relatively stable and moderately volatile investment categories, respectively. In contrast, the hypothetical portfolio is constructed to exhibit atypical or extreme weight distributions, allowing for the examination of entropy behavior under concentrated and high-risk allocation scenarios. The first three portfolio datasets employed in this chapter are obtained from an actual investor with an interest in the Indian stock market, particularly the NIFTY50 index. The data are sourced from ICICI Direct Research (`https://www.icicidirect.com/research`). However, specific investor details are withheld to preserve confidentiality and privacy. For each portfolio, entropy values are computed using the Ubriaco fractional entropy formulation given in (2.2.2), and the resulting values are summarized in Table 2.3.5. The corresponding ordering of entropy values with respect to increasing fractional order α is presented in Table 2.3.6. All computations of H_U^α and related measures are carried out using *MATLAB R2022b*. Algorithm 1 outlines the computational procedure for applying fractional order entropy to analyze perceived uncertainty and decision-making patterns associated with individual risk attitudes, as represented by the parameter α, across the four portfolio categories.

Algorithm 1: Computation of H_U^α, I_U^α, and h_U^α for Portfolio Data.

Input: Set of stocks $x = \{x_1, x_2, \ldots, x_n\}$;
Portfolio weights $p = [p(1), p(2), \ldots, p(n)]$;
Number of stocks n;
Selected α values: $\alpha = [0.1, 0.3, 0.5, 0.7, 0.9, 1.0]$.
Output: Entropy values H_U^α, information gain I_U^α, and entropy functions h_U^α.

for $i \leftarrow 1$ **to** *length*(p) **do**
  foreach α *in* $[0.1, 0.3, 0.5, 0.7, 0.9, 1.0]$ **do**
    Compute H_U^α using Eq. (2.2.2) for stock x_i;
  end
end
Arrange H_U^α in ascending order for each portfolio to examine entropy trends;
Plot I_U^α and h_U^α to analyze their behavior graphically;

For the first three real-time portfolio models (Tables 2.3.1 – 2.3.3), the entropy values increase monotonically with α, attaining their maximum at $\alpha = 1$, which corresponds to

Table 2.3.1: Portfolio model 1 (Diversified).

Sl. No.	Company (Diversified)	Probabilities ($p(x)$)
1.	Pl Industries	0.03
2.	Eicher Motors	0.025
3.	Balkrishna Industries	0.03
4.	Minda Corp	0.03
5.	HDFC Bank	0.05
6.	HDFC Limited	0.04
7.	Bajaj Finance	0.04
8.	State Bank of India	0.04
9.	Bajaj Finserv	0.04
10.	Multi Commodity Exchange	0.03
11.	Larsen & Toubro	0.03
12.	KSB Pumps	0.03
13.	Thermax	0.03
14.	Bharat Electronics	0.04
15.	UltraTech Cement	0.2
16.	KNR Construction	0.03
17.	Jubilant Food	0.025
18.	Tata Consumer	0.025
19.	Titan Co	0.025
20.	Pidilite Industries	0.03
21.	Radico Khaitan	0.03
22.	Bata India	0.03
23.	Infosys	0.04
24.	Info Edge	0.02
25.	Tata Consultancy Services	0.03
26.	Tech Mahindra Limited	0.02
27.	TeamLease Services	0.03
28.	Container Corporation of India	0.03
29.	Reliance Industries	0.04
30.	Divis Laboratories	0.025
31.	Syngene International	0.03
32.	Brigade Enterprises	0.03
Total		1

Table 2.3.2: Portfolio model 2 (Large Cap).

Sl. No.	Company (Large Cap)	Probabilities ($p(x)$)
1.	HDFC Bank	0.1
2.	HDFC Limited	0.08
3.	Bajaj Finance	0.08
4.	State Bank of India	0.08
5.	Eicher Motors	0.05
6.	Larsen & Toubro	0.06
7.	UltraTech Cement	0.04
8.	Jubilant Food	0.05
9.	Tata Consumer	0.05
10.	Titan Co	0.05
11.	Infosys	0.08
12.	Info Edge	0.05
13.	Tata Consultancy Services	0.06
14.	Tech Mahindra Limited	0.04
15.	Reliance Industries	0.08
16.	Divis Laboratories	0.05
Total		1

Table 2.3.3: Portfolio model 3 (Mid Cap).

Sl. No.	Company (Mid Cap)	Probabilities ($p(x)$)
1.	Balkrishna Industries	0.06
2.	Pl Industries	0.06
3.	Minda Corp	0.06
4.	Bajaj Finserv	0.08
5.	Multi Commodity Exchange	0.06
6.	KSB Pumps	0.06
7.	Thermax	0.06
8.	Bharat Electronics	0.08
9.	Pidilite Industries	0.06
10.	Radico Khaitan	0.06
11.	Bata India	0.06
12.	TeamLease Services	0.06
13.	Container Corporation of India	0.06
14.	Syngene International	0.06
15.	Brigade Enterprises	0.06
16.	KNR Construction	0.06
Total		1

Table 2.3.4: Portfolio model 4 (Hypothetical).

Sl. No.	Company	Probabilities ($p(x)$)
1.	Guj. State Petro Ltd.	0.5
2.	Birla Corporation	0.04
3.	Oberoi Realty	0.2
4.	Tata Chemicals	0.06
5.	Century Textiles	0.2
Total		1

Table 2.3.5: Values of Ubriaco entropy for different portfolios.

Type	$\alpha = 0.1$	$\alpha = 0.3$	$\alpha = 0.5$	$\alpha = 0.7$	$\alpha = 0.9$	Shannon
Diversified (Di)	1.1314	1.4486	1.8549	2.3756	3.0429	3.4440
Large-cap (Lc)	1.1053	1.3508	1.6515	2.0199	2.4716	2.7344
Mid-cap (Mc)	1.1071	1.3569	1.6632	2.0388	2.4994	2.7674
Hypothetical (Hy)	0.9319	0.816	0.7224	0.6467	0.5854	0.5593

Table 2.3.6: Ordering of entropy values for different portfolios.

Di portfolio:	$H_U^{0.1} < H_U^{0.3} < H_U^{0.5} < H_U^{0.7} < H_U^{0.9} <$ Shannon
Lc portfolio:	$H_U^{0.1} < H_U^{0.3} < H_U^{0.5} < H_U^{0.7} < H_U^{0.9} <$ Shannon
Mc portfolio:	$H_U^{0.1} < H_U^{0.3} < H_U^{0.5} < H_U^{0.7} < H_U^{0.9} <$ Shannon
Hy portfolio:	Shannon $< H_U^{0.9} < H_U^{0.7} < H_U^{0.5} < H_U^{0.3} < H_U^{0.1}$.

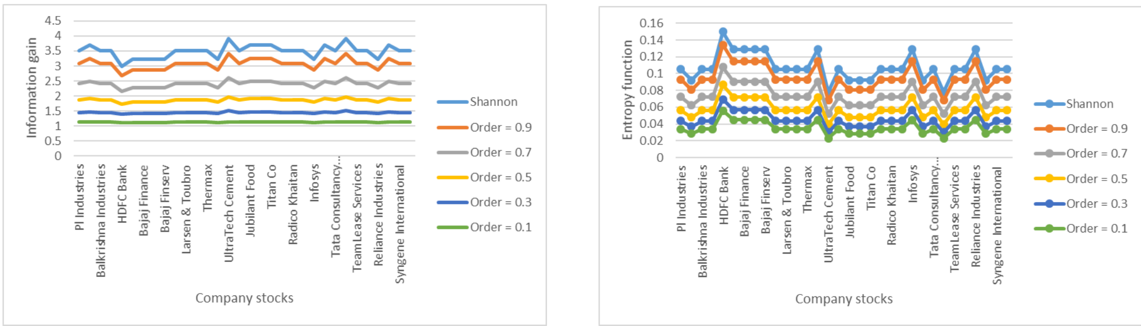

Figure 2.3.5: Variation of information gain (left) and entropy (right) functions with different α values for the Di portfolio.

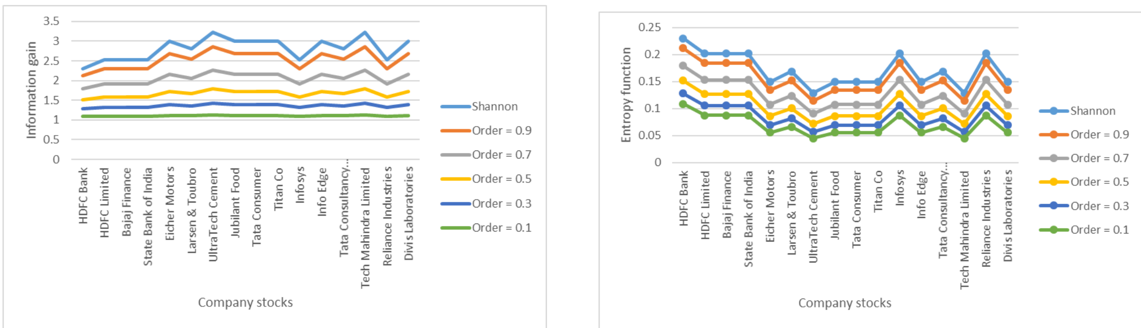

Figure 2.3.6: Variation of information gain (left) and entropy (right) functions with different α values for the Lc portfolio.

Shannon entropy and is consistent with theoretical expectations. In contrast, the hypothetical portfolio (Table 2.3.4) exhibits an opposite trend, wherein the entropy attains its maximum at $\alpha = 0.1$ and its minimum at $\alpha = 1$. This reversal in the trend indicates that, in this case, entropy measures associated with larger values of α yield lower information gain for high-return outcomes, whereas smaller values of α capture a greater degree of uncertainty. Such behavior, which is distinct from that observed in the other portfolios, is consistent with the implications of Theorem 2.3.1. Consequently, these four types of portfolio help in examining the sensitivity of entropy to variations in investors' risk tolerance, as governed by the parameter α, as well as to different combinations of portfolio weights represented by the probability values p.

Figs. 2.3.5 – 2.3.8 visually depict the variation of the information gain function $I_U^\alpha(p)$ and the corresponding entropy function $h_U^\alpha(p)$ across different portfolio categories as the fractional parameter α varies. In particular, when α is close to zero, both functions exhibit minimal variation with respect to the probability values $p(x)$, reflecting a heightened level of conservatism associated with low values of α. Moreover, Figs. 2.3.5, 2.3.6, and 2.3.7

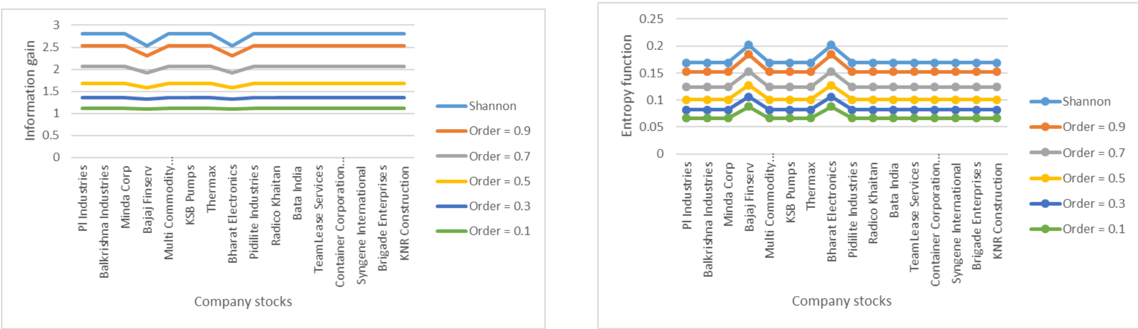

Figure 2.3.7: Variation of information gain (left) and entropy (right) functions with different α values for the Mc portfolio.

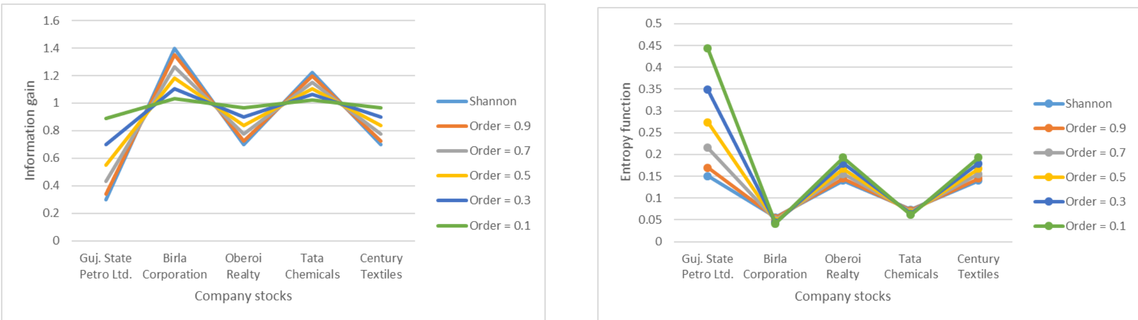

Figure 2.3.8: Variation of information gain (left) and entropy (right) functions with different α values for the Hy portfolio.

show that, for the diversified, large-cap, and mid-cap portfolios, $I_U^\alpha(p)$ remains nearly constant when both p and α are relatively small (< 0.5), indicating increase in conservatism or reduced sensitivity to uncertainty as α approaches zero. In contrast, the hypothetical portfolio, depicted in Fig. 2.3.8, exhibits comparatively larger fluctuations in the information gain function across all selected values of α. This behavior suggests increased sensitivity of the gain function at higher probability levels ($p \geq 0.5$), corresponding to the portfolio weight structure $p(x)$ reported in Table 2.3.4. Furthermore, the behavior of the associated entropy functions shown in Figs. 2.3.5 – 2.3.8 provides strong empirical support for the theoretical results established in Theorem 2.3.1 and Remark 2.3.3.

Thus, these portfolio datasets provide empirical evidence of sensitivity of the information gain and entropy functions to variations in the parameters α and p. This evidence reinforces the relevance of fractional order entropy in modeling human decision-making processes, such as portfolio stock selection. By capturing subjective uncertainty arising from individual risk tolerance, Ubriaco entropy emerges as a valuable and effective tool for decision analysis under risk and uncertainty.

2.4 Fractional order entropy-based decision analysis models

Definition 2.4.1. *Consider a general decision analysis model $G = (\Theta, A, u)$, with an increasing utility function $u = u(X(a, \theta))$ corresponding to action $a \in A$. Then, the expected utility- fractional entropy (EU-FE) measure of risk associated with an action a is defined by*

$$R(a) = \lambda H_a^{\alpha}(\theta) - (1-\lambda)\frac{E[u(X(a,\theta))]}{\max\limits_{a\in A}\{|E[u(X(a,\theta))]|\}}, \tag{2.4.1}$$

where $\lambda \in \mathcal{R}$ is the risk-tradeoff factor such that $0 \leq \lambda \leq 1$ and $H_a^{\alpha}(\theta)$ is the fractional entropy of the distribution of the state of nature corresponding to action a. Here, we assume that $\max\limits_{a\in A}\{|E[u(X(a,\theta))]|\}$ exists and is non-zero. When $\max\limits_{a\in A}\{|E[u(X(a,\theta))]|\} =$ 0, then

$$R(a) = \lambda H_a^{\alpha}(\theta).$$

Definition 2.4.2. *Given a general decision analysis model $G = (\Theta, \mathcal{B}, u)$, with an increasing utility function $u = u(X(b, \theta))$ corresponding to action $b \in \mathcal{B}$. Then, the expected utility- fractional entropy and variance (EU-FEV) measure of risk associated with an action b is defined by*

$$R(b) = \frac{\lambda}{2}\left[H_b^{\alpha}(\theta) + \frac{Var[X(b,\theta)]}{\max\limits_{b\in\mathcal{B}}\{Var[X(b,\theta)]\}}\right] - (1-\lambda)\frac{E[u(X(b,\theta))]}{\max\limits_{b\in\mathcal{B}}\{|E[u(X(b,\theta))]|\}}, \tag{2.4.2}$$

where $\lambda \in \mathcal{R}$ is the risk-tradeoff factor such that $0 \leq \lambda \leq 1$ and $H_b^{\alpha}(\theta)$ is the fractional entropy of the distribution of the state of nature corresponding to action b. Here, we assume that $\max\limits_{b\in\mathcal{B}}\{|E[u(X(b,\theta))]|\}$ exists and is non-zero. When $\max\limits_{b\in\mathcal{B}}\{|E[u(X(b,\theta))]|\} = 0$, then

$$R(b) = \frac{\lambda}{2}\left[H_b^{\alpha}(\theta) + \frac{Var[X(b,\theta)]}{\max\limits_{b\in\mathcal{B}}\{Var[X(b,\theta)]\}}\right].$$

Remark 2.4.1. *The proposed EU-FE and EU-FEV measures are constructed as fractional extensions of the expected utility–entropy (EU-E) and expected utility–entropy–variance (EU-EV) frameworks. This construction preserves comparability with the classical Shannon entropy-based models. However, the replacement of Shannon entropy by Ubriaco entropy is not only formal, since the fractional parameter α modifies the sensitivity of the information gain term. Hence, α provides an additional risk-sensitivity mechanism through which different decision-maker attitudes toward uncertainty can be represented.*

To assess decisions made by individuals across a finite set of actions based on a risk measure, the risk values $(R(y), y = a$ or $b)$ associated with each action are compared. These risk values are determined by the subjective uncertainty of the outcomes and their perceived utility. The action with the lowest $R(y)$ value is selected. Therefore, the EU-FE and EU-FEV decision models can be defined as follows:

Definition 2.4.3. *Consider a general decision analysis model $G = (\Theta, Y, u)$ If the action space $Y = A$ or $\mathcal{B}$ consists of two actions $y_1, y_2 \in Y$ with related risk measures $R(y_1)$ and $R(y_2)$, respectively, then we have the following result:*
(i) action y_1 is selected, i.e., $y_1 > y_2$, if $R(y_1) < R(y_2)$;
(ii) action y_2 is selected, i.e., $y_1 < y_2$, if $R(y_1) > R(y_2)$;
(iii) no action is superior i.e., any action can be selected or, $y_1 = y_2$, if $R(y_1) = R(y_2)$.
Hence, if Y is a discrete set of n objects, i.e., $Y = \{y_1, y_2, \ldots, y_n\}$, then the EU-FE and the EU-FEV order of preferences of actions will be in accordance with decreasing order of risk values. The most preferred action will then be

$$R(y_i) = \min_{y_j \in Y} R(y_j).$$

We can observe that when $\alpha = 1$, both the EU-FE and EU-FEV decision models reduce to the EU-E and EU-EV models, respectively. Moreover, for $\lambda = 0$, the proposed decision models reduce to the expected utility model ($y_1 > y_2$ or $R(y_1) < R(y_2)$ iff $E[u(y_1)] > E[u(y_2)]$).

2.4.1 Properties of the EU-FE and EU-FEV measures of risk

The EU-FE and EU-FEV risk measures adhere to the core principles of risk measures, similar to those of previously established risk measures. This section will explore some of the key properties of these proposed risk measures.

Theorem 2.4.1. *Let a_1 and a_2 be two different actions in the action space associated with a general decision model $G = (\Theta, A, u)$ having equal expected utility, $H^{\alpha}_{a_1}(\theta)$ and $H^{\alpha}_{a_2}(\theta)$ denote fractional entropies of the corresponding states of nature, then $R(a_1) < R(a_2)$ when $H^{\alpha}_{a_1}(\theta) < H^{\alpha}_{a_2}(\theta)$ for some α. For the EU-FEV model, $R(b_1) < R(b_2)$ if and only if*

$$\left[H^{\alpha}_{b_1}(\theta) + \frac{Var[X(b_1, \theta)]}{\max\limits_{b_1 \in \mathcal{B}}\{Var[X(b_1, \theta)]\}}\right] < \left[H^{\alpha}_{b_2}(\theta) + \frac{Var[X(b_2, \theta)]}{\max\limits_{b_2 \in \mathcal{B}}\{Var[X(b_2, \theta)]\}}\right].$$

Proof. The result follows from Definitions 2.4.1 and 2.4.2. $\square$

Intuitively, according to the theorem mentioned above, an action with lower entropy and smaller variance will be associated with reduced risk.

Theorem 2.4.2. *Let $G = (\Theta, A, u)$ be a general decision analysis model, with the action space comprised of two actions a_1 and a_2, $H^\alpha_{a_1}(\theta)$ and $H^\alpha_{a_2}(\theta)$ denoting the fractional entropies of the corresponding states of nature θ, respectively, then $R(a_1) < R(a_2)$ when $H^\alpha_{a_1}(\theta) = H^\alpha_{a_2}(\theta)$ for a particular value of α and $E[u(X(a_1, \theta))] > E[u(X(a_2, \theta))]$. Further, when $H^\alpha_{b_1}(\theta) = H^\alpha_{b_2}(\theta) = 0$, then $R(b_1) < R(b_2)$ if and only if $E[u(X(b_1, \theta))] > E[u(X(b_2, \theta))]$.*

Proof. This result follows directly from Definitions 2.4.1 and 2.4.2, together with the observation that, for a decision model $G(\Theta, Y, u)$, the condition $H^\alpha_y(\theta) = 0$ implies $\mathrm{Var}(X(y, \theta)) = 0$. □

From Theorem 2.4.2, we get that the action with higher expected utility will be less riskier when the fractional entropy values of the corresponding outcomes are equal. Further, the validity of the EU-FE and EU-FEV risk measures defined in (2.4.1) and (2.4.2) is examined by exploring several properties in relation to prior studies on decision models involving Shannon entropy and individual's perception about risk.

Theorem 2.4.3. *Let $G = (\Theta, Y, u)$ be a general decision analysis model with non-negative outcomes:*

1. *Let the action space be described as $Y = \{y, y + k\}$, where $k > 0$ is a constant, then*

$$R(y + k) < R(y),$$

i.e., risk decreases with the addition of a positive constant to all outcomes of an action.

2. *If the action space contains two elements, namely, $Y = \{y, ty\}$, where $t > 1$ is a constant, then for the EU-FE decision model*

$$R(ty) < R(y),$$

i.e., EU-FE risk decreases if all the outcomes of an action are multiplied by a positive constant.

For the EU-FEV decision model,

$$R(ty) < R(y),$$

if and only if

$$\lambda \in \left[0,\ \frac{1-\frac{E[u(X)]}{E[u(kX)]}}{\frac{3}{2}-\frac{1}{2k^2}-\frac{E[u(X)]}{E[u(kX)]}}\right).$$

Proof.

1. As we know that the utility function $u(X)$ is increasing, then for $k>0$, we have

$$u(X+k)>u(X).$$

If $Y=\{y,y+k\}$, then

$$\max_{y\in Y}\{|E[u(X(y,\theta))]|\}=E[u(X+k)] \text{ and } Var(X+k)=Var(X).$$

Hence, from Definition 2.4.2, we get that

$$R(b)=\frac{\lambda}{2}\left[H_b^{\alpha}(\theta)+1\right]-(1-\lambda)\frac{E[u(b)]}{E[u(b+k)]}$$

and

$$R(b+k)=\frac{\lambda}{2}\left[H_{b+k}^{\alpha}(\theta)+1\right]-(1-\lambda).$$

Similarly, from Definition 2.4.1, we have

$$R(a)=\lambda H_a^{\alpha}(\theta)-(1-\lambda)\frac{E[u(a)]}{E[u(a+k)]}$$

and

$$R(a+k)=\lambda H_{a+k}^{\alpha}(\theta)-(1-\lambda).$$

Since, $H_{y+k}^{\alpha}(\theta)=H_y^{\alpha}(\theta)$ ($y=a$ or b) for a fixed value of $\alpha\in[0,1]$, one gets that $R(y+k)<R(y)$.

2. As we have an increasing utility function and non-negative outcomes $X=X(b,\theta)$ such that $E[X]=0$, then we get $u(tX)>u(X)$ for $t>1$. Since, $\mathcal{B}=\{b,tb\}$, therefore

$$\max_{b\in\mathcal{B}}\{|E[u(X(b,\theta))]|\}=E[u(kX)] \text{ and } Var(kX)=k^2E[X^2]>Var(X)=E[X^2].$$

Hence, from Definition 2.4.2, we get that

$$R(b)=\frac{\lambda}{2}\left[H_b^{\alpha}(\theta)+\frac{1}{k^2}\right]-(1-\lambda)\frac{E[u(X)]}{E[u(kX)]}$$

and
$$R(kb) = \frac{\lambda}{2}\Big[H^{\alpha}_{kb}(\theta) + 1\Big] - (1-\lambda).$$
Since entropy depends on the probabilities of the states of nature $p(i)$ and α, for a particular value of α, $H^{\alpha}_{kb}(\theta) = H^{\alpha}_{b}(\theta)$. Hence, it follows that $R(kb) < R(b)$ if and only if
$$\lambda\left(\frac{3}{2} - \frac{1}{2k^2} - \frac{E[u(X)]}{E[u(kX)]}\right) - \left(1 - \frac{E[u(X)]}{E[u(kX)]}\right) > 0.$$
Therefore, we have that for $R(kb) < R(b)$ if and only if
$$\lambda \in \left[0,\ \frac{1 - \frac{E[u(X)]}{E[u(kX)]}}{\frac{3}{2} - \frac{1}{2k^2} - \frac{E[u(X)]}{E[u(kX)]}}\right).$$
Similarly, it follows from Definition 2.4.1 that
$$R(a) = \lambda H^{\alpha}_{a}(\theta) - (1-\lambda)\frac{E[u(X)]}{E[u(kX)]}$$
and
$$R(ka) = \lambda H^{\alpha}_{ka}(\theta) - (1-\lambda).$$
Thus, we obtain $R(ka) < R(a)$, since for actions a and ka, $H^{\alpha}_{ka}(\theta) = H^{\alpha}_{a}(\theta)$.

2.4.2 Decision problems and solutions

In order to investigate the effectiveness of the proposed risk measures, we consider the following decision problems and paradoxes used by Brito (2020). Additionally, by comparing these models to conventional decision-making approaches (EU-E and EU-EV), we highlight their distinct benefits in evaluating complex investment decisions and addressing well-known decision-making paradoxes.

Before presenting the numerical decision problems, it is useful to clarify that different choices of $u(x)$ correspond to different behavioural assumptions. For example, a linear utility function represents approximately risk-neutral behaviour, a concave utility function such as $u(x) = \sqrt{x}$ or $u(x) = \log x$ represents risk-averse or conservative behaviour, while a convex utility function such as $u(x) = x^2$ represents risk-seeking or aggressive behaviour. Therefore, the use of multiple utility functions is not arbitrary; it allows the proposed risk measures to be tested under different investor attitudes toward uncertain outcomes.

The computational steps shown in Algorithm 2 is followed to evaluate the values of the risk function $R(y_i)$ corresponding to the action space under varying α values, keeping λ fixed so as to analyze the decision outcomes based on EU-FE and EU-FEV risk measures.

Algorithm 2: Computation of $R(y_i)$ for EU–FE or EU–FEV Risk Measures

Input: Action space $A = \{y_1, y_2, \dots, y_n\}$;

State space $x = \{x_{i1}, x_{i2}, \dots, x_{im}\}$ for $i = 1, \dots, n$;

Probability distribution of states $\theta = \{p_{i1}, p_{i2}, \dots, p_{im}\}$;

Number of actions n and states m;

Normalized expected utility $NE[u(x)] = \sum_{j=1}^{m} u(x_{ij})\, p_{ij}$;

Normalized variance;

Trade-off parameter $\lambda = 0.5$.

Output: Risk values $R(y_i)$ corresponding to each action y_i.

Initialize $\alpha = \text{linspace}(0, 1, 50)$;

Initialize arrays: `entropy` $\leftarrow$ zeros(1, length(α)), `R` $\leftarrow$ zeros(1, length(α));

for $i \leftarrow 1$ **to** *length*(α) **do**

  Compute entropy$(i) = \sum_{j=1}^{m} p_{ij} \left(-\log p_{ij} \right)^{\alpha(i)}$;

  Compute risk $R(i) = R(y_i)$ based on EU–FE or EU–FEV definitions (Definitions 2.4.1, 2.4.2);

end

Plot α versus R to analyze the variation of risk with α;

Table 2.4.1: Nawrocki and Harding problem with two different actions.

		θ_1	θ_2	θ_3	θ_4	θ_5	Expected value	Variance	Entropy
y_1	x_{1j}	1	2	3	4	5	3	1.2	1.47
	p_{1j}	0.1	0.2	0.4	0.2	0.1			
y_2	x_{2j}	1	2	3	4	5	3	1.8	1.47
	p_{1j}	0.2	0.1	0.4	0.1	0.2			

Nawrocki and Harding investment problem

Nawrocki and Harding (1986) introduced a security investment problem, where two securities have the same Shannon entropy value but different risk levels. This showed the inadequacy of the Shannon entropy as a measure of security risk. So he defined a state-value weighted entropy to depict the dispersion of frequency classes of securities. The details of this problem can be found in Table 2.4.1, where we have that y_2 is riskier than y_1 according to the mean-variance (MV) criterion since $Var(y_2) > Var(y_1)$. The investment problem described in Table 2.4.1 has been chosen to illustrate the role of fractional entropy-based decision models, viz., EU-FE and EU-FEV models in analyzing decision

Table 2.4.2: Risk measures for Nawrocki and Harding problem when $\alpha = 0.4$.

Utility function	$H^{0.4}(\theta)$	$R(y),\ y = a$ or b	EU-E	EU-EV	EU-FE	EU-FEV
$u(x) = x$	0.70	$R(y_1)$	$2.47\lambda - 1$	$2.07\lambda - 1$	$1.70\lambda - 1$	$1.68\lambda - 1$
	1.21	$R(y_2)$	$2.47\lambda - 1$	$2.24\lambda - 1$	$2.21\lambda - 1$	$1.94\lambda - 1$
$u(x) = \log(x)$	0.70	$R(y_1)$	$2.47\lambda - 1$	$2.07\lambda - 1$	$1.70\lambda - 1$	$1.68\lambda - 1$
	1.21	$R(y_2)$	$2.42\lambda - 0.95$	$2.19\lambda - 0.95$	$2.16\lambda - 0.95$	$2.06\lambda - 0.95$
$u(x) = \sqrt{x}$	0.70	$R(y_1)$	$2.47\lambda - 1$	$2.07\lambda - 1$	$1.70\lambda - 1$	$1.68\lambda - 1$
	1.21	$R(y_2)$	$2.46\lambda - 0.99$	$2.23\lambda - 0.99$	$2.20\lambda - 0.99$	$2.10\lambda - 0.99$

problems where the Shannon entropy values are equal. Using the current models, the decision choices of this problem are analyzed for risk-neutral utility function $u(x) = x$ and risk-averse utility functions $u(x) = \log(x)$ and $u(x) = \sqrt{x}$. We start by computing the risk measure functions in terms of the risk-tradeoff factor λ for each of the utility functions $u(x)$ using fractional parameter $\alpha = 0.4$. The results can be found in Table 2.4.2. We get different entropy values corresponding to our models due to the presence of the fractional parameter α.

Therefore, from Table 2.4.2. we find that the EU-FE and EU-FEV models assign different risk measure values $1.70\lambda - 1$ and $2.21\lambda - 1$ to y_1 and y_2, respectively, for a risk-neutral utility function $u(x) = x$. However, the EU-E model gives $R(y_1) = R(y_2) = 2.47\lambda - 1\ \forall\ \lambda \in [0, 1]$. So, an individual cannot reach to a conclusion based on the previous EU-E model. Hence, for risk-neutral utility function, the individual decisions based on their risk preferences can be analyzed by the fractional entropy function alone without the aid of variance. This highlights the advantages of using the fractional entropy function over Shannon entropy function in human decision analysis models. Moreover, from Table 2.4.3, we find that the range of λ values supporting a risky decision $(R(y_1) < R(y_2))$ defined on the basis of the MV criterion aligns well with the predictions of the fractional entropy-based risk models for all the types of utility functions considered in our study. For the risk-neutral utility function $u(x) = x$, we get $R(y_1) = R(y_2)$ for $\lambda = 0$. In this case, the decision maker shows no specific preference for any action. Further, the variations in the MV defined decision outcomes $(R(y_1) < R(y_2))$ are shown with respect to variations in the risk sensitivity parameter α, keeping λ fixed, as illustrated in Fig. 2.4.1.

Remark 2.4.2. *For a decision analysis model $G(\Theta, Y, u)$ with risk-neutral utility function, $u(x) = bx + c,\ b > 0$, if $E(y_1) = E(y_2)$ and $Var(y_1) = Var(y_2)\ \forall\ y_1, y_2 \in Y$, then the EU-FE and EU-FEV risk measures can be ordered according to the entropy values, i.e., for a particular value of α, we have*

$$R(y_1) < R(y_2) \iff H^{\alpha}_{y_1}(\theta) < H^{\alpha}_{y_1}(\theta).$$

Table 2.4.3: Risk tradeoff factors for EU-FE and EU-FEV models corresponding to Nawrocki and Harding decision problem.

Utility function	Risk decision	EU-E	EU-EV	EU-FE	EU-FEV
$u(x) = x$	$R(y_1) < R(y_2)$	-	$0 < \lambda \leq 1$	$0 < \lambda \leq 1$	$0 < \lambda \leq 1$
	$R(y_1) = R(y_2)$	$0 \leq \lambda \leq 1$	$\lambda = 0$	$\lambda = 0$	$\lambda = 0$
$u(x) = \log(x)$	$R(y_1) < R(y_2)$	$0 \leq \lambda < 1$	$0 \leq \lambda \leq 1$	$0 \leq \lambda \leq 1$	$0 \leq \lambda \leq 1$
	$R(y_1) = R(y_2)$	$\lambda = 1$	-	-	-
$u(x) = \sqrt{x}$	$R(y_1) < R(y_2)$	$0 \leq \lambda < 1$	$0 \leq \lambda \leq 1$	$0 \leq \lambda \leq 1$	$0 \leq \lambda \leq 1$
	$R(y_1) = R(y_2)$	$\lambda = 1$	-	-	-

Levy paradoxical problem

The decision paradoxical problem, as proposed by Lévy (1992) is described in Table 2.4.4. The decision results of this problem based on the MV criterion considers y_2 to be riskier than y_1 since $E[y_1] > E[y_2]$ and $Var[y_1] < Var[y_2]$. Now, we interpret this result in terms of the proposed decision models. For this we have evaluated the risk measure expressions in terms of λ associated with each action for $\alpha = 0.4$. The computed results are provided in Table 2.4.5. From the risk expressions, we obtained the range of λ satisfying the M-V based decision outcome ($R(y_1) < R(y_2)$). The outputs of λ connected to the decision outcomes based on the proposed risk measures are provided in Table 2.4.6.

Table 2.4.4: Levy problem with two actions and two states of nature.

		θ_1	θ_2	Expected value	Variance	Entropy
y_1	x_{1j}	1	100	20.8	1568	0.5
	p_{1j}	0.8	0.2			
y_2	x_{2j}	10	1000	19.9	9703	0.06
	p_{2j}	0.99	0.01			

Table 2.4.5: Risk measures for $\alpha = 0.4$ corresponding to Levy problem.

Utility function	$H^{0.4}(\theta)$	$R(y),\ y = a$ or b	EU-E	EU-EV	EU-FE	EU-FEV
$u(x) = x$	0.68	$R(y_1)$	$1.50\lambda - 1$	$1.33\lambda - 1$	$1.68\lambda - 1$	$1.42\lambda - 1$
	0.18	$R(y_2)$	$1.02\lambda - 0.96$	$1.49\lambda - 0.96$	$1.14\lambda - 0.96$	$1.55\lambda - 0.96$
$u(x) = \log(x)$	0.68	$R(y_1)$	$0.89\lambda - 0.39$	$0.72\lambda - 0.39$	$1.07\lambda - 0.39$	$0.81\lambda - 0.39$
	0.18	$R(y_2)$	$1.06\lambda - 1$	$1.53\lambda - 1$	$1.18\lambda - 1$	$1.59\lambda - 1$
$u(x) = \sqrt{x}$	0.68	$R(y_1)$	$1.31\lambda - 0.81$	$1.14\lambda - 0.81$	$1.49\lambda - 0.81$	$1.23\lambda - 0.81$
	0.18	$R(y_2)$	$1.06\lambda - 1$	$1.53\lambda - 1$	$1.18\lambda - 1$	$1.59\lambda - 1$

From the results of Table 2.4.6, we find that for a risk-neutral function $u(x) = x$, the EU-EV and EU-FEV models gives the same decision outcome ($R(y_1) < R(y_2)$ as

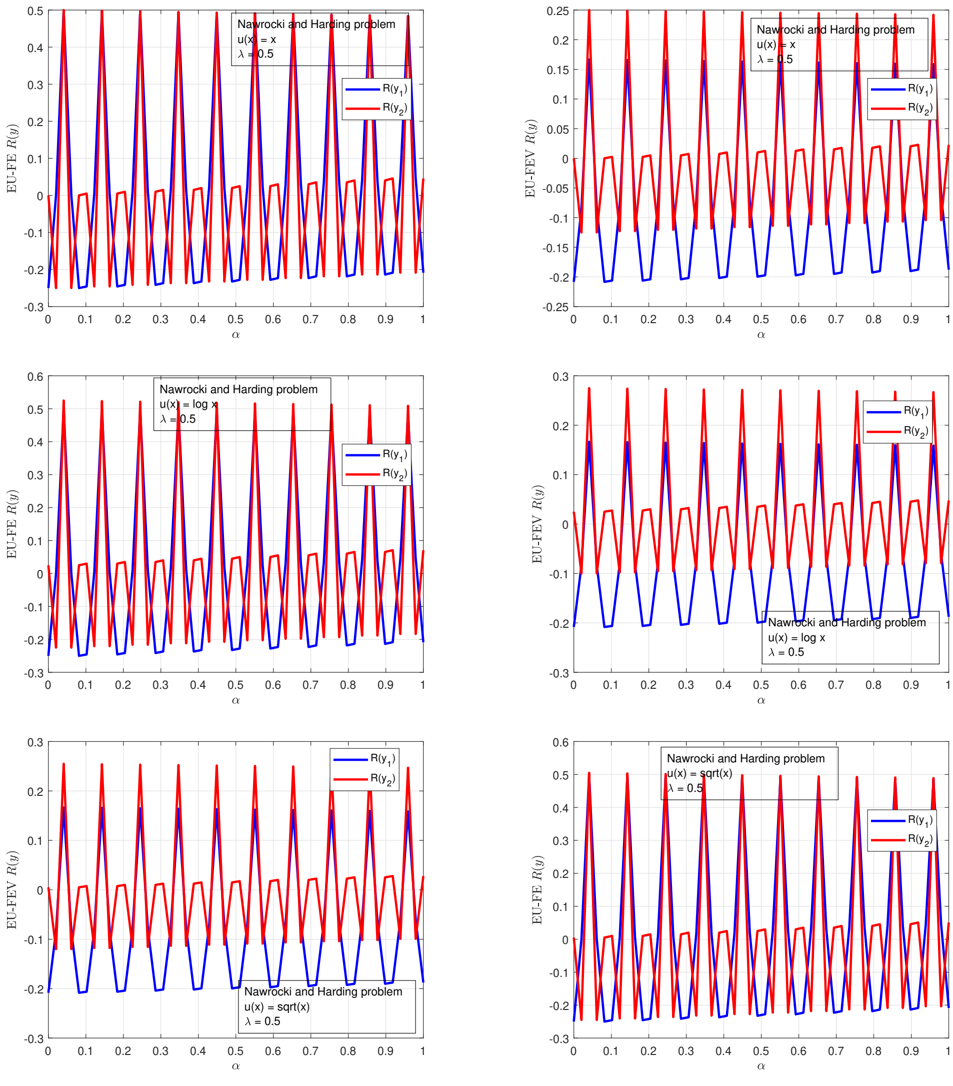

Figure 2.4.1: Risk measures for actions y_3 and y_4 for different α and $u(x)$ in Nawrocki and Harding problem.

Table 2.4.6: Risk tradeoff factors for EU-FE and EU-FEV models due to Levy problem.

Utility function	Risk decision	EU-E	EU-EV	EU-FE	EU-FEV
$u(x) = x$	$R(y_1) < R(y_2)$	$0 \leq \lambda < 0.08$	$0 \leq \lambda \leq 1$	$0 \leq \lambda < 0.07$	$0 \leq \lambda \leq 1$
	$R(y_1) > R(y_2)$	$0.08 < \lambda \leq 1$	-	$0.07 < \lambda \leq 1$	-
$u(x) = \log(x)$	$R(y_1) < R(y_2)$	-	$0.75 < \lambda \leq 1$	-	$0.78 < \lambda \leq 1$
	$R(y_1) > R(y_2)$	$0 \leq \lambda \leq 1$	$0 \leq \lambda < 0.75$	$0 \leq \lambda \leq 1$	$0 \leq \lambda < 0.78$
$u(x) = \sqrt{x}$	$R(y_1) < R(y_2)$	-	$0.49 < \lambda \leq 1$	-	$0.53 < \lambda \leq 1$
	$R(y_1) > R(y_2)$	$0 \leq \lambda \leq 1$	$0 \leq \lambda < 0.49$	$0 \leq \lambda \leq 1$	$0 \leq \lambda < 0.53$

predicted by the MV criterion for all values of $\lambda \in [0, 1]$. However, the EU-FE decision model prefers the action y_1 over y_2 for $\lambda \in [0, 0.07)$. This result is almost similar to that of the EU-E model. However, the decision outcomes based on EU-FE and EU-FEV risk measures or the range of λ for which the action y_1 will be preferred over y_2 may change with values of α other than 0.4 (such as 0.6 or 0.8). These adjustments were not possible with the previous models using Shannon entropy, thereby failing to take the individual risk preferences due to uncertainty of outcomes into account. This highlights the superiority of the EU-FEV and EU-FE models, attributed to the inclusion of the sensitivity parameter α in the Ubriaco entropy function.

Further, for the risk averse function $u(x) = \log(x)$, the EU-EV and EU-FEV risk models give that for $\alpha = 0.4$, y_2 is riskier than y_1 for $\lambda \in (0.75, 1]$ and $\lambda \in (0.78, 1]$, respectively. So there is not much disparity in the results for the EU-FEV model with $\alpha = 0.4$ and the EU-EV model. However, both EU-E and EU-FE models indicate that y_1 is riskier than y_2 for all values of λ. The same result follows with $u(x) = \sqrt{x}$ for the EU-E and EU-FE models. Further, for a fixed value of the risk tradeoff factor $\lambda = 0.5$, the variations in the decision outcomes are also demonstrated with respect to changing values of α through Fig. 2.4.2.

Proposition 2.4.1. *For a decision analysis model $G(\Theta, Y, u)$ with risk-neutral utility function, $u(x) = bx + c,\ b > 0$, if*

$$E(y_1) > E(y_2)\ \forall\ y_1, y_2 \in, Y$$

and for a particular value of α,

$$\frac{Var[y_1] - Var[y_2]}{max_{y \in Y}\{Var[y]\}} + H^{\alpha}_{y_1}(\theta) - H^{\alpha}_{y_2}(\theta) < 0,$$

then $R(y_1) < R(y_2)\ \forall\ \lambda \in [0, 1]$ with EU-FEV decision model.

Remark 2.4.3. *In case of the Levy paradoxical problem,*

$$\frac{Var[y_1] - Var[y_2]}{max_{y \in Y}\{Var[y]\}} = -0.84 \text{ and } H^{0.4}_{y_1}(\theta) - H^{0.4}_{y_2}(\theta) = 0.5.$$

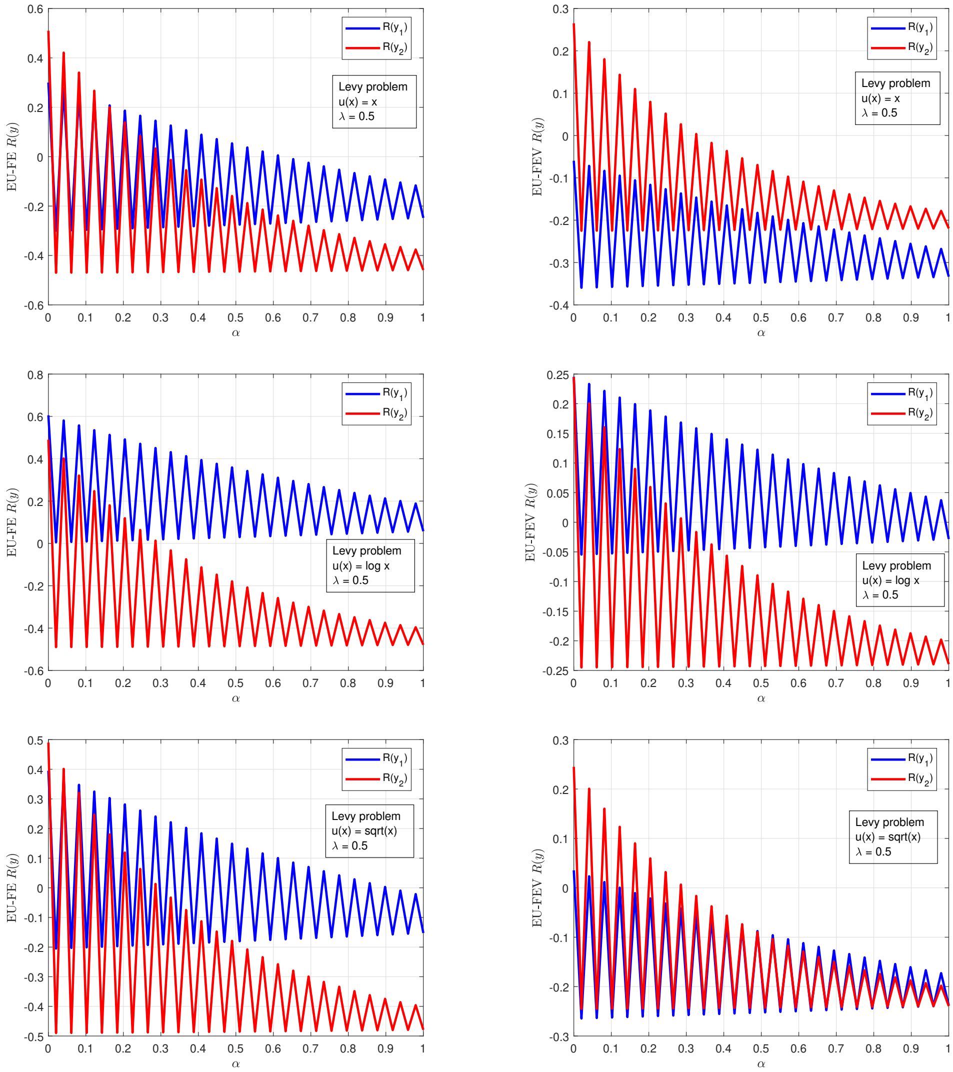

Figure 2.4.2: Risk measures for actions y_3 and y_4 for different α and $u(x)$ in Levy problem.

Hence, a decision maker will always choose the action y_1 under EU-FEV decision model.

Allais paradoxical problem

The well-known economic decision paradox, introduced by Allais (1953), demonstrates that expected utility alone is insufficient to capture individuals' decision-making behavior in situations involving risk and uncertainty. This paradox involves two experiments where individuals are given the choice between two prospects with potential capital gains, viz., y_1 or y_2 in the first experiment and y_3 or y_4 in the second one as shown in Table 2.4.7. Further, it is well established that decision-makers tend to prefer y_1 over y_2 and y_4 over y_3. So this preference is compared with the proposed EU-FE and EU-FEV models taking three types of utility functions, viz., risk-neutral ($u(x) = x$), risk-averse ($u(x) = \sqrt{x}$) and risk-seeking ($u(x) = x^2$) to assess how well the current decision models align with existing models in anticipating decision paradoxes.

Table 2.4.7: Allais problem with four actions and three states.

		θ_1	θ_2	θ_3	Expected value	Variance	Entropy
y_1	x_{1j}	1					
	p_{1j}	1			1	0	0
y_2	x_{2j}	1	5	0			
	p_{2j}	0.89	0.1	0.01	1.39	1.46	0.38
y_3	x_{3j}	1		0			
	p_{2j}	0.11		0.89	0.11	0.1	0.35
y_4	x_{4j}		5	0			
	p_{2j}		0.1	0.9	0.5	2.25	0.33

The computed risk measure values in terms of λ are displayed in Table 2.4.8 to get the range of λ that meets the desired conditions obtained from the MV criterion. From Table 2.4.9, it is evident that the EU-FE model with $\alpha = 0.4$ demonstrates greater alignment in the range of λ values with the preference patterns derived from the MV criterion, as compared to the EU-E model. Further, with the inclusion of variance in the risk measure, we get improved results for the first experiment of choosing actions between y_1 and y_2 for the risk-neutral and risk-averse utility functions. However, the EU-FE model gives better results than the EU-FEV and EU-EV models as par the M-V criterion outcome for the second experiment of choices between actions y_3 and y_4. It also gives better result than the EU-FEV model for the first experiment for the risk-seeking utility function. This highlights the importance of both the fractional entropy-based models with and without the inclusion of variance. Hence, the inclusion of variance is not always necessary with the fractional-entropy based decision models for better predictions of choices. This is due to the dependence of individual decisions on both expected utility and subjective uncertainty of outcomes, which can be portrayed well with EU-FE and EU-FEV decision models. This dependence of the decision outcomes on the risk attitudes towards uncertainty of outcomes is depicted in Fig. 2.4.3 which showed the variations of individual preferences with respect to α, keeping λ fixed. This underscores the importance of using Ubriaco entropy in risk measures for predicting decisions based on the subjective uncertainty of outcomes or states and their subjective utilities, even when the cardinality of the set of outcomes or states differs across actions, as demonstrated in the Allais problem.

These decision results indicate that the proposed model is highly compatible and outperforms previous EU-E and EU-EV models in many situations for $\alpha = 0.4$. This is

Table 2.4.8: Risk measures for $\alpha = 0.4$ corresponding to Allais problem.

Utility function	$H^{0.4}(\theta)$	$R(y),\ y = a$ or b	EU-E	EU-EV	EU-FE	EU-FEV
$u(x) = x$	0	$R(y_1)$	$0.72\lambda - 0.72$	$0.72\lambda - 0.72$	$0.72\lambda - 0.72$	$0.72\lambda - 0.72$
	0.54	$R(y_2)$	$1.38\lambda - 1$	$1.69\lambda - 1$	$1.54\lambda - 1$	$1.59\lambda - 1$
	0.53	$R(y_3)$	$0.43\lambda - 0.08$	$0.27\lambda - 0.08$	$0.61\lambda - 0.08$	$0.36\lambda - 0.08$
	0.51	$R(y_4)$	$0.69\lambda - 0.36$	$1.02\lambda - 0.36$	$0.86\lambda - 0.36$	$1.11\lambda - 0.36$
$u(x) = \sqrt{x}$	0	$R(y_1)$	$0.9\lambda - 0.9$	$0.9\lambda - 0.9$	$0.9\lambda - 0.9$	$0.9\lambda - 0.9$
	0.54	$R(y_2)$	$1.38\lambda - 1$	$1.69\lambda - 1$	$1.54\lambda - 1$	$1.59\lambda - 1$
	0.53	$R(y_3)$	$0.44\lambda - 0.1$	$0.29\lambda - 0.1$	$0.63\lambda - 0.1$	$0.39\lambda - 0.1$
	0.51	$R(y_4)$	$0.53\lambda - 0.2$	$0.86\lambda - 0.2$	$0.71\lambda - 0.2$	$0.96\lambda - 0.2$
$u(x) = x^2$	0	$R(y_1)$	$0.29\lambda - 0.29$	$0.29\lambda - 0.29$	$0.29\lambda - 0.29$	$0.29\lambda - 0.29$
	0.54	$R(y_2)$	$1.38\lambda - 1$	$1.69\lambda - 1$	$1.54\lambda - 1$	$1.37\lambda - 1$
	0.53	$R(y_3)$	$0.38\lambda - 0.03$	$0.22\lambda - 0.03$	$0.56\lambda - 0.03$	$0.32\lambda - 0.03$
	0.51	$R(y_4)$	$1.06\lambda - 0.74$	$1.40\lambda - 0.74$	$1.24\lambda - 0.74$	$1.49\lambda - 0.74$

Table 2.4.9: Risk tradeoff factors for EU-FE and EU-FEV models corresponding to Allais problem.

Utility function	Risk decision	EU-E	EU-EV	EU-FE	EU-FEV
$u(x) = x$	$R(y_1) < R(y_2)$	$0.42 < \lambda \leq 1$	$0.28 < \lambda \leq 1$	$0.34 < \lambda \leq 1$	$0.32 < \lambda \leq 1$
	$R(y_4) < R(y_3)$	$0 \leq \lambda \leq 1$	$0 \leq \lambda < 0.37$	$0 \leq \lambda \leq 1$	$0 \leq \lambda < 0.37$
$u(x) = \sqrt{x}$	$R(y_1) < R(y_2)$	$0.21 < \lambda \leq 1$	$0.13 < \lambda \leq 1$	$0.16 < \lambda \leq 1$	$0.14 < \lambda \leq 1$
	$R(y_4) < R(y_3)$	$0 \leq \lambda \leq 1$	$0 \leq \lambda < 0.18$	$0 \leq \lambda \leq 1$	$0 \leq \lambda < 0.18$
$u(x) = x^2$	$R(y_1) < R(y_2)$	$0.65 < \lambda \leq 1$	$0.51 < \lambda \leq 1$	$0.57 < \lambda \leq 1$	$0.66 < \lambda \leq 1$
	$R(y_4) > R(y_3)$	$0 \leq \lambda \leq 1$	$0 \leq \lambda < 0.60$	$0 \leq \lambda \leq 1$	$0 \leq \lambda < 0.61$

possible because of the flexibility of the Ubriaco entropy function to accommodate the risk tolerance levels of individuals associated with uncertainty of outcomes to derive desired results by tuning the risk sensitivity parameter α. This level of adaptability was not attainable with earlier decision models that utilized Shannon entropy, which described only the objective uncertainty of outcomes and couldn't represent the conservative attitude of decision-makers.

Economic interpretation of the decision results. The numerical decision examples show that the proposed EU-FE and EU-FEV measures have a direct economic interpretation. The fractional parameter α represents the decision maker's sensitivity to uncertainty. Lower values correspond to more conservative behaviour, while higher values represent greater tolerance toward risky outcomes. The trade-off parameter λ controls the relative importance of uncertainty and expected utility in the decision rule. Therefore, changes in

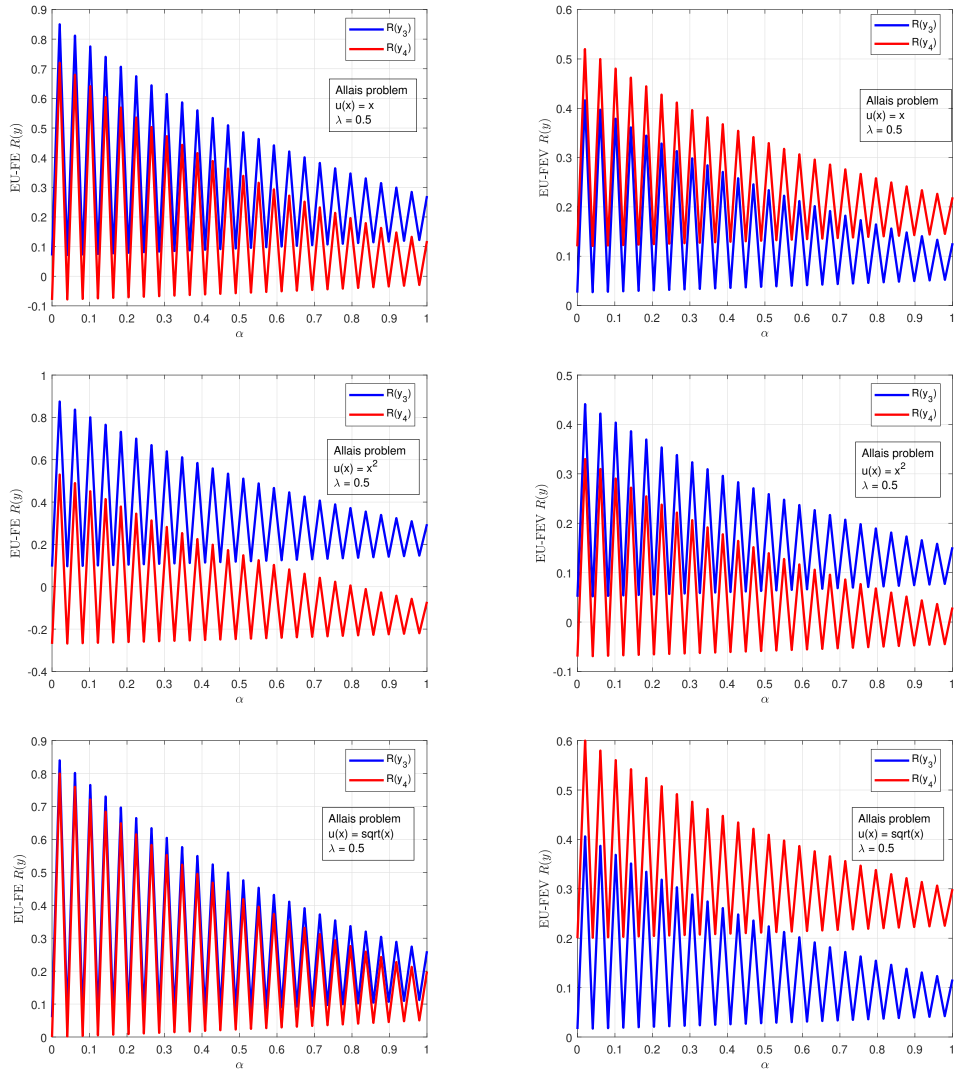

Figure 2.4.3: Risk measures for actions y_3 and y_4 for different α and $u(x)$ in Allais problem.

α and λ may alter the preference ordering of actions, reflecting different investor attitudes toward risk.

The EU-FE model captures utility-adjusted entropy risk, whereas the EU-FEV model additionally penalizes payoff dispersion through variance. Hence, EU-FEV is more suitable when an investor is concerned with both distributional uncertainty and volatility of outcomes. This provides an economic interpretation of the proposed models in terms of risk tolerance, uncertainty sensitivity, and preference under uncertain market conditions.

Comparison with the classical mean–variance framework. The classical mean–variance framework evaluates investment alternatives by balancing expected return against variance. It is simple and widely used in portfolio theory, but variance captures only dispersion around the mean and may not fully describe uncertainty arising from probability concentration, rare events, asymmetry, or investor-specific risk perception.

The proposed EU-FE and EU-FEV models extend this viewpoint by incorporating fractional entropy into the decision criterion. In EU-FE, expected utility is combined with fractional entropy-based uncertainty, while in EU-FEV, variance is also included to capture payoff dispersion. Thus, the proposed framework does not replace mean–variance analysis; rather, it generalizes it by adding an entropy-based uncertainty component and the fractional sensitivity parameter α. This makes the model more flexible for investor-specific decision-making under uncertainty.

2.4.3 Simulation-based validation of the proposed models

The proposed entropy-based decision-making models are formulated by integrating expected utility with the fractional order entropy and variance measures. Before investigating their practical performance using real financial data, it is desirable to examine their behaviour under controlled probabilistic settings. The objective of this simulation study is to examine the theoretical behaviour and robustness of the proposed EU-FE and EU-FEV risk measures under controlled probabilistic environments. While the previous subsection established the mathematical properties of the proposed measures, their practical behaviour under different uncertainty structures remains to be investigated. Therefore, simulation experiments are conducted using standard parametric probability models representing diverse stochastic characteristics. The study particularly investigates:

- the sensitivity of the proposed risk measures to the fractional order parameter α;
- the influence of the risk–tradeoff parameter λ;
- the behaviour of the measures under different probability structures;
- the contribution of the variance component in EU-FEV;
- the stability of risk rankings under varying distributional assumptions.

Accordingly, simulation experiments were conducted under representative discrete and continuous parametric probability models. The Binomial and Poisson distributions were considered to represent discrete stochastic processes, whereas the Normal distribution was employed as a representative continuous probability model. Since the proposed fractional entropy-based risk measure introduced in this chapter is formulated for discrete probability distributions, the normal density was discretized over a sufficiently fine finite grid and subsequently normalized to obtain an equivalent probability mass representation. This discretization enables the same entropy formulation to be employed uniformly across all probability models, thereby ensuring computational consistency throughout the simulation study.

For each probability model, probability masses were obtained either directly from the pmf (Binomial and Poisson distributions) or through discretization of the pdf (Normal distribution). The proposed fractional entropy was subsequently evaluated using Eq. (2.2.2). To isolate the contribution of the entropy component, the expected utility was evaluated using the linear utility function $u(x) = x$.

The proposed EU-FE and EU-FEV measures were then computed using Equations (2.4.1) and (2.4.2), respectively. For each probability model, the expected utility and variance were normalized using the maximum values obtained over the corresponding set of simulated alternatives, consistent with the normalization adopted in the proposed decision models.

The simulation settings adopted in the present study are summarized in Table 2.4.10. Although a larger grid of parameter combinations was employed during the computational experiments, only representative simulation results are reported to facilitate interpretation without affecting the observed trends.

Table 2.4.10: Simulation settings adopted for validating the proposed EU-FE and EU-FEV models.

Distribution	**Parameter settings**
Binomial	$n = 20,\ p = 0.20,\ 0.50,\ 0.80$
Poisson	$\mu = 2,\ 5,\ 10$
Normal	$\mu = 0,\ \sigma = 0.5,\ 1.0,\ 2.0$
Fractional order	$\alpha = 0.25,\ 0.50,\ 1.00$
Risk-tradeoff parameter	$\lambda = 0.25,\ 0.50,\ 0.75$
Utility function	$u(x) = x$

Representative simulation results obtained under the selected probability models are presented in Table 2.4.11, whereas the behaviour of the proposed EU-FE and EU-FEV measures under the Binomial distribution is illustrated in Figs. 2.4.4 and 2.4.5.

Table 2.4.11: Representative simulation results of the proposed EU-FE and EU-FEV models under different parametric probability distributions.

Distribution	Parameter	α	λ	H^α	$E[u(X)]$	Var(X)	EU-FE	EU-FEV
				Binomial distribution				
Binomial	$p = 0.20$	0.20	0.20	1.1397	4.0000	3.2000	0.0595	0.0095
Binomial	$p = 0.20$	0.50	0.50	1.3947	4.0000	3.2000	0.5921	0.4034
Binomial	$p = 0.20$	1.00	0.50	1.9883	4.0000	3.2000	0.8889	0.5518
Binomial	$p = 0.50$	0.20	0.20	1.1666	10.0000	5.0000	-0.1877	-0.2044
Binomial	$p = 0.50$	0.50	0.50	1.4774	10.0000	5.0000	0.4755	0.3562
Binomial	$p = 0.50$	1.00	0.50	2.2234	10.0000	5.0000	0.8486	0.5427
Binomial	$p = 0.80$	0.20	0.20	1.1397	16.0000	3.2000	-0.4458	-0.4957
Binomial	$p = 0.80$	0.50	0.50	1.3947	16.0000	3.2000	0.2763	0.0876
Binomial	$p = 0.80$	1.00	0.50	1.9883	16.0000	3.2000	0.5731	0.2360
				Poisson distribution				
Poisson	$\mu = 2$	0.25	0.25	1.1318	2.0000	2.0000	0.1330	0.0165
Poisson	$\mu = 5$	0.50	0.50	1.4708	5.0000	5.0000	0.4854	0.2427
Poisson	$\mu = 10$	1.00	0.75	2.5614	10.0000	10.0000	1.6711	1.0855
				Normal distribution (discretized)				
Normal	$\sigma = 0.5$	0.25	0.25	1.4466	0.0000	0.2500	0.1742	0.0019
Normal	$\sigma = 1.0$	0.50	0.50	2.2554	0.0000	1.0000	0.8777	0.3823
Normal	$\sigma = 2.0$	1.00	0.75	5.7449	0.0000	3.6497	4.0587	2.2793

The simulation results illustrated in Fig. 2.4.4 show that both EU-FE and EU-FEV increase smoothly with the fractional order parameter α for all representative probability values. Although the rate of increase varies across different probability settings, the absence of abrupt changes demonstrates the numerical stability of the proposed decision models with respect to variations in the fractional order parameter. Consequently, the increasing trends with respect to α indicate a greater contribution of the entropy component to the overall risk measure. This behaviour is consistently observed across all three probability models considered in the simulation study.

Similarly, the influence of the risk-tradeoff parameter is clearly evident from Fig. 2.4.5. Smaller values of λ assign greater emphasis to the expected utility component, whereas larger values progressively increase the contribution of the entropy component. Con-

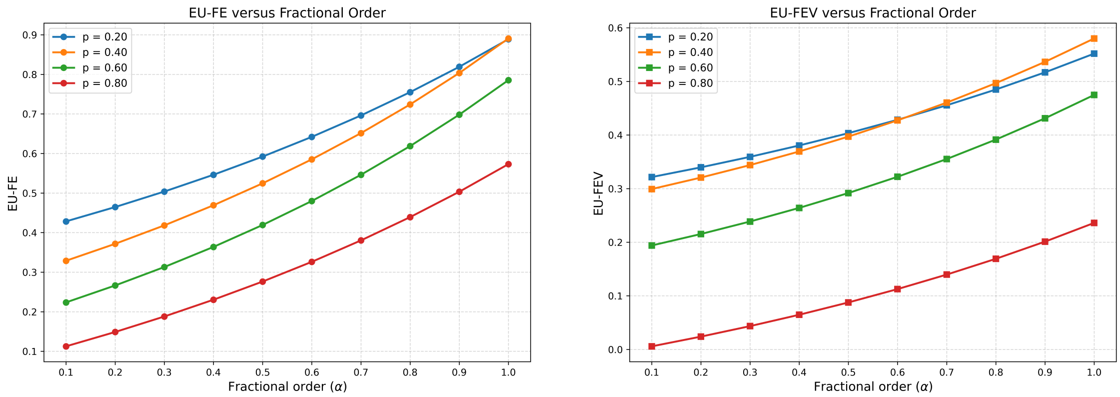

Figure 2.4.4: Sensitivity of EU-FE (left) and EU-FEV (right) risk measures w.r.t α.

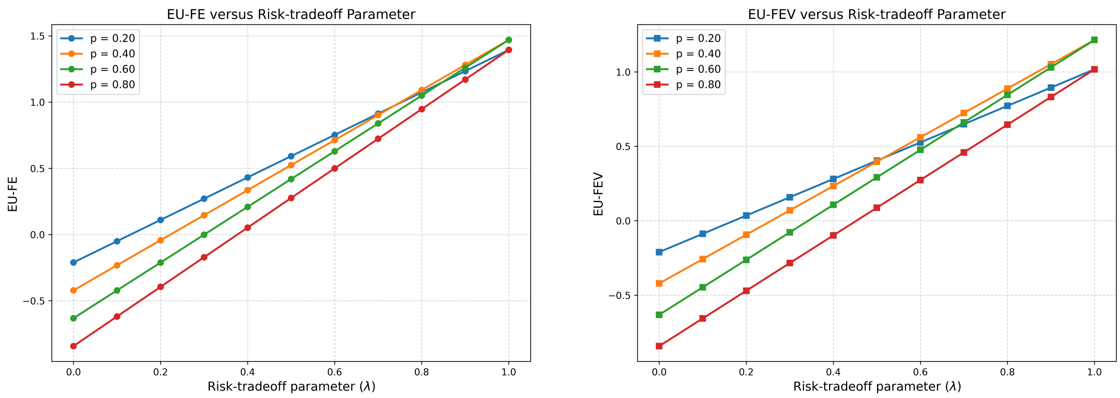

Figure 2.4.5: Sensitivity of EU-FE (left) and EU-FEV (right) risk measures w.r.t λ.

sequently, the proposed EU-FE and EU-FEV models provide a flexible mechanism for balancing expected utility against uncertainty according to the decision-maker's risk preference. The approximately linear variation of the proposed risk measures with respect to λ follows directly from their analytical formulation and indicates that the relative contributions of the entropy and expected utility components can be adjusted in a smooth and predictable manner.

The representative simulation results obtained under the Poisson and discretized Normal probability models, summarized in Table 2.4.11, exhibit qualitative behaviour consistent with that observed for the Binomial distribution. In particular, the proposed EU-FE and EU-FEV measures vary smoothly with both the fractional order parameter and the risk-tradeoff parameter, without exhibiting abrupt numerical changes across the selected parameter settings. Although the numerical values differ because of the distinct characteristics of the underlying probability distributions, the overall trends remain consistent across all three models. These results demonstrate that the proposed entropy-based decision framework is computationally stable and robust under both discrete and continuous parametric probability models, thereby supporting the wider applicability of the proposed EU-FE and EU-FEV measures for uncertainty-based decision-making and risk assessment.

Overall, the simulation results indicate that the proposed entropy-based decision models remain stable under both discrete and continuous parametric probability models. The consistency of the observed trends across different probability distributions demonstrates the robustness of the proposed EU-FE and EU-FEV measures with respect to the underlying probabilistic assumptions and supporting their applicability to uncertainty-based decision-making and risk-ranking problems. Furthermore, the risk measures vary smoothly with both the fractional order parameter and the risk-tradeoff parameter, indicating the absence of abrupt numerical instabilities and demonstrating the computational stability of the proposed decision models.

The simulation study establishes the robustness of the proposed entropy-based decision models under controlled probabilistic settings. Having verified their theoretical behaviour through representative simulation experiments, the applicability of the proposed framework is now investigated using real financial market data. The following section presents the empirical validation of the proposed EU-FE and EU-FEV models using the PSI20 stock market index.

2.4.4 Validity of the proposed models using real market data

In the previous subsection, the potential of the proposed fractional Ubriaco entropy-based decision-analysis models in addressing several important investment problems and decision paradoxes was examined. The resulting decisions indicate that, in certain cases, these models outperform traditional Shannon entropy-based decision frameworks. To further investigate their strengths and to substantiate their superiority in modeling decision-making under risk, a detailed statistical analysis is conducted using real market data from the Portuguese stock market index (PSI20), collected from `https://www.investing.com`. Machine learning techniques, particularly artificial neural networks (ANNs), are employed for this purpose, and all computations are carried out in MATLAB R2022b. For additional discussions on the application of ANNs in analyzing the influence of input features on decision outcomes, the reader may refer to Raghavendran et al. (2024) and Liu and Yeh (2017). Furthermore, to examine the behavior of the proposed models with respect to their key parameters, α representing the risk attitudes of decision-makers toward uncertainty, while λ governing the trade-off between risk and reward, a sensitivity analysis is performed. Stock market states, or returns, are first predicted using ANN-based models trained on selected input features. The resulting predictions are then utilized to evaluate decision outcomes based on the proposed EU-FE and EU-FEV risk measures, which incorporate both return uncertainty and subjective utility associated with stock investments.

To analyze the influence of the input features on the risk-based decision outcomes, we used a feedforward ANN (MLP) with the following structure:

- Input layer: 5 inputs (features)
- Hidden layers: A single layer of 10 neurons or two layers with 20 and 10 neurons respectively (The neurons contained in each layer apply weighted sums followed by an activation function such as sigmoid or ReLu).
- Output layer: Single neuron predicting the risk

The hidden layers allow the network to accurately model complex interactions between input variables (α (risk sensitivity), λ (risk aversion), Ubriaco entropy, Normalized Variance (NVar), and Normalized Expected Utility (NEU)) and output variable (risk), suggesting that risk perception and decision behavior may be nonlinear in nature. We have used scaled conjugate gradient algorithm as the training function and the data sets are divided into 70% training, 15% validation and 15% testing. Once trained, the ANN predicts the risk for each stock for all combinations of α and λ using the formulated fractional order entropy-based risk measures.

Firstly, to study the usefulness of the ANNs in studying the relation between input parameters on the decision outcomes, we consider an investor willing to choose a set of m stock components from n options. Then the action of selecting stock M_i will be represented by a_i for $i = 1, 2, \ldots, m$ and the action space will be given by $A = \{a_1, a_2, \ldots, a_n\}$. Next, the historical data of closing prices for each stock component is collected for PSI 20 data series from 01/01/2019 to 31/12/2020. The stock components included in the PSI 20 data collected are listed in Table 2.4.12. We obtain a set of 512 entries for each stock M_i denoted by $\{p_{i0}, p_{i2}, \ldots, p_{iL}\}$, where $L = 511$. Then the returns for each stock M_i can be obtained as:

$$r_{il} = \log\left(\frac{p_{il}}{p_{i(l-1)}}\right), \tag{2.4.3}$$

where i = 1, ..., 15 and $l = 1, 2, \ldots, 511$. Then we obtain a set of returns given by $\{r_{i1}, r_{i2}, \ldots, r_{i511},\}$ for stock M_i. Among all the stock returns obtained, we find that the minimum return value $r_{min} = -0.0929$ and the maximum value $r_{max} = 0.0751$. This gives us that

$$r_{il} \in [-0.0929, 0.0751],$$

for $i = 1, 2, \ldots, 15$ and $l = 1, \ldots, 511$. The interval $[r_{min}, r_{max}]$ is partitioned into $J = 15$ sub-intervals of equal length $\Delta = \frac{r_{max} - r_{min}}{J} = 0.0112$. Thus we get 15 sub-intervals of the form $J_1 = [-0.0929, -0.0817), J_2 = [-0.0817, -0.0705), \ldots, J_{15} = [0.0751, 0.0639]$, each of length $\Delta = 0.0112$. The utility function considered in this study is a S-shaped utility function, known to be concave for profits and convex for losses, as introduced by Kahneman and Tversky (1979) to represent the degree of risk aversion among decision-makers. The utility function is defined as:

$$u(x) = \begin{cases} \log(1 + x) & x \geq 0, \\ -\log(1 - x) & x < 0. \end{cases} \tag{2.4.4}$$

Table 2.4.12: Stock components of PSI 20 stock market index.

Stock	Components	Stock	Components	Stock	Components
M_1	ALSS	M_6	EDPR	M_{11}	NOS
M_2	BCP	M_7	GALP	M_{12}	NVGR
M_3	CORA	M_8	IBS	M_{13}	RENE
M_4	CTT	M_9	JMT	M_{14}	SEM
M_5	EDP	M_{10}	MOTA	M_{15}	YSO

Therefore, the EU-FE and EU-FEV risk measures are defined using this utility function for each stock components. The values of the risk factors used in defining the fractional order entropy-based risk measures, given by (2.4.1) and (2.4.2), are provided in Table 2.4.13. To check the performance of the model, all the stock components $\{M_1, \ldots, M_{15}\}$ is chosen from the list of 15 stocks provided in Table 2.4.12.

In real stock-market data, the direct analytical evaluation of the proposed EU-FE and EU-FEV risk measures is not straightforward because the return distribution is not known in closed form. The probability weights must be estimated from empirical return observations, and the resulting risk measures depend jointly on fractional entropy, expected

Table 2.4.13: Risk factors of EU-FE and EU-FEV decision models for PSI 20 data.

Stocks M_i	$\mathrm{NEU}(a_i) = \frac{E[u(x_{in})]}{maxE[u(x_{in})]}$	$\mathrm{NVar}(a_i) = \frac{V(x_{in})}{maxV(x_{in})}$	$H_U^\alpha(X_i)$
M_1	-0.2386	0.6712	1.189223
M_2	-0.7733	0.7184	1.138423
M_3	0.1676	0.3313	1.218279
M_4	-0.3357	0.5658	1.233337
M_5	0.4833	0.3486	1.097892
M_6	1.0000	0.3499	1.161922
M_7	-0.6201	0.5955	1.086162
M_8	-0.6936	1.0000	0.983342
M_9	0.1974	0.3002	1.137902
M_{10}	-0.4411	0.9628	1.058261
M_{11}	-0.7326	0.3635	1.161297
M_{12}	-0.4576	0.4529	1.225268
M_{13}	-0.0905	0.1576	1.068735
M_{14}	-0.4427	0.4243	1.209417
M_{15}	-0.2730	0.3809	1.237089

utility, variance, the fractional order parameter α, and the trade-off parameter λ. This produces a nonlinear and data-dependent mapping from observed returns to risk scores. Therefore, a computational algorithm is required to make the proposed entropy-based risk measures operational for real financial data and finding the optimal values of the parameters. The basic steps that outline the application of EU-FE and EU-FEV decision analysis models to stock selection are presented in Algorithm 3. The computations are performed using MATLAB R2022b.

Next, the ANN prediction errors (residuals) are fitted with a linear model, where the residuals are computed by the formula:

$$Res_i = y_i - \hat{y}_i, \tag{2.4.5}$$

where y_i =actual value of the target variable (the true risk value from our decision model) and $\hat{y}_i$ = predicted value from the ANN for the same input vector x_i. Averaging the squares of the residuals (MSEs) given in (2.4.5) per stock helps identify:

- Stocks where the model overestimated or underestimated risk

Algorithm 3: Computation of EU-FE and EU-FEV Risk Measures for Stock Returns of PSI 20 data.

Input: Return series of stock M_i: $R_i = \{r_{i1}, \dots, r_{iT}\}$ determined from Eq. (2.4.3);
Trade-off parameter $\lambda \in [0, 1]$;
Risk sensitivity parameter $\alpha \in [0, 1]$;
Normalized expected utility $NEU(k_i)$ and normalized variance $NVar(k_i)$ for each stock M_i, $i = 1, \dots, 15$;
Fractional order entropy $H_U^\alpha(X_i)$ from Eq. (2.2.2);
Number of histogram bins N_{bins}.

Output: EU-FE and EU-FEV risk scores $R_{EU\text{-}FE}$ and $R_{EU\text{-}FEV}$ for each stock.

Normalize return series R_i if required;
foreach *stock* $i = 1$ **to** 15 **do**
  Compute histogram bins over the range of R_i;
  Compute probabilities p_{in} for each bin;
  Compute fractional order entropy $H^\alpha(X_i) = \sum(p_{in} \cdot (-\log p_{in})^\alpha)$;
  Compute mean and variance of returns;
  Compute expected utility using the utility function:

$$u(x) = \begin{cases} \log(1+x), & \text{if } x \geq 0, \\ -\log(1-x), & \text{if } x < 0 \end{cases}$$

end
Normalize variance and expected utility across all stocks;
Compute $R_{EU\text{-}FE}$ and $R_{EU\text{-}FEV}$ for each stock using Eqs. (2.4.1) and (2.4.2).

- Stocks that show more consistency or less surprise in risk

The objective of the ANN training is to minimize the mean square of the residuals (MSE), computed as:

$$MSE = \frac{1}{N} \sum_{j=1}^{N} (Res_i)^2, \tag{2.4.6}$$

where N is the number of samples.

To evaluate the performance characteristics of the proposed fractional entropy-based decision models, a linear regression analysis is performed on the residuals obtained from

Table 2.4.14: Linear regression model for EU-FEV risk measure (PSI 20 data).

Input features	Estimate	SE	$t-$stat	$p-$value
Intercept	-0.0003339	0.0029072	-0.11485	0.90857
Alpha (α)	-0.0018146	0.0015974	-1.136	0.25606
Lambda (λ)	-0.0001587	0.00073888	-0.21478	0.82995
Entropy(H^α)	0.0012435	0.0025338	0.49075	0.62364
NVar	-0.00055227	0.002042	-0.27045	0.78683
NEU	-0.00029215	0.00074247	-0.39348	0.69399

the ANN predictions. Table 2.4.14 summarizes the regression results for the EU-FEV model, yielding an RMSE of 0.0123, a coefficient of determination $R^2 = 0.000916$, an adjusted $R^2 = -0.000705$, an F-statistic of 0.565 relative to the intercept-only model, and a corresponding p-value of 0.727. The extremely low value of R^2 indicates that only 0.0916% of the variability in the predicted risk is explained by the linear regression, implying negligible linear dependence between the EU-FEV risk and the explanatory variables. The adjusted R^2, which accounts for the number of regressors and penalizes unnecessary model complexity, is defined as:

$$\bar{R}^2 = 1 - (1 - R^2)\,\frac{n-1}{n-k-1},$$

where n denotes the number of observations and k represents the number of explanatory variables in the model. In the present case, the adjusted R^2 is negative, indicating that the linear regression model explains less variability than a constant-only (mean) model, thereby confirming that the assumed linear relationship is inadequate for describing the underlying data structure. This further confirms that the assumed linear relationship is inadequate for describing the underlying data structure. Consistent with this observation, the high p-value associated with the F-statistic suggests that the regression model is statistically insignificant. Furthermore, the regression coefficients reported in Table 2.4.14 reveal that the entropy term has a positive coefficient, indicating that increases in entropy lead to systematic underestimation of risk by the linear EU-FEV model. Collectively, these findings highlight the inherently nonlinear nature of the relationship between entropy-based risk measures and the input features, thereby justifying the use of nonlinear learning approaches such as artificial neural networks to capture the complex interactions among entropy, risk attitudes, and return uncertainty in the proposed decision framework.

On the other hand, the EU-FE model is characterized by: RMSE = 0.0265, R^2 =0.000602,

Table 2.4.15: Linear regression model for EU-FE risk measure (PSI 20 data).

Input features	Estimate	SE	$t-$stat	$p-$value
(Intercept)	-0.0050995	0.0027907	-1.8273	0.067701
Alpha (α)	-0.001876	0.0018282	-1.0261	0.30487
Lambda (λ)	0.00037361	0.0010777	0.34668	0.72884
Entropy(H^α)	0.0049428	0.0028052	1.762	0.078114
NEU	-0.00037022	0.00068007	-0.54439	0.58619

Adjusted R^2 = -2.93e-06, F-statistic vs. constant model= 0.995, p-value = 0.409. This implies that the model explains only 0.0602% of the variance in the response variable (risk), indicating that the predictors have almost no explanatory power for the output. Thus, the results of linear regression model for EU-FE model displayed in Table 2.4.15 indicates that none of the input predictors are statistically significant at the 5% level, the closest being entropy ($p = 0.078$). This imply nonlinear relationships or interactions that a linear model cannot capture. Therefore, the results of Tables 2.4.14 and 2.4.15 strongly suggests the use of non-linear models like ANN for capturing the influence of the input parameters on the predicted risk. This motivates us to use ANN and Lasso regression to study the non-linear interactions between the input and output variables.

Linear regression is included as a simple interpretable baseline representing linear relationships between the entropy-based risk measures and the explanatory variables. Lasso regression is considered because it performs simultaneous coefficient shrinkage and variable selection, thereby providing a robust regularized benchmark for financial data. The ANN is incorporated as a flexible nonlinear approximation model capable of capturing complex interactions among the fractional order parameter, entropy, variance and expected utility without requiring an explicit functional specification. Comparing these complementary models enables us to assess whether the proposed fractional entropy-based decision measures exhibit predominantly linear or nonlinear behaviour.

The efficiency of predicted results of the linear model and the non-linear models (ANN and Lasso) for the fractional entropy-based risk measures are compared with that of the Shannon entropy-based decision models. The results are displayed in Table 2.4.16. From the results of Table 2.4.16, we find that adding variance to the Shannon entropy-based EU-E model worsened both RMSE and R^2. Further the ANN performance degraded significantly for the decision model based on EU-EV risk measure, with very poor R^2,

Table 2.4.16: Performance comparison metrics for different entropy-based risk measures (PSI 20 data).

Risk Measure	**Linear Regression**		**ANN**		**Lasso Regression**	
	RMSE	R^2	RMSE	R^2	RMSE	R^2
EU-E	0.3085	0.6359	0.3869	0.4273	0.2963	0.6122
EU-EV	0.3204	0.3646	0.3921	0.0482	0.2996	0.3560
EU-FE	0.1557	0.8620	0.0291	0.9952	0.1559	0.8598
EU-FEV	0.1322	0.8603	0.0091	0.9993	0.1337	0.8618

suggesting the additional variance term may introduce noise or overfitting. However, we witness substantial improvement in performance with the fractional entropy based risk measures due to the introduction of a tunable sensitivity parameter α in the Ubriaco entropy. The EU-FE and EU-FEV risk measures give much lower RMSE and higher R^2 compared to EU-E and EU-EV measures. Adding variance here slightly improves RMSE, with negligible change in R^2. Moreover, the results of both ANN and Lasso regression shows outstanding performance with fractional entropy, especially with ANN. The addition of variance further boosts performance. This shows that Shannon entropy based decision models may not fully capture investor behavior. It further strengthens the idea that fractional entropy is likely better at modeling risk sensitivity and decision uncertainty. Addition of variance in the risk measure helps slightly with the performance of the risk models.

To further investigate the nonlinear approximation capability of the proposed entropy-based decision framework, an additional comparison was carried out using Sinusoidal Regression. This model was selected because sinusoidal functions are widely employed for modeling periodic and seasonal behaviour in hydrology and finance. Table 2.4.17 compares the prediction accuracy and computational efficiency of Linear Regression, Lasso Regression, Sinusoidal Regression and ANN under identical experimental settings.

From Table 2.4.17, it is observed that Linear Regression and Lasso Regression exhibit comparable prediction accuracy, indicating that regularization alone provides only marginal improvement for the proposed entropy-based risk formulation. The Sinusoidal Regression model also produced prediction accuracy similar to the linear models, suggesting that the relationship between the entropy-derived variables and the proposed risk measure is nonlinear but not intrinsically periodic. In contrast, the ANN substantially

Table 2.4.17: Performance comparison of linear and nonlinear learning models for entropy-based risk prediction.

Model	**RMSE**	**MSE**	$\mathbf{R^2}$	**Training Time**	**Prediction Time**
Linear Regression	0.140248	0.019669	0.886955	0.003158 s	0.001399 s
Lasso Regression	0.140210	0.019659	0.887016	0.003749 s	0.001223 s
Sinusoidal Regression	0.140616	0.019773	0.886360	0.004527 s	0.000787 s
ANN	0.030956	0.000958	0.994492	0.275908 s	**0.000421 s**

improved the predictive performance, yielding the lowest RMSE and MSE together with the highest coefficient of determination ($R^2 = 0.994492$) among the compared models. These results demonstrate that the nonlinear interactions among the fractional order parameter, entropy, variance and expected utility are more effectively captured by the ANN than by linear or harmonic regression models.

The computational efficiency analysis further shows that although the ANN required a higher one-time training cost than the regression-based models, it achieved the lowest prediction time (0.000421 s) among all compared methods. Since model training is performed only once whereas prediction is repeatedly executed during practical deployment, the ANN provides an efficient computational surrogate for rapid entropy-based risk estimation after training.

It is important to emphasize that the ANN is not intended to replace the proposed entropy-based decision model. Rather, the entropy-based formulation provides the theoretical basis for quantifying financial risk, while the ANN learns the nonlinear relationship between the entropy-derived input variables and the corresponding risk measure. Consequently, the ANN serves as a computational surrogate that rapidly approximates the entropy–risk mapping after the entropy-based features have been computed, thereby facilitating efficient large-scale screening and decision support without repeatedly evaluating the analytical risk equation.

The comparative analysis demonstrates that the ANN substantially improves predictive performance over the linear, Lasso and sinusoidal regression models while providing the lowest prediction time after training. These findings support the use of ANN as an efficient computational surrogate for approximating the proposed entropy–risk relationship.

Remark 2.4.4. *Since ANN models are flexible and parameter-dependent, possible overfitting must be considered when interpreting the empirical validation results. Overfitting may occur when the network learns noise or sample-specific fluctuations instead of the underlying relationship between entropy-based inputs and the risk measure. This issue is particularly relevant for financial data because market observations are noisy and the available sample size may be limited.*

To reduce this concern, ANN is used here only as a flexible nonlinear validation tool and not as the sole basis for validating the proposed EU-FE and EU-FEV measures. The interpretation of the results is supported by comparison with simpler benchmark models and by evaluating prediction performance on test data rather than relying only on in-sample fit. Additional safeguards such as early stopping, cross-validation, regularization, and repeated train–test splits has been used in the next chapter to further reduce architecture-dependent conclusions.

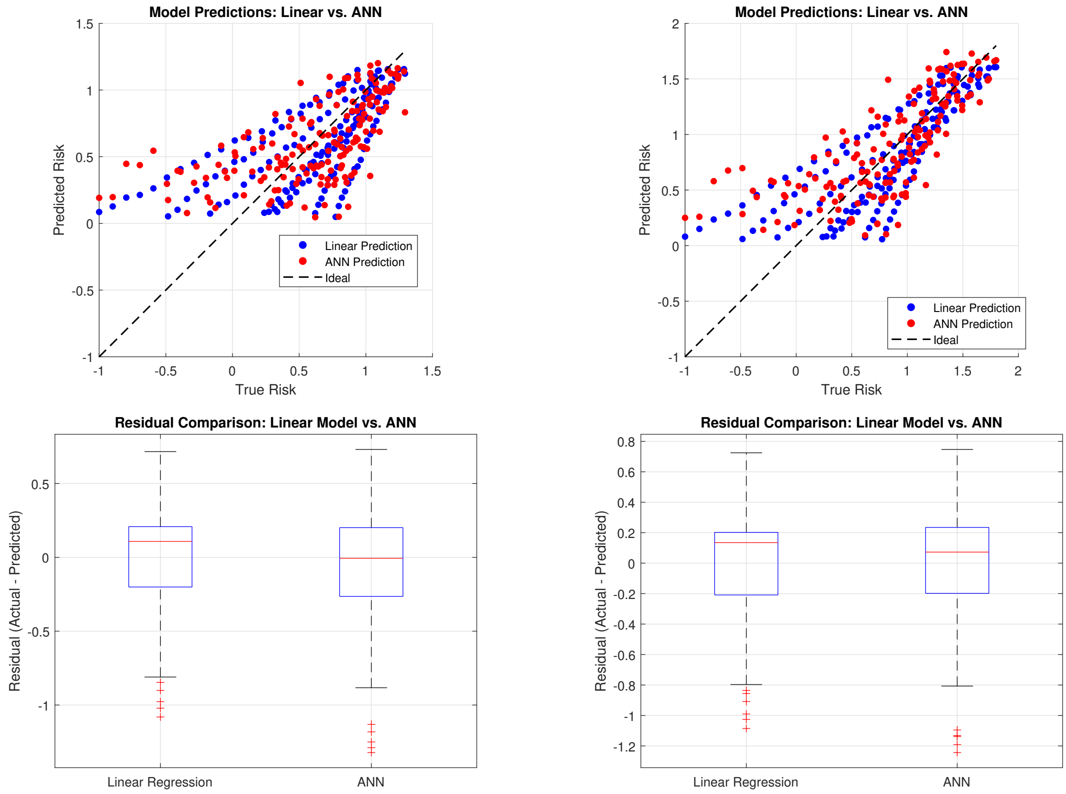

Figure 2.4.6: Model Performance Metrics for EU-E (left) and EU-EV models (right).

Additionally, the performance of the Shannon entropy and fractional entropy-based decision models are further illustrated through Figs. 2.4.6 and 2.4.7. Through these illustrations, one can see that the EU-FE and EU-FEV models exhibit better performance than EU-E and EU-EV models with non-linear fitting of the data with ANN since ANN shows tighter and lower-centered box than the linear model for EU-FE and EU-FEV models. Henceforth, we can deduce that the real stock market data features non-linear interactions between the input variables and risk. This can be captured in a better way through the EU-FE and EU-FEV based decision analysis models with the help of machine learning methods like ANNs.

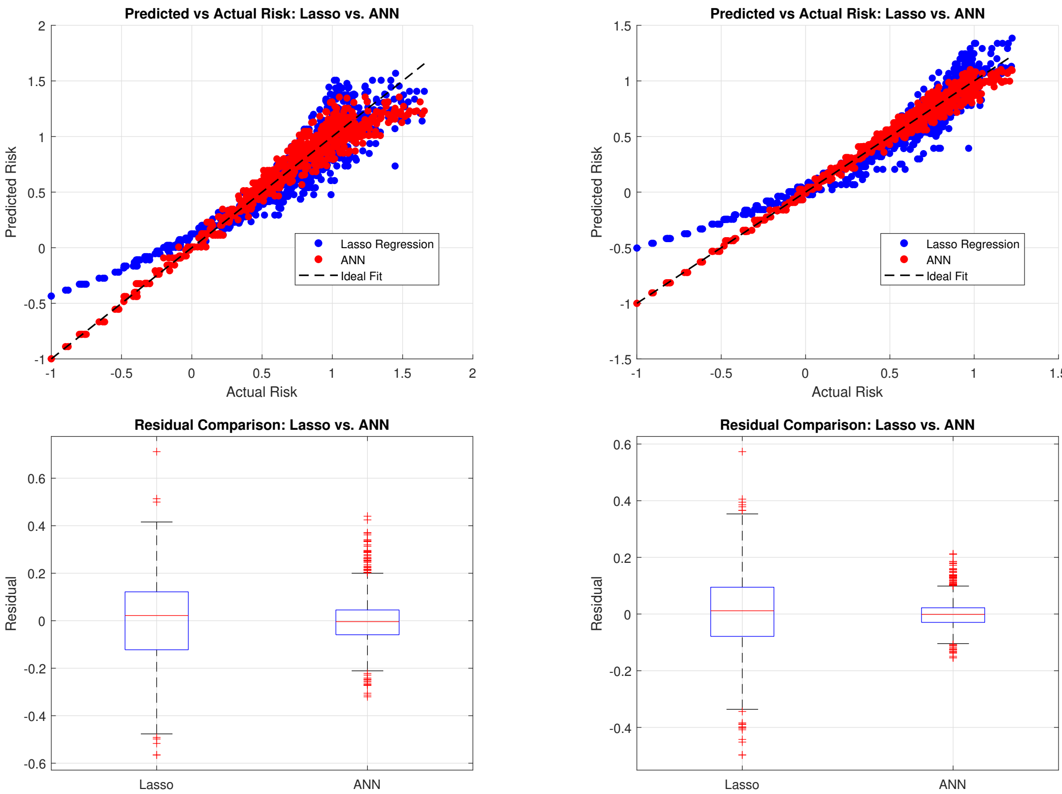

Figure 2.4.7: Model Performance Metrics for EU-FE (left) and EU-FEV models (right).

Further, to visualize the marginal influence of the model parameters α and λ on the ANN residuals, we used Partial Dependence Plots (PDPs). For this we have applied the fitted linear model from the previous step. These plots show how the ANN residuals change on average as we vary one variable (α or λ) while keeping the others fixed. From Fig. 2.4.8, we observe linear increase of the PDP of ANN residual for α for EU-FE model, suggesting more sensitivity to rare events (via high α) implying higher entropy associated with more risk or uncertainty. This model penalizes investors who are modeled with low α values, as they under estimate risk. On the other hand, a linear decrease of the PDP for α is witnessed for EU-FEV model. This indicates that lower α values

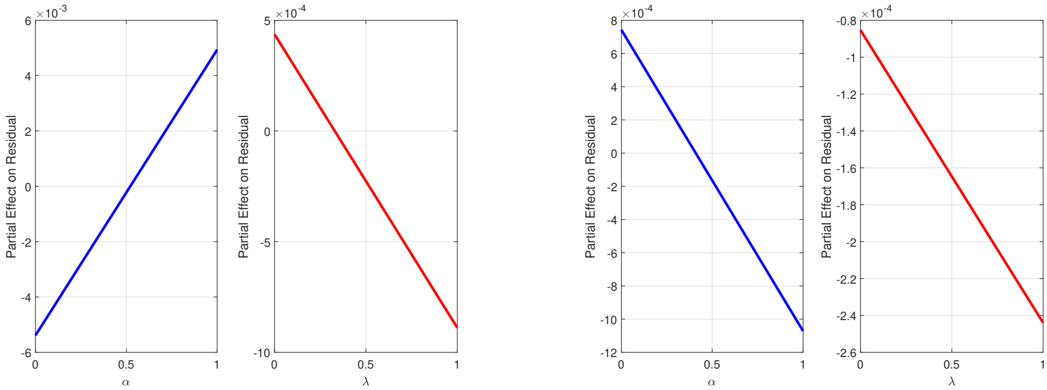

Figure 2.4.8: Marginal influence of the parameters α and λ on EU-FE (left) and EU-FEV (right) risk measures.

are preferred, as it results in lower perceived risk. Thus, the contribution of entropy to the perceived risk increases with increase in α for EU-FEV model. This represents the inclination of the decision model to favor interpretations of uncertainty that are less sensitive to rare/extreme events and penalization of investors who are modeled with higher α values, since they overestimate risks. Moreover, we observe a linearly decreasing PDP curve for λ for both the EU-FE and EU-FEV models. This indicates that the models penalizes high λ values because it weights entropy (risk) more than utility. Investors with higher risk aversion (higher λ) are assigned higher risk scores by the model. This implies that the proposed models favors stocks with low entropy and high utility when λ is low. Furthermore, the linear relationships of the prediction errors with α and λ reveals that there is a predictable and constant rise in perceived risk with unit change in one of the parameters keeping the other fixed.

Further, through correlation analysis illustrated by Figs. 2.4.9 and 2.4.10, we analyzed the performance and reliability of our proposed decision models. The Pearson correlation coefficient is given by:

$$\rho = \frac{Cov(y_i, \hat{y}_i)}{\sigma_{y_i} \cdot \sigma_{\hat{y}_i}}, \tag{2.4.7}$$

where σ_{y_i} and $\sigma_{\hat{y}_i}$ denote the standard deviation (s.d) of true values y_i and s.d of predicted values $\hat{y}_i$, respectively. The correlation coefficients for the EU-FE and EU-FEV models show stronger correlation between the input parameters and risk as compared to that for the Shannon entropy based models (EU-E and EU-EV). A negative correlation between normalized expected utility (NEU) and risk is observed for all the models since the utility function has a reverse effect on the risk. Thus, these findings support the contribution of incorporating the fractional Ubriaco entropy in place of the Shannon entropy inside the risk measures in enhancing the performance of the risk-based decision models.

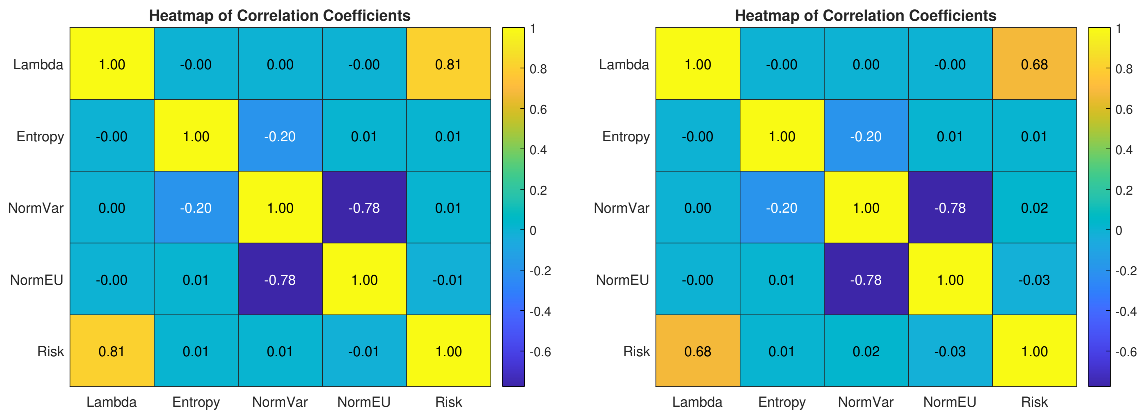

Figure 2.4.9: Correlation Coefficient matrix for EU-E (left) and EU-EV models (right).

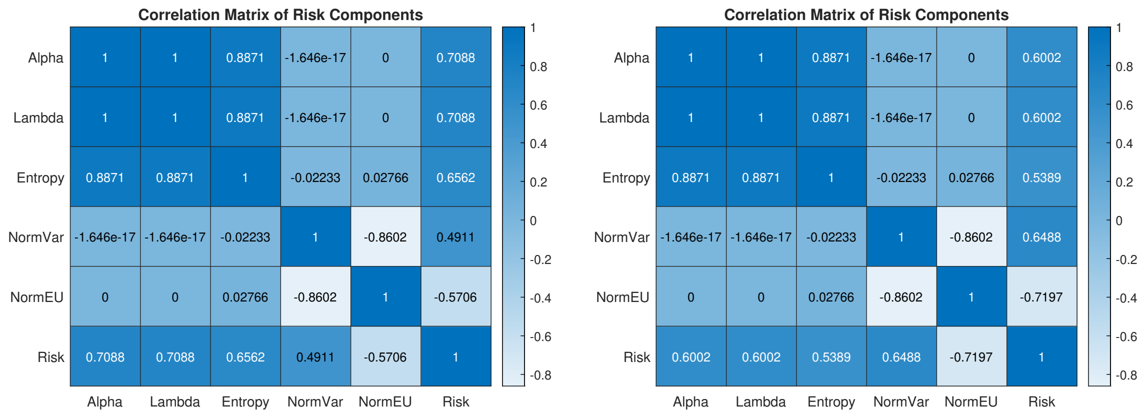

Figure 2.4.10: Correlation Coefficient matrix for EU-FE (left) and EU-FEV models (right).

Furthermore, low p-values (close to or equal to zero) is obtained for the input parameters with respect to risk (see Fig. 2.4.11). This indicates that the input parameters significantly contributes to explaining variations in the risk score. Therefore, the results of Fig. 2.4.11 suggest that the considered features are statistically significant predictors of the EU-FEV risk measure, implying that these variables are not random fluctuations but possess a meaningful and systematic relationship with the modeled risk structure. Thus the proposed decision models under risk using ANN shows more robustness of the findings across real market data (PSI 20) as compared to the existing entropy-based decision models.

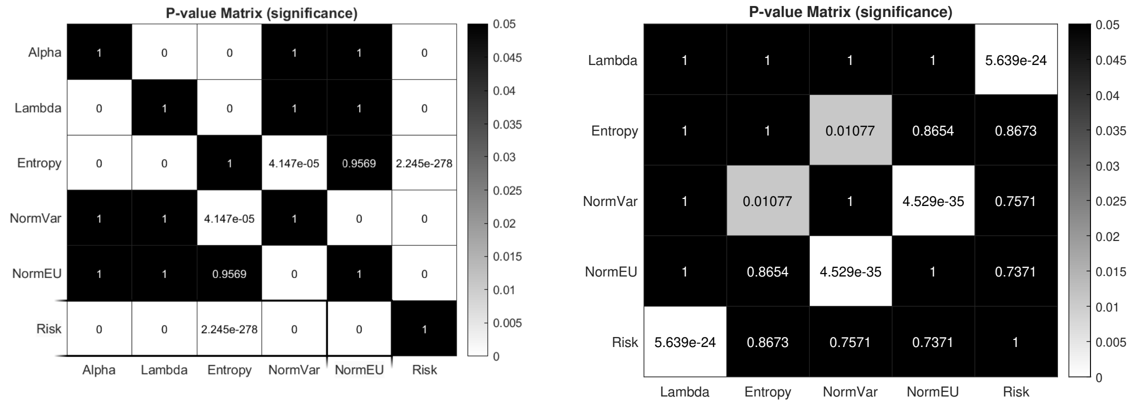

Figure 2.4.11: p-values of the input variables with respect to fractional entropy (left) and Shannon entropy (right)-based risk measures.

A sensitivity analysis is also conducted for the stock M_1 to show the influence of α and λ on the proposed EU-FEV risk measure. We can observe from Fig. 2.4.12 that the sensitivity of EU-FEV risk measure with respect to α increases with increase in λ. Further, the sensitivity of the EU-FEV measure with respect to λ increases with increase in α. Thus the EU-FEV measure shows increasing sensitivity at higher values of both α and λ. Moreover, Fig. 2.4.13 shows that EU-FEV risk values increases with increase in λ values for a fixed α value. Similar trend is observed for the EU-FEV measure as α increases for a fixed λ value. The associated risk tolerance curves are also presented in Fig. 2.4.13 to show the behavior of the proposed EU-FEV risk measure with respect to either parameter (α or λ) keeping the other fixed.

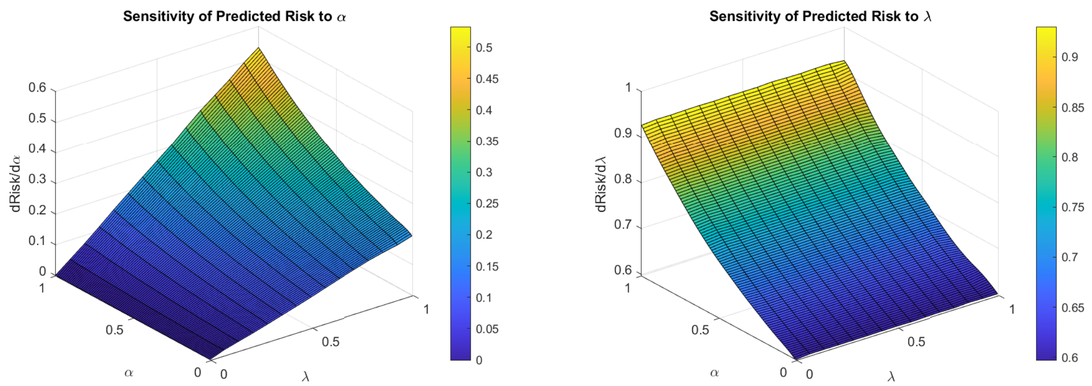

Figure 2.4.12: Gradient of EU-FEV risk measure with respect to α (left) and λ (right) for Stock M_1 of PSI 20 data.

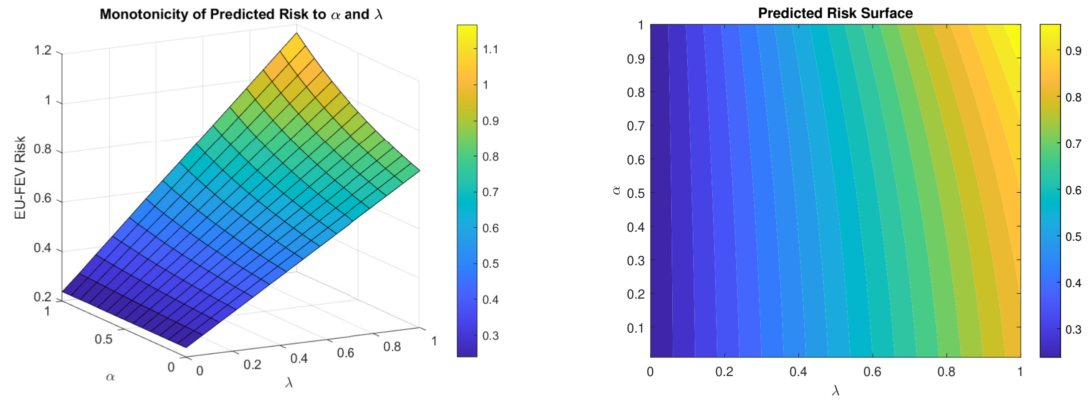

Figure 2.4.13: Monotonicity (left) and risk tolerance curves (right) of EU-FEV risk measure with respect to α and λ for Stock M_1.

2.5 Portfolio stock selection using EU-FE and EU-FEV models

The developed EU-FE and EU-FEV models introduced in the previous section have been applied to select the optimal combination of stock components from the Portuguese Stock Index PSI 20 index for generating efficient portfolios. The set comprising of all the efficient portfolios with a given number of stocks gives the efficient frontier. In the current study, the mean-variance portfolio optimization method is adopted after selecting an optimal combination of stocks for generating efficient frontiers as done in Brito (2023).

Firstly, the 15 selected stocks are ranked using a bootstrapped ANN approach based on predicted risk values from the proposed EU-FE and EU-FEV models. A total of 100 bootstrap iterations are used, generating multiple predictions for each sample and enabling the computation of confidence intervals (CIs). The average predicted risk across bootstrap runs is then obtained for each stock. Stocks are ranked in ascending order of their fractional entropy-based risk scores, where lower risk and narrower CIs indicate better performance (see Table 2.5.1). The top 7 ranked stocks are subsequently used to construct efficient frontiers (Fig. 2.5.1).

From Fig. 2.5.1, we can observe that the efficient frontier of selected subset of top 7 stocks almost intersects the frontier of portfolios having all 15 stock components of PSI 20 data for return values above 0.5×10^{-3}. This shows that the efficiency of a portfolio with 7 stocks is almost equal to that of a portfolio set of all stocks for a fixed return range. Thus, the EU-FE and EU-FEV models can be effectively used as a stock selection

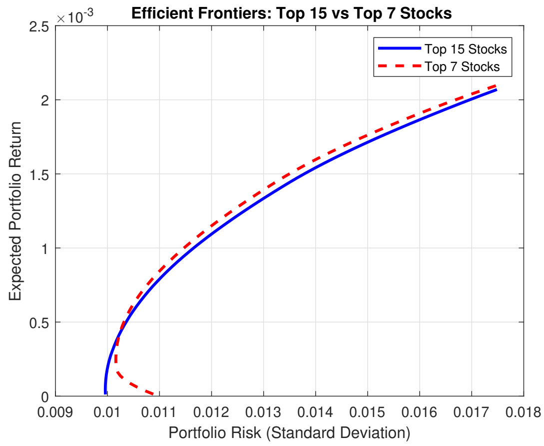

Figure 2.5.1: Comparison of Efficient Frontiers of portfolio of 7 stocks with that of a portfolio with all the stock components.

Table 2.5.1: Ranks of stock components of PSI 20 data.

Ranks	Stock	Mean Risk	Confidence Interval (CI)
1	6	0.1152	[0.0203, 0.2083]
2	5	0.3509	[0.2793, 0.4298]
3	9	0.5096	[0.4516, 0.5695]
4	3	0.5449	[0.4791, 0.6006]
5	13	0.6118	[0.5475, 0.6980]
6	1	0.7616	[0.6952, 0.8340]
7	10	0.7751	[0.7181, 0.8475]
8	15	0.8042	[0.7370, 0.8589]
9	4	0.8209	[0.7697, 0.8740]
10	8	0.8578	[0.7992, 0.9161]
11	14	0.8762	[0.8270, 0.9221]
12	12	0.8806	[0.8354, 0.9279]
13	7	0.9198	[0.8670, 0.9772]
14	2	0.9601	[0.8930, 1.0177]
15	11	0.9780	[0.9140, 1.0399]

model before the construction of efficient frontiers of portfolios. From this result, we can hereby state that portfolios with less than half the total number of stocks (7 out of 15) in a real stock market data (Portuguese stock market data in this case) can generate equally efficient frontiers as that of portfolios with all the stock components. This also gives us the necessary information about the optimal sample size of stock components to construct a well diversified portfolio, maintaining a balance between risk and return. Thus, the current fractional entropy based models can be effectively applied to decrease the number of stocks without affecting the diversification or efficiency of the constructed portfolio.

2.6 Conclusion

The current chapter highlights that the risk-seeking behavior or tolerance levels of decision makers significantly influence decisions made under uncertainty and risk. The parameter α in the fractional order entropy proposed by Ubriaco is interpreted as a measure of an individual's risk tolerance or risk sensitivity to uncertainty. Specifically, lower values of α (closer to zero) indicate lower risk tolerance (conservative attitude), while values approaching one correspond to individuals with higher tolerance for risk (adventurous attitude). From the findings of this study, it can be remarked that the fractional entropy-based (EU-FE, EU-FEV) decision analysis models is a much better choice for modeling stock selection decisions under risk as compared to the existing Shannon entropy-based counterparts. The selected stocks can be effectively used to generate efficient frontiers of portfolios using mean-variance optimization method. The proposed decision models also helps in solving some famous investment problems and decision paradoxes. Moreover, the addition of variance in the decision model helps only when combined with fractional entropy, but not with standard Shannon entropy. It is found that ANN performs best with EU-FEV, indicating its capability to capture complex non-linear patterns in investor decision modeling.

Linear Regression and Lasso Regression were included as interpretable baseline statistical models because they remain among the most widely used regression approaches in financial risk modeling. Sinusoidal Regression was additionally considered as a nonlinear benchmark due to its effectiveness in modeling periodic relationships. The comparable performance of the linear and sinusoidal models indicates that the relationship between the entropy-derived variables and the proposed risk measure is nonlinear but not intrinsically periodic. The ANN achieved substantially better predictive performance by effectively capturing the complex nonlinear interactions among the fractional order parameter, entropy, variance and investor preference parameter without requiring an explicit functional specification. These findings further support the use of ANN as a computational surrogate for efficiently approximating the proposed entropy-based risk measure after the entropy-derived features have been computed. Such machine learning techniques can also be employed to estimate the optimal parameter values under varying market conditions.

Further, we have considered the mean-variance method for portfolio optimization. But there are other entropy-based optimization techniques in literature, which are not utilized in this study to compare the performance of the models. In addition to the real-data validation, the proposed EU-FE and EU-FEV measures were further investigated under controlled simulation settings using representative discrete and continuous parametric probability models. Specifically, the Binomial and Poisson distributions were considered to represent discrete probability models, whereas the Normal distribution was employed as a representative continuous probability model through an appropriate discretization of its probability density function. The simulation results demonstrate that the proposed fractional order entropy-based risk measures exhibit stable and consistent behaviour across different uncertainty structures, thereby providing additional evidence regarding the robustness and general applicability of the proposed decision-making framework. Future research may further extend this analysis by considering additional probability models, such as the Bernoulli, multinomial, lognormal, Student-t, and mixture-normal distributions, to investigate the performance of the proposed measures under a broader class of uncertainty structures.

However, the bootstrapping method considered in this study can be too complicated and computationally expensive for large data sets, which can be addressed in future works. Additionally, we have assumed that the risk sensitivity of individuals can always be scaled between 0 and 1 and no-short selling is considered for implementation of the probabilistic decision model. However, real stock market includes short-selling too. The existing market fluctuations or any potential biases are apparently not considered in this study, which might lead to over-fitting or under-fitting of the data with ANN, Linear and Lasso regression methods.

Chapter 3

Normalized Fractional Order Entropy-Based Decision-Making Models under Risk [1]

"All models are wrong, but some are useful."
— George E. P. Box

Building on the developments of fractional order Ubriaco entropy, introduced in the previous chapter as a behavioral measure of uncertainty, this chapter develops a normalized fractional entropy framework and proposes two novel risk measures that jointly integrate expected utility, variance, and fractional entropy. Investor risk sensitivity is governed by a fractional parameter α, ranging from conservative ($\alpha \to 0$) to adventurous ($\alpha \to 1$) preferences, enabling flexible modeling of risk-return trade-offs. The resulting decision-making frameworks are applied to NIFTY50 data to identify efficient low-risk stock subsets and construct optimized portfolios. Comparative analyses with existing fractional order entropy-based decision-making models, supported by machine learning techniques, demonstrate superior risk-return efficiency and robustness. Statistical significance tests further validate the effectiveness of the proposed approach in ranking assets consistent with investor preferences.

[1] A manuscript containing the work presented here is under review.

3.1 Introduction

The formalization of information theory by Shannon (1948), through the introduction of entropy as a quantitative measure of uncertainty, stands as one of the most influential contributions to modern research across statistics, computer science, electrical engineering, and related interdisciplinary fields. Since its inception, information-theoretic concepts have evolved substantially, finding widespread application in the characterization and analysis of complex physical and stochastic systems. A major conceptual advancement in this evolution was achieved by Yang and Qiu (2005), who introduced entropy into decision theory by formulating the expected utility-entropy (EU-E)-based risk measure for modeling decision-making under risk. The EU-E framework integrates subjective components of decision-making, such as individual attitudes toward risk or cost, through an expected utility function, while simultaneously accounting for objective uncertainty via the Shannon entropy measure. Within this formulation, risk is quantified as a composite score derived from both utility and entropy, and optimal decisions are identified by minimizing this score over the available action space represented by its corresponding states of nature. In financial decision-making contexts, this notion of risk naturally corresponds to uncertainty in the future value or cost of assets and securities arising from market fluctuations and other unpredictable events. As such, the EU–E model provides a foundational link between information theory and rational decision-making under uncertainty, motivating further extensions and refinements explored in this chapter.

The EU-E risk measure is grounded in the general decision-making framework, which asserts that individuals tend to select actions characterized by low uncertainty and high expected utility. This model provides a normative basis for rational decision-making and can also describe observed economic behaviors. The general decision-making model $\mathcal{G} = (\Theta, \mathcal{A}, u)$ comprises of the state space represented by $\Theta = \{\theta\}$, the action space symbolized by $\mathcal{A}$ and the utility function $u(X)$ representing an individual risk preference or risk aversion attitude. The payoff function defined on the space $\mathcal{A} \times \Theta$ is denoted by $X = X(a, \theta)$. Consequently, when the action space $\mathcal{A} = \{A_1, A_2, \dots, A_l\}$ and the state space θ_i corresponding to action A_i represented by $\theta_i = \{\theta_{i1}, \theta_{i2}, \dots, \theta_{im_i}\}$ are considered to be finite, then we obtain a payoff $X = X(A_i, \theta_{ij}) = x_{ij}$ corresponding to action A_i with state θ_i having a probability distribution $\{p_{ij} = P(X = x_{ij})\}$ which is the probability of occurrence of the payoff outcome x_{ij}, where $i = 1, 2, \dots, l; \quad j = 1, 2, \dots m_i$. This combination of outcomes and their associated probabilities for the action A_i can be written as (see Yang and Qiu, 2014, and references therein):

$$A_i = \begin{pmatrix} x_{i1} & x_{i2} & \dots & x_{im_i} \\ p_{i1} & p_{i2} & \dots & p_{im_i} \end{pmatrix} \tag{3.1.1}$$

or can be expressed as $A_i = (x_{i1}, p_{i1}; x_{i2}, p_{i2}; \dots; x_{im_i}, p_{im_i})$. The tabulated form of the general decision model can be found in Yang and Qiu (2005).

However, as the complexity and risk associated with decision-making increases, or as individual attitudes toward risk become more pronounced, the Yang and Qiu model was found to be inadequate in accurately describing risky decisions. In particular, it was observed that the expected utility-entropy (EU-E) model does not consistently align with empirically observed patterns of human behavior and individual risk perceptions (Fischer and Kleine, 2007). In response to these limitations, several extensions and refinements were proposed to enhance the descriptive and explanatory power of entropy-based decision models, including the works of Marley and Luce (2008) and Luce et al. (2005). A notable advancement was made by Yang and Qiu (2014), who standardized the EU-E framework by introducing the normalized expected utility-entropy (NEU-E) risk measure, in which Shannon entropy is replaced by its normalized form. In their formulation, Shannon entropy is normalized by dividing it by its maximum attainable value. The normalized Shannon entropy is defined as:

$$NH_S(p) = \begin{cases} -\sum_{x=1}^{n} p(x)\log p(x)/\log(n), & \text{for } n > 1 \\ 0 & \text{for } n = 1; \end{cases} \tag{3.1.2}$$

where $H_S(p) = -\sum_{x=1}^{n} p(x)\log p(x)$ is the Shannon entropy and $\log(n)$ is the maximum value of Shannon entropy computed from actions with equally likely outcomes as in uniform distributions. The normalization of entropy is particularly significant because it removes scale dependency, ensures comparability across different distributions, and enhances interpretability of uncertainty levels within the utility framework. This normalized measure (3.1.2) provides reasonable explanations for solutions to risky decision problems, including the certainty effects, which encompass two important empirical phenomena called the common ratio effect and the common consequence effect (Machina, 1987). The decision outcomes associated with the certainty effect, as described in Prospect theory by Kahneman and Tversky (1979), can also be meaningfully interpreted using the NEU-E model. Dong et al. (2016) further explored the expected utility and entropy-based decision-making framework, emphasizing the pivotal role of Shannon entropy in risk-based decision analysis.

Recently, Brito (2020) advanced the classical EU-E framework by integrating variance into the decision criterion, leading to the expected utility-entropy-variance (EU-EV) model. The inclusion of variance played a crucial role in capturing the sensitivity of decisions to outcome dispersion, an aspect that entropy alone could not fully represent. This enhancement allowed the model to resolve several long-standing decision paradoxes, such as the Levy paradox (Lévy, 1992) and the Allais paradox (Allais, 1953), which could not be satisfactorily explained within either the EU-E or NEU-E frameworks. Building upon this contribution, Brito (2022) further generalized the approach by incorporating normalized Shannon entropy (3.1.2). This extension resulted in the normalized expected utility-entropy-variance (NEU-EV) model, offering a more comprehensive and balanced representation of investor behaviour by jointly accounting for utility, uncertainty, and variability in outcomes. Consequently, this extension offers a more robust and interpretable framework for analyzing risk–uncertainty trade-offs in decision-making under risk.

Nevertheless, the existing decision-theoretic models place excessive emphasis on the utility function to capture the perceived riskiness of decision-makers, yet they do not clarify which aspects of individual risk attitudes should be represented by entropy. For instance, in Prospect theory, individual attitudes toward changes in wealth are captured by the value function, whereas the "pure" attitude toward risk is reflected in the probability weighting function (see Kahneman and Tversky, 1979). Consequently, the extant risk measures fall short in incorporating the dynamic nature of investors' risk attitudes with respect to the uncertainty of risky actions. Moreover, they often fail to leverage machine learning (ML) tools effectively to analyze the nonlinear relationships between input and output variables. Moreover, the existing literature has largely overlooked the potential of generalized entropy measures of order α, such as Rényi (Rényi, 1961), Tsallis (Tsallis, 1988), or fractional (Ubriaco, 2009) entropy forms, in developing risk-based decision-making frameworks that reflect heterogeneous risk attitudes. The choice of utility functions and the specification of trade-off parameters in many models also remain largely ad hoc, lacking robust empirical calibration or behavioral justification. As a result, the relationship between an investor's sensitivity to uncertainty and the expected utility associated with alternative choices is often insufficiently supported by real-world decision behaviors.

More recently, Paul and Kundu (2026) addressed several of these limitations by proposing two fractional entropy-based risk measures, namely expected utility-fractional entropy (EU–FE) and expected utility-fractional entropy-variance (EU-FEV). These models extend traditional Shannon entropy-based frameworks by incorporating fractional entropy, as introduced by Ubriaco (2009), thereby enabling a more flexible representation of individual sensitivity to risk and uncertainty. By jointly integrating subjective preferences through expected utility and uncertainty of a risky prospect through fractional order entropy, the EU-FE and EU-FEV models provide a more comprehensive basis for decision-making under risk, which is formally defined below.

Definition 3.1.1. *Let a discrete random variable (r.v.) have n states of nature, with probability mass function $p(x) = P(X = x)$ for the x-th outcome. The fractional order entropy introduced by Ubriaco is then defined as:*

$$S_\alpha(p) = \sum_{x=1}^{n} p(x)(-\log p(x))^\alpha; \ \alpha \in [0, 1]. \tag{3.1.3}$$

where $s_x(p) = p(x)(-\log p(x))^\alpha$ and $I_\alpha(p) = (-\log p(x))^\alpha$ are treated as the fractional order entropy function and fractional order information gain function, respectively.

It is straightforward to verify that, when $\alpha = 1$, the fractional-order entropy defined in (3.1.3) reduces to the classical Shannon entropy defined for discrete r.vs.

Paul and Kundu (2026) employed Ubriaco entropy in the development of decision-making models for risky and uncertain choices by explicitly incorporating heterogeneous risk tolerance levels through the fractional parameter α. The inclusion of α introduces additional flexibility into the entropy formulation, enabling it to capture distinct risk attitudes of decision-makers with respect to outcome probabilities. In this fractional entropy framework, both risk-seeking and risk-averse behaviors can be effectively modeled. Risk-seeking individuals, characterized by an adventurous attitude, tend to assign greater significance to low-probability outcomes, reflecting a higher willingness to embrace uncertainty. Conversely, risk-averse individuals exhibit a conservative attitude by placing less weight on such unlikely events and expressing greater skepticism regarding their occurrence (see Aggarwal, 2021a,b). The resulting fractional-entropy-based (FE-based) risk measures arise within a general decision analysis framework under risk, wherein each available action is associated with a set of possible states of nature, and each state is characterized by its own probability distribution.

However, the fractional entropy proposed by Ubriaco can take any positive real value, which makes it difficult to compare uncertainty across actions or prospects that differ in the number or structure of their possible outcomes. In decision-making models, especially those involving multiple alternatives with varying outcome spaces, such unbounded entropy values can distort the assessment of uncertainty and risk, leading to inconsistent or scale-dependent evaluations. To overcome this limitation, we normalize the Ubriaco fractional entropy so that its values lie within the fixed interval $[0, 1]$. This normalization ensures that the entropy measure remains comparable across prospects regardless of their dimensionality, number of outcomes, or payoff structure. A bounded, unit-free entropy scale also enhances interpretability: values closer to 0 represent low uncertainty, whereas values closer to 1 indicate high uncertainty, enabling a clearer distinction among risky choices. By incorporating this normalized fractional order entropy into the decision-making criterion, the present work introduces a new risk measure that unifies expected utility, variance, and fractional order uncertainty in a consistent framework. This normalized formulation allows more balanced risk assessment, avoids biases arising from unbounded entropy values, and ultimately provides a more robust tool for resolving decisions among risky prospects.

Having outlined the motivation, theoretical background, and key contributions of this chapter, the remainder of the chapter is organized as follows: In Section 3.2, we introduce a normalized form of the fractional order entropy due to Ubriaco. Based on the formulated entropy, we propose two normalized fractional-order entropy-based risk measures (NEU-FE and NEU-FEV) and the corresponding decision models. We further explore some fundamental properties of the proposed risk measures. In Section 3.3, we apply the proposed decision-making framework to a stock selection problem using real market data from the Indian stock market index (NIFTY50) for obtaining an optimal set of five stocks with minimum risk. Next, we present a detailed sensitivity analysis of the proposed entropy and risk measures with respect to the parameters in Section 3.4. Thereafter, we provide a comprehensive performance comparison of the proposed risk measures against existing fractional entropy-based risk models through error-based metrics and R^2 analyses using different ML tools such as Random Forest (RF), Ridge Regression (Ridge), Lasso Regression (Lasso) and Artificial Neural Network (ANN). Further interpretations derived from statistical significance tests validate model reliability and identify the most competent approach for ranking stocks in line with investor risk preferences. Finally, Section 3.5 concludes the present study with key findings and limitations.

3.2 Normalized fractional entropy-based decision analysis models

Ubriaco showed that the fractional entropy $S_\alpha(p)$ is always positive and the corresponding entropy function $s_x(p)$ achieves a maximum value at $p(x) = e^{-\alpha}$. Therefore, we get a loose upper bound for each term of the Ubriaco entropy given as $s_x(p) = \alpha^\alpha e^{-\alpha}$. Thus, by summing up the maximum values of each s_x for $n-$states of the system we obtain an upper bound of the entropy such that $S_\alpha \leq n\alpha^\alpha e^{-\alpha}$. Hence, the normalized fractional Ubriaco entropy can be defined as:

$$NS_\alpha(p) = \frac{S_\alpha(p)}{n\alpha^\alpha e^{-\alpha}} \tag{3.2.1}$$

so that $0 \leq NS_\alpha(p) \leq 1, \ \alpha \in [0,1]$.

Effect of normalization on entropy properties:

The normalization in (3.2.1) rescales the fractional Ubriaco entropy by the positive reference factor $n\alpha^\alpha e^{-\alpha}$. Therefore, for a fixed number of states n and a fixed fractional order $\alpha \in (0,1]$, the normalization does not change the basic concavity property of the entropy with respect to the probability vector $p = (p_1, \ldots, p_n)$. Indeed, the entropy component

$$s_\alpha(p_x) = p_x[-\log(p_x)]^\alpha$$

satisfies the following condition given as:

$$\frac{d^2}{dp_x^2} s_\alpha(p_x) = \frac{\alpha[-\log(p_x)]^{\alpha-2}}{p_x}\left[(\alpha-1) + \log(p_x)\right] \leq 0, \qquad 0 < p_x \leq 1, \quad 0 < \alpha \leq 1.$$

Thus, $S_\alpha(p) = \sum_x s_\alpha(p_x)$ is concave in the probability distribution. Since $NS_\alpha(p)$ is obtained from $S_\alpha(p)$ by division by a positive constant, the normalized entropy remains concave:

$$NS_\alpha(\eta p + (1-\eta)q) \geq \eta NS_\alpha(p) + (1-\eta)NS_\alpha(q), \qquad 0 \leq \eta \leq 1.$$

Hence, normalization preserves the uncertainty-ordering structure of the underlying fractional entropy for a fixed n and α. In particular, for two actions having the same number of states and the same fractional order,

$$S_\alpha(p) < S_\alpha(q) \quad \Longleftrightarrow \quad NS_\alpha(p) < NS_\alpha(q).$$

Therefore, normalization does not alter the qualitative comparison of uncertainty within a common decision environment; it only converts the entropy values to a bounded and comparable scale.

Normalization also affects the numerical sensitivity of the entropy measure. For the non-normalized fractional entropy, the local sensitivity with respect to a probability component is

$$\frac{\partial S_\alpha(p)}{\partial p_x} = [-\log(p_x)]^\alpha - \alpha[-\log(p_x)]^{\alpha-1}.$$

For the normalized entropy, this becomes

$$\frac{\partial NS_\alpha(p)}{\partial p_x} = \frac{[-\log(p_x)]^\alpha - \alpha[-\log(p_x)]^{\alpha-1}}{n\alpha^\alpha e^{-\alpha}}.$$

Thus, normalization preserves the direction and qualitative pattern of probability sensitivity, but rescales its magnitude. This is important in financial applications because stocks may have different empirical probability structures and different levels of dispersion in their return distributions. Without normalization, larger entropy magnitudes may dominate the risk score even when they mainly arise from scale or dimensional effects. After normalization, the sensitivity of the entropy component becomes more stable and comparable across assets.

The dependence on the fractional order α is also modified in a useful way. Since

$$NS_\alpha(p) = \frac{S_\alpha(p)}{n\alpha^\alpha e^{-\alpha}},$$

we have

$$\frac{\partial NS_\alpha(p)}{\partial \alpha} = \frac{1}{n\alpha^\alpha e^{-\alpha}} \left[\sum_{x=1}^{n} p_x[-\log(p_x)]^\alpha \log[-\log(p_x)] - S_\alpha(p)\log(\alpha)\right].$$

This expression shows that normalization does not remove the role of α; rather, it adjusts the scale of its influence. The fractional parameter continues to control how strongly the entropy responds to small or large probability events, while the normalization prevents the resulting entropy values from becoming difficult to compare across heterogeneous stocks. Consequently, the normalized fractional entropy retains the behavioral interpretation of α as a risk-sensitivity parameter, but improves numerical interpretability, boundedness, and comparability in stock-ranking applications.

While evaluating risky alternatives, traditional expected utility entropy based risk measures often lead to inconsistencies, particularly when applied to classic paradoxes observed in empirical decision making experiments. A prominent example is the Allais paradox, which illustrates the certainty effect, which states the tendency of individuals to prefer a risk-free choice with sure gain having high probability over a riskier option, even when the latter offers a higher expected payoff. Other behavioural phenomena, such as the common ratio effect and the common consequence effect, also remain unexplained under conventional utility functions combined with Shannon entropy. The normalized entropy-based risk measures developed by Yang and Qiu (2014) and Brito (2022) successfully solved the inconsistencies in these decision problems to some extent. In these studies, the Shannon entropy was used to measure the objective uncertainty related to the risk or predictability of the occurrence of desired outcomes. However, the uncertainty is subjective to the risk tolerance levels or degree of conservatism of decision-makers. To take the subjective uncertainty into account, the fractional order entropy was incorporated into risk measures, where the fractional parameter was used to reflect the degree of risk tolerance of individuals. The lower value of the fractional parameter q close to zero was used to identify the conservative individuals, while the higher values closer to one represented the adventurous individuals (Paul and Kundu, 2026). The fractional order entropy-based decision model emphasized the potentials of fractional order entropy as an uncertainty measure in finance, both theoretically and empirically. It also investigated the strengths of fractional entropy in quantifying uncertainty in portfolio management by applying to the Portuguese stock market (PSI 20), collected from `https://www.investing.com`, verifying its effectiveness as an important component in risk measures and risk-based decision models.

Intrigued by the potentials of the fractional order entropy and motivated by the works of Yang and Qiu (2014) and Brito (2022), we intoduce a standardized form of the fractional entropy by normalizing it and integrating the proposed normalized entropy (3.2.1) in the risk measure defined as follows:

Definition 3.2.1. *If we consider a general decision-making model $G = (\Theta, \mathcal{A}_1, u)$, where $u = u(X(A_1, \theta))$ is an increasing utility function associated with action $A_1 \in \mathcal{A}_1$, then the normalized expected utility–fractional entropy (NEU-FE) risk measure for an action A_1 is defined as*

$$R(A_1) = \begin{cases} \lambda NS_\alpha(A_1,\theta) - (1-\lambda)\frac{E[u(X(A_1,\theta))]}{\max_{A_1\in\mathcal{A}}\{|E[u(X(A_1,\theta))]|\}} & \textit{for } \max_{A_1\in A}\{|E[u(X(A_1,\theta))]|\} \neq 0 \\ \lambda NS_\alpha(A_1,\theta) & \textit{for } \max_{A_1\in A}\{|E[u(X(A_1,\theta))]|\} = 0 \end{cases} \tag{3.2.2}$$

where $0 \leq \lambda \leq 1$ *is the risk–return tradeoff parameter, and* $NS_\alpha(A_1, \theta)$ *denotes the normalized fractional entropy of the state-of-nature distribution corresponding to action* A_1*. Throughout, we assume that*

$$\max_{A_1 \in \mathcal{A}_1} \{|E[u(X(A_1, \theta))]|\}$$

exists and is nonzero.

Definition 3.2.2. *Let us consider a general decision-making model* $G = (\Theta, \mathcal{A}_2, u)$*, with an increasing utility function* $u = u(X(A_2, \theta))$ *associated with action* $A_2 \in \mathcal{A}_2$*. Then, the normalized expected utility- fractional entropy and variance (NEU-FEV) risk measure corresponding to an action* A_2 *is defined as*

$$R(A_2) = \frac{\lambda}{2}\left[NS_\alpha(A_2, \theta) + \frac{Var[X(A_2, \theta)]}{\max_{A_2 \in \mathcal{A}_2}\{Var[X(A_2, \theta)]\}}\right] - (1-\lambda)\frac{E[u(X(A_2, \theta))]}{\max_{A_2 \in \mathcal{A}_2}\{|E[u(X(A_2, \theta))]|\}}, \tag{3.2.3}$$

where $\lambda \in \mathcal{R}$ *is the risk–return balancing parameter such that* $0 \leq \lambda \leq 1$ *and* $NS_\alpha(A_2, \theta)$ *represents the normalized fractional entropy of the probability distribution over the states of nature linked to action* A_2*. Assuming that* $max_{A_2 \in \mathcal{A}_2}\{|E[u(X(A_2, \theta))]|\}$ *exists and is non-zero, we find that when* $max_{A_2 \in \mathcal{A}_2}\{|E[u(X(A_2, \theta))]|\} = 0$*, it gives*

$$R(A_2) = \frac{\lambda}{2}\left[NS_\alpha(A_2, \theta) + \frac{Var[X(A_2, \theta)]}{max_{A_2 \in \mathcal{A}_2}\{Var[X(A_2, \theta)]\}}\right].$$

To evaluate decisions across a finite set of actions using a risk measure, the corresponding risk values $R(\mathcal{A})$ (for $\mathcal{A} = \mathcal{A}_1$ or $\mathcal{A}_2$) are compared. These values reflect both the subjective uncertainty of outcomes and their perceived utilities. The action yielding the smaller $R(\mathcal{A})$ is chosen. Therefore, the NEU-FE and NEU-FEV risk-based decision-making models can be redefined as:

Definition 3.2.3. *We consider* $G = (\Theta, \mathcal{A}, u)$ *to be a general decision-making model.*

1. *Let us consider an action space* $\mathcal{A} = \{\mathcal{A}_1, \mathcal{A}_2\}$ *consisting of two actions* $A_{i1}, A_{i2} \in \mathcal{A}$, $i = 1, 2$, *with corresponding risk measures* $R(A_{i1})$ *and* $R(A_{i2})$*. Then:*

   (i) action A_{i1} *is preferred (i.e.,* $A_{i1} > A_{i2}$*) if* $R(A_{i1}) < R(A_{i2})$*;*

   (ii) action A_{i2} *is preferred (i.e.,* $A_{i1} < A_{i2}$*) if* $R(A_{i1}) > R(A_{i2})$*;*

   (iii) neither action is preferred (i.e., $A_{i1} = A_{i2}$*) when* $R(A_{i1}) = R(A_{i2})$*.*

2. *If $\mathcal{A}$ is a discrete set of n actions, $\mathcal{A} = \{A_{i1}, A_{i2}, \ldots, A_{in}\}$, then the NEU-FE and NEU-FEV preference ordering is obtained by ranking the actions in decreasing order of their risk values. The most preferred action is the one achieving*

$$R(A_{ij}) = \min_{A_{ij} \in \mathcal{A}} R(A_{ij}).$$

Moreover, for $\lambda = 0$, the proposed decision models reduce to the expected utility model ($A_{i1} > A_{i2}$ or $R(A_{i1}) < R(A_{i2})$ iff $E[u(A_{i1})] > E[u(A_{i2})]$).

The above discussion shows that normalization does not alter the essential fractional entropy structure. For fixed n and α, it acts as a positive rescaling and therefore preserves concavity and uncertainty ordering. At the same time, it stabilizes the magnitude of entropy values and their probability-level sensitivities, making the resulting NEU-FE and NEU-FEV risk scores more comparable across heterogeneous stocks in real market datasets.

3.2.1 Properties of the NEU-FE and NEU-FEV-base risk measures

The NEU-FE and NEU-FEV risk measures satisfy the fundamental principles of risk measurement, consistent with established measures in the literature. In this section, we investigate the central properties of these proposed measures.

Theorem 3.2.1. *Let A_{11} and A_{12} be two distinct actions in the action space associated with a general decision model $G = (\Theta, \mathcal{A}_1, u)$, and suppose they yield the same expected utility. If $NS_\alpha(A_{11}, \theta)$ and $NS_\alpha(A_{12}, \theta)$ denote the normalized fractional entropies corresponding to the states of nature θ, then $R(A_{11}) < R(A_{12})$ whenever $NS_\alpha(A_{11}, \theta) < NS_\alpha(A_{12}, \theta)$ for some q.*

For the NEU-FEV model, the inequality $R(A_{21}) < R(A_{22})$ holds if and only if

$$NS_\alpha(A_{21}, \theta) + \frac{\mathrm{Var}[X(A_{21}, \theta)]}{\max_{A_{21} \in \mathcal{A}_2}\{\mathrm{Var}[X(A_{21}, \theta)]\}} < NS_\alpha(A_{22}, \theta) + \frac{\mathrm{Var}[X(A_{22}, \theta)]}{\max_{A_{22} \in \mathcal{A}_2}\{\mathrm{Var}[X(A_{22}, \theta)]\}}.$$

Proof. This result is an immediate consequence of Definitions 3.2.1 and 3.2.2. □

Intuitively, the preceding theorem suggests that an action exhibiting lower entropy and smaller variance is naturally associated with reduced risk.

Theorem 3.2.2. *Let $G = (\Theta, \mathcal{A}, u)$ be a general decision analysis model, where the action space consists of two actions A_{11} and A_{12}. Let $NS_\alpha(A_{11}, \theta)$ and $NS_\alpha(A_{12}, \theta)$ denote the corresponding normalized fractional entropies of the states of nature θ. Then, $R(A_{11}) < R(A_{12})$ whenever $NS_\alpha(A_{11}, \theta) = NS_\alpha(A_{12}, \theta)$ for some value of q and $E[u(X(A_{11}, \theta))] > E[u(X(A_{12}, \theta))]$. Furthermore, if $NS_\alpha(A_{21}, \theta) = NS_\alpha(A_{22}, \theta)$, then $R(A_{21}) < R(A_{22})$ if and only if $E[u(X(A_{21}, \theta))] > E[u(X(A_{22}, \theta))]$.*

Proof. This result follows immediately from Definitions 3.2.1 and 3.2.2, along with the fact that for a decision model $G = (\Theta, \mathcal{A}, u)$, we have $Var(X(A, \theta)) = 0$ whenever $NS_\alpha(A, \theta) = 0$. $\square$

Theorem 3.2.2 implies that when the normalized fractional entropy values of the outcomes associated with two actions are equal, the action with the higher expected utility is considered less risky. Moreover, the validity of the NEU-FE and NEU-FEV risk measures defined in (3.2.2) and (3.2.3) is further supported by examining several of their properties in relation to prior studies on decision models involving Shannon entropy and individual risk perception.

Intuitively, according to the theorem mentioned above, an action with lower entropy and smaller variance will be associated with lower risk.

Theorem 3.2.3. *Let $G = (\Theta, \mathcal{A}, u)$ be a general decision-making model with positive outcomes:*

1. *Let us consider an action space $\mathcal{A} = \{A,\ A + c\}$ with $c > 0$ being a constant. Then, we have*
$$R(A + c) < R(A),$$
indicating that the risk decreases when a positive constant is added to every outcome of an action.

2. *If the action space contains two actions, $\mathcal{A} = \{A,\ kA\}$, where $k > 1$ is a positive constant, then under the NEU-FE decision model the following relation holds:*
$$R(kA) < R(A),$$
This indicates that scaling all outcomes of an action by a factor greater than one leads to a reduction in the NEU-FE risk. In other words, amplifying every pay-off proportionally lowers the assessed risk level, reflecting the model's sensitivity to positive linear transformations of the outcome space.

For the NEU-FEV decision model,

$$R(kA) < R(A),$$

if and only if

$$\lambda \in \left[0,\ \frac{1-\frac{E[u(X)]}{E[u(kX)]}}{\frac{3}{2}-\frac{1}{2k^2}-\frac{E[u(X)]}{E[u(kX)]}}\right).$$

Proof:

1. Since we consider the utility function $u(X)$ to be increasing, we find that for $c > 0$,

$$u(X+c) > u(X).$$

If $\mathcal{A} = \{A, A+c\}$, then

$$max_{A\in Y}\{|E[u(X(A,\theta))]|\} = E[u(X+c)] \text{ and } Var(X+c) = Var(X).$$

Hence, from Definition 3.2.2, we get that

$$R(A_2) = \frac{\lambda}{2}\Big[NS_\alpha(A_2,\theta)+1\Big] - (1-\lambda)\frac{E[u(A_2)]}{E[u(A_2+c)]}$$

and

$$R(A_2+c) = \frac{\lambda}{2}\Big[NS_\alpha(A_2+c,\theta)+1\Big] - (1-\lambda).$$

Analogously, using Definition 3.2.1, we obtain that

$$R(A_1) = \lambda NS_\alpha(A_1,\theta) - (1-\lambda)\frac{E[u(A_1)]}{E[u(A_1+c)]}$$

and

$$R(A_1+c) = \lambda NS_\alpha(A_1+c,\theta) - (1-\lambda).$$

Given that $NS_\alpha(A+c,\theta) = NS_\alpha(A,\theta)$ for $A \in \{A_1, A_2\}$ and a fixed $\alpha \in [0,1]$, it follows that $R(A+c) < R(A)$.

2. As the utility function is increasing and the non-negative outcomes $X = X(A_2,\theta)$ satisfy $E[X] = 0$, we deduce that $u(kX) > u(X)$ for $k > 1$. Consequently, since $\mathcal{A}_2 = \{A_2, kA_2\}$, it follows that

$$\max_{A_2\in\mathcal{A}_2}\{|E[u(X(A_2,\theta))]|\} = E[u(kX)] \text{ and } Var(kX) = k^2E[X^2] > Var(X) = E[X^2].$$

Hence, from Definition 3.2.2, we get that

$$R(A_2) = \frac{\lambda}{2}\left[NS_\alpha(A_2,\theta) + \frac{1}{k^2}\right] - (1-\lambda)\frac{E[u(X)]}{E[u(kX)]}$$

and

$$R(kA_2) = \frac{\lambda}{2}\Big[NS_\alpha(kA_2,\theta) + 1\Big] - (1-\lambda).$$

Since the entropy term depends only on the probabilities of the states of nature $p(i)$ and the parameter α, it follows that for any fixed value of α, we have

$$NS_\alpha(kA_2,\theta) = NS_\alpha(A_2,\theta).$$

Therefore, $R(kA_2) < R(A_2)$ holds if and only if

$$\lambda\left(\frac{3}{2} - \frac{1}{2k^2} - \frac{E[u(X)]}{E[u(kX)]}\right) - \left(1 - \frac{E[u(X)]}{E[u(kX)]}\right) > 0.$$

This inequality is equivalent to the condition

$$\lambda \in \left[0, \frac{1 - \frac{E[u(X)]}{E[u(kX)]}}{\frac{3}{2} - \frac{1}{2k^2} - \frac{E[u(X)]}{E[u(kX)]}}\right).$$

Similarly, Definition 3.2.1 yields

$$R(A_1) = \lambda\, NS_\alpha(A_1,\theta) - (1-\lambda)\frac{E[u(X)]}{E[u(kX)]},$$

and

$$R(kA_1) = \lambda\, NS_\alpha(kA_1,\theta) - (1-\lambda).$$

Since the normalized fractional entropy remains unchanged under positive scalar multiplication, i.e.,

$$NS_\alpha(kA_1,\theta) = NS_\alpha(A_1,\theta),$$

it follows immediately that

$$R(kA_1) < R(A_1).$$

In other words, multiplying all outcomes of an action by a constant factor $k > 1$ reduces the associated NEU-FE risk whenever the entropy component is unaffected by such scaling.

3.2.2 Mathematical sensitivity of NEU-FEV to variance

Let $r = (r_1, \ldots, r_n)$ be the return sample for a given asset, with sample mean $\bar{r}$ and sample variance

$$s^2 = \frac{1}{n-1}\sum_{i=1}^{n}(r_i - \bar{r})^2.$$

We consider the normalized-variance termed as NVar which can be the linear normalization. $\mathrm{NVar} = s^2/Var_{\max}$ for simplicity of exposition. The qualitative conclusions below hold for other monotone normalizations as well.

The NEU–FEV target (for a fixed $\lambda \in [0, 1]$) is

$$R(r) = \frac{\lambda}{2}\big(\mathrm{NS}_\alpha(r) + \mathrm{NVar}(r)\big) - (1-\lambda)\,\mathrm{NEU}(r),$$

where NS_α is the normalized fractional entropy and NEU the normalized expected utility. The partial sensitivity of R to the variance component is obtained by differentiation:

$$\frac{\partial R}{\partial s^2} = \frac{\lambda}{2}\frac{\partial \mathrm{NVar}}{\partial s^2} = \frac{\lambda}{2}\frac{1}{Var_{\max}} \qquad (\text{for NVar} = s^2/Var_{\max}).$$

Thus, at the pointwise (local) level, the contribution of variance to the target scales linearly with the prefactor $\lambda/2$ and inversely with the normalization constant $Var_{\max}$. In other words, any change of Δs^2 in the sample variance moves the target by

$$\Delta R \approx \frac{\lambda}{2Var_{\max}}\,\Delta s^2.$$

Influence of a single extreme return: A more revealing view uses the influence of a contamination at a single observation r_i. The influence function of the variance functional (population variance σ^2) is proportional to the centred squared deviation. For an observation x the influence is (up to scaling)

$$\mathrm{IF}(x; \mathrm{Var}) = (x-\mu)^2 - \sigma^2.$$

Hence, inserting an extreme value x (large $|x - \mu|$) changes the variance approximately by $(x - \mu)^2 - \sigma^2$. The corresponding change in the target is

$$\Delta R \approx \frac{\lambda}{2Var_{\max}}\big[(x-\mu)^2 - \sigma^2\big],$$

which grows *quadratically* with the extremeness $|x - \mu|$. This quadratic dependence explains why outliers and heavy tails have an outsized effect on NEU-FEV but not on NEU-FE (which lacks the s^2 term).

Propagation into target variance: To quantify the effect of variance on the uncertainty of R, we compute the variance of R (treating NS_α, NVar, and NEU as random variables driven by the sample r):

$$\mathrm{Var}[R] = \left(\frac{\lambda}{2}\right)^2 \mathrm{Var}[\mathrm{NS}_\alpha] + \left(\frac{\lambda}{2}\right)^2 \mathrm{Var}[\mathrm{NVar}] - 2\left(\frac{\lambda}{2}\right)(1-\lambda)\,\mathrm{Cov}[\mathrm{NVar}, \mathrm{NEU}] + (\text{other terms}),$$

where the dominant new term introduced by augmentation is $\left(\frac{\lambda}{2}\right)^2 \mathrm{Var}[\mathrm{NVar}]$. Using $\mathrm{NVar} = s^2/Var_{\max}$, we have

$$\mathrm{Var}[\mathrm{NVar}] \;=\; \frac{1}{Var_{\max}^2}\,\mathrm{Var}[S^2].$$

For the sample variance the variance (asymptotically) depends on the fourth central moment $\mu_4 = \mathbb{E}[(r-\mu)^4]$. A standard expression (for independent draws) is

$$\mathrm{Var}[s^2] \approx \frac{1}{n}\left(\mu_4 - \sigma^4\right) + o\left(\tfrac{1}{n}\right),$$

so that

$$\mathrm{Var}[\mathrm{NVar}] \approx \frac{1}{nVar_{\max}^2}\left(\mu_4 - \sigma^4\right).$$

Consequently, the variance contribution to $\mathrm{Var}[R]$ scales as

$$\left(\frac{\lambda}{2}\right)^2 \frac{1}{nVar_{\max}^2}\left(\mu_4 - \sigma^4\right).$$

Because μ_4 (the kurtosis-related moment) increases substantially for heavy-tailed distributions, the sampling variability of s^2 (and hence of the target risk R) increases accordingly. This establishes that NEU-FEV inherits an extra term in its sampling variance that is proportional to the fourth moment of returns, whereas NEU-FE lacks this extra source of uncertainty.

Consequences (intuitive summary):

- The variance term enters the target linearly, but the sample variance itself depends quadratically on deviations and has sampling variance controlled by the fourth central moment. Therefore, NEU-FEV is *more sensitive* to outliers and heavy tails than NEU-FE.

- An extreme return x perturbs NEU-FEV by an amount proportional to $(x-\mu)^2$, whereas NEU-FE is affected only via entropy or utility terms that typically scale more weakly with extreme deviations.

- In finite samples the extra contribution $\propto (\lambda/2)^2 \operatorname{Var}[S^2]$ increases the uncertainty of the target. As a result, models predicting NEU-FEV will generally exhibit larger prediction error and (empirically) lower R^2 when compared to NEU-FE, unless the sample size n is large or the distribution is light-tailed.

3.3 Application to stock selection using real data

The potentials of the fractional order entropy-based decision analysis models in solving some important decision paradoxes and stock selection problems have recently been explored by Paul and Kundu (2026). The decision results reveal that the fractional entropy (FE)-based models outperform the existing Shannon entropy based decision models in most of the cases and are consistent with the theoretical and empirical decision model results. In the present section, we explore the properties of the decision models depending on the proposed normalized fractional order entropy (3.2.1) and analyze their performance in modeling risky decisions such as stock selection for investment in financial portfolios using real data of NIFTY 50 collected from `https://www.investing.com`.

It is also useful to clarify the change of empirical dataset from the previous chapter to the present chapter. The previous chapter 2 uses PSI20 stock-market data to validate the non-normalized fractional entropy-based risk measures, EU-FE and EU-FEV. In contrast, the present chapter uses NIFTY50 data from the Indian stock market because the objective here is to examine the normalized versions of these measures in a larger and more heterogeneous stock-market setting. Since normalization is intended to reduce scale dependence and improve comparability across assets under heterogeneous asset behaviour, a broader dataset containing a larger and more sectorally diverse group of stocks than the PSI20 dataset such as NIFTY50 provides a more appropriate empirical environment for testing the stability and stock-selection performance of the proposed NEU-FE and NEU-FEV models.

For performing this study, we use a one year stocks data of NIFTY 50 Index of the Indian market collected from *Investing.com* from 04/03/2017 to 04/03/2018. The list of all the stock components used in this study are provided in Table 3.3.1. Let us consider an investor interested to invest in l stocks components from s available choices. Consequently, the decision of selecting the stock M_i will be defined on the action space $\mathcal{A} = \{A_i\},\ i = 1, 2, \ldots, l$. The $l = 48$ available asset choices of the NIFTY 50 data are based on Table 3.3.1. We obtain a time series of 246 closing prices for the selected time

Table 3.3.1: The constituent stocks of the NIFTY50 index.

Index	Stock	Index	Stock	Index	Stock	Index	Stock
S_1	ADEL	S_{13}	REDY	S_{25}	ITC	S_{37}	SBI
S_2	APSE	S_{14}	EICH	S_{26}	JSTL	S_{38}	SHMF
S_3	APLH	S_{15}	GRAS	S_{27}	KTKM	S_{39}	SUN
S_4	ASPN	S_{16}	HCLT	S_{28}	LART	S_{40}	TCS
S_5	AXBK	S_{17}	HDBK	S_{29}	MAHM	S_{41}	TACN
S_6	BAJA	S_{18}	HDFL	S_{30}	MRTI	S_{42}	TAMO
S_7	BJFN	S_{19}	HROM	S_{31}	NEST	S_{43}	TISC
S_8	BJFS	S_{20}	HALC	S_{32}	NTPC	S_{44}	TEML
S_9	BRTI	S_{21}	HLL	S_{33}	ONGC	S_{45}	TITN
S_{10}	BAJE	S_{22}	ICBK	S_{34}	PGRD	S_{46}	TREN
S_{11}	CIPL	S_{23}	INBK	S_{35}	RELI	S_{47}	ULTC
S_{12}	COAL	S_{24}	INFY	S_{36}	SBIL	S_{48}	WIPR

interval corresponding to each stock S_i denoted by $\{p_{i0}, p_{i1}, \dots, p_{iT}\}$, where $T = 245$. Then the returns for each stock S_i can be obtained as:

$$r_{it} = \log\left(\frac{p_{it}}{p_{i(t-1)}}\right), \quad i = 1, \dots, 48; \ t = 1, 2, \dots, 245. \tag{3.3.1}$$

Then (3.3.1) leads to a series of returns given by $\{r_{i1}, r_{i2}, \dots, r_{i245},\}$ with respect to stock S_i. Amongst all the available asset returns, we find that the minimum achievable return value $r_{min} = -0.187$ and the maximum value $r_{max} = 0.128$. This implies that

$$r_{it} \in [-0.187,\ 0.128], \qquad i = 1, 2, \dots, 48, \ t = 1, \dots, 245.$$

The interval $[r_{\min}, r_{\max}]$ is subdivided into $\mathcal{J} = 15$ sub-intervals $\mathcal{J}_k$, each of length $\Delta = \frac{r_{\max} - r_{\min}}{\mathcal{J}} = 0.021$. Accordingly, we obtain 15 sub-intervals given by $\mathcal{J}_1 = [-0.187, -0.166)$, $\mathcal{J}_2 = [-0.166, -0.145)$, $\dots$, $\mathcal{J}_{14} = [0.086, 0.107)$, $\mathcal{J}_{15} = [0.107, 0.128]$. Here, the probability distribution or the relative frequency of the collected returns over T previous days for the i^{th} stock S_i in the sub-interval $\mathcal{J}_k$ is computed as:

$$p_{ik} = \frac{||r_{it} \in \mathcal{J}_k | t = 1, \dots, T||}{T}, \ i = 1, \dots, l, \ k = 1, \dots, \mathcal{J}, \tag{3.3.2}$$

where $||\cdot||$ represents the cardinality of a set and the k^{th} sub-interval is obtained as:

$$\mathcal{J}_k = \begin{cases} [r_{k-1}, r_{k-1} + \Delta), & k = 1, \dots, \mathcal{J} \\ [r_{k-1}, r_k], & k = \mathcal{J}, \end{cases} \tag{3.3.3}$$

where we have $r_{max} = r_{\mathcal{J}}$. Then the expected return for the stock S_i belonging to the sub-interval $\mathcal{J}$ collected over T days, is evaluated as:

$$x_{ik} = \frac{1}{||r_{it} \in \mathcal{J}_k | t = 1, \ldots, T||} \sum_{r_{it} \in \mathcal{J}_k, t=1,\ldots,T} r_{it}, \ i = 1, \ldots, l, \ k = 1, \ldots, \mathcal{J}. \tag{3.3.4}$$

Finally, by substituting the results from (3.3.2) and (3.3.3) into (3.3.1) and (3.3.4), we obtain the risky action space represented by $A_i = (x_{i1}, p_{i1}; \ldots; x_{i15}, p_{i15})$ of selecting the i^{th} stock $S_i, i \in \{1, \ldots, 48\}$ from Indian market under NIFTY 50 index. The utility function employed in this study is a widely used S-shaped function, exhibiting concavity over gains and convexity over losses. Originally introduced by Kahneman and Tversky (1979), it captures the degree of risk aversion exhibited by decision-makers. The function is given by

$$u(x) = \begin{cases} \log(1 + x), & x \geq 0, \\ -\log(1 - x), & x < 0, \end{cases} \tag{3.3.5}$$

Using results from equations (3.3.1) and (3.3.3), we evaluate the states of assets, or equivalently, the corresponding returns based on the chosen feature set. The FE and variance of these return values, together with the corresponding subjective expected utilities, are then used to compute the proposed NEU-FE and NEU-FEV risk measures given by (3.2.2) and (3.2.3), respectively. Consequently, we fix the parameters at α and λ ($\alpha = 0.5, \lambda = 0.4$) and then evaluate the NEU-FE, NEU-FEV, EU-FE and EU-FEV risk values by using the expressions given by equations (3.3.1) – (3.3.5). The computed risk values are displayed in Table 3.3.2.

Based on the risk values in Table 3.3.2, the five least-risky stocks are identified for NEU-FE, NEU-FEV, EU-FE, and EU-FEV, and their rankings are reported in Table 3.3.3. For $\alpha = 0.5$ and $\lambda = 0.4$, all four measures consistently select *Titan Company (TITN)* and *Tata Consumer Products (TACN)* as the two most preferred stocks, showing robustness across model specifications. However, the ordering of *JSW Steel (JSTL)*, *Bajaj Finance (BJFN)*, and *Hindustan Unilever (HLL)* varies across the measures, motivating a systematic performance comparison to identify the most reliable risk criterion.

Table 3.3.2: Risk measures ($\alpha = 0.5$, $\lambda = 0.4$) for 48 NIFTY50 stocks.

Stock	**NEU-FE**	**NEU-FEV**	**EU-FE**	**EU-FEV**	**Stock**	**NEU-FE**	**NEU-FEV**	**EU-FE**	**EU-FEV**
ADEL	-0.156501	-0.068526	0.224967	0.122208	**JSTL**	-0.264642	-0.212361	0.059238	-0.050422
APSE	0.005304	-0.015197	0.490576	0.227439	**KTKM**	-0.032836	-0.047048	0.333160	0.135950
APLH	0.102743	0.085027	0.556077	0.311694	**LART**	0.040342	0.028221	0.406623	0.211362
ASPN	0.044249	0.008610	0.544855	0.258913	**MAHM**	0.012161	-0.006259	0.405310	0.190316
AXBK	0.089686	0.071480	0.518644	0.285959	**MRTI**	-0.193989	-0.164415	0.079619	-0.027610
BAJA	0.033905	0.000516	0.515591	0.241359	**NEST**	-0.015218	-0.017387	0.280957	0.130700
BJFN	-0.247455	-0.201901	0.087656	-0.034345	**NTPC**	0.088498	0.053227	0.586382	0.302168
BJFS	-0.055593	-0.052860	0.322137	0.136005	**ONGC**	0.045716	0.015338	0.552275	0.268617
BRTI	0.059021	0.056891	0.463108	0.258934	**PGRD**	0.098254	0.061460	0.601919	0.313292
BAJE	0.072980	0.050126	0.562810	0.295041	**REDY**	0.177111	0.193812	0.528194	0.369353
CIPL	0.118114	0.098210	0.555963	0.317134	RELI	-0.079985	-0.078209	0.270769	0.097168
COAL	0.144967	0.117948	0.616141	0.353535	**SBIL**	0.096508	0.073552	0.450322	0.250458
EICH	0.011132	-0.008703	0.453208	0.212335	SBI	0.171367	0.185716	0.542693	0.371378
GRAS	-0.043328	-0.045257	0.342583	0.147698	**SHMF**	-0.043431	-0.026180	0.328582	0.159826
HCLT	0.002947	-0.019389	0.424143	0.191209	**SUN**	0.241182	0.276624	0.575824	0.443945
HDBK	-0.119793	-0.111254	0.102404	-0.000155	**TACN**	-0.350356	-0.257676	-0.035502	-0.100249
HDFL	-0.023586	-0.007979	0.210927	0.109278	**TAMO**	0.187397	0.220449	0.518313	0.385907
HROM	0.029105	0.004469	0.450893	0.215363	**TCS**	-0.056556	-0.068771	0.313673	0.116344
HALC	0.029087	0.015996	0.496626	0.249765	**TEML**	-0.145313	-0.115292	0.194336	0.054533
HLL	-0.234108	-0.203974	0.003454	-0.085193	**TISC**	-0.090805	-0.076553	0.257763	0.097731
ICBK	0.065638	0.052140	0.480725	0.259684	**TITN**	-0.549444	-0.374722	-0.274761	-0.237380
INBK	-0.098926	-0.098007	0.209377	0.056144	**TREN**	-0.055634	-0.047286	0.312860	0.136962
INFY	0.010679	-0.007802	0.427417	0.200567	**ULTC**	0.025274	-0.004162	0.499514	0.232958
ITC	0.055925	0.044709	0.416572	0.225033	**WIPR**	0.095519	0.073481	0.503793	0.277618

Table 3.3.3: Top 5 preferred stocks (lowest risk Values) under each risk measure.

Rank	NEU-FE	NEU-FEV	EU-FE	EU-FEV
1	TITN	TITN	TITN	TITN
2	TACN	TACN	TACN	TACN
3	JSTL	JSTL	HLL	HLL
4	BJFN	HLL	JSTL	JSTL
5	HLL	BJFN	MRTI	BJFN

3.3.1 Simulation-based robustness and nonlinear benchmark feasibility

Before validating the proposed EU-FE and EU-FEV measures on real stock-market data, we also examine their feasibility under controlled probability models. These simulation-based checks are included only as supporting robustness evidence, while the main focus of the chapter remains real-data validation.

For the discrete setting, Bernoulli, binomial, Poisson, and multinomial probability models are considered. For the continuous setting, samples are generated from normal, lognormal, Student-t, skew-normal, mixture-normal, and sinusoidal-noise models. In each case, the fractional Ubriaco entropy

$$H^{\alpha}(p) = \sum_{i} p_i[-\log(p_i)]^{\alpha}$$

and its normalized counterpart are computed. For continuous models, samples of size $n = 1000$ are generated, grouped into 10 empirical probability classes, and the experiment is repeated 500 times at $\alpha = 0.4$. The purpose is to check whether the entropy measure remains stable and interpretable under symmetric, skewed, heavy-tailed, mixture-type, and oscillatory uncertainty structures.

Table 3.3.4 shows that the fractional entropy values vary smoothly with α across finite-state probability models. The normalized entropy values remain bounded and comparable even when the underlying probability structures differ. This supports the use of normalized fractional entropy when heterogeneous discrete uncertainty structures are being compared.

Table 3.3.5 shows that the entropy measure is sensitive to distributional shape and tail behaviour. Heavy-tailed and skewed models, such as the Student-t and skew-normal

Table 3.3.4: Robustness check for discrete probability models.

Discrete model	$\boldsymbol{\alpha}$	$\boldsymbol{H^{\alpha}}$	**Normalized** $\boldsymbol{H^{\alpha}}$
Bernoulli($p = 0.35$)	0.25	0.8809	0.9654
Bernoulli($p = 0.35$)	0.40	0.8210	0.9506
Bernoulli($p = 0.35$)	0.50	0.7852	0.9432
Bernoulli($p = 0.35$)	0.75	0.7086	0.9328
Bernoulli($p = 0.35$)	1.00	0.6474	0.9341
Binomial($n = 10, p = 0.40$)	0.25	1.1566	0.9295
Binomial($n = 10, p = 0.40$)	0.40	1.2654	0.8918
Binomial($n = 10, p = 0.40$)	0.50	1.3450	0.8686
Binomial($n = 10, p = 0.40$)	0.75	1.5737	0.8167
Binomial($n = 10, p = 0.40$)	1.00	1.8536	0.7730
Poisson($\mu = 3$), truncated	0.25	1.1693	0.9239
Poisson($\mu = 3$), truncated	0.40	1.2874	0.8832
Poisson($\mu = 3$), truncated	0.50	1.3741	0.8580
Poisson($\mu = 3$), truncated	0.75	1.6240	0.8013
Poisson($\mu = 3$), truncated	1.00	1.9313	0.7530
Multinomial, five states	0.25	1.1100	0.9855
Multinomial, five states	0.40	1.1833	0.9782
Multinomial, five states	0.50	1.2356	0.9740
Multinomial, five states	0.75	1.3794	0.9653
Multinomial, five states	1.00	1.5445	0.9596

Table 3.3.5: Robustness check for continuous probability models at $\alpha = 0.4$.

Continuous model	**Mean** $H^{0.4}$	**SD**	**Mean normalized** $H^{0.4}$	**SD**
Normal$(0, 1)$	1.2655	0.0205	0.9067	0.0144
Lognormal$(0, 0.35)$	1.2033	0.0418	0.8668	0.0238
Student-t, df $= 4$	1.0306	0.0916	0.7483	0.0572
Skew-normal proxy	1.0625	0.0617	0.7681	0.0376
Mixture normal	1.3196	0.0151	0.9453	0.0108
Sinusoidal-noise model	1.3384	0.0115	0.9587	0.0083

cases, produce lower normalized entropy and higher variability. In contrast, mixture-normal and sinusoidal-noise models produce higher normalized entropy under the chosen binning scheme. These results indicate that the proposed fractional entropy component responds to uncertainty concentration, asymmetry, and tail behaviour.

In addition to linear, Ridge, Lasso, and ANN-based validation, nonlinear parametric benchmark models may be considered as supporting comparisons. Polynomial, interaction, logarithmic, power-law, exponential, and sinusoidal/harmonic regressions can be fitted using the same entropy, expected utility, variance, α, and λ inputs. Such models provide interpretable nonlinear alternatives between simple linear regression and black-box machine-learning models. However, sinusoidal models are most relevant when the dominant signal has a clear periodic or seasonal component. Since the present chapter focuses on risk ranking and stock-selection decisions rather than periodic time-series forecasting, these nonlinear and sinusoidal benchmarks are treated as useful supporting checks or future extensions, not as core competitors to the proposed entropy-based decision measures.

3.4 Performance analysis and statistical validation using real data

To rigorously assess the reliability and robustness of the proposed normalized fractional order entropy-based measures of risk, it is essential to evaluate their predictive behaviour across multiple machine learning (ML) frameworks. Accordingly, we conduct a comprehensive performance analysis using real stock market data by comparing the prediction errors (MSE) and goodness-of-fit (R^2) for four widely used ML models, namely, RF, Ridge, Lasso, and a two-layer ANN. This data-driven evaluation framework through ML models allow us to assess predictive accuracy, robustness, and parameter sensitivity while verifying whether the risk measures meaningfully capture real financial decision-making. The selected ML models serve this purpose by learning the functional relationship between the risk measures and their predictive performance on historical return data. Instead of assuming the optimal risk sensitivity parameter α (associated with entropy) or the trade-off parameter λ (balancing uncertainty and utility), the ML approach evaluates a grid of (α, λ) combinations and identifies the region that yields the most reliable stock rankings. Furthermore, since prior work identified the ANN as the most effective predictor for EU-FE and EU-FEV risk measures, we perform formal statistical significance tests (paired t-test, Wilcoxon signed-rank test, and F-test) to validate whether its relative performance advantage persists in the present setting. Together, these analyses provide a robust empirical foundation for comparing the proposed risk measures and establishing the statistical validity of the resulting conclusions.

Since different values of α correspond to varying attitudes toward extreme events, volatility concentration, and distributional irregularities, evaluating the robustness of the proposed NEU-FE and NEU-FEV models also requires a systematic sensitivity analysis across a range of α values. Therefore, we examine the behaviour of the proposed models with respect to the parameters α, representing the decision-makers' attitudes toward uncertainty, and λ, capturing the investors' risk aversion tendency, through a comprehensive sensitivity analysis. The variations of the normalized FE-based risk measures with respect to α are depicted in Figs. 3.4.1 and 3.4.2. As shown in these figures, the level of entropy and consequently the perceived uncertainty increases as the value of α rises for each stock component. This analysis enables us to understand how changes in α influence the perceived uncertainty and resulting risk rankings, thereby ensuring that the decision-making framework remains stable, interpretable, and reliable before advancing to the subsequent performance evaluation and statistical validation.

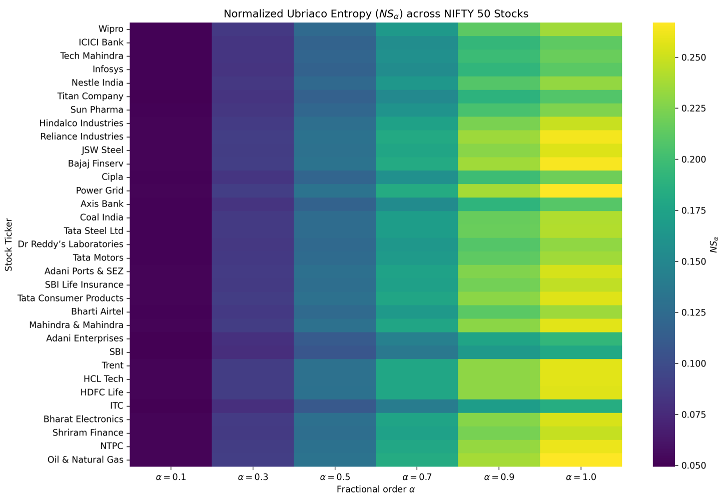

Figure 3.4.1: Heatmap of variations of NEU-FEV measure w.r.t α for NIFTY50 stocks.

Moreover, the heatmaps in Fig. 3.4.3 illustrate the smooth variation of the four FE-based risk measures, EU-FE, EU-FEV, NEU-FE, and NEU-FEV, across the (α, λ) parameter space. A clear monotonic trend is observed, wherein risk values increase with higher fractional order α (reflecting greater sensitivity to uncertainty) and with larger λ (placing more weight on entropy relative to utility). This pattern indicates that stronger

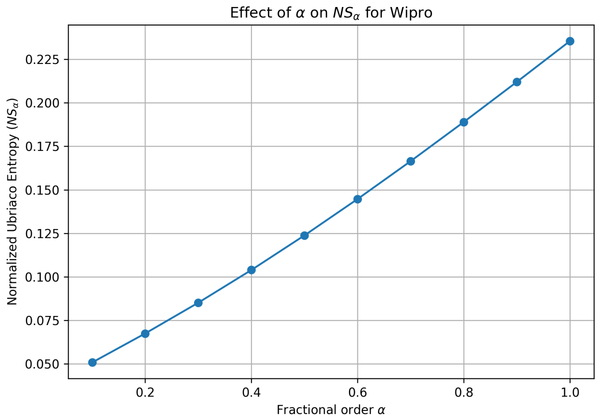

Figure 3.4.2: Heatmap variations of NEU-FEV measure w.r.t α for a single NIFTY50 stock.

aversion to uncertainty or greater emphasis on entropy components systematically elevates the perceived risk. Each heatmap exhibits a well-behaved, convex-like surface without discontinuities or irregular fluctuations, demonstrating that the measures remain stable and well-conditioned across the full parameter domain. Such structural regularity is essential for optimization, ensuring that searches for optimal (α, λ) pairs are not hindered by numerical instabilities or non-convex irregularities. This smoothness supports reliable gradient-free or grid-based exploration, enabling robust sensitivity analysis and practical investor-specific calibration. Overall, the heatmaps confirm that all FE-based measures align with theoretical expectations, which claims that risk increases with both α and λ, and NEU-based formulations show reduced scale effects compared to their EU counterparts.

3.4.1 Performance metrics comparison of the proposed risk measures

In this subsection, we limit our comparative analysis to the most recent FE-based risk measures, namely EU-FE and EU-FEV (see Paul and Kundu, 2026), as these models currently represent the strongest and most relevant alternatives within the fractional order decision making framework. The recent studies have shown that the FE-based formulations consistently outperform the traditional Shannon entropy based EU-E and EU-EV criteria in resolving paradoxical choice patterns and capturing behavioural nuances in risky decision environments. Therefore in this section, to avoid redundancy and to ensure a meaningful and focused comparison, we benchmark our proposed normalized fractional

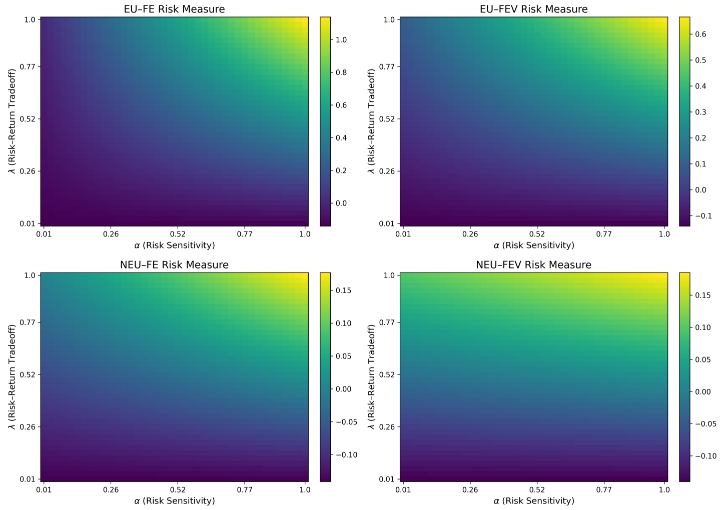

Figure 3.4.3: Heatmap of variations of NEU-FEV measure w.r.t α and λ for a single NIFTY50 stock.

entropy (NFE)-based risk measures, NEU-FE and NEU-FEV, only against the existing fractional entropy-based counterparts, EU-FE and EU-FEV, as developed by Paul and Kundu (2026), using three supervised learning models: *Random Forest (RF)*, *Ridge Regression (Ridge)*, *Lasso Regression (Lasso)* and *ANN*. This shall serve as the appropriate state of the art baselines for evaluating further improvements. The four chosen ML models are used to predict the normalized risk measures derived from the entropy–utility-variance framework. Each model was trained on the feature matrix X constructed from histogram-based fractional order entropy, expected utility and variance measures. The response variable y represents the empirical risk metric associated with each financial asset.

Model performance. All models were trained using an 80–20 train–test split:

$$(X_{\text{tr}}, X_{\text{te}}, y_{\text{tr}}, y_{\text{te}}) = \text{train\_test\_split}(X_{\text{mat}}, y, 0.2).$$

The Random Forest model,

$$\texttt{RandomForestRegressor}(n\_estimators = 200, \texttt{max\_depth} = 6),$$

achieved strong predictive accuracy with low mean squared error (MSE) and a high coefficient of determination (R^2). The ensemble's depth-limited structure effectively avoids overfitting, allowing the model to capture nonlinear dependencies between the decision model components, particularly interactions between fractional order entropy and normalized utility.

The ANN model,

$$\texttt{MLPRegressor}((32, 16),\ \texttt{tanh},\ \texttt{early\_stopping=True}),$$

showed comparable performance while displaying smoother generalization behaviour due to early stopping and an adaptive validation strategy. The nonlinear activation allowed the ANN to learn subtler curvature patterns in the risk surface that are not accessible to linear estimators.

Table 3.4.1: Performance comparison of different risk measures.

Model	NEU-FE/EU-FE		NEU-FEV / EU-FEV	
	MSE	R^2	MSE	R^2
Random Forest	$\mathbf{8.44 * 10^{-5}}/0.0006$	**0.9920**/0.9708	**0.0001**/0.0002	**0.9840**/0.9797
Ridge	$\mathbf{7.82 * 10^{-5}}/7.41 * 10^{-5}$	0.9963/ 0.9966	0.0001 / 0.0001	0.9886/ 0.9915
Lasso	$\mathbf{2.54 * 10^{-6}}/2.26 * 10^{-6}$	**0.9999**/0.9999	$\mathbf{1.12 * 10^{-5}}/1.19 * 10^{-5}$	0.9992/0.9994
ANN	**0.0011**/0.0087	**0.8959**/0.6066	**0.0011**/0.0099	**0.8851**/0.3050

In Table 3.4.1, we present the comparative performance analysis of the four chosen ML models (RF, Ridge, Lasso and a two-layer ANN) for predicting the proposed NFE-based risk measures introduced in Section 3.2. The evaluation is conducted using the MSE and R^2, assessed for both the normalized fractional entropy–utility–variance formulations (NEU-FE and NEU-FEV) and their non-normalized counterparts (EU-FE and EU-FEV). This enables a systematic evaluation of how well the proposed risk scores relate to realized future performance, allow detection of nonlinear relationships overlooked by traditional methods and offer quantitative validation through metrics such as R^2 and MSE.

An important trend emerges when comparing normalized versus non-normalized risk formulations. For Random Forest, Ridge, and Lasso regression, the performance of the normalized variants (NEU-FE and NEU-FEV) is nearly identical to that of the EU-FE and EU-FEV models. This demonstrates that normalization preserves the essential structure of the decision model while improving numerical robustness. In several cases, particularly with Lasso and Ridge, the normalized measures show slightly higher R^2 values, underscoring the advantages of scale invariance and stable optimization introduced by normalization. The ANN exhibits larger discrepancies across normalized and non-normalized versions, further reinforcing that normalization primarily benefits linear models and tree-based ensembles. Further, Fig. 3.4.4 illustrates the R^2 differences of the models, which displays good agreement with the theoretical results of risk measures. Thus, Table 3.4.1 and Fig. 3.4.4 identifies that across all risk formulations, Lasso regression consistently achieves the lowest MSE and the highest R^2 values, indicating near-perfect agreement between predicted and actual risk scores. Moreover, for the NEU-FE and EU-FE models, Lasso attains MSE values on the order of 10^{-6} with $R^2 = 0.9999$, demonstrating exceptional predictive precision and numerical stability. Its performance remains superior even for the variance-augmented formulations (NEU-FEV and EU-FEV), where the MSE stays within the 10^{-5} range while R^2 remains above 0.999.

This performance comparison shows that the regularized models, especially Ridge and Lasso, provide stable prediction results for the proposed risk measures. This can be explained by the fact that the input variables, such as fractional order entropy, expected utility, variance, and normalized variance, may be correlated or affected by scale differences. Ridge regression improves stability by shrinking large coefficients, while Lasso regression can additionally reduce the influence of less informative variables.

The normalized risk measures further improve comparability by reducing scale effects across stocks. As a result, the learning models receive cleaner and more stable input-output relationships. Therefore, the better performance of regularized models does not only indicate statistical accuracy; it also suggests that normalization improves the stability and interpretability of entropy-based risk prediction. In contrast, ANN is useful as a flexible nonlinear benchmark, but its performance may be more sensitive to architecture, sample size, and overfitting.

Remark 3.4.1. *The comparison in Table 3.4.1 should be interpreted in light of the normalization discussed earlier under a common empirical setting. Since the normalized measures reduce scale dependence, the ML models receive more comparable input-output structures across stocks. This helps explain why the normalized measures, especially NEU-FE and NEU-FEV, show improved numerical stability in several model comparisons when evaluated on the same NIFTY50 dataset using the same input structure, the same validation design, and the same performance metrics. Thus, the empirical improvement is not merely a computational effect. It is connected with the theoretical purpose of normalization, namely to improve comparability while preserving the fractional entropy-based sensitivity structure.*

Interpretation of variance augmentation in NEU-FEV models. The results in Fig. 3.4.4 show that Lasso consistently achieves the highest predictive accuracy across all

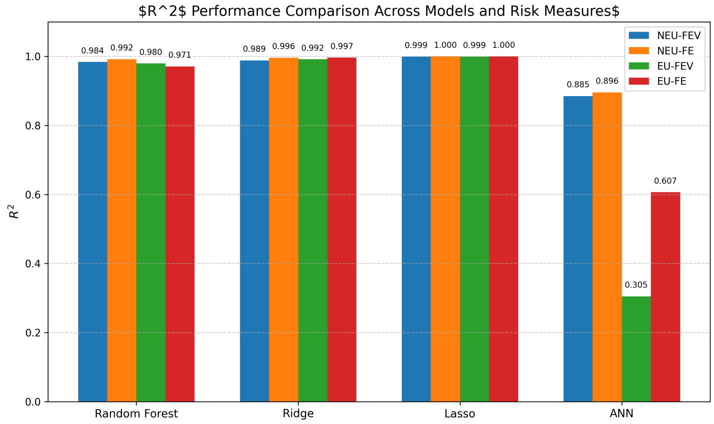

Figure 3.4.4: Comparison of R^2 for all the fractional order entropy-based models.

risk measures, whereas the ANN performs notably worse, particularly for the variance-augmented models. The normalized formulations (NEU-FE, NEU-FEV) also display improved numerical stability, reflected in higher and less volatile R^2 values for the linear models.

From Fig. 3.4.4 and Table 3.4.1, it is clear that NEU-FE delivers the most accurate and stable predictions across all learning methods, outperforming its variance-augmented counterpart, NEU-FEV. This difference arises from the structural role of the variance term, incorporating variance increases curvature and dispersion in the risk surface, amplifying the influence of extreme returns and making the target more volatile. As a result, the mapping from features to the risk output becomes harder to learn, especially in small-sample financial settings. On the other hand, NEU-FE, which depends only on entropy and expected utility, exhibits a smoother and more monotonic structure that is easier for both linear and nonlinear models to approximate. Although normalization improves conditioning for both measures, the destabilizing effect of variance remains evident in the lower R^2 values of NEU-FEV. Overall, the findings show that adding variance increases model complexity without proportional predictive gain, explaining the superior empirical performance of the NEU-FE formulation.

Therefore, from Table 3.3.3, the most reliable risk-based ordering of the top 5 most preferred stocks will be the one corresponding to NEU-FE risk measure for $\alpha = 0.5$ and $\lambda = 0.4$, given as:

$$TITN > TACN > JSTL > BJFN > HLL,$$

and the general predicted rank ordering corresponding to Lasso regression method across a optimal combination of α and λ is:

$$TACN > BRTI > TITN > TREN > TCS.$$

3.4.2 Statistical validation of the ML models

In this subsection, we evaluate the predictive performance of the two-layer (32,16) ANN model relative to the other ML models using paired t-tests, Wilcoxon signed-rank tests, and F-tests. This assessment is motivated by earlier studies that reported strong ANN performance in FE-based decision-making frameworks under risk (see Paul and Kundu, 2026). The results of the paired t-tests, Wilcoxon signed-rank tests, and F-tests presented in Table 3.4.2 establish a consistent hierarchy in model performance across all four risk formulations (NEU-FEV, NEU-FE, EU-FEV and EU-FE).

Table 3.4.2: Statistical significance tests (paired t-test, Wilcoxon signed-rank test, and F-test) comparing prediction errors of ANN with Lasso, Ridge, and RF across all risk formulations.

Risk Model	**Comparison**	**t-stat**	**p-value**	**Wilcoxon W**	**p-value**	**F (variance) (p)**
NEU–FEV	ANN vs Lasso	1.1922	0.2637	15.0	0.2324	1122.26 (2.48×10^{-12})
	ANN vs Ridge	1.1565	0.2773	15.0	0.2324	109.52 (8.23×10^{-8})
	ANN vs RF	1.3830	0.2000	14.0	0.1934	23.94 (6.10×10^{-5})
NEU–FE	ANN vs Lasso	1.4997	0.1679	14.0	0.1934	5244.49 (2.44×10^{-15})
	ANN vs Ridge	1.4572	0.1791	14.0	0.1934	122.28 (5.04×10^{-8})
	ANN vs RF	1.6677	0.1297	13.0	0.1602	6.20 (1.21×10^{-2})
EU–FEV	ANN vs Lasso	0.1844	0.8578	25.0	0.8457	980.95 (4.53×10^{-12})
	ANN vs Ridge	0.1776	0.8629	25.0	0.8457	95.69 (1.50×10^{-7})
	ANN vs RF	0.2252	0.8268	25.0	0.8457	8.04 (4.74×10^{-3})
EU–FE	ANN vs Lasso	1.2194	0.2537	17.0	0.3223	6234.71 (1.11×10^{-15})
	ANN vs Ridge	1.2048	0.2590	18.0	0.3750	127.92 (4.13×10^{-8})
	ANN vs RF	0.9987	0.3440	19.0	0.4316	3.05 (1.12×10^{-1})

Across all pairwise comparisons, both the paired t-tests and Wilcoxon signed-rank tests yield non-significant mean-difference p-values, implying that the chosen two-layer ANN does not achieve superior central prediction accuracy relative to any competing model for the dataset used in this work. However, the F-tests uncover a clear pattern, showing that the error variance of the ANN is *orders of magnitude larger* than that of Lasso, Ridge, and Random Forest, with variance ratios often exceeding 10^2–10^4 and corresponding p-values below 10^{-8}. Consequently, even when mean errors appear comparable, the ANN exhibits pronounced instability across bootstrap replicates, which severely undermines its predictive reliability. Lasso regression, on the other hand, consistently attains the lowest mean error and the smallest variance, and these benefits are statistically significant under all three testing procedures. Ridge regression emerges as the next-best method, delivering stable yet slightly less accurate predictions. Random Forest offers intermediate performance, with moderate accuracy but increased dispersion, situating it between the linear models and the ANN in overall behaviour.

Therefore, through the combined findings, we statistically establish the following hierarchy of model performance:

$$\text{Lasso} \gg \text{Ridge} > \text{Random Forest} \gg \text{ANN}.$$

This hierarchy is preserved uniformly across all entropy-utility-variance risk frameworks, confirming that Lasso regression is the most statistically reliable model for predicting the proposed normalized fractional order entropy-based financial risk measures, combining good accuracy, minimal variability, and strong robustness.

Computational complexity and scalability. Since the empirical validation involves repeated computation of entropy-based risk measures and comparison through machine-learning models, it is useful to comment briefly on computational complexity. The entropy-based measures themselves are computationally manageable. Once empirical probabilities or normalized inputs are obtained, their evaluation mainly involves summation, logarithmic transformations, and parameter-wise repetition. If n denotes the number of observations, m the number of assets, and q the number of fractional-order values, the basic entropy evaluation has computational cost of order $O(mnq)$. If B bootstrap or resampling repetitions are used, the cost increases approximately to $O(Bmnq)$, excluding the cost of model training.

The more expensive part of the empirical framework arises from repeated model fitting and validation, especially for ANN, Random Forest, cross-validation, bootstrap procedures, and hyperparameter tuning. Computational efficiency can therefore be improved by using vectorized implementation, fixed fractional-order grids, parallel computation over assets or parameter values, early stopping in ANN training, and limiting hyperparameter search to interpretable ranges. Although ANN can capture nonlinear relationships between entropy-based inputs and risk measures, its flexibility may lead to overfitting, especially when the dataset is noisy or the number of observations is limited. In the present analysis, this risk is addressed by treating ANN as one validation benchmark rather than as the only predictive model. Its performance is compared with Ridge, Lasso, and Random Forest using the same train–test split and common performance metrics.

The comparison is important because regularized models such as Ridge and Lasso control coefficient instability and provide more interpretable benchmarks. If ANN achieves high in-sample accuracy but weaker test performance or larger error variance, this may indicate overfitting or sensitivity to architecture. Therefore, the conclusions are not based solely on ANN performance. Additional techniques such as early stopping, cross-validation, dropout/regularization, and repeated train–test splits may be used as further safeguards in future computational studies.

Heteroscedasticity diagnostic for regression benchmarks. Since Ridge and Lasso are used as regression-based benchmark models, it is useful to examine whether their residuals show evidence of heteroscedasticity. For this purpose, the Breusch–Pagan and White tests are applied to the residuals obtained from the Ridge and Lasso models for EU-FE, EU-FEV, NEU-FE, and NEU-FEV. These diagnostics are used only to assess the reliability of the regression benchmarks; they do not affect the mathematical definition of the proposed entropy-based risk measures.

Table 3.4.3: Heteroscedasticity diagnostics for regression-based benchmark models using NIFTY50 data.

Risk measure	**Benchmark model**	**Breusch–Pagan p-value**	**White test p-value**
NEU-FE	Ridge	0.7989	0.4047
NEU-FE	Lasso	0.0250	7.99×10^{-6}
NEU-FEV	Ridge	0.5394	0.7037
NEU-FEV	Lasso	0.8120	0.0143
EU-FE	Ridge	0.8055	0.6173
EU-FE	Lasso	0.0051	1.24×10^{-7}
EU-FEV	Ridge	0.5101	0.6820
EU-FEV	Lasso	0.3662	0.3535

Table 3.4.3 shows that the Ridge residuals do not provide strong evidence of heteroscedasticity for any of the four risk measures, since all corresponding p-values are greater than 0.05. For the Lasso benchmark, heteroscedasticity is detected for the FE-type measures, especially EU-FE and NEU-FE, while the evidence is weaker or model-dependent for the FEV-type measures. These results indicate that heteroscedasticity

diagnostics are useful when interpreting regression-based benchmark performance. If heteroscedasticity is present, robust standard errors or weighted regression may be used in future comparisons. However, since the proposed risk measures are distributional entropy-based scores rather than conditional variance regression models, heteroscedasticity does not invalidate the proposed EU-FE, EU-FEV, NEU-FE, and NEU-FEV formulations.

3.5 Conclusion

In this chapter, we extend the fractional entropy-based decision-making framework of Paul and Kundu (2026) by introducing a normalized fractional-order entropy (NFE) and developing two associated risk-based decision models, NEU-FE and NEU-FEV. After establishing the key properties of these risk measures, we apply the proposed frameworks to real-world stock selection using NIFTY50 data by identifying the five most preferred stocks for a representative investor. A comprehensive comparative analysis is then performed against existing fractional entropy-based risk measures using widely adopted machine learning techniques, including Lasso and Ridge Regression, Random Forest, and a two-layer artificial neural network (ANN).

Empirical results demonstrate that machine learning methods substantially enhance the modeling of fractional entropy-utility risk measures. Regularized linear models (Lasso and Ridge) offer strong predictive stability and interpretability by mitigating multicollinearity and highlighting the most influential entropy-utility components. Random Forest effectively captures nonlinear interactions and higher-order dependencies, while the ANN provides flexible function approximation but exhibits high error variability. Our findings further show that both normalized risk formulations, NEU-FE and NEU-FEV, retain or improve predictive performance relative to their non-normalized counterparts, confirming that normalization enhances numerical stability without altering the underlying decision structure. Moreover, incorporating variance increases model complexity without proportional predictive benefits, explaining the superior empirical performance of NEU-FE over NEU-FEV.

Statistical significance tests (paired t-tests, Wilcoxon tests, and F-tests) reinforce these conclusions. Although the ANN's mean errors are not statistically different from those of the other models, its substantially higher error dispersion undermines its reliability for risk prediction. Lasso achieves the lowest mean errors and the smallest variance across all measures, establishing it as the most robust and dependable predictive model, closely followed by Ridge. Overall, integrating interpretable fractional entropy-based risk measures with modern machine learning techniques yields a coherent and empirically validated framework for financial decision-making. The results highlight a practical synergy between fractional entropy modeling and predictive analytics, enabling more informed and risk-efficient portfolio decisions.

Since the empirical validation in this chapter uses regression and machine-learning models on the NIFTY50 dataset, it is useful to note that preliminary econometric diagnostics may be performed before interpreting the prediction results. In particular, residual-based heteroscedasticity checks such as the Breusch–Pagan test, White test, and residual-versus-fitted plots can be applied to the regression benchmark models. If heteroscedasticity is detected, heteroscedasticity-consistent standard errors, weighted regression, or robust comparison criteria may be used for the regression models. These checks do not alter the proposed entropy-based risk measures, but help improve the reliability of model comparison.

Chapter 4

Fractional Differential Entropy and its Application in Modeling One-Dimensional Flow Velocity[1]

"The entropy of the universe tends to a maximum."
— Rudolf Clausius

The fractional order generalization of Shannon entropy proposed by Ubriaco for discrete distributions has been studied for discrete distributions in the last two chapters. This chapter investigates its continuous counterpart, referred to as fractional differential entropy. We systematically analyze its theoretical properties and demonstrate its distinct features which makes it stand out among the existing entropy measures in literature. The entropy is evaluated both analytically and numerically for several standard continuous distributions, highlighting its potential relevance in reliability analysis and the statistical characterization of complex systems. Further, the proposed framework is applied to model the one-dimensional vertical velocity profile of turbulent flows in wide open channels using a single-parameter spatial distribution. The model's validity is established through regression analysis of experimental and field data, and a comparative assessment confirms its superior performance relative to existing entropy-based approaches.

[1]A manuscript containing the work presented here is under review and is archived with the DOI: *https://doi.org/10.48550/arXiv.2507.02323*.

4.1 Introduction

Intrigued by the thermodynamic notion of entropy as a quantitative measure of disorder in physical systems, Shannon introduced an analogous concept in information theory to characterize the uncertainty or randomness associated with information sources and communication processes. This formulation provides a fundamental framework for quantifying information content and predicting the statistical behavior of source outputs (see Shannon, 1948). For a discrete random variable (r.v), the Shannon entropy is defined as:

$$H_S(p) = -\sum_{i=1}^{n} p_i \log p_i, \tag{4.1.1}$$

where p_i is the pmf of the discrete r.v.

Thereafter, extensive research has been devoted to the parametric generalization of Shannon entropy (4.1.1) with the objective of characterizing chaotic and complex physical systems that cannot be adequately described within the classical Shannon framework. In this context, a wide range of entropy generalizations have been developed using tools from fractional calculus (see Machado and Lopes, 2021; Valério et al., 2013, for further details), which permit the relaxation of certain axiomatic properties of Shannon entropy and thereby improve its ability to capture complexity and dynamic behavior in physical processes. Comprehensive accounts of recent developments and applications of fractional and generalized entropy measures can be found in (see Foroghi et al., 2022; Karci, 2016; Lopes and Machado, 2020, and the references therein).

Among the various generalizations of Shannon entropy, a unifying viewpoint has emerged in which entropy functionals are generated by replacing the classical derivative in suitable differential representations of Shannon entropy by more general operators. A notable example is the Tsallis entropy, which can be obtained by replacing the ordinary derivative with the Jackson q-derivative (Abe, 1997; Tsallis, 1988). Motivated by this perspective, Ubriaco (2009) introduced a fractional order generalization of Shannon entropy for discrete r.vs by invoking tools from fractional calculus. The Ubriaco entropy for discrete r.vs is defined as:

$$H_U^{\alpha}(p) = \sum_{i=1}^{n} p(i) \left(-\log p(i) \right)^{\alpha}, \qquad \alpha \in [0,1]. \tag{4.1.2}$$

The entropy (4.1.2) reduces to the Shannon entropy when $\alpha = 1$ and preserves positivity and concavity, while relaxing additivity. In this sense, Ubriaco's fractional entropy plays a role analogous to Tsallis entropy, with the Jackson q-derivative replaced by a fractional derivative, thereby embedding fractional calculus directly into the foundations of generalized entropy theory.

The parameter α in (4.1.2) governs the sensitivity of the entropy measure to variations in the probability distribution. In particular, the classical Shannon entropy is recovered as a special case when $\alpha = 1$, whereas values of $\alpha \in (0, 1)$ introduce a fractional weighting of the information content, thereby enhancing the contribution of lower probability events and allowing for a more flexible characterization of complexity in discrete systems.

Later, Machado (2014) extended Ubriaco entropy to fractional orders defined on the real line and demonstrated that the resulting fractional order entropy exhibits enhanced sensitivity to variations in mathematical, financial, and biological time series. By appropriately tuning the fractional parameter, the proposed measure was shown to be more sensitive to signal evolutions, therby providing more reliable and informative characterizations of underlying system dynamics.

This interplay between fractional calculus and entropy theory presents both conceptual challenges and significant opportunities for gaining deeper insight into the intrinsic structure of physical systems. While the fractional order entropy due to Ubriaco has been extensively investigated in the discrete setting, comparatively little attention has been given to its continuous analogue, primarily due to the mathematical difficulties and conceptual limitations it entails.

Motivated by the effectiveness of the fractional order formulation in the discrete setting, it is natural to seek a corresponding extension to continuous r.vs, analogous to the continuous counterpart of Shannon entropy known as *differential entropy*. Let X be an absolutely continuous nonnegative r.v with cumulative distribution function (cdf) $F(\cdot)$ and probability density function (pdf) $f(\cdot) = \frac{dF(x)}{dx}$. The Shannon differential entropy of X is defined as:

$$H_S(f) = \mathbb{E}[-\log f(X)] = -\int_0^\infty f(x) \log f(x)\, dx, \tag{4.1.3}$$

where $\mathbb{E}[\cdot]$ denotes the expectation operator and represents the average uncertainty associated with the density function f. It is well known that, unlike its discrete counterpart (4.1.1), the continuous extension of Shannon entropy given by (4.1.3) is not invariant under one-to-one transformations of the r.v and may take negative values even for well-behaved pdfs. As a result, it lacks a direct interpretation as an absolute measure of uncertainty and instead quantifies randomness relative to the chosen coordinate system.

These limitations motivate the careful formulation and rigorous analysis of generalized entropy measures in the continuous domain.

Similarly, the transition of Ubriaco entropy (4.1.2) to the continuous domain is nontrivial and raises several conceptual and mathematical challenges, including issues related to non-negativity, invariance, finiteness, and interpretability. These difficulties necessitate a careful reformulation of the entropy measure, leading to what is referred to in this work as the *fractional differential entropy (FDE)*. Therefore, the subsequent sections are devoted to a systematic analysis of this continuous analogue of the fractional order entropy due to Ubriaco, with emphasis on its properties, limitations, and potential applicability to complex hydraulic systems.

The remainder of this study is organized as follows: Section 4.2 is devoted to the investigation of key statistical properties and bounds of the FDE. Its behavior is analyzed numerically for varying values of the fractional parameter α and compared with the classical Shannon differential entropy. This section also derives closed-form analytical expressions of the proposed entropy for several important and commonly used continuous distributions, with particular relevance to reliability and survival analysis. In Section 4.3, the fractional entropy framework is applied to model the vertical velocity distribution in wide open channels under the assumption that the maximum velocity occurs at the free surface, thereby neglecting the dip phenomenon. The estimated velocity profiles are validated against experimental and field data and compared with existing entropy-based models to demonstrate the effectiveness of the proposed approach. Finally, Section 4.4 summarizes the main findings and conclusions of the study.

4.2 Some properties of fractional differential entropy

We begin by recalling the definition of fractional differential entropy (FDE) for absolutely continuous r.vs, which forms the basis for the analysis presented in this section.

Definition 4.2.1. *Let X be a nonnegative absolutely continuous r.v with pdf $f(\cdot)$. The FDE of order α, with $0 < \alpha < 1$, is defined as (Foroghi et al., 2022)*

$$H^{\alpha}(f) = \int_0^{\infty} f(x)\left(-\log f(x)\right)^{\alpha} dx. \tag{4.2.1}$$

The expression in (4.2.1) can be interpreted as the expected value of the fractional order negative log-likelihood $\left(-\log f(X)\right)^{\alpha}$, which quantifies the information content associated with the r.v X. Moreover, when $\alpha = 1$, the fractional differential entropy reduces to the classical Shannon differential entropy, thereby recovering the standard continuous entropy measure as a special case.

We next introduce the dynamic extensions of the FDE, which account for the temporal evolution of uncertainty in reliability systems. Consider a system that starts operating at time $t_1 = 0$ and is observed to fail before time $t_2 = t$. Let $X_t = [X \mid X \leq t]$ denote the failure time of the system within the interval $(0, t)$. The *past FDE* is then defined as

$$\bar{H}^\alpha(f; t) = \int_0^t \frac{f(x)}{F(t)} \Big[-\log \frac{f(x)}{F(t)} \Big]^\alpha dx. \tag{4.2.2}$$

It can be readily observed that, as $\alpha \to 1$, $\bar{H}^\alpha(f; t)$ reduces to the past entropy introduced by Di Crescenzo and Longobardi (2002). Moreover, as $t \to \infty$, the past fractional differential entropy converges to the FDE (4.2.1).

Similarly, suppose that a system has survived up to time t. Let $X_t = [X \mid X \geq t]$ denote the remaining lifetime of the used system. The corresponding *residual FDE* is defined by

$$H^\alpha(f; t) = \int_t^\infty \frac{f(x)}{S(t)} \Big[-\log \frac{f(x)}{S(t)} \Big]^\alpha dx, \tag{4.2.3}$$

where $S(t) = 1 - F(t)$ is the survival function (sf). In this case, as $\alpha \to 1$, $H^\alpha(f; t)$ reduces to the residual entropy proposed by Ebrahimi (1996), and as $t \to 0$, it converges to the FDE. In the present study, we restrict our attention to the FDE and defer a detailed investigation of its dynamic extensions to future work.

The past FDE quantifies the uncertainty associated with early failures occurring before a specified inspection time, while the residual FDE measures the uncertainty in the remaining lifetime of a system that has survived up to a given time. The fractional parameter α provides additional flexibility in emphasizing rare or extreme events, making these measures particularly suitable for modeling systems with complex aging mechanisms and nonstandard failure behaviors.

A direct extension of the fractional entropy proposed by Ubriaco from the discrete to the continuous setting, however, raises certain conceptual and mathematical concerns. In particular,

(i) the FDE may assume both positive and negative values when $f(x) \leq 1$;

(ii) more critically, for $f(x) > 1$, the fractional power of $(-\log f(x))$ may become non-real.

The latter issue is clearly undesirable from both mathematical and interpretational perspectives. Consequently, in order to ensure the meaningful applicability of the fractional order uncertainty measure, we restrict our analysis to absolutely continuous r.vs whose pdfs satisfy $0 < f(x) \leq 1$.

This condition can be enforced either by appropriately limiting the support of the r.v or by constraining the parameters of the underlying distribution. For instance, in the case of a uniform r.v with density

$$f(x; A, B) = \frac{1}{B - A},$$

the condition $0 < f(x) \leq 1$ is satisfied whenever $B - A \geq 1$, with $B > A$. Similarly, for an exponential r.v with density $f(x) = \lambda e^{-\lambda x}$, the desired condition holds for rate parameters $\lambda \in (0, 1]$. Analogous parameter restrictions may be imposed for other continuous distributions, allowing the FDE to be studied within a well-defined and physically meaningful framework. Alternatively, the restriction $0 < f(x) \leq 1$ can also be relaxed by introducing a normalization that keeps the argument of the logarithm within $(0, 1]$, thereby ensuring that the fractional power remains real for $\alpha \in (0, 1)$. One convenient approach is to select a constant $c \geq \|f\|_\infty$ (when $\|f\|_\infty < \infty$) and consider the scaled form

$$H_c^\alpha(f) = \int_0^\infty f(x)\Big(- \log \frac{f(x)}{c}\Big)^\alpha \, dx = \mathbb{E}\Bigg[\Big(- \log \frac{f(X)}{c}\Big)^\alpha\Bigg],$$

for which $0 < \frac{f(x)}{c} \leq 1$ holds and hence $H_c^\alpha(f)$ is real-valued. This construction may be interpreted as a fractional information measure defined relative to the reference level c, analogous to the scale dependence inherent in differential entropy.

In what follows, we derive closed form analytical expressions of the fractional order entropy (4.2.1) for ten important families of univariate continuous distributions, selected from Nadarajah and Zografos (2003), Nanda and Maiti (2007), and Song (2001). These results are expected to be useful for characterizing pdfs that commonly arise in a wide range of statistical and scientific applications. The scope of the proposed entropy measure can be further extended to the study of heavy-tailed distributions, such as the Student's t distribution with arbitrary degrees of freedom, as well as the Cauchy, Cramér, and Pareto distributions, some of which do not possess finite first-order moments.

Throughout this analysis, we assume that the expectation of the fractional power of the negative logarithm of the density function, $\big(- \log f(x)\big)^\alpha$, exists over the entire support $[0, C]$ of the r.v, where $0 \leq x \leq C$ and $0 < \alpha < 1$.

1. **Uniform distribution**

$$f(x;A,B) = \frac{1}{B-A};\ A \leq x \leq B,\ A \geq 0$$

$$\textit{and}\ \ H^{\alpha}(f) = \big(\log(B-A)\big)^{\alpha}.$$

2. **Normal distribution**

$$f(x;\mu,\sigma) = \frac{1}{\sqrt{2\pi}\sigma}\exp\Big(-\frac{(x-\mu)^2}{2\sigma^2}\Big);\ x,\mu,\sigma > 0$$

$$\textit{and}\ \ H^{\alpha}(f) = \frac{1}{2\sqrt{\pi}}\int_{\frac{\mu^2}{2\sigma^2}}^{\infty} e^{-x}x^{-1/2}\Big(x - \log\Big(\sqrt{2\pi}\sigma\Big)\Big)^{\alpha}\ dx.$$

Particular cases:

$$H^{\alpha}(f) = \begin{cases} \frac{1}{2\sqrt{\pi}}\Gamma\Big(\alpha+\frac{1}{2},\frac{\mu^2}{2\sigma^2}\Big) & ;\ \text{for}\ \sigma = \frac{1}{\sqrt{2\pi}}, \mu > 0 \\ \frac{1}{2\sqrt{\pi}}\Gamma\big(\alpha+\frac{1}{2},1\big) = \frac{1}{2\sqrt{\pi}}E_{\frac{1}{2}-\alpha}(1) = \frac{1}{2\sqrt{\pi}}\varphi_{\alpha-\frac{1}{2}}(1) & ;\ \text{for}\ \mu^2 = 2\sigma^2 = \frac{1}{\pi}\ , \end{cases}$$

where

$$\Gamma(n,x) = \int_x^{\infty} e^{-s}s^{n-1}\ ds\ \ \&\ \ E_m(n) = \int_1^{\infty} e^{-nx}x^{-m}dx$$

are the upper incomplete gamma function and generalized exponential integral, respectively and $\varphi_m(x) = E_{-m}(x)$ is the Misra function (see Misra, 1940). $E_m(n)$ can also be expressed as a particular case of the upper incomplete gamma function as follows:

$$E_m(n) = n^{m-1}\Gamma(1-m,n).$$

3. **Exponential distribution**

$$f(x;\lambda) = \lambda e^{-\lambda x};\ x \geq 0$$

$$\textit{and}\ \ H^{\alpha}(f) = \frac{1}{\lambda}\Gamma\big(1+\alpha,\log(1/\lambda)\big).$$

For $\lambda = \frac{1}{e}$, we have

$$H^{\alpha}(f) = eE_{-\alpha}(1) = e\varphi_{\alpha}(1).$$

4. **Pareto II distribution**

$$f(x;k,\sigma) = \frac{k^{\sigma}\sigma}{(x+k)^{\sigma+1}};\ x > 0,\ k,\sigma > 0$$

$$\textit{and}\ \ H^{\alpha}(f) = \Big(\frac{k}{\sigma}\Big)^{\frac{\sigma}{\sigma+1}}\Big(\frac{\sigma+1}{\sigma}\Big)^{\alpha}\Gamma\Big(1+\alpha,\Big(\frac{\sigma}{\sigma+1}\Big)\log\Big(\frac{k}{\sigma}\Big)\Big).$$

5. **Triangular distribution**

$$f(x;\beta) = \begin{cases} \frac{2x}{\beta} & ; \text{for } 0 \le x \le \beta \\ \frac{2(1-x)}{\beta} & ; \text{for } \beta < x \le 1 \end{cases}$$

$$\textit{and}\;\; H^\alpha(f) = \frac{1}{4\cdot 2^\alpha}\Gamma\big(1+\alpha, \log(1/4)\big).$$

6. **Folded t-distribution**

$$f(x;\gamma) = \frac{2}{\sqrt{\gamma}\beta(\frac{\gamma}{2},\frac{1}{2})}\Big(1+\frac{x^2}{\gamma}\Big)^{-\frac{\gamma+1}{2}}; x > 0, \gamma > 0,$$

where $\beta(m,n) = \int_0^1 u^{m-1}(1-u)^{n-1}du$ is the complete beta function for $m,n > 0$, and

$$H^\alpha(f) = \frac{2}{(\gamma+1)\beta(\frac{\gamma}{2},\frac{1}{2})}\int_0^1 (-\log(Ax))^\alpha x^{\frac{-1}{\gamma+1}}\left(1 - x^{\frac{2}{\gamma+1}}\right)^{-\frac{1}{2}} dx,$$

where $A = \frac{2}{\sqrt{\gamma}\beta(\frac{\gamma}{2},\frac{1}{2})}$. So, for the parameter $\gamma = 1, A = \frac{2}{\pi}$ and we have:

$$\begin{aligned} H^\alpha(f) &= \frac{1}{\beta(\frac{1}{2},\frac{1}{2})}\int_0^1 (-\log(Ax))^\alpha x^{\frac{-1}{2}}(1-x)^{-\frac{1}{2}}\; dx \\ &= \frac{1}{\pi}\int_0^1 (-\log(Ax))^\alpha x^{\frac{-1}{2}}(1-x)^{-\frac{1}{2}}\; dx \\ &= \frac{1}{2}\sum_{k=0}^{\infty}\binom{\frac{1}{2}}{k}\frac{\Gamma\big(1+\alpha, \big(\log\big(\frac{\pi}{2}\big)(k+\frac{1}{2})\big)\big)(k+\frac{1}{2})^{-(1+\alpha)}}{(2/\pi)^{k-\frac{1}{2}}} \\ &= \frac{1}{2}\sum_{k=0}^{\infty}\binom{\frac{1}{2}}{k}\frac{(\log\big(\frac{\pi}{2}\big))^{1+\alpha}E_{-\alpha}\big((k+\frac{1}{2})\log\big(\frac{\pi}{2}\big)\big)}{(2/\pi)^{k-\frac{1}{2}}} \\ &= \frac{1}{2}\sum_{k=0}^{\infty}\binom{\frac{1}{2}}{k}\frac{(\log\big(\frac{\pi}{2}\big))^{1+\alpha}\varphi_\alpha\big((k+\frac{1}{2})\log\big(\frac{\pi}{2}\big)\big)}{(2/\pi)^{k-\frac{1}{2}}}, \end{aligned}$$

$$\textit{where}\;\; \binom{\frac{1}{2}}{k} = \frac{\prod_{i=0}^{k-1}(\frac{1}{2}-i)}{k!}; i \in \mathcal{Z}^+ \cup \{0\}.$$

7. **Cramér distribution**

$$f(x;\theta) = \frac{\theta}{2(1+\theta x)^2};\;\; x \ge 0,\;\; \theta > 0$$

$$\begin{aligned} \textit{and}\;\; H^\alpha(f) &= 2^{\alpha-\frac{1}{2}}\Gamma(1+\alpha, \log\sqrt{2}) \\ &= 2^{\alpha-\frac{1}{2}}(\log\sqrt{2})^{1+\alpha}E_{-\alpha}(\log\sqrt{2}) \\ &= 2^{\alpha-\frac{1}{2}}(\log\sqrt{2})^{1+\alpha}\varphi_\alpha(\log\sqrt{2}). \end{aligned}$$

8. **Cauchy distribution**

$$f(x;\sigma,\mu)=\frac{1}{\pi\sigma(1+(\frac{x-\mu}{\sigma})^2)};\ \mu\geq 0,\ \sigma>0$$

$$\begin{aligned}
and\ \ H^{\alpha}(f) &= \frac{1}{2}\sqrt{\frac{\sigma}{\pi}}\sum_{k=0}^{\infty}\binom{\frac{1}{2}}{k}(\pi\sigma)^k\int_{\log A}^{\infty}x^{\alpha}e^{-(k+\frac{1}{2})x}dx\\
&= \frac{1}{2}\sqrt{\frac{\sigma}{\pi}}\sum_{k=0}^{\infty}\binom{\frac{1}{2}}{k}\frac{(\pi\sigma)^k}{(k+\frac{1}{2})^{1+\alpha}}\Gamma\Big(1+\alpha,\big(k+\frac{1}{2}\big)\log A\Big)\\
&= \frac{1}{2}\sqrt{\frac{\sigma}{\pi}}\sum_{k=0}^{\infty}\binom{\frac{1}{2}}{k}(\pi\sigma)^k(\log A)^{1+\alpha}E_{-\alpha}\Big(\big(k+\frac{1}{2}\big)\log A\Big)\\
&= \frac{1}{2}\sqrt{\frac{\sigma}{\pi}}\sum_{k=0}^{\infty}\binom{\frac{1}{2}}{k}(\pi\sigma)^k(\log A)^{1+\alpha}\varphi_{\alpha}\Big(\big(k+\frac{1}{2}\big)\log A\Big),
\end{aligned}$$

where $A=\pi\sigma\left(1+\frac{\mu^2}{\sigma^2}\right)$.

9. **Gamma distribution**

$$f(x;m,n)=\frac{m^n x^{n-1}\exp\{-mx\}}{\Gamma(n)};\ m,n>0,\ x>0$$

$$and\ \ H^{\alpha}(f)=\int_0^{\infty}f(x;m,n)[-\log f(x;m,n)]^{\alpha}\ dx.$$

Particular case $(n=1)$**:**

$$H^{\alpha}(f)=\frac{1}{m}\Gamma\big(1+\alpha,\log(1/m)\big).$$

10. **Beta distribution**

$$f(x;m,n)=\frac{x^{m-1}(1-x)^{n-1}}{B(m,n)};\ m,n>0,\ 0<x<1$$

$$and\ \ H^{\alpha}(f)=\begin{cases}\dfrac{B(m,1)^{\frac{1}{m-1}}(m-1)^{\alpha}}{m^{1+\alpha}}\Gamma\big(1+\alpha,\dfrac{m}{m-1}\log B(m,1)\big) & ;\text{ for } n=1\\ \dfrac{B(1,n)^{\frac{1}{n-1}}(n-1)^{\alpha}}{n^{1+\alpha}}\Gamma\big(1+\alpha,\dfrac{n}{n-1}\log B(1,n)\big) & ;\text{ for } m=1.\end{cases}$$

4.2.1 Bounds and monotonicity

Since it is not possible to derive closed form expressions for the entropy measure for all distributions, we obtain different bounds for the entropy and thereby examine some monotonicity properties of FDE defined by (4.2.1). Before proceeding with the discussion on the bounds, we first need to understand the nature of the entropy function $h^\alpha(f) = f(x)(-\log f(x))^\alpha$. It is to be noted that the properties are analyzed with respect to f since the entropy function is considered to be a function of f.

In the following proposition, we investigate the point or the value of f for which the entropy function $h^\alpha(f)$ assumes the maximum value in the region of our study. The proof is immediate from the case of Ubriaco entropy function $(s_i(p) = p(i)(-\log p(i))^\alpha)$ as discussed in Ubriaco (2009) and hence omitted.

Proposition 4.2.1. *The entropy function $h^\alpha(f)$ attains maximum value at $f(x) = e^{-\alpha}$, where α is the order of the entropy function.*

Theorem 4.2.1. *(i) $h^\alpha(f)$ decreases and hence the entropy (4.2.1) decreases with increase in α when $I(f) = -\log(f(x)) \in (0, 1)$, i.e., when $\frac{1}{e}(= 0.368) < f(x) < 1$.*

(ii) Again, $h^\alpha(f)$ shows an increasing pattern resulting in an increase of entropy with α when $I(f) \geq 1$, i.e., when $0 < f(x) \leq 0.368$.

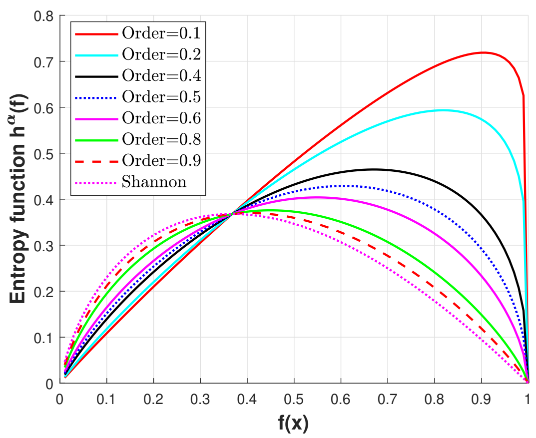

Figure 4.2.1: FDE function for different orders α.

Fig. 4.2.1 illustrates that the entropy function $h^\alpha(f)$ is a nonnegative and concave function of f over the region $0 < f \leq 1$. Moreover, it is observed that $h^\alpha(f)$ is increasing for $0 < f \leq 0.368$ and decreasing for $0.368 < f < 1$. It is noteworthy that when the information content $I(f) < 0$, or equivalently when $f(x) > 1$, the function $h^\alpha(f)$ may attain complex values. Such cases are excluded from the present analysis, since studies of uncertainty and randomness in the literature are typically confined to real-valued measurable functions.

It is well known that the Shannon differential entropy (4.1.3) is invariant under translations but does not remain invariant under changes of scale or more general invertible transformations (Shannon, 1948). In the following proposition, we show that the FDE (4.2.1) exhibits analogous behavior.

Proposition 4.2.2. *Under the linear transformations $Y = X + c$ and $Z = mX$, with $m > 0$ and $c \geq 0$, the FDE satisfies (see Bickel and Lehmann, 1976):*

$$H^\alpha(f_Y) = H^\alpha(f_X), \tag{4.2.4}$$

$$H^\alpha(f_Z) \neq m\, H^\alpha(f_X). \tag{4.2.5}$$

Proof: The translation invariance in (4.2.4) and the non-homogeneity under scaling in (4.2.5) follow directly from the relations

$$f_Y(x) = f_X(x-c) \quad \text{and} \quad f_Z(x) = \frac{1}{m} f_X\left(\frac{x}{m}\right), \qquad x \in \mathbb{R}. \tag{4.2.6}$$

These relations given by (4.2.6) indicate that while a mere translation of the r.v preserves the shape of the probability density and hence leaves the FDE unchanged, a scaling transformation alters the magnitude of the density and consequently affects the associated fractional information content. □

In the subsequent propositions, we establish several bounds for the FDE in terms of the Shannon differential entropy (4.1.3), under the assumption that the pdf satisfies $0 < f \leq 1$.

Proposition 4.2.3. *For a non-negative r.v X with pdf $f(x)$*

$$H^\alpha(f) \leq (H_S(f))^\alpha$$

for $0 < \alpha \leq 1$ and $0 < f \leq 1$.

Proof: The result can be achieved from the relation that $f(x) \leq (f(x))^\alpha$ for $x > 0$, $0 < f \leq 1$ and $0 < \alpha \leq 1$. □

Proposition 4.2.4. *If X has a bounded support $[0, b]$, then for $0 < \alpha \leq 1$ and $0 < f \leq 1$.*

$$H^\alpha(f) \geq A(\alpha) e^{H_S(f)} \tag{4.2.7}$$

where $A(\alpha) = \exp\left[\int_0^b f(x) \log(f(x)[-\log f(x)]^\alpha)\, dx\right]$.

Proof: Using the log-sum inequality, we have

$$\int_0^\infty f(x)\log\frac{f(x)}{f(x)[-\log f(x)]^\alpha}dx \geq \log\frac{1}{\int_0^\infty f(x)[-\log f(x)]^\alpha\,dx} = \log\frac{1}{H^\alpha(f)}. \tag{4.2.8}$$

Moreover, the L.H.S of (4.2.8) can be written as

$$\int_0^\infty f(x)\log\frac{f(x)}{f(x)[-\log f(x)]^\alpha}dx = -H_S(f) - \int_0^\infty f(x)\log(f(x)[-\log f(x)]^\alpha)\,dx. \tag{4.2.9}$$

Now, using the result of Proposition 4.2.1, we get that

$$\log(f(x)[-\log f(x)]^\alpha) \leq \alpha\log\frac{\alpha}{e}. \tag{4.2.10}$$

Hence, if X has a bounded support $[0,b]$, then from Eqs. (4.2.8) – (4.2.10), we get that

$$A(\alpha) = \exp\left[\int_0^b f(x)\log(f(x)[-\log f(x)]^\alpha)\,dx\right] \leq b\log\big(e^{-\alpha}\cdot\alpha^\alpha\big), \tag{4.2.11}$$

where we can find that the function $\log(e^{-\alpha}\cdot\alpha^\alpha)$ is monotonically decreasing w.r.t $\alpha \in (0,1]$ and hence $A(\alpha) < \infty$ is bounded. Therefore, from (4.2.9) and (4.2.11), we get (4.2.7). □

Proposition 4.2.5. *Let X be bounded with support $[0,b]$, $b > 0$. Then for $0 < \alpha \leq 1$ and $0 < f \leq 1$,*

$$H^\alpha(f) \leq b^{1-\alpha}(H_S(f))^\alpha.$$

Proof: The proof follows from Proposition 4.2.3 and Jensen's inequality for integrals defined as:

$$\int_\Omega \varphi(g(x))\,d\mu(x) \leq \varphi\left(\int_\Omega g(x)\,d\mu(x)\right). \tag{4.2.12}$$

where $\varphi : \mathbb{R} \to \mathbb{R}$, defined as $\varphi(x) = x^\alpha$, $0 < \alpha \leq 1$, is a concave function on $x \geq 0$ and $g : \Omega \to \mathbb{R}$, defined as $g(x) = -\log f(x)$, is an integrable function from the measure space $(\Omega, \mathcal{F}, \mu)$ with $\mu(\Omega) = 1$ and $d\mu = f(x)\,dx$. □

In the next two propositions, we obtain some more bounds for the FDE with respect to the negative loglikelihood function and some integrals over a bounded domain $[0,b]$.

Proposition 4.2.6. *Let X be bounded in L^1 space having support $[0,b]$, $b > 0$, then*

$$H^\alpha(f) \leq \int_0^b I^\alpha(f)\;dx,$$

for $0 < f \leq 1$, where $I^\alpha(f) = [-\log f(x)]^\alpha$ is the information gain function of FDE.

Proof: This result follows from Holder's inequality which states that for measurable real valued functions f_1 and f_2 defined on a domain D bounded in L^1 space with closed support $[0,b]$, we have that

$$\left|\int f_1(x)f_2(x)\,d\mu(x)\right| \leq \left(\int |f_1(x)|\,d\mu(x)\right)\left(\int |f_2(x)|\,d\mu(x)\right).$$

Here, we have taken $f_1(x) = f(x)$, $f_2(x) = (-\log f(x))^\alpha$. □

Proposition 4.2.7. *For a r.v X with bounded support $[0,b]$ and $H^\alpha(f) < \infty$, we have*

(i) $\int_0^b f(x)\big(1-f(x)\big)^\alpha\,dx \leq H^\alpha(f) \leq \int_0^b f(x)\left(\frac{1}{f(x)}-1\right)^\alpha dx,$

(ii) $H^\alpha(f) \leq b\big(\frac{\alpha}{e}\big)^\alpha,$

if $0 < f \leq 1$ *and* $\alpha > 0$.

Proof:

(i) The inequalities in (i) can be achieved by using the relation

$$1-\frac{1}{x} \leq \log x \leq x-1 \;\; for\ x > 0.$$

(ii) For the second part, we have used the fact that $f(x)[-\log f(x)]^\alpha$ is non-negative and concave for $0 < f(x) \leq 1\ \forall\ \alpha \in (0,1]$ such that

$$f(x)[-\log f(x)]^\alpha \leq [-\log a]^{\alpha-1}[\alpha a - f(x)(\alpha+\log a)],$$

with $\alpha \in (0,1]$ and $a \in (0,1]$ Therefore, from Eq. (4.2.1), we have

$$H^\alpha(f) \leq [-\log a]^{\alpha-1}[\alpha ab - (\alpha+\log a)].$$

By substituting $a = e^{-\alpha}$, we get the final expression given by (ii). □

In the following proposition, we inspect the non-additivity property of FDE and used it to obtain a bound for the entropy measure for bivariate distribution.

Proposition 4.2.8. *For two non-negative absolutely continuous independent r.vs X and Y,*

$$H^\alpha(f_X, f_Y) \leq H^\alpha(f_X) + H^\alpha(f_Y),\;\; 0 < \alpha \leq 1, \tag{4.2.13}$$

for $0 < f \leq 1$ *with equality only if* $\alpha = 1$.

Proof: The proof follows from the relation that

$$\iint f(x,y)\,dx\,dy = \int f_X(x)\,dx \int f_Y(y)\,dy$$

for independent r.vs X and Y and then using the inequality

$$(x+y)^{\alpha} \leq x^{\alpha} + y^{\alpha}; \quad 0 < \alpha \leq 1, \quad x, y > 0,$$

with equality only if $\alpha = 1$. □

In reliability modeling, the practical relevance of an entropy measure is often assessed through its numerical magnitude. A higher entropy value indicates greater associated uncertainty or information content, thereby enhancing the descriptive capability of the underlying distribution for a given system. Motivated by this principle, we examine the comparative effectiveness of FDE $H^{\alpha}(f)$ relative to the classical Shannon differential entropy $H_S(f)$. As established in Theorem 4.2.1, the fractional entropy can capture higher information content for suitable choices of the fractional parameter α, particularly as α approaches zero. In contrast, the Shannon differential entropy attains comparatively lower values for distributions whose density functions satisfy $f(x) \in (0.368, 1)$, thereby indicating reduced sensitivity in such regimes.

4.2.2 Numerical comparison

According to the foundational principles of information theory, an entropy measure that yields a higher value for a given distribution, when fitted to empirical data from a physical or reliability system, is generally regarded as more effective in characterizing the system's uncertainty. In this subsection, we numerically examine the implications of Theorem 4.2.1(i) by identifying distributions for which the FDE $H^{\alpha}(f)$ provides a more informative description than the Shannon differential entropy $H_S(f)$. In particular, we analyze the behavior of $H^{\alpha}(f)$ as the fractional parameter α varies, noting that $H^{\alpha}(f)$ attains its maximum as $\alpha \to 0$ and reduces to the Shannon entropy at $\alpha = 1$. To this end, several important continuous distributions commonly encountered in reliability and survival analysis are considered, as listed in Table 4.2.1.

Referring to the numerically computed entropy values for different choices of α reported in Table 4.2.2, it is observed that for the Weibull and uniform distributions, under suitable parameter settings, the entropy assumes its minimum value at $\alpha = 1$ and its maximum for values of α close to zero. In contrast, an opposite trend is exhibited by the remaining distributions considered, namely the standard normal, generalized Pareto, exponential, and finite-range distributions, for which the entropy is minimized for α near zero and increases monotonically with α. This distribution-dependent variation in the behavior of $H^\alpha(f)$ can be attributed to the structural properties of the integrand $h^\alpha(f)$ established in Theorem 4.2.1. Consequently, FDE offers greater flexibility than the Shannon differential entropy in assessing the adequacy and fitness of probabilistic models used to describe complex physical and reliability systems.

Table 4.2.1: Some important continuous distributions.

Distributions	**Probability Density Function**
Weibull	$f(x;a,b) = \frac{b}{a}(\frac{x}{a})^{b-1}\exp\left(-(\frac{x}{a})^b\right),\ x \geq 0$
Uniform	$f(x;A,B) = \frac{1}{B-A},\ A \leq x \leq B$
Standard Normal	$f(x) = \frac{1}{\sqrt{2\pi}}\exp\left(-\frac{x^2}{2}\right),\ 0 < x < \infty$
Generalized Pareto	$f(x;k,\sigma,\theta) = \left(\frac{1}{\sigma}\right)\left(1+\frac{k(x-\theta)}{\sigma}\right)^{-1-\frac{1}{k}},\ \theta < x \text{ for } k > 0$
Exponential	$f(x;\lambda) = \lambda e^{-\lambda x},\ x \geq 0,\ \lambda > 0$
Finite Range	$f(x;a,\theta) = \frac{a}{x}\left(\frac{x}{\theta}\right)^a,\ 0 \leq x \leq \theta,\ a,\theta > 0.$

Table 4.2.2: Fractional order entropy values for continuous distributions.

Distributions	$\alpha = 1$	$\alpha = 0.9$	$\alpha = 0.8$	$\alpha = 0.6$	$\alpha = 0.4$	$\alpha = 0.2$
Weibull $(a = 1, b = 2)$	0.2300	0.2389	0.2499	0.2790	0.3201	0.3768
Uniform $(A = 0, B = 2)$	0.6931	0.7190	0.7459	0.8026	0.8636	0.9293
Standard Normal	1.4183	1.3580	1.3030	1.2068	1.2161	1.0579
GPD $(k = 1, \sigma = 2, \theta = 2)$	1.4025	1.3229	1.2485	1.1136	0.9953	0.8914
Exponential$(\lambda = 1)$	1.0000	0.9618	0.9314	0.8935	0.8873	0.9182
Finite Range $(p = 2, \theta = 10)$	1.4071	1.3520	1.2912	1.2074	1.1257	1.0537

4.3 Modeling of one-dimensional vertical velocity distribution through FDE

Complex physical systems such as open-channel flows exhibit inherent nonlinear and chaotic behavior. Accurate characterization of key hydraulic variables, including flow velocity, suspended sediment concentration, and shear stress, is therefore essential for effective flood management, river engineering, and water quality assessment. Among these variables, the vertical distribution of flow velocity plays a central role in understanding momentum transfer and sediment transport processes in open channels. Classical approaches for modeling one-dimensional vertical velocity profiles include the linear law for the near-bed viscous sublayer, the Prandtl–von Kármán logarithmic law for the intermediate region, and power-law formulations for the near-surface zone (see Sarma et al., 1983, and references therein). While these formulations provide reasonable local approximations, they fail to yield a single unified expression capable of describing the velocity distribution over the entire depth of the channel, from the bed to the free surface. Furthermore, the modeling of velocity distributions in unsteady turbulent open-channel flows using deterministic frameworks is often challenged by high computational cost, sensitivity to boundary conditions, and limited or uncertain field data arising from measurement errors and sampling constraints. To address these limitations, probabilistic and information-theoretic approaches have been increasingly adopted in hydraulic studies. In particular, entropy-based methods offer notable advantages, as they do not rely on assumptions of symmetry, require minimal metric information, and remain effective even for relatively small datasets. These features lead to reduced computational complexity while maintaining reliable predictive capability.

Motivated by these advantages, several entropy-based models have been proposed for estimating one-dimensional vertical velocity distributions in open channels, assuming maximum velocity at the free surface. Existing formulations are primarily based on Shannon entropy (Chiu, 1987), Tsallis entropy (Singh and Luo, 2011), Rényi entropy (Kumbhakar and Ghoshal, 2016), and fractional Machado entropy (Kumbhakar and Tsai, 2023). To the best of our knowledge, however, the FDE has not yet been explored in the context of open-channel flow velocity modeling. This observation motivates the present study, in which we employ FDE to construct an entropy-based framework for determining the vertical velocity distribution of turbulent flows in wide rectangular open channels, such as rivers. In practical situations, the presence of physical constraints prevents the entropy-maximizing distribution from being uniform. Consequently, the maximum entropy solution represents the least biased distribution that satisfies the governing constraints, providing a natural and physically consistent framework for modeling velocity distributions in complex hydraulic systems.

4.3.1 Methodology: construction of entropy-based optimization problem

The one-dimensional vertical velocity distribution in wide open channels is modeled within the framework of the principle of maximum entropy (POME) proposed by Jaynes (1957a). In this approach, the pdf that best represents the system is obtained by maximizing an appropriate entropy measure subject to physically meaningful constraints derived from prior information about the flow.

Let $\hat{\mathcal{V}}$ denote the dimensionless velocity r.v defined as $\hat{\nu} = \frac{\nu}{\nu_{\max}}$, where ν is the local flow velocity and $\nu_{\max}$ is the maximum velocity occurring at a specific elevation above the channel bed. The corresponding pdf $f(\hat{\nu})$ is supported on the interval $[0, 1]$. The FDE of order $\alpha \in (0, 1)$ associated with $f(\hat{\nu})$ is given by

$$H^{\alpha}(f) = \int_0^1 f(\hat{\nu}) \left[-\log f(\hat{\nu}) \right]^{\alpha} d\hat{\nu}. \tag{4.3.1}$$

The entropy functional (4.3.1) is maximized subject to the following constraints:

$$\int_0^1 f(\hat{\nu})\, d\hat{\nu} = 1, \tag{4.3.2}$$

$$\int_0^1 \hat{\nu}\, f(\hat{\nu})\, d\hat{\nu} = \hat{\nu}_m, \tag{4.3.3}$$

$$\int_0^1 \hat{\nu}^2 f(\hat{\nu})\, d\hat{\nu} = \delta\, \hat{\nu}_m^2, \tag{4.3.4}$$

$$\int_0^1 \hat{\nu}^3 f(\hat{\nu})\, d\hat{\nu} = \beta\, \hat{\nu}_m^3. \tag{4.3.5}$$

Here, $\hat{\nu}_m$ represents the dimensionless cross-sectional mean velocity, while δ and β are the momentum and energy correction coefficients, respectively. Constraint (4.3.2) enforces normalization of the pdf, whereas constraints (4.3.3)–(4.3.5) correspond to the first-, second-, and third-order moments of $\hat{\mathcal{V}}$, which are associated with the conservation of mass, momentum, and energy, respectively, across the channel section.

Since conservation of mass is fundamental to all flows and the influence of momentum and energy correction terms on the vertical velocity profile is assumed to be negligible in the present formulation, only constraints (4.3.2) and (4.3.3) are retained. Under these assumptions, the Lagrangian functional is constructed as

$$L(f, \hat{\nu}) = \int_0^1 f(\hat{\nu}) \left[-\log f(\hat{\nu}) \right]^{\alpha} d\hat{\nu} - a\left(\int_0^1 f(\hat{\nu})\, d\hat{\nu} - 1 \right) - b\left(\int_0^1 \hat{\nu}\, f(\hat{\nu})\, d\hat{\nu} - \hat{\nu}_m \right), \tag{4.3.6}$$

where a and b are Lagrange multipliers associated with the normalization and mass conservation constraints, respectively.

To obtain the entropy-maximizing distribution, we apply the calculus of variations. Since the integrand depends only on $f(\hat{\nu})$ and not on its derivatives, the Euler–Lagrange condition defined as:

$$\frac{\partial L}{\partial f(\hat{\nu})} - \frac{d}{d\hat{\nu}}\Big(\frac{\partial L}{\partial f(\hat{\nu})'}\Big) = 0,$$

reduces to a pointwise stationarity condition $\frac{\partial L}{\partial f} = 0$. Defining

$$\Phi(f) = f\big[-\log f\big]^{\alpha},$$

the first order derivaive of L with respect to f yields

$$\Phi'(f(\hat{\nu})) - a - b\hat{\nu} = 0, \qquad 0 \le \hat{\nu} \le 1. \tag{4.3.7}$$

A straightforward computation gives

$$\Phi'(f) = (-\log f)^{\alpha} - \alpha(-\log f)^{\alpha-1},$$

which leads to the Euler–Lagrange equation

$$(-\log f(\hat{\nu}))^{\alpha} - \alpha\,(-\log f(\hat{\nu}))^{\alpha-1} = a + b\hat{\nu}. \tag{4.3.8}$$

For $\alpha = 1$, equation (4.3.8) reduces to

$$-\log f(\hat{\nu}) - 1 = a + b\hat{\nu},$$

yielding the familiar exponential-form solution associated with Shannon entropy. For $0 < \alpha < 1$, (4.3.8) constitutes an implicit equation for the density function $f(\hat{\nu})$. Introducing the transformation

$$y(\hat{\nu}) = -\log f(\hat{\nu}),$$

the stationarity condition may be rewritten as

$$y(\hat{\nu})^{\alpha} - \alpha\, y(\hat{\nu})^{\alpha-1} = a + b\hat{\nu}, \tag{4.3.9}$$

which can be solved pointwise for $y(\hat{\nu})$ and subsequently inverted to obtain

$$f(\hat{\nu}) = \exp\big(-y(\hat{\nu})\big).$$

A closed-form expression for $f(\hat{\nu})$ is obtainable only for special fractional orders (e.g., $\alpha = \frac{1}{2}, \frac{2}{3}, \frac{3}{4}$), where the transformed Euler-Lagrange equation reduces to a polynomial in $y^{1/k}$. For a general $0 < \alpha < 1$, the relation remains implicit and is most reliably handled by pointwise numerical inversion.

Explicit entropy-maximizing pdf for $\alpha = \frac{1}{2}$

For the special case $\alpha = \frac{1}{2}$, the Euler-Lagrange equation (4.3.8) becomes

$$(-\log f(\hat{\nu}))^{1/2} - \frac{1}{2}(-\log f(\hat{\nu}))^{-1/2} = a + b\hat{\nu}. \tag{4.3.10}$$

Introducing the transformation

$$y(\hat{\nu}) = -\log f(\hat{\nu}) > 0, \qquad s(\hat{\nu}) = \sqrt{y(\hat{\nu})}.$$

Then (4.3.10) can be rewritten as

$$s(\hat{\nu}) - \frac{1}{2s(\hat{\nu})} = a + b\hat{\nu}.$$

Multiplying by $2s(\hat{\nu})$ yields the quadratic equation

$$2s(\hat{\nu})^2 - 2(a + b\hat{\nu})s(\hat{\nu}) - 1 = 0, \tag{4.3.11}$$

or equivalently,

$$s(\hat{\nu})^2 - (a + b\hat{\nu})s(\hat{\nu}) - \frac{1}{2} = 0.$$

Solving (4.3.11) and selecting the positive root (since $s(\hat{\nu}) > 0$) gives

$$s(\hat{\nu}) = \frac{(a + b\hat{\nu}) + \sqrt{(a + b\hat{\nu})^2 + 2}}{2}. \tag{4.3.12}$$

Therefore,

$$y(\hat{\nu}) = s(\hat{\nu})^2 = \left[\frac{(a + b\hat{\nu}) + \sqrt{(a + b\hat{\nu})^2 + 2}}{2}\right]^2,$$

and the corresponding entropy-maximizing pdf is obtained as

$$f(\hat{\nu}) = \exp\left(-\left[\frac{(a + b\hat{\nu}) + \sqrt{(a + b\hat{\nu})^2 + 2}}{2}\right]^2\right), \qquad 0 \le \hat{\nu} \le 1. \tag{4.3.13}$$

The Lagrange multipliers a and b are determined by enforcing the constraints $\int_0^1 f(\hat{\nu})\, d\hat{\nu} = 1$ and $\int_0^1 \hat{\nu} f(\hat{\nu})\, d\hat{\nu} = \hat{\nu}_m$.

Substituting the value of $f(\hat{\nu})$ from (4.3.13) in (4.3.1), we obtain the maximum entropy of $f(\hat{\nu})$ of $\hat{\mathcal{V}}$. Therefore, we have the FDE which can be computed as follows:

$$H^\alpha(f) = \int_0^1 \exp\left[-\frac{(1 + (a + b\hat{\nu})^2) + (a + b\hat{\nu})\sqrt{(a + b\hat{\nu})^2 + 2}}{2}\right] \times \\ \left(\frac{(1 + (a + b\hat{\nu})^2) + (a + b\hat{\nu})\sqrt{(a + b\hat{\nu})^2 + 2}}{2}\right) d\hat{\nu}.$$

Physical interpretation of the fractional order. In the present FDE-based velocity model, the fractional order parameter should be understood as a sensitivity parameter rather than as a direct physical constant. It controls how strongly the entropy functional responds to changes in the normalized velocity distribution. In turbulent open-channel flow, the vertical velocity profile is affected by wall resistance, eddy mixing, nonlocal momentum transfer, and history-dependent interactions among different flow layers. The fractional order therefore provides an effective way to represent the influence of nonlocality, heterogeneity, and memory-like behaviour on the entropy-based velocity distribution.

It should be emphasized that the fractional order is not equivalent to viscosity, roughness height, shear velocity, or any other directly measurable hydraulic parameter. Rather, it is a phenomenological modelling parameter that adjusts the sensitivity of the entropy model to profile shape and turbulence-induced variability. Different values of the fractional order allow the model to adapt to different velocity-profile behaviours observed in experimental and field data.

4.3.2 Estimation of the velocity distribution

From the preceding analysis, the entropy-maximizing velocity distribution is characterized by the fractional parameter α and the Lagrange multipliers a and b, which are determined from the imposed constraints. To obtain a practical expression for the one-dimensional vertical velocity profile in an open channel, it is necessary to relate the cdf of the normalized (dimensionless) velocity $\hat{\mathcal{V}}$ to the normalized vertical coordinate y/M, where M denotes the total flow depth and y is the distance measured upward from the channel bed.

This spatial form of the cdf, denoted by $F(\hat{\nu})$, is hypothesized by incorporating the physically reasonable assumptions that the vertical flow velocity increases monotonically from 0 at the bed ($y = 0$) to its maximum value at the free surface ($y = M$), and that the velocity gradient is influenced by channel geometry and suspended sediment characteristics throughout the flow domain. Consequently, $F(\hat{\nu})$ is assumed to be continuous and differentiable on $(0, M)$ with values in $[0, 1]$. The corresponding probability density function is then obtained by differentiating $F(\hat{\nu})$ with respect to $\hat{\nu}$. By the chain rule, we have

$$f(\hat{\nu}) = \frac{dF(\hat{\nu})}{d\hat{\nu}} = \frac{dF(\hat{\nu})}{dy} \cdot \frac{dy}{d\hat{\nu}}. \tag{4.3.14}$$

Since $f(\hat{\nu}) \geq 0$ and $\frac{dy}{d\hat{\nu}} \geq 0$ under the monotonicity assumption, it follows from (4.3.14) that $\frac{dF(\hat{\nu})}{dy} \geq 0$. Hence, the cdf must be a nondecreasing function of the normalized height

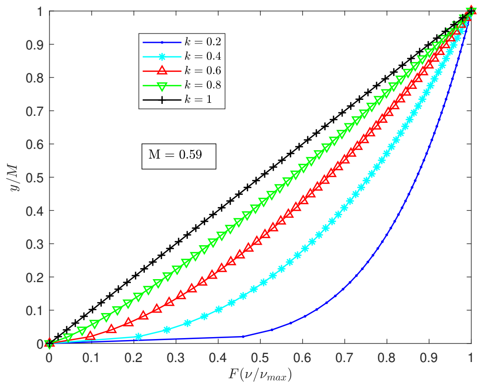

Figure 4.3.1: Variation of cdf with respect to the fitting parameter k.

y/M.

Motivated by these considerations, we adopt the following one-parameter spatial representation for the cdf:

$$F(\hat{\nu}) = \left(\frac{y}{M}\right)^k, \tag{4.3.15}$$

where $k \in [0,1]$ is treated as a fitting parameter reflecting the influence of suspended sediment characteristics on the vertical distribution of velocity, and may be estimated via least squares using available observations (Cui and Singh, 2014). Smaller values of k correspond to weaker sediment-induced effects and therefore a slower increase of the cdf with height, whereas larger values of k indicate stronger influence, leading to a more rapid increase of $F(\hat{\nu})$ with y/M. The effect of varying k on the hypothesized relation (4.3.15) is illustrated in Fig. 4.3.1. In particular, $k = 1$ yields a linear dependence of $F(\hat{\nu})$ on y/M, a scenario often associated with clear-water channels or relatively steady flows where the velocity increases approximately uniformly with depth.

Using the entropy-maximizing density obtained for $\alpha = \frac{1}{2}$ in (4.3.13), the corresponding FDE-based cdf over the velocity domain can be constructed, noting that $F(\hat{\nu})$ is an increasing function of $\hat{\nu}$. Hence,

$$\begin{aligned} F(\hat{\nu}) &= \int_0^{\hat{\nu}} f(u)\,du \\ &= \int_0^{\hat{\nu}} \exp\left(- \left[\frac{(a+bu) + \sqrt{(a+bu)^2 + 2}}{2} \right]^2 \right) du. \end{aligned} \tag{4.3.16}$$

Expanding the square and simplifying the exponent yields the equivalent representation

$$\left[\frac{(a+bu) + \sqrt{(a+bu)^2 + 2}}{2} \right]^2 = \frac{(1 + (a+bu)^2) + (a+bu)\sqrt{(a+bu)^2 + 2}}{2},$$

and therefore (4.3.16) can be written as

$$F(\hat{\nu}) = \int_0^{\hat{\nu}} \exp\left[-\frac{(1+(a+bu)^2)+(a+bu)\sqrt{(a+bu)^2+2}}{2}\right] du.$$

Next, using the substitution $t=(a+bu)^2$ (so that $dt = 2b(a+bu)\,du$ and $du = \frac{1}{2b}\,t^{-1/2}\,dt$), we obtain

$$F(\hat{\nu}) = \frac{e^{-1/2}}{2b}\int_{a^2}^{(a+b\hat{\nu})^2} t^{-1/2}\exp\left[-\frac{t+\sqrt{2t+t^2}}{2}\right] dt. \tag{4.3.17}$$

To obtain a tractable series-form expression, we employ the power series expansion $e^{-x} = \sum_{i=0}^{\infty}(-1)^i\frac{x^i}{i!}$, valid for all $x\in\mathbb{R}$, in (4.3.17), which gives

$$F(\hat{\nu}) = \frac{e^{-1/2}}{2b}\int_{a^2}^{(a+b\hat{\nu})^2} t^{-1/2}\sum_{i=0}^{\infty}\frac{(-1)^i}{i!}\left(\frac{t+\sqrt{2t+t^2}}{2}\right)^i dt.$$

Applying the binomial expansion $(x+y)^i = \sum_{j=0}^{i}\binom{i}{j}x^{i-j}y^j$, and writing

$$\sqrt{2t+t^2} = (2t)^{1/2}\left(1+\frac{t}{2}\right)^{1/2},$$

followed by the generalized binomial series $(1+x)^r = \sum_{k=0}^{\infty}\binom{r}{k}x^k$ (for $|x|<1$), we obtain

$$\begin{aligned}
F(\hat{\nu}) &= \frac{e^{-1/2}}{2b}\sum_{i=0}^{\infty}\frac{(-1)^i}{2^i i!}\sum_{j=0}^{i}\binom{i}{j}\int_{a^2}^{(a+b\hat{\nu})^2} t^{-1/2}\,t^{i-j}\,(2t+t^2)^{j/2}\,dt \\
&= \frac{e^{-1/2}}{2b}\sum_{i=0}^{\infty}\frac{(-1)^i}{2^i i!}\sum_{j=0}^{i}\binom{i}{j}2^{j/2}\int_{a^2}^{(a+b\hat{\nu})^2} t^{-\frac{1}{2}+i-\frac{j}{2}}\left(1+\frac{t}{2}\right)^{j/2} dt \\
&= \frac{e^{-1/2}}{2b}\sum_{i=0}^{\infty}\frac{(-1)^i}{2^i i!}\sum_{j=0}^{i}\binom{i}{j}2^{j/2}\int_{a^2}^{(a+b\hat{\nu})^2} t^{-\frac{1}{2}+i-\frac{j}{2}}\sum_{k=0}^{\infty}\binom{j/2}{k}\left(\frac{t}{2}\right)^k dt.
\end{aligned}$$

Interchanging summation and integration (under the assumed convergence conditions) and evaluating the resulting power integrals yield the series representation

$$F(\hat{\nu}) = \frac{e^{-1/2}}{b}\sum_{i=0}^{\infty}\sum_{j=0}^{i}\sum_{k=0}^{\infty}\binom{i}{j}\binom{j/2}{k}\frac{(-1)^i\,2^{j/2-i-k}}{i!}\,\frac{(a+b\hat{\nu})^{1+2(i+k)-j}-a^{1+2(i+k)-j}}{1+2(i+k)-j}. \tag{4.3.18}$$

For computational convenience, we assume $|a|<1$ and $|a+b|<1$, so that the series representation (4.3.18) may be truncated after the leading terms and higher-order powers of a and $(a+b\hat{\nu})$ can be neglected. Under this approximation, retaining the contribution corresponding to ($i=0,1;\ k=0$) yields an explicit closed-form expression for the cdf:

$$F(\hat{\nu}) = -\frac{e^{-1/2}}{2\sqrt{2}\,b}\left[(a+b\hat{\nu})^2-a^2\right]. \tag{4.3.19}$$

Next, by equating the spatial cdf model (4.3.15) with the FDE-based cdf (4.3.19), we obtain the closed-form expression for the normalized velocity profile:

$$\hat{\nu} = \frac{1}{b}\left[-a \pm \sqrt{a^2 - 2\sqrt{2}\,b\,e^{1/2}\left(\frac{y}{M}\right)^k}\,\right]. \tag{4.3.20}$$

Equation (4.3.20) represents the FDE-based dimensionless vertical velocity distribution in wide open channels under the assumption that the maximum velocity occurs at the free surface (i.e., neglecting the dip phenomenon), and is therefore applicable to the central region of such flows.

The admissible branch and parameter range are chosen so that the discriminant remains nonnegative and $\hat{\nu} \in [0,1]$ for $y \in [0,M]$. To ensure an increasing velocity profile and the boundary condition $\hat{\nu}(0) = 0$, we select the negative branch in (4.3.20) and require $a \leq 0$, yielding

$$\hat{\nu}(y) = \frac{1}{b}\left[-a - \sqrt{a^2 - 2\sqrt{2}\,b\,e^{1/2}\left(\frac{y}{M}\right)^k}\,\right]. \tag{4.3.21}$$

$a^2 - 2\sqrt{2}\,b\,e^{1/2}\left(\frac{y}{M}\right)^k \geq 0$ for all $y \in [0,M]$, which is ensured by $a^2 \geq 2\sqrt{2}\,b\,e^{1/2}$. Finally, the spatial cdf model $F(\hat{\nu}) = (y/M)^k$ is increasing for $k > 0$ (and we take $k \in (0,1]$). The resulting formulation (4.3.21) generalizes the classical Shannon entropy-based velocity models and provides a flexible probabilistic framework for capturing the variability of turbulent open-channel flows through FDE.

4.3.3 Determination of Lagrange multipliers

The FDE-based normalized velocity profile (4.3.21) involves three unknown parameters, namely the Lagrange multipliers a and b, and the spatial fitting parameter k. The parameter k is estimated independently from the spatial cdf relation (4.3.15) using regression (least squares) on observed $(y/M, F)$ data. The multipliers a and b are determined by enforcing the normalization and mean constraints (4.3.2)–(4.3.3) using the entropy-maximizing pdf $f(\hat{\nu})$ obtained for $\alpha = \frac{1}{2}$ in (4.3.13).

Constraint (1): Normalization. Substituting (4.3.13) into (4.3.2) gives

$$\int_0^1 f(\hat{\nu})\,d\hat{\nu} = \int_0^1 \exp\left(-\left[\frac{(a+b\hat{\nu}) + \sqrt{(a+b\hat{\nu})^2+2}}{2}\right]^2\right)\,d\hat{\nu}.$$

Using the change of variables $t = (a + b\hat{\nu})^2$ and the identity

$$\left[\frac{(a + b\hat{\nu}) + \sqrt{(a + b\hat{\nu})^2 + 2}}{2}\right]^2 = \frac{(1 + t) + \sqrt{2t + t^2}}{2},$$

we obtain

$$\int_0^1 f(\hat{\nu})\, d\hat{\nu} = \frac{e^{-1/2}}{2b} \int_{a^2}^{(a+b)^2} t^{-1/2} \exp\left[-\frac{t + \sqrt{2t + t^2}}{2}\right] dt. \tag{4.3.22}$$

Proceeding as in the derivation of the FDE-based cdf expansion (4.3.18), the left-hand side of (4.3.22) admits the triple-series representation

$$\int_0^1 f(\hat{\nu})\, d\hat{\nu} = \frac{e^{-1/2}}{b} \sum_{i=0}^{\infty} \sum_{j=0}^{i} \sum_{k=0}^{\infty} \binom{i}{j} \binom{j/2}{k} \frac{(-1)^i\, 2^{\frac{j}{2}-k-i}}{i!} \frac{(a + b)^{1+2i-j+2k} - a^{1+2i-j+2k}}{1 + 2i - j + 2k}. \tag{4.3.23}$$

Imposing the normalization condition $\int_0^1 f(\hat{\nu})\, d\hat{\nu} = 1$ yields

$$\sum_{i=0}^{\infty} \sum_{j=0}^{i} \sum_{k=0}^{\infty} \binom{i}{j} \binom{j/2}{k} \frac{(-1)^i\, 2^{\frac{j}{2}-k-i}}{i!} \frac{(a + b)^{1+2i-j+2k} - a^{1+2i-j+2k}}{1 + 2i - j + 2k} = b\, e^{1/2}. \tag{4.3.24}$$

For computational convenience, we adopt the same small-parameter approximation used in Section 4.3.2, namely $|a| < 1$ and $|a + b| < 1$, and truncate (4.3.24) by retaining only the lowest-order terms (corresponding to $i = 0, 1$ and $k = 0$). This leads to the linear relation

$$b + 2a = -2\sqrt{2}\, e^{1/2}. \tag{4.3.25}$$

Constraint (2): Mean (first moment). Substituting (4.3.13) into (4.3.3) gives

$$\int_0^1 \hat{\nu}\, f(\hat{\nu})\, d\hat{\nu} = \int_0^1 \hat{\nu} \exp\left(-\left[\frac{(a + b\hat{\nu}) + \sqrt{(a + b\hat{\nu})^2 + 2}}{2}\right]^2\right) d\hat{\nu}. \tag{4.3.26}$$

With the substitution $t = a + b\hat{\nu}$ (so that $\hat{\nu} = (t - a)/b$ and $d\hat{\nu} = dt/b$), (4.3.26) becomes

$$\begin{aligned} \int_0^1 \hat{\nu}\, f(\hat{\nu})\, d\hat{\nu} &= \frac{1}{b} \int_a^{a+b} \left(\frac{t - a}{b}\right) \exp\left(-\left[\tfrac{t+\sqrt{t^2+2}}{2}\right]^2\right) dt \\ &= \frac{e^{-1/2}}{b^2} \left[\int_a^{a+b} t \exp\left(-\frac{t^2 + \sqrt{2t^2 + t^4}}{2}\right) dt - a \int_a^{a+b} \exp\left(-\frac{t^2 + \sqrt{2t^2 + t^4}}{2}\right) dt\right]. \end{aligned} \tag{4.3.27}$$

Denote

$$I_1 := \int_a^{a+b} t \exp\left(-\frac{t^2 + \sqrt{2t^2 + t^4}}{2}\right) dt. \tag{4.3.28}$$

Expanding the exponential term as in the cdf derivation yields

$$I_1 = \sum_{i=0}^{\infty} \frac{(-1)^i}{2^i i!} \sum_{j=0}^{i} \binom{i}{j} \int_a^{a+b} t^{\,1+2(i-j)} \, (2t^2 + t^4)^{j/2} \, dt, \tag{4.3.29}$$

and a similar series representation can be obtained for the second integral in (4.3.27). Finally, enforcing the mean constraint $\int_0^1 \hat{\nu} f(\hat{\nu})\, d\hat{\nu} = \hat{\nu}_m$ provides a second equation in a and b, which, together with (4.3.25), determines the multipliers for the adopted approximation scheme.

Assume $|a| < 1$ and $|a+b| < 1$. Since $0 \le \hat{\nu} \le 1$, it follows that $t = a + b\hat{\nu}$ satisfies $|t| < 1$ on $[0,1]$, and hence $\left|\frac{t^2}{2}\right| < 1$. Using this, we expand the exponential term in (4.3.27) as in the previous subsection. In particular, for

$$I_1 = \int_a^{a+b} t \, \exp\!\left(-\frac{t^2 + \sqrt{2t^2 + t^4}}{2} \right) dt,$$

we obtain

$$\begin{aligned}
I_1 &= \sum_{i=0}^{\infty} \frac{(-1)^i}{2^i i!} \sum_{j=0}^{i} \binom{i}{j} \int_a^{a+b} t^{\,1+2(i-j)+j} \, 2^{j/2} \left(1 + \frac{t^2}{2}\right)^{j/2} dt, \qquad \left|\frac{t^2}{2}\right| < 1 \\
&= \sum_{i=0}^{\infty} \frac{(-1)^i}{2^i i!} \sum_{j=0}^{i} \binom{i}{j} \sum_{k=0}^{\infty} \binom{j/2}{k} 2^{j/2-k} \int_a^{a+b} t^{\,1+2i-j+2k} \, dt \\
&= \sum_{i=0}^{\infty} \sum_{j=0}^{i} \sum_{k=0}^{\infty} \binom{i}{j} \binom{j/2}{k} \frac{(-1)^i \, 2^{j/2-i-k}}{i!} \, \frac{(a+b)^{2(1+i+k)-j} - a^{2(1+i+k)-j}}{2(1+i+k)-j}.
\end{aligned} \tag{4.3.30}$$

Similarly, for

$$I_2 = \int_a^{a+b} \exp\!\left(-\frac{t^2 + \sqrt{2t^2 + t^4}}{2} \right) dt,$$

we have

$$\begin{aligned}
I_2 &= \sum_{i=0}^{\infty} \frac{(-1)^i}{2^i i!} \sum_{j=0}^{i} \binom{i}{j} \int_a^{a+b} t^{\,2(i-j)+j} \, 2^{j/2} \left(1 + \frac{t^2}{2}\right)^{j/2} dt, \qquad \left|\frac{t^2}{2}\right| < 1 \\
&= \sum_{i=0}^{\infty} \frac{(-1)^i}{2^i i!} \sum_{j=0}^{i} \binom{i}{j} \sum_{k=0}^{\infty} \binom{j/2}{k} 2^{j/2-k} \int_a^{a+b} t^{\,2i-j+2k} \, dt \\
&= \sum_{i=0}^{\infty} \sum_{j=0}^{i} \sum_{k=0}^{\infty} \binom{i}{j} \binom{j/2}{k} \frac{(-1)^i \, 2^{j/2-i-k}}{i!} \, \frac{(a+b)^{1+2(i+k)-j} - a^{1+2(i+k)-j}}{1+2(i+k)-j}.
\end{aligned} \tag{4.3.31}$$

Substituting (4.3.30)–(4.3.31) into the mean constraint (4.3.27),

$$\int_0^1 \hat{\nu} f(\hat{\nu}) \, d\hat{\nu} = \frac{e^{-1/2}}{b^2} \big(I_1 - a I_2 \big) = \hat{\nu}_m,$$

yields the nonlinear relation

$$\sum_{i=0}^{\infty}\sum_{j=0}^{i}\sum_{k=0}^{\infty}\binom{i}{j}\binom{j/2}{k}\frac{(-1)^i\ 2^{j/2-i-k}}{i!}\cdot\left[\left(\frac{(a+b)^{2(1+i+k)-j}-a^{2(1+i+k)-j}}{2(1+i+k)-j}\right)\right.$$
$$\left.-a\left(\frac{(a+b)^{1+2(i+k)-j}-a^{1+2(i+k)-j}}{1+2(i+k)-j}\right)\right]=b^2e^{1/2}\hat{\nu}_m. \tag{4.3.32}$$

Finally, under the same small-parameter approximation $|a| < 1$ and $|a + b| < 1$, truncating (4.3.32) to the leading terms (corresponding to $i = 0, 1$ and $k = 0$) yields a second linear relation between a and b:

$$3a + 2b = -6\sqrt{2}\,e^{1/2}\hat{\nu}_m. \tag{4.3.33}$$

Therefore, within the adopted truncation scheme, the Lagrange multipliers a and b are obtained by solving the linear system (4.3.25) and (4.3.33), which in turn provides a simplified closed-form model for the normalized velocity distribution $\hat{\nu}$. This assumption is introduced solely to justify truncation of the series expansions and obtain an explicit closed-form approximation.

Remark 4.3.1. *Classical hydraulic models such as the logarithmic law, power-law velocity distribution, and empirical semi-theoretical profile relations are usually inexpensive to evaluate once the required hydraulic parameters, such as shear velocity, roughness length, friction factor, or empirical constants, are already known. Their computational cost is therefore low for direct profile evaluation. However, their practical use often depends on flow-regime assumptions, calibration of empirical coefficients, and the availability of reliable hydraulic input parameters. In more detailed deterministic hydraulic models, especially those based on turbulence closure or numerical solution of the governing flow equations, the computational effort increases substantially because iterative solvers, boundary-condition treatment, and mesh-dependent discretization are required.*

In comparison, the proposed FDE-based model does not require the numerical solution of the full governing turbulent-flow equations. Its main computational steps are: evaluation of the entropy-based probability density function, estimation of the spatial fitting parameter k, solution of a small system of equations for the Lagrange multipliers a and b, and computation of the velocity profile over the selected vertical grid points. Thus, if m denotes the number of measured vertical points, the profile evaluation cost is essentially of order $O(m)$ once the parameters are known. The parameter estimation step is also low-dimensional because only a few parameters are involved. Therefore, the FDE-based *formulation has modest computational cost. It is more flexible than fixed-form classical velocity-profile laws, but far less expensive than full numerical turbulent-flow simulations.*

4.3.4 Validation of model with experimental and field data

The one-dimensional velocity distribution (4.3.20) derived from FDE (4.2.1) are investigated using a set of laboratory data collected by Einstein and Chien (1955) and field data collected by Afzalmehr (2008) for channels in Iran. The data sets can be found in Luo (2009). There are 4 sets of velocity data which were used in this study.

The experimental data collected by Einstein and Chien (1955) were used to analyze the effect of suspended sediment and the roughness of channel bed on the velocity profile near the channel bed. Among a total of 29 runs, 13 were conducted with clear water and the remaining 16 were made with sediment-laden flow. The experiments were conducted in a painted steel flume with a width of 1.006 ft, depth of 1.17 ft and a length of 40 ft. The slope was adjusted with the help of a jack and made to vary within the range 0.0185 to 0.025. The water depth ranged from 0.36 to 0.49 ft and the average velocity of different runs fluctuated from 6.1 ft/s to 8.7 ft/s. Data from rivers in Iran was gathered from wide rectangular channels with clear flow, with observations spanning the entire water depth (Afzalmehr, 2008). Five runs were conducted to evaluate the overall performance of the FDE entropy-based velocity distribution.

To assess the feasibility and validity of the proposed FDE-based velocity distribution model (4.3.21), we adopt a two-stage validation strategy. In the first stage, the FDE-based cumulative distribution function derived from the pdf of the normalized velocity r.v $\hat{\mathcal{V}}$, given by (4.3.19), is fitted to the hypothesized spatial cdf (4.3.15) using the least-squares method. Specifically, for a given dataset consisting of normalized vertical coordinates $\{y_i/M\}_{i=1}^N$ and the corresponding empirical cumulative probabilities $\{F_i\}_{i=1}^N$, the fitting parameter k is estimated by minimizing the objective function

$$\mathcal{J}(k) = \sum_{i=1}^{N} \left[F(\hat{\nu}_i) - \left(\frac{y_i}{M}\right)^k \right]^2, \tag{4.3.34}$$

where $F(\hat{\nu}_i)$ denotes the FDE-based cdf values computed from (4.3.19). The minimization of (4.3.34) yields the optimal estimate of the spatial parameter k, which captures the influence of flow structure and suspended sediment characteristics on the vertical velocity distribution. The resulting best-fit curve, along with the corresponding data points, is illustrated in Fig. 4.3.2.

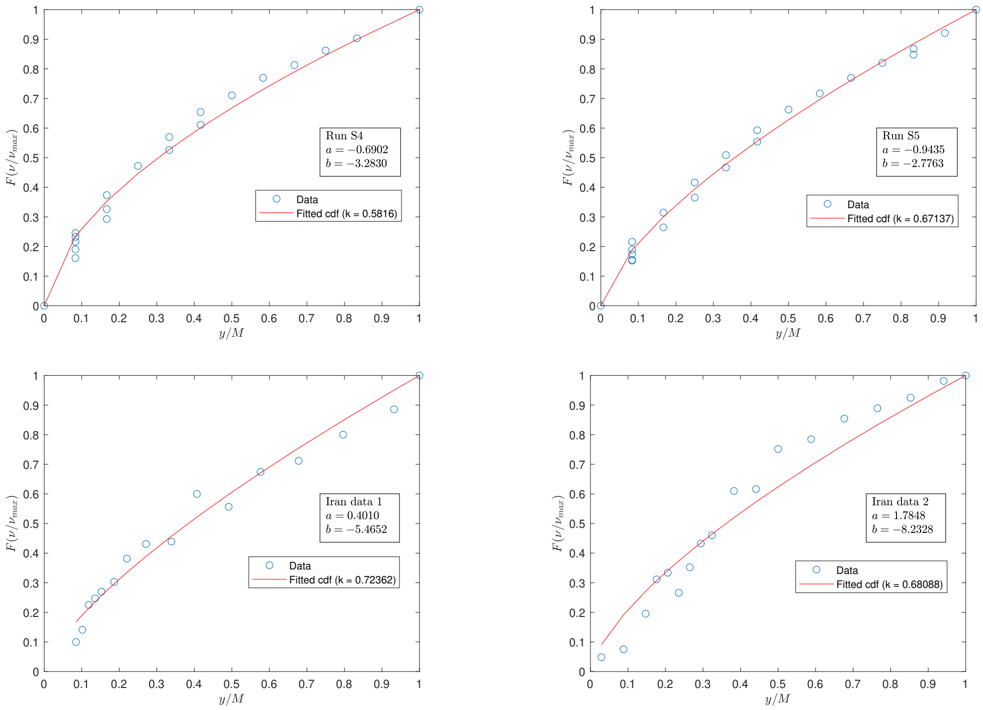

Figure 4.3.2: Validation of the fitted hypothetical cdf (4.3.15) with the computed cdf (4.3.19) for Einstein & Chien and Iran series data of Luo.

In the second stage of validation, the estimated value of k is substituted into the closed-form FDE-based velocity distribution (4.3.21). The predictive performance of the resulting model is then evaluated using selected experimental and field datasets by examining the relationship between the normalized dimensionless velocity $\hat{\nu}$ and the normalized vertical coordinate y/M. The comparison between the observed data and the model-predicted velocity profiles is presented in Fig. 4.3.3, thereby demonstrating the applicability of the proposed FDE-based framework for modeling vertical velocity distributions in wide open channels. Subsequently, the estimated value of k is incorporated into the FDE-based velocity distribution (4.3.21), and the predictive performance of the resulting model is evaluated using experimental and field measurements of the normalized velocity $\hat{\nu}$ and normalized depth y/M, as shown in Fig. 4.3.3.

To quantitatively assess the quality of the least-squares fit, standard regression analysis is performed between the computed velocity values obtained from (4.3.21) and the observed normalized velocities $\hat{\nu} = \nu/\nu_{\max}$ to validate the close agreement between the model predictions and observations. In particular, the coefficient of determination (R^2)

is computed. The coefficient of determination or regression coefficient (R^2) is given by

$$R^2 = 1 - \frac{\sum_{i=1}^{N}\left[F(\hat{\nu}_i) - \left(\frac{y_i}{M}\right)^k\right]^2}{\sum_{i=1}^{N}\left[F(\hat{\nu}_i) - \overline{F}\right]^2}, \tag{4.3.35}$$

where $\overline{F} = \frac{1}{N}\sum_{i=1}^{N} F(\hat{\nu}_i)$ denotes the sample mean of the FDE-based cdf values. R^2 values close to unity indicate a superior fit of the proposed spatial cdf to the FDE-based cumulative distribution.

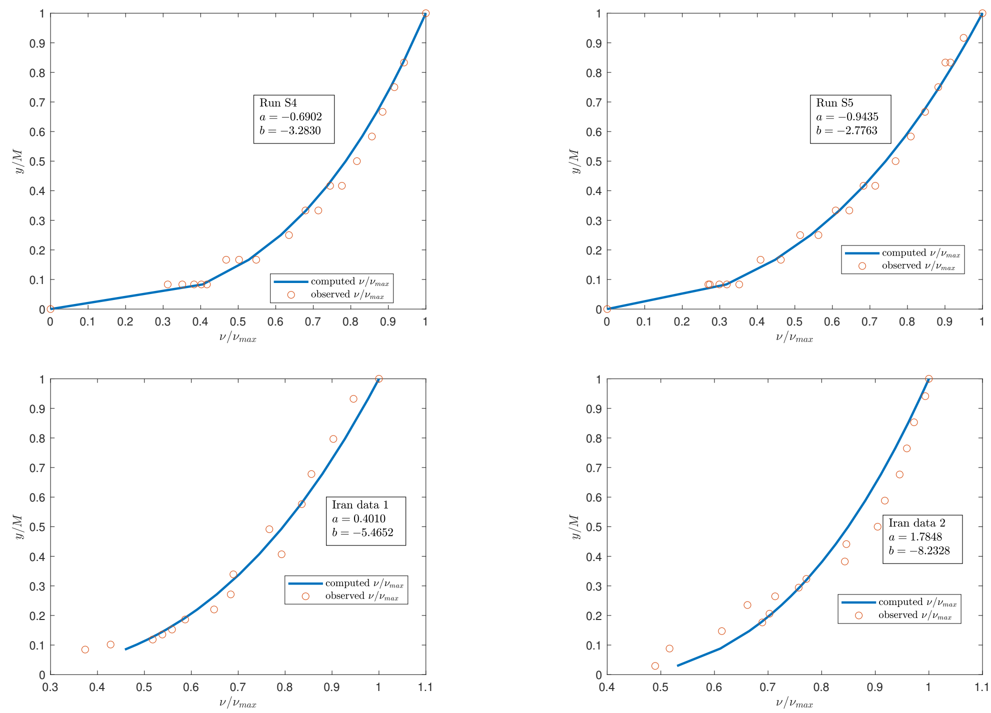

Figure 4.3.3: Normalized velocity (ν/ν_{max}) with respect to normalized height (y/M).

The corresponding correlation plots are presented in Fig. 4.3.4. The accuracy and reliability of the proposed one-dimensional vertical velocity model are strongly supported by the high values of R^2, which range from 0.97233 to 0.99996 across the selected datasets. The closeness of these values to unity indicates an excellent correlation between the observed and computed velocities, thereby demonstrating the strong predictive capability of the proposed FDE-based velocity distribution model. These quantitative measures, together with the visual agreement illustrated in Fig. 4.3.2, confirm the robustness of the least-squares estimation of the parameter k.

Next, to examine the influence of the Lagrange multipliers on the velocity distribution, the normalized velocity $\hat{\nu}$ is plotted against the normalized vertical coordinate y/M for

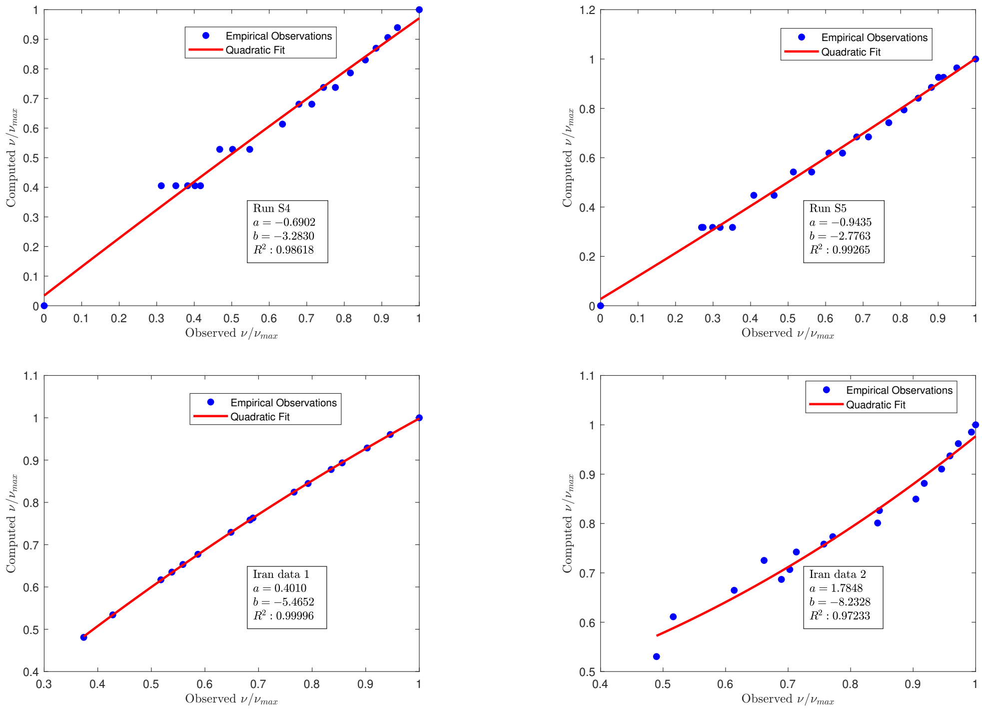

Figure 4.3.4: Regression analysis for computed ν/ν_{max} with respect to observed ν/ν_{max}.

the selected datasets, as shown in Figs. 4.3.5 and 4.3.6. In this analysis, one Lagrange multiplier is varied while the other is held fixed for a given dataset, allowing the individual effects of each multiplier on the velocity profile to be isolated. From Figs. 4.3.5 and 4.3.6, it is observed that the vertical velocity distribution exhibits a higher sensitivity to variations in the Lagrange multiplier a, which is associated with the normalization constraint. In particular, for identical magnitudes of perturbation in the multipliers, changes in a lead to more pronounced fluctuations in the gradient of the velocity profile with respect to the normalized height y/M. This behavior indicates that the normalization-related constraint plays a dominant role in shaping the curvature and overall structure of the FDE-based velocity distribution.

For further validation, we have compared the current FDE-based velocity distribution model (4.3.21) with the existing entropy-based models with maximum surface velocity referred to as the Chiu (Shannon entropy), SL (Tsallis entropy), KG (Rényi entropy) and KT 1 and KT 2 (fractional Machado entropy) models defined in Chiu (1987), Singh and Luo (2011), Kumbhakar and Ghoshal (2016) and Kumbhakar and Tsai (2023), respectively. For this purpose, we have done error analysis for the normalized velocity $\hat{\nu}$. The types of errors considered in this study for comparison purpose have been defined in

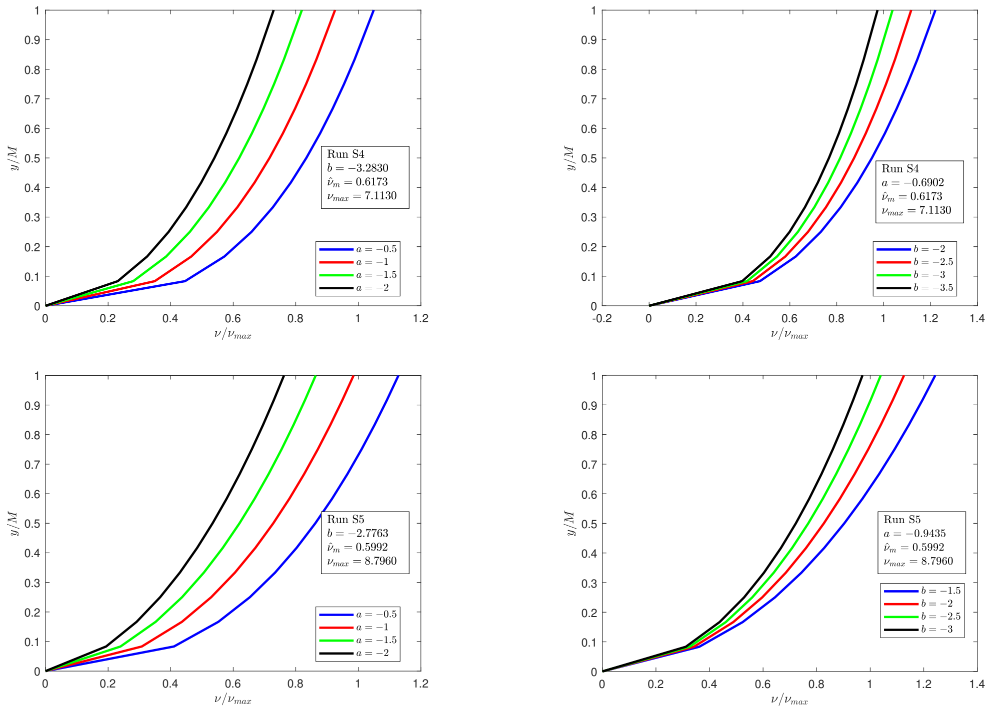

Figure 4.3.5: Variation of normalized flow velocity with Lagrange multipliers for Einstein and Chien data.

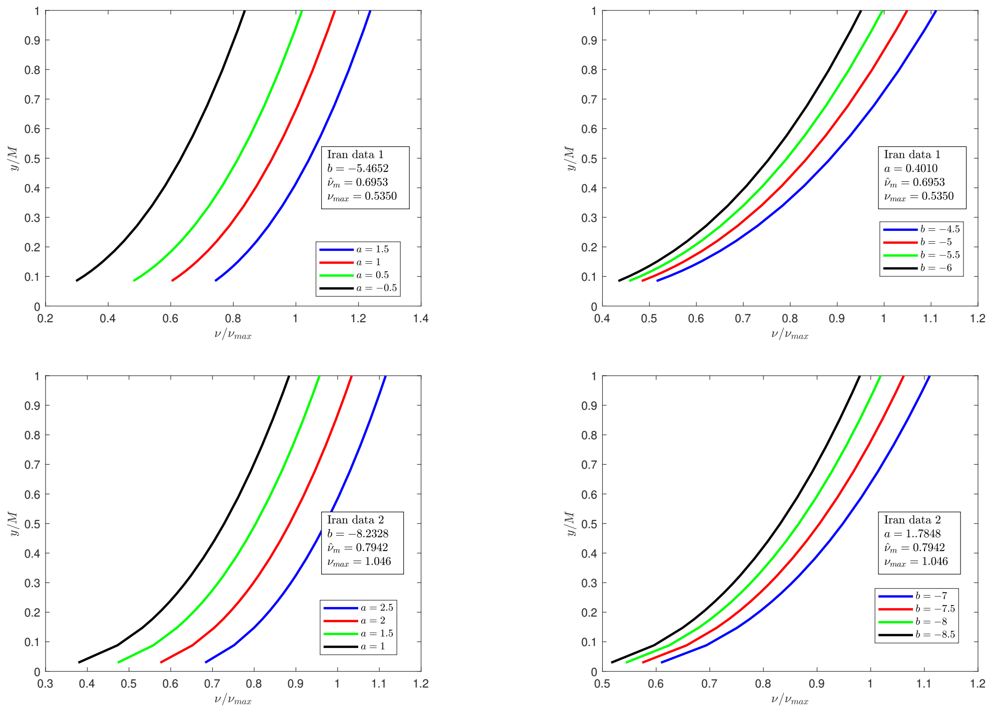

Figure 4.3.6: Variation of normalized flow velocity with Lagrange multipliers for Iran series data of Luo.

Table 4.3.1: Comparison of the present model with other vertical profile of velocity distribution models

SSC models	Proposed model	Chiu model	SL model	KG model	KT model 1	KT model 2
Run S4 of Einstein & Chien data						
MRAE	0.0529	0.0291	0.1046	0.0264	0.0880	0.0239
RMSE	0.0340	0.0142	0.0456	0.0125	0.0381	0.0114
Run S5 of Einstein & Chien data						
MRAE	0.0449*	0.0607	0.1241	0.0530	0.1330	0.0499
RMSE	0.0243	0.0265	0.0460	0.0240	0.0495	0.0234
Iran series 1 of Luo data						
MRAE	0.0456	0.0475	0.0484	0.0479	0.0889	0.0450
RMSE	0.0336*	0.0381	0.0422	0.0393	0.0601	0.0363
Iran series 2 of Luo data						
MRAE	0.0417*	0.0675	0.0775	0.0690	0.0639	0.0622
RMSE	0.0384*	0.0641	0.0658	0.0634	0.0588	0.0584

Note: * indicates the minimum values of each of the errors for a given data source.

Kumbhakar and Tsai (2023). The errors can be described as follows:

- Mean relative absolute error (MRAE) $= \frac{1}{n}\sum_{k=1}^{n} \frac{\left|\hat{\nu}_{k(comp)} - \hat{\nu}_{k(obs)}\right|}{\hat{\nu}_{k(obs)}}$

- Root-mean-square error (RMSE) $= \sqrt{\dfrac{1}{n}\displaystyle\sum_{k=1}^{n}(\hat{\nu}_{k(comp)} - \hat{\nu}_{k(obs)})^2}$,

where n is the total number of data points in a particular data set, $\hat{\nu}_{k(comp)}$ and $\hat{\nu}_{k(obs)}$ denote the computed and observed concentration of sediment at the k^{th} data point. These errors measures the average deviation between the FDE-based velocity values and the observed values of a particular dataset.

We show that our model has minimum errors for most of the data sets. The KT model 2 with the momentum coefficient β obtained from eqn. (29) of Kumbhakar and Tsai (2023) also shows better results in many cases as indicated in Table 4.3.1. In conclusion, both our proposed model and KT Model 2 outperform other existing entropy-based models that rely on the maximum surface velocity assumption, demonstrating their superiority. However, KT Model 2 requires the estimation of additional parameters when determining the Lagrange multipliers, making it more complex. In contrast, our model offers a simplified approach by computing the Lagrange multipliers through a system of linear equations. Additionally, our model demonstrates greater efficiency in supporting field data. Therefore, compared to KT Model 2, our proposed model is both simpler and more effective.

The S4 and S5 datasets of Einstein and Chien (1955) are selected deliberately and not randomly. These datasets provide clear and reliable measurements for testing the proposed FDE-based suspended sediment concentration model. Since they correspond to relatively coarse sediment conditions, they are useful for examining whether the entropy-based formulation can capture stronger near-bed concentration variation and sharper vertical concentration gradients.

At the same time, this choice limits the range of sediment conditions examined in the present study. Medium and fine sand datasets may exhibit different suspension behaviour, weaker settling effects, and smoother concentration profiles. Therefore, extending the validation to medium and fine sand data from Einstein and Chien (1955), as well as other benchmark sediment datasets, would be useful for testing the robustness of the model across a wider range of particle-size regimes and flow conditions.

4.4 Conclusion

Entropy serves as a fundamental quantitative measure of randomness and uncertainty associated with real-world stochastic phenomena, such as the hydraulic velocity field investigated in this study. Among the various entropy formulations available in the literature, the FDE, defined in terms of the pdf, was adopted owing to its enhanced flexibility and robustness in characterizing complex systems. Closed-form analytical expressions of FDE were derived for several commonly used univariate distributions in reliability and survival analysis. For distributions where explicit expressions were not attainable, rigorous bounds and monotonicity properties of FDE were established, thereby providing valuable theoretical insights into its behavior.

Building upon this theoretical framework, the FDE formulation was employed to derive a one-dimensional vertical velocity distribution model for turbulent flows in wide open channels, assuming the maximum velocity to occur at the free surface. The model was constructed using the principle of maximum entropy proposed by Jaynes, enabling the incorporation of physical constraints in a probabilistically consistent manner. The fractional parameter α was shown to play a crucial role in capturing the intrinsic variability and uncertainty inherent in hydrological data, thereby offering additional modeling flexibility compared to classical entropy-based approaches. A one-parameter spatial cdf was used to relate the velocity distribution to the normalized flow depth, with the fitting parameter k accounting for the influence of sediment characteristics and flow structure. Furthermore, a simplified yet effective procedure for determining the Lagrange multipliers was developed using a leading term approximation technique, significantly reducing computational complexity relative to conventional deterministic and entropy-based models.

The proposed FDE-based velocity distribution model was validated using both experimental and field data, yielding low error measures and consistently high regression coefficients. Comparative analyses with existing entropy-based models demonstrated superior predictive performance, particularly for field datasets. These results establish FDE as an effective and versatile tool for modeling vertical velocity profiles in open-channel flows, with strong potential for broader applications in hydraulics and complex system analysis.

The present FDE-based velocity model has been developed and validated mainly for free-surface open-channel flows where the maximum velocity occurs near the free surface, which is a common approximation for wide channels. Hence, in its current form, the model is most directly applicable to wide or moderately wide channels without strong secondary currents or surface constraints.

For narrow channels, sidewall effects and secondary currents may produce a dip phenomenon, where the maximum velocity occurs below the free surface. To extend the present entropy-based formulation to such cases, an additional constraint or shape parameter representing the dip location would be required, together with a modified coordinate transformation or boundary condition. For ice-covered channels, the upper boundary is no longer shear-free; the ice cover introduces additional roughness and shear stress. In that case, the optimization framework would need to include modified upper-boundary conditions reflecting both bed and ice-cover resistance. These extensions are outside the scope of the present chapter, but they provide useful directions for future research.

Chapter 5

Modeling of Vertical Distribution of Suspended Sediment Concentration in Open Channel Turbulent Flows using Fractional Differential Entropy [1]

"Truth is much too complicated to allow anything but approximations."
— John von Neumann

The vertical distribution of suspended sediment concentration (SSC) is governed by the flow velocity structure, as velocity gradients and turbulence control sediment entrainment and suspension. Building on the FDE-based vertical velocity distribution developed in the previous chapter, this study extends the same entropy framework to sediment transport in open channel flows. SSC is treated as a continuous random variable with a physically realistic zero-concentration condition at the water surface, and a simplified maximum entropy formulation yields a closed-form SSC profile. The proposed model is validated using laboratory and field data, showing improved accuracy and computational efficiency over existing methods, with robustness of estimated parameter confirmed through bootstrap and jackknife resampling techniques.

[1] A manuscript containing the work presented here is under review in *Journal of Hydraulic Engineering* and is archived with the DOI: *https://arxiv.org/abs/2507.05986*.

5.1 Introduction

A sound understanding of sediment-laden flow dynamics is essential for river engineering, water resources planning, and environmental management. In open-channel systems such as rivers, irrigation canals, and estuaries, sediment transport primarily occurs in two forms: bed load, which consists of relatively coarse particles moving close to the channel bed, and suspended load, comprising finer particles maintained within the flow by turbulent motion (Dey, 2012). The boundary separating these two transport modes is commonly defined by a reference level, which plays a central role in modeling sediment transport processes.

Among the various aspects of sediment dynamics, the vertical distribution of SSC has attracted sustained attention. SSC data are continuous physical profiles governed by vertical gradients, near-bed concentration dominance, and turbulent mixing. Reliable prediction of the vertical SSC profile is critical not only for estimating sediment fluxes but also for assessing water quality, evaluating aquatic ecosystem health, and understanding sediment-related hazards during extreme events such as floods. Numerous deterministic models have been proposed to describe vertical SSC distributions (see Chanson, 2004; Mazumder and Ghoshal, 2006; Dey, 2014; Kundu and Ghoshal, 2014; Kundu, 2015, for further details). Among these, the classical Rouse model (Rouse, 1937) remains one of the most widely used formulations for uniform, sediment-laden turbulent flows.

The Rouse model,

$$\frac{c}{c_r} = \left[\frac{(y_* - y)}{y}\frac{r}{(y_* - r)}\right]^{R_0}, \tag{5.1.1}$$

is derived from a balance between downward gravitational settling and upward turbulent diffusion of sediment particles. In this expression, y_* denotes the total flow depth, c_r is the reference concentration at the level $y = r = 0.05y_*$ and R_0 represents the Rouse number. Although this model has served as a foundational tool in sediment transport studies, its predictive capability deteriorates near the bed and close to the free surface, where the assumptions of equilibrium flow and logarithmic velocity profiles are no longer valid. In addition, deterministic approaches often require extensive calibration data, which restricts their applicability in data-scarce environments.

In recent years, entropy-based formulations have emerged as effective probabilistic alternatives to deterministic SSC models. Rooted in the principle of maximum entropy (Jaynes, 1957a,b) and following the seminal work of Chiu (1987), these approaches require fewer assumptions, naturally incorporate uncertainty, and are better suited to complex and variable flow conditions. Several extensions of the classical Shannon entropy framework, including Tsallis, Rényi, and other generalized entropy measures, have been successfully applied to sediment transport modeling (see Chiu, 1987; Chiu et al., 2000; Choo, 2000; Luo, 2009; Singh and Luo, 2011; Cui and Singh, 2014; Kumbhakar and Ghoshal, 2016; Ghoshal et. al, 2018; Ahamed and Kundu, 2023, for comprehensive reviews).

Notably, fractional entropy-based models have demonstrated superior performance in situations where flow behavior exhibits non-extensivity or long-range correlations, characteristics commonly observed in turbulent open-channel flows (Ahamed and Kundu, 2023). Motivated by these findings, the present study focuses on *fractional differential entropy (FDE)*, a fractional generalization of Shannon differential entropy originally proposed by Ubriaco (2009) and subsequently extended to continuous domains by Foroghi et al. (2022). The inclusion of a fractional parameter introduces controlled non-additivity, thereby enhancing the model's ability to represent complex sediment–turbulence interactions.

The primary objective of this work is to derive a closed-form analytical expression for the vertical distribution of SSC in turbulent open-channel flows by combining the maximum entropy principle with the FDE framework. The formulation assumes a zero-concentration condition at the water surface and treats the normalized SSC as a continuous random variable (r.v). Particular emphasis is placed on Type I SSC profiles, in which sediment concentration increases from the free surface to a near-bed reference level before decreasing toward the channel bottom. The contribution of this chapter lies in using FDE within a structured entropy-optimization and parameter-estimation framework for modeling vertical SSC profiles with experimental and field validation.

The remainder of this thesis chapter is organized as follows. Section 5.2 presents the necessary preliminaries and reviews existing approaches to SSC modeling. Section 5.3 details the derivation of the FDE-based SSC distribution and introduces the resulting analytical model. Section 5.4 evaluates the performance of the proposed model using laboratory experiments and field observations, with comparisons against classical deterministic and entropy-based formulations. Section 5.5 examines the sensitivity of the model parameters through uncertainty analysis using bootstrap and jackknife resampling techniques. Finally, Section 5.6 summarizes the main findings, discusses the limitations of the proposed approach, and outlines directions for future research.

5.2 Preliminary concepts

The application of entropy theory to hydraulic and sediment transport problems has expanded significantly since the pioneering work of Chiu (1987), who first employed Shannon entropy to describe the probabilistic structure of flow variables. Following this approach, a range of entropy-based models has been developed to represent the vertical distribution of SSC in open-channel flows.

An early Shannon entropy–based formulation proposed by Chiu et al. (2000) expressed the vertical SSC profile as

$$\frac{c}{c_0} = \left[\frac{1-\frac{y}{D}}{1+(e^M-1)\frac{y}{D}}\right]^{\lambda'}; \quad \lambda' = \frac{\omega_s u_{max}(1-e^{-M})}{\beta u_* 2M}, \tag{5.2.1}$$

where ω_s denotes the particle settling velocity, u_* the shear velocity, M an entropy parameter governing the velocity distribution, D the flow depth, y the vertical distance from the bed, and c_0 the near-bed concentration. Although physically consistent, this model involves multiple parameters that are difficult to estimate in practical field applications, particularly when data availability is limited.

To enhance computational simplicity, Choo (2000) introduced a reduced Shannon entropy formulation given by

$$\frac{c}{c_0} = \frac{1}{N}\log\left[e^N - (e^N-1)\frac{y}{D}\right], \tag{5.2.2}$$

where N is an entropy parameter derived from the ratio of mean concentration (c_m) to near-bed concentration (c_0). While this formulation reduces the number of free parameters, it remains limited in its ability to capture the strong nonlinearity and variability of SSC profiles under highly turbulent flow conditions.

Recognizing these shortcomings, Cui and Singh (2014) extended the entropy framework by adopting Tsallis entropy and introducing a cumulative distribution function (cdf) to better represent nonlinear sediment dynamics:

$$\frac{c}{c_0} = 1 - \frac{1}{N}\left(1 - \left\{(1-N)^{\frac{m}{m-1}} + \left[1-(1-N)^{\frac{m}{m-1}}\right]F(c)\right\}^{\frac{m-1}{m}}\right), \tag{5.2.3}$$

where $F(c)$ denotes the assumed cdf and N is a dimensionless entropy parameter. Although this approach improves flexibility and accounts for long-tailed behavior, its reliance on empirically prescribed distribution functions reduces its general applicability.

Further generalization was achieved by Ghoshal et. al (2018) using Rényi entropy, allowing for non-zero sediment concentration at the water surface:

$$\frac{c}{c_a} = \frac{\mu}{1-\mu} + \left\{ \left(\frac{\mu}{\mu-1} + \hat{c}_D \right)^{m/(m-1)} + \left[\left(\frac{2\mu-1}{\mu-1} \right)^{m/(m-1)} - \left(\frac{\mu}{\mu-1} + \hat{c}_D \right)^{m/(m-1)} \right] [F(\hat{c})]^{(m-1)/m} \right\}, \tag{5.2.4}$$

with $m = 3/2$ and remaining parameters defined in Ghoshal et. al (2018). This formulation provides additional modeling flexibility but at the expense of increased mathematical and computational complexity.

More recently, Ahamed and Kundu (2023) employed fractional entropy in Wang's formulation and derived Type I and Type II SSC profiles using the Mittag-Leffler function. Their model successfully captured incomplete phase-space information, a characteristic feature of turbulent flows with long-range correlations, and showed improved agreement with experimental and field data. These results demonstrated that fractional order entropy models can outperform classical entropy formulations when system information is partial or highly irregular. A concise comparison of existing entropy-based SSC models is provided in Table 5.2.1.

Despite these developments, the application of FDE, a continuous-domain generalization of Ubriaco's fractional entropy, has received little attention in SSC modeling. FDE introduces a fractional parameter that induces non-additivity, allowing the representation of complex, non-extensive transport processes and potential long-range interactions. This makes FDE a promising yet largely unexplored framework for sediment transport modeling, particularly under data-sparse or highly variable flow conditions. Moreover, the vertical distribution of SSC is intrinsically linked to the vertical structure of flow velocity, since velocity gradients and turbulence intensity control sediment entrainment, upward diffusion, and settling. In classical deterministic formulations, this coupling is represented through eddy diffusivity and settling velocity balances, while in entropy-based approaches it is embedded indirectly through velocity-dependent constraints. The FDE-based velocity distribution developed in the previous chapter provides a physically consistent statistical description of turbulent flow structure. Extending this entropy framework to SSC allows velocity statistics to enter the sediment formulation in a natural and unified manner, thereby preserving flow-sediment coupling while avoiding ad hoc parameterization. This conceptual linkage motivates the use of FDE as a common framework for modeling both velocity and sediment concentration in turbulent open-channel flows.

Table 5.2.1: Summary of major entropy-based SSC distribution models in open-channel flows

Model & Reference	**Entropy Type**	**Core Concept / Formulation**	**Advantages**	**Eq. Ref.**
Chiu et al. (2000)	Shannon	SSC profile expressed via maximum entropy with velocity profile parameter M and near-bed concentration c_0; requires multiple flow and sediment parameters.	Theoretically rigorous; accommodates detailed velocity structure.	(5.2.1)
Choo (2000)	Shannon (simplified)	Logarithmic form with entropy parameter N from mean-to-bed concentration ratio; fewer input parameters.	Simplified computation; reduced data demand.	(5.2.2)
Cui and Singh (2014)	Tsallis	Uses CDF-based non-linear formulation; adaptable to non-extensive distributions.	Captures long-tailed, non-linear SSC profiles better than Shannon models.	(5.2.3)
Ghoshal et. al (2018)	Rényi	Considers non-zero surface concentration; combines non-linear height function with exponential form.	More realistic for Type II profiles; flexible shape control.	(5.2.4)
Ahamed and Kundu (2023)	Fractional entropy (Wang)	Employs Mittag–Leffler CDF; models incomplete phase-space information in turbulent conditions.	Effective for chaotic flows with long-range correlations; fits experimental/field data well.	—

5.3 Estimation of sediment concentration

The primary objective of this chapter is to derive an analytically tractable expression for the vertical distribution of SSC using the FDE framework within the principle of maximum entropy. The formulation is developed under physically meaningful constraints and is intended to represent SSC behavior in sediment-laden turbulent open-channel flows.

Let $\mathcal{C}$ denote the time-averaged sediment concentration, modeled as a r.v. For a Type I SSC profile, $\mathcal{C}$ attains a maximum value c_r at a reference elevation y_r near the channel bed, and then decreases with height, reaching a minimum value c_h (not necessarily zero) at the free surface $y = h$.

The FDE-based SSC distribution is derived through the following steps:

(i) define the FDE appropriate for SSC modeling;

(ii) prescribe constraint relations that represent known SSC properties and boundary information;

(iii) construct the Lagrangian functional by maximizing FDE subject to these constraints;

(iv) determine the Lagrange multipliers and obtain the pdf of $\mathcal{C}$;

(v) introduce a suitable cdf hypothesis to express SSC explicitly as a function of the vertical coordinate.

In what follows, we implement the above procedure to obtain a closed-form expression for the FDE-based SSC profile along the vertical water column of an open channel.

5.3.1 FDE for continuous random variables

The *Ubriaco fractional entropy* (Ubriaco, 2009), originally defined for discrete systems, is given by

$$H_U^\alpha(p) = \sum_{i=1}^{n} p(i) \left[-\log p(i) \right]^\alpha, \quad \alpha \in [0, 1], \tag{5.3.1}$$

where $p(i)$ denotes the probability associated with the ith outcome of a discrete r.v, and $\left[-\log p(i) \right]^\alpha$ represents the corresponding *fractional-order information content*. The fractional parameter α quantifies the degree of non-extensivity of the system. In the limiting case $\alpha = 1$, Eq. (5.3.1) reduces to the classical Shannon entropy.

Since the present study aims to describe SSC using a fractional entropy framework, the discrete formulation in Eq. (5.3.1) must be extended to continuous r.vs. To this end, we consider the *normalized* time-averaged sediment concentration

$$\hat{\mathcal{C}} = \frac{\mathcal{C}}{c_r} \in [\hat{c}_h,\, 1],$$

where c_r denotes the reference concentration at elevation $y = y_r$, and $\hat{c}_h$ represents the normalized concentration at the free surface $y = h$. The normalization of sediment concentration ensures that the support of the r.v $\hat{\mathcal{C}}$ is bounded within a finite interval, which is essential for meaningful entropy evaluation and comparison across different flow conditions. In contrast to unbounded differential entropy measures, the FDE for normalized concentration variable yields well-scaled entropy values whose variation is governed by the fractional parameter α. This property improves interpretability and numerical stability, particularly when entropy is used as a modeling constraint under limited or noisy data conditions.

The FDE of the continuous r.v $\hat{\mathcal{C}}$ is then defined as

$$H^{\alpha}(f) = \int_{\hat{c}_h}^{1} f(\hat{c}) \left[-\log f(\hat{c}) \right]^{\alpha} d\hat{c}, \tag{5.3.2}$$

where $f(\hat{c})$ denotes the pdf of $\hat{\mathcal{C}}$. The fractional parameter α introduces controlled non-additivity into the entropy measure, enabling the representation of non-extensive behavior and long-range correlations commonly observed in turbulent open-channel sediment transport.

5.3.2 Constraints for maximum entropy formulation

To model the vertical distribution of SSC in a physically consistent manner, appropriate constraints must be imposed on the pdf of the normalized concentration. In this study, the following fundamental constraints are considered:

$$\int_{\hat{c}_h}^{1} f(\hat{c})\, d\hat{c} = 1, \tag{5.3.3}$$

$$\int_{\hat{c}_h}^{1} \hat{c}\, f(\hat{c})\, d\hat{c} = \hat{c}_m, \tag{5.3.4}$$

where $\hat{c}_m = c_m/c_r$ denotes the normalized mean sediment concentration over the flow depth.

Constraint (5.3.3) enforces the *normalization condition*, ensuring that the total probability over the admissible concentration range equals unity. Constraint (5.3.4) represents the *mass conservation principle* for suspended sediment, prescribing the mean concentration of the vertical profile based on physical measurements or observations. Since infinitely many probability distributions can satisfy these two constraints, an additional criterion is required to select a unique and physically meaningful solution. Following the *Principle of Maximum Entropy* (POME) (Jaynes, 1957a), the least biased distribution, consistent with the available information, is obtained by maximizing the FDE defined in Eq. (5.3.2) subject to the above constraints. Although additional constraints may be introduced to incorporate higher-order moments or boundary effects, previous studies (Ahamed and Kundu, 2023) have demonstrated that the normalization and mean constraints alone are sufficient to yield accurate SSC predictions while maintaining analytical tractability and model simplicity.

The bounded support of the normalized concentration $\hat{\mathcal{C}} \in [\hat{c}_h, 1]$ ensures that the associated FDE remains well-scaled and finite. This boundedness plays an important role in parameter estimation, as it prevents excessive sensitivity of the Lagrange multipliers to small fluctuations or noise in the data. As a result, the estimated model parameters exhibit improved numerical stability and robustness, particularly when inferred from limited or heterogeneous laboratory and field measurements.

5.3.3 Lagrangian formulation and derivation of the pdf

We now determine the pdf that maximizes the Fractional Differential Entropy (FDE) defined in Eq. (5.3.2), subject to the normalization and mean-concentration constraints given in Eqs. (5.3.3) and (5.3.4). To this end, we construct the following Lagrangian functional:

$$\begin{aligned} L = \int_{\hat{c}_h}^{1} f(\hat{c}) \big[-\log f(\hat{c}) \big]^{\alpha} \, d\hat{c} + \lambda_0 \left[\int_{\hat{c}_h}^{1} f(\hat{c}) \, d\hat{c} - 1 \right] \\ + \lambda_1 \left[\int_{\hat{c}_h}^{1} \hat{c} \, f(\hat{c}) \, d\hat{c} - \hat{c}_m \right], \end{aligned} \tag{5.3.5}$$

where λ_0 and λ_1 are Lagrange multipliers associated with the normalization and mean-concentration constraints, respectively.

The optimal pdf is obtained by applying the Euler-Lagrange condition for functional maximization, with $f(\hat{c})$ as the dependent variable:

$$\frac{\partial L}{\partial f(\hat{c})} - \frac{d}{d\hat{c}} \left(\frac{\partial L}{\partial f'(\hat{c})} \right) = 0.$$

Since the Lagrangian does not depend on derivatives of $f(\hat{c})$, the second term vanishes, yielding the stationarity condition

$$\alpha\left[-\log f(\hat{c})\right]^{\alpha-1}-\left[-\log f(\hat{c})\right]^{\alpha}+\lambda_0+\lambda_1\hat{c}=0. \tag{5.3.6}$$

Equation (5.3.6) is nonlinear in $f(\hat{c})$ and, in general, requires numerical treatment. However, for the special case $\alpha=\frac{1}{2}$, the equation reduces to a quadratic form in $\sqrt{-\log f(\hat{c})}$, allowing an explicit analytical solution. The resulting pdf is given by

$$f(\hat{c})=\exp\left[-\frac{1+\left(\lambda_0+\lambda_1\hat{c}\right)^2 \pm \left(\lambda_0+\lambda_1\hat{c}\right)\sqrt{\left(\lambda_0+\lambda_1\hat{c}\right)^2+2}}{2}\right]. \tag{5.3.7}$$

The negative sign is selected to ensure positivity and proper normalization of the pdf. Accordingly, the final expression for the optimal pdf becomes

$$f(\hat{c})=\exp\left[-\frac{1+\left(\lambda_0+\lambda_1\hat{c}\right)^2 - \left(\lambda_0+\lambda_1\hat{c}\right)\sqrt{\left(\lambda_0+\lambda_1\hat{c}\right)^2+2}}{2}\right]. \tag{5.3.8}$$

Substituting Eq. (5.3.8) into the entropy definition (5.3.2), the corresponding FDE is expressed as:

$$\begin{aligned}H^{\alpha}(f)=\int_{\hat{c}_h}^{1}&\exp\left[-\frac{1+\left(\lambda_0+\lambda_1\hat{c}\right)^2 - \left(\lambda_0+\lambda_1\hat{c}\right)\sqrt{\left(\lambda_0+\lambda_1\hat{c}\right)^2+2}}{2}\right]\\ &\times\left(\frac{1+\left(\lambda_0+\lambda_1\hat{c}\right)^2 - \left(\lambda_0+\lambda_1\hat{c}\right)\sqrt{\left(\lambda_0+\lambda_1\hat{c}\right)^2+2}}{2}\right)^{\alpha} d\hat{c}.\end{aligned} \tag{5.3.9}$$

For a given dataset, the entropy in Eq. (5.3.9) can be evaluated numerically once the Lagrange multipliers λ_0 and λ_1 are determined. These multipliers are obtained by solving the nonlinear system formed by substituting Eq. (5.3.8) into the constraint equations (5.3.3) and (5.3.4).

The Lagrange multiplier λ_0 acts as a normalization parameter that adjusts the overall amplitude of the pdf to satisfy the total probability constraint. In physical terms, it reflects the baseline level of sediment concentration variability permitted by the available information. The multiplier λ_1 governs the linear dependence of the pdf on the normalized concentration $\hat{c}$ and is directly linked to the prescribed mean concentration $\hat{c}_m$. Physically, λ_1 controls the skewness and vertical gradient of the SSC profile, and can be interpreted as a statistical measure of the competition between downward settling and upward turbulent diffusion.

The choice of the fractional order $\alpha = \frac{1}{2}$ is motivated by both physical considerations of turbulent sediment transport and prior studies on fractional entropy formulations. Ubriaco (2009) showed that fractional entropy with $\alpha < 1$ naturally represents systems with incomplete information and partial phase-space mixing, a hallmark of turbulent flows. In sediment-laden open-channel flows, turbulence is dominated by intermittent burst-sweep events and multiscale eddy interactions, which lead to long-range correlations and non-Gaussian fluctuations in SSC (Nezu and Nakagawa, 1995). Such dynamics violate the assumptions of extensivity implicit in Shannon entropy, making fractional order measures more appropriate. Several studies have demonstrated that intermediate fractional orders, particularly $\alpha = \frac{1}{2}$, provide a balanced description of non-extensive transport processes while retaining analytical tractability and numerical stability (Ubriaco, 2009; Foroghi et al., 2022). In the context of sediment transport, Ahamed and Kundu (2023) showed that fractional entropy formulations outperform classical entropy models in capturing Type I SSC profiles under turbulent conditions, with lower fractional orders yielding improved agreement with experimental and field data. Choosing $\alpha = \frac{1}{2}$ therefore reflects a physically meaningful compromise. It departs sufficiently from the extensive Shannon case ($\alpha = 1$) to account for turbulence-induced intermittency, while enabling a closed-form solution for the pdf. This choice is thus consistent with both turbulence physics and practical modeling considerations.

5.3.4 Determination of Lagrange multipliers

The unknown constants λ_0 and λ_1 appearing in the optimal pdf (5.3.8) are determined by enforcing the two constraints (5.3.3) and (5.3.4). This is done by substituting (5.3.8) into the constraint integrals and simplifying the resulting expressions.

Constraint from the normalization condition

We introduce the change of variable $s = \lambda_0 + \lambda_1 \hat{c}$, and then we set $t = s^2$ (hence $dt = 2s\,ds$). Starting from the normalization constraint (5.3.3) and substituting the optimal pdf (5.3.8), we obtain

$$\int_{\hat{c}_h}^{1} \exp\left[-\frac{1 + \left(\lambda_0 + \lambda_1 \hat{c}\right)^2 - \left(\lambda_0 + \lambda_1 \hat{c}\right)\sqrt{\left(\lambda_0 + \lambda_1 \hat{c}\right)^2 + 2}}{2}\right] d\hat{c} = 1. \tag{5.3.10}$$

Step 1: Linear change of variable. First, note that the limits transform as

$$\hat{c} = \hat{c}_h \;\Rightarrow\; s = \lambda_0 + \lambda_1 \hat{c}_h, \qquad \hat{c} = 1 \;\Rightarrow\; s = \lambda_0 + \lambda_1.$$

Hence (5.3.10) becomes

$$\frac{1}{\lambda_1} \int_{\lambda_0+\lambda_1\hat{c}_h}^{\lambda_0+\lambda_1} \exp\left[-\frac{1+s^2 - s\sqrt{s^2+2}}{2}\right] ds = 1. \tag{5.3.11}$$

Step 2: Quadratic substitution. Introducing

$$t = s^2, \qquad \text{so that} \qquad dt = 2s\, ds.$$

Assuming $s > 0$ on the integration interval (which holds in our application under the small-argument/leading-order regime used later), we have

$$s\sqrt{s^2+2} = \sqrt{t}\,\sqrt{t+2} = \sqrt{t(t+2)} = \sqrt{t^2+2t}.$$

Also, the limits become

$$s = \lambda_0 + \lambda_1\hat{c}_h \Rightarrow t = (\lambda_0 + \lambda_1\hat{c}_h)^2, \qquad s = \lambda_0 + \lambda_1 \Rightarrow t = (\lambda_0 + \lambda_1)^2.$$

Therefore (5.3.11) transforms into

$$\frac{1}{2\lambda_1} \int_{(\lambda_0+\lambda_1\hat{c}_h)^2}^{(\lambda_0+\lambda_1)^2} \exp\left[-\frac{1+t-\sqrt{t^2+2t}}{2}\right] \frac{dt}{\sqrt{t}} = 1, \tag{5.3.12}$$

which is the desired form. If s changes sign on the integration interval, then $ds = dt/(2|s|) = dt/(2\sqrt{t})$ still holds, and the same expression (5.3.12) is obtained by interpreting $\sqrt{t} = |s|$.

Step 3: Separation into the product form used for series expansion. Rewrite the exponent as

$$-\frac{1+t-\sqrt{t^2+2t}}{2} = -\frac{1}{2} - \frac{t}{2} + \frac{1}{2}\sqrt{t^2+2t}.$$

Hence the integrand can be factorized as

$$\exp\left[-\frac{1+t-\sqrt{t^2+2t}}{2}\right] = e^{-1/2}\, \exp\left[-\frac{t}{2}\right]\, \exp\left[\frac{\sqrt{t^2+2t}}{2}\right],$$

and (5.3.12) may equivalently be written as

$$\frac{1}{2\lambda_1} \int_{(\lambda_0+\lambda_1\hat{c}_h)^2}^{(\lambda_0+\lambda_1)^2} e^{-1/2}\, \exp\left[-\frac{t}{2}\right]\, \exp\left[\frac{\sqrt{t^2+2t}}{2}\right] \frac{dt}{\sqrt{t}} = 1, \tag{5.3.13}$$

which is the exponential-product representation used in the subsequent Taylor/binomial expansions.

Next, we factor out the constant term $e^{-1/2}$ and expand the remaining exponential via the Taylor series $e^{-x} = \sum_{i=0}^{\infty} \frac{(-1)^i}{i!} x^i$, with $x = \frac{t-\sqrt{t^2+2t}}{2}$. This gives

$$\frac{e^{-1/2}}{2\lambda_1} \int_{(\lambda_0+\lambda_1\hat{c}_h)^2}^{(\lambda_0+\lambda_1)^2} t^{-1/2} \sum_{i=0}^{\infty} \frac{(-1)^i}{i!} \left(\frac{t-\sqrt{t^2+2t}}{2} \right)^i dt = 1. \tag{5.3.14}$$

Expanding $\left(\frac{t-\sqrt{t^2+2t}}{2}\right)^i$ using the binomial identity $(x-y)^i = \sum_{j=0}^{i} (-1)^j \binom{i}{j} x^{i-j} y^j$ together with $\sqrt{t^2+2t} = t^{1/2}(t+2)^{1/2}$ and the generalized binomial expansion $(1+z)^p = \sum_{k=0}^{\infty} \binom{p}{k} z^k$ (valid for $|z| < 1$), yields

$$\frac{e^{-1/2}}{2\lambda_1} \sum_{i=0}^{\infty} \sum_{j=0}^{i} \sum_{k=0}^{\infty} \frac{(-1)^{i+j}}{2^i i!} \binom{i}{j} 2^{\frac{j}{2}-k} \binom{j/2}{k} \int_{(\lambda_0+\lambda_1\hat{c}_h)^2}^{(\lambda_0+\lambda_1)^2} t^{-\frac{1}{2}+i-\frac{j}{2}+k}\, dt = 1. \tag{5.3.15}$$

Special case: zero surface concentration.

Under the physically motivated assumption $\hat{c}_h = 0$ (zero concentration at the free surface), Eq. (5.3.15) reduces to

$$\sum_{i=0}^{\infty} \sum_{j=0}^{i} \sum_{k=0}^{\infty} \binom{i}{j} \binom{j/2}{k} \frac{(-1)^{i+j} 2^{\frac{j}{2}-k-i}}{i!} \left[\frac{(\lambda_0+\lambda_1)^{1+2i-j+2k} - \lambda_0^{1+2i-j+2k}}{1+2i-j+2k} \right] = \lambda_1 e^{1/2}. \tag{5.3.16}$$

Assuming $|\lambda_0 + \lambda_1 \hat{c}| < 1$ for $\hat{c} \in [0,1]$, the series in Eq. (5.3.16) is truncated using a leading-order approximation. Specifically, we retain only the lowest-order contributions corresponding to $i = 0$ and $i = 1$ with $j = 0$ and $k = 0$, which generate terms up to first order in λ_0 and λ_1. All higher-order terms ($i \geq 2$, $k \geq 1$), which contribute powers of $(\lambda_0 + \lambda_1 \hat{c})^2$ and higher, are neglected. Under this approximation, Eq. (5.3.16) reduces to the linear relation

$$2\lambda_0 + \lambda_1 = 2\sqrt{2}\, e^{1/2}. \tag{5.3.17}$$

Constraint from the mean concentration condition

Substituting (5.3.8) into the mean constraint (5.3.4) and using $s = \lambda_0 + \lambda_1 \hat{c}$ (i.e., $\hat{c} = (s-\lambda_0)/\lambda_1$ and $d\hat{c} = ds/\lambda_1$), we obtain

$$\frac{e^{-1/2}}{\lambda_1^2} \left[\int_{\lambda_0+\lambda_1\hat{c}_h}^{\lambda_0+\lambda_1} s \exp\left(-\frac{s^2 - \sqrt{s^4+2s^2}}{2} \right) ds - \lambda_0 \int_{\lambda_0+\lambda_1\hat{c}_h}^{\lambda_0+\lambda_1} \exp\left(-\frac{s^2 - \sqrt{s^4+2s^2}}{2} \right) ds \right] = \hat{c}_m. \tag{5.3.18}$$

Define

$$I_1 = \int_{\lambda_0+\lambda_1\hat{c}_h}^{\lambda_0+\lambda_1} s\ \exp\left(-\frac{s^2 - \sqrt{s^4+2s^2}}{2}\right) ds,$$
$$I_2 = \int_{\lambda_0+\lambda_1\hat{c}_h}^{\lambda_0+\lambda_1} \exp\left(-\frac{s^2 - \sqrt{s^4+2s^2}}{2}\right) ds. \tag{5.3.19}$$

A similar leading-order truncation is applied to solve eq. (5.3.19). Retaining only the dominant terms arising from $i = 0$ and $i = 1$ with $j = 0$ and $k = 0$ yields contributions up to first order in λ_0 and λ_1, while all higher-order terms involving quadratic and higher powers of $(\lambda_0 + \lambda_1\hat{c})$ are discarded. This approximation is consistent with the normalization constraint truncation and ensures analytical tractability. As a result, Eq. (5.3.19) simplifies to the linear relation

$$3\lambda_0 + 2\lambda_1 = 6\sqrt{2}\, e^{1/2}\, \hat{c}_m. \tag{5.3.20}$$

Solution for λ_0 and λ_1

Finally, the Lagrange multipliers are obtained by solving the linear system (5.3.17) and (5.3.20). Let $A = \sqrt{2}\, e^{1/2}$. From $2\lambda_0 + \lambda_1 = 2A$ and $3\lambda_0 + 2\lambda_1 = 6A\hat{c}_m$, we obtain

$$\lambda_0 = 2\sqrt{2}\, e^{1/2}\,(2 - 3\hat{c}_m), \qquad \lambda_1 = 6\sqrt{2}\, e^{1/2}\,(2\hat{c}_m - 1).$$

These expressions provide a closed-form approximation for the multipliers in terms of the normalized mean concentration $\hat{c}_m$, and they are subsequently used to obtain an explicit SSC profile along the vertical water column.

5.3.5 Spatial characterization of the vertical SSC profile

To obtain an explicit spatial representation of the SSC, the pdf $f(\hat{c})$ must be related to the vertical coordinate y. This is achieved by introducing a hypothetical cdf that maps sediment concentration to the normalized vertical position in the flow domain. Following earlier entropy-based sediment studies (e.g., Cui and Singh, 2014; Ghoshal et. al, 2018), the cdf is postulated as a function of the normalized height:

$$F(\hat{c}) = \left(1 - \left(\frac{y - y_r}{h - y_r}\right)^a\right) \exp\left[-\left(\frac{y - y_r}{h - y_r}\right)^a\right], \tag{5.3.21}$$

where

- y denotes the vertical coordinate measured from the channel bed,
- y_r is the reference level near the bed where the concentration is maximum,
- h is the total flow depth,
- $a \in (0, 1)$ is a decay parameter that controls the rate at which concentration decreases toward the free surface and is determined empirically.

The functional form in Eq. (5.3.21) ensures that the cdf satisfies the physical boundary conditions of sediment transport: $F(\hat{c}) = 1$ at the reference level ($y = y_r$), and $F(\hat{c}) = 0$ at the free surface ($y = h$). This behavior is consistent with the observed decrease in SSC away from the bed in turbulent open-channel flows.

Independently, the cdf associated with the entropy-maximized pdf in Eq. (5.3.8) is obtained by direct integration:

$$F(\hat{c}) = \int_{\hat{c}_h}^{\hat{c}} \exp\left[-\frac{(1 + (\lambda_0 + \lambda_1 \hat{c})^2) - (\lambda_0 + \lambda_1 \hat{c})\sqrt{(\lambda_0 + \lambda_1 \hat{c})^2 + 2}}{2}\right] d\hat{c}, \tag{5.3.22}$$

where the negative branch of Eq. (5.3.7) is selected to ensure monotonicity of the cdf, so that $F(\hat{c})$ increases with concentration, consistent with the physical directionality of SSC (higher concentration near the bed and lower near the surface).

Equating the cdfs for spatial mapping. To establish a one-to-one correspondence between concentration and vertical position, the two expressions for the cdf are equated:

$$\int_{\hat{c}_h}^{\hat{c}} \exp\left[-\frac{(1 + (\lambda_0 + \lambda_1 \hat{c})^2) - (\lambda_0 + \lambda_1 \hat{c})\sqrt{(\lambda_0 + \lambda_1 \hat{c})^2 + 2}}{2}\right] d\hat{c} = (1 - \hat{Y}^a) \exp\left(-\hat{Y}^a\right), \tag{5.3.23}$$

where $\hat{Y} = (y - y_r)/(h - y_r)$ is the normalized vertical coordinate.

Assuming zero surface concentration ($\hat{c}_h = 0$) and introducing the substitution $t = (\lambda_0 + \lambda_1 \hat{c})^2$, the left-hand side of Eq. (5.3.23) becomes

$$\frac{e^{-1/2}}{2\lambda_1} \int_{\lambda_0^2}^{(\lambda_0 + \lambda_1 \hat{c})^2} t^{-1/2} \exp\left[-\frac{1}{2}\left(t - \sqrt{t^2 + 2t}\right)\right] dt. \tag{5.3.24}$$

For $|\lambda_0 + \lambda_1 \hat{c}| < 1$, the integrand is expanded using Taylor and binomial series. Retaining only the leading-order contributions corresponding to $i = 0, 1$ and $k = 0$ (linear order in λ_0 and λ_1), the cdf simplifies to

$$F(\hat{c}) \approx \frac{e^{-1/2}}{2\sqrt{2}\lambda_1}\left[(\lambda_0 + \lambda_1 \hat{c})^2 - \lambda_0^2\right]. \tag{5.3.25}$$

Explicit spatial–concentration relationship. Equating the approximate cdf in Eq. (5.3.25) with the spatial cdf in Eq. (5.3.21) and solving for $\hat{c}$ yields

$$\hat{c} = \frac{1}{\lambda_1}\left[-\lambda_0 \pm \sqrt{\lambda_0^2 + 2\sqrt{2}e^{1/2}\lambda_1(1-\hat{Y}^a)\exp\left(-\hat{Y}^a\right)}\right]. \tag{5.3.26}$$

The physically admissible branch is chosen to ensure $\hat{c} \geq 0$ throughout the domain.

Finally, the dimensional SSC profile along the vertical direction is obtained as

$$c(y) = c_r\,\hat{c}(y),$$

where c_r is the reference concentration at $y = y_r$.

Eq. (5.3.26) thus provides an explicit and analytically tractable expression for the vertical distribution of SSC in open-channel flows, directly linking spatial position to sediment concentration through the FDE-based framework.

5.4 Validation through experimental and field data

To assess the authenticity and predictive accuracy of the proposed FDE-based SSC model (5.3.26), we validate it using both experimental datasets (Coleman, 1986; Einstein and Chien, 1955) and field observations (McQuivey, 1973). In all cases, the reference level y_r is set as the lowest recorded height with available concentration measurements, thereby avoiding under-estimation or over-estimation of y_r as may occur with deterministic approaches (Mazumder and Ghoshal, 2006).

Experimental datasets:

Einstein and Chien (1955): Measurements recorded in laboratory using painted steel flume (length= 40 ft, width= 1.006 ft, depth = 1.17 ft). The experiments comprised of 29 runs using sand particles of varying diameters d, classified as fine ($d = 0.94$ mm), medium ($d = 1.14$ mm), and coarse ($d = 1.3$ mm). Of these, 13 runs were conducted with clear water, while the remaining runs involved sediment-laden flows. For the present model validation, Run S13 with fine sediment particles is considered. The experimental details can also be obtained from Cui (2011).

Coleman (1986): Experiments conducted in a recirculating flume with a rectangular Plexiglas channel (length= 1.5 m, width= 35.6 cm, depth = 17.2 cm). A total of 40 runs were conducted with particle sizes ranging from fine (diameter $d = 0.105$ mm) to medium

(d = 0.210 mm) and coarse (d = 0.420 mm). Runs 3, 10, 25, and 40 are selected for validation. Dataset details are also available in Cui (2011); Ahamed and Kundu (2023).

Field datasets:

Rio Grande Conveyance Channel (RGC Run 18): Measurement location is 36 ft from the left bank; flat channel bed with depth $h = 3$ ft; sediment particle diameter $d = 0.202$ mm.

Atrisco Feeder Canal (AFC): Measurement location is 28 ft from the left bank; dunes as bed form with depth $h = 1.86$ ft; sediment particle diameter $d = 0.235$ mm.

Missouri River (Run 3): Measurement location is 440 ft from the left bank; dunes as bed form with depth $h = 13.6$ ft; sediment particle diameter $d = 0.252$ mm.

CDF fitting and parameter estimation

For each dataset, we fit the hypothetical cdf (5.3.21) with the generalized cdf (5.3.25) estimated from the entropy-based pdf so as to determine the parameter a. Fig. 5.4.1 illustrates the fitting for the datasets considered.

Using the fitted a values, we plot the normalized concentration profiles c/c_r computed from (5.3.26) against depth ratio y/h (Fig. 5.4.2). The proposed model matches both experimental and field data closely. The results confirm that the governing expression for the concentration distribution is:

$$\hat{c} = \frac{1}{\lambda_1}\left[-\lambda_0 + \sqrt{\lambda_0^2 + \lambda_1\left(1 - \left(\frac{y - y_r}{h - y_r}\right)^a\right)\exp\left(-\left(\frac{y - y_r}{h - y_r}\right)^a\right)2\sqrt{2}e^{1/2}}\right]. \tag{5.4.1}$$

Regression analysis

The regression analysis of computed versus observed $\hat{c}$ values (Fig. 5.4.3) yields consistently high coefficients of determination (R^2 ranging from 0.9958 to 0.9603), indicating strong agreement between model predictions and observations. The highest R^2 was obtained for the Coleman formulation (Coleman, 1986), followed by Einstein & Chien (Einstein and Chien, 1955), and McQuivey (McQuivey, 1973). This performance hierarchy likely reflects the influence of particle size distributions and dataset-specific hydraulic conditions, with models calibrated under similar conditions to the present data exhibiting superior predictive capability.

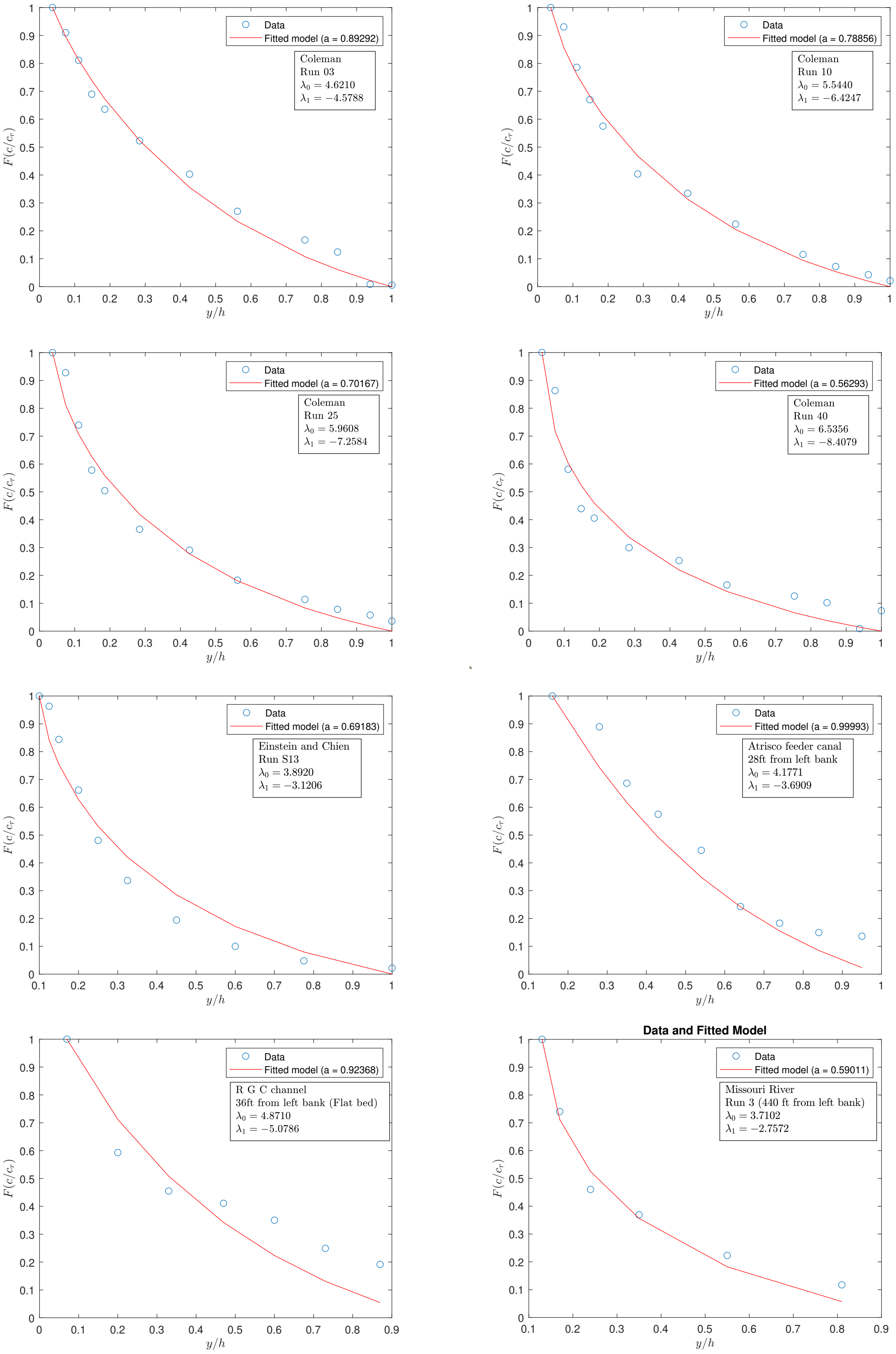

Figure 5.4.1: Validation of fitted hypothetical cdf (5.3.21) against estimated cdf (5.3.25) for Coleman, Einstein & Chien, and McQuivey datasets.

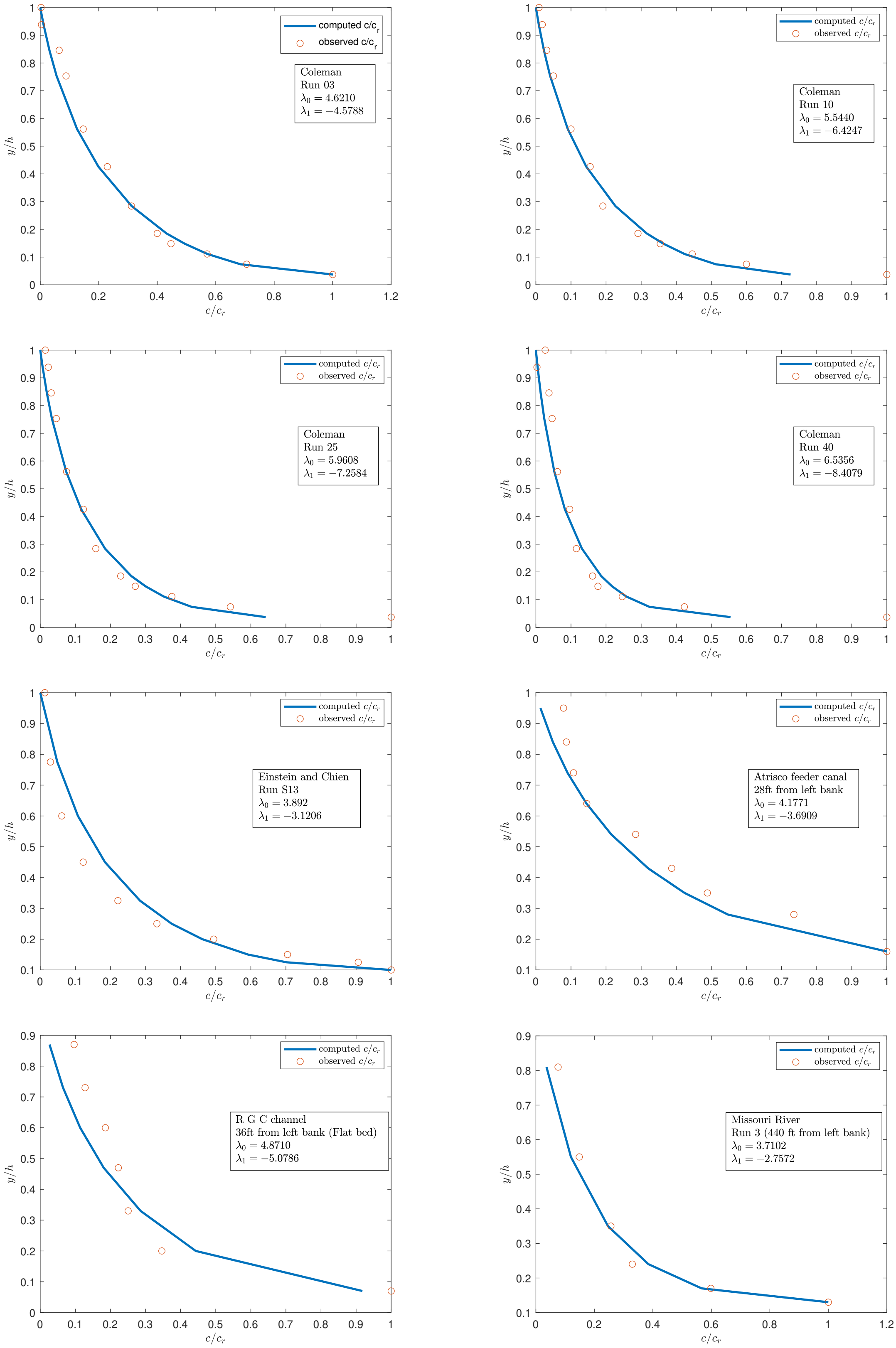

Figure 5.4.2: Comparison of dimensionless concentration c/c_r profiles with y/h for experimental and field datasets.

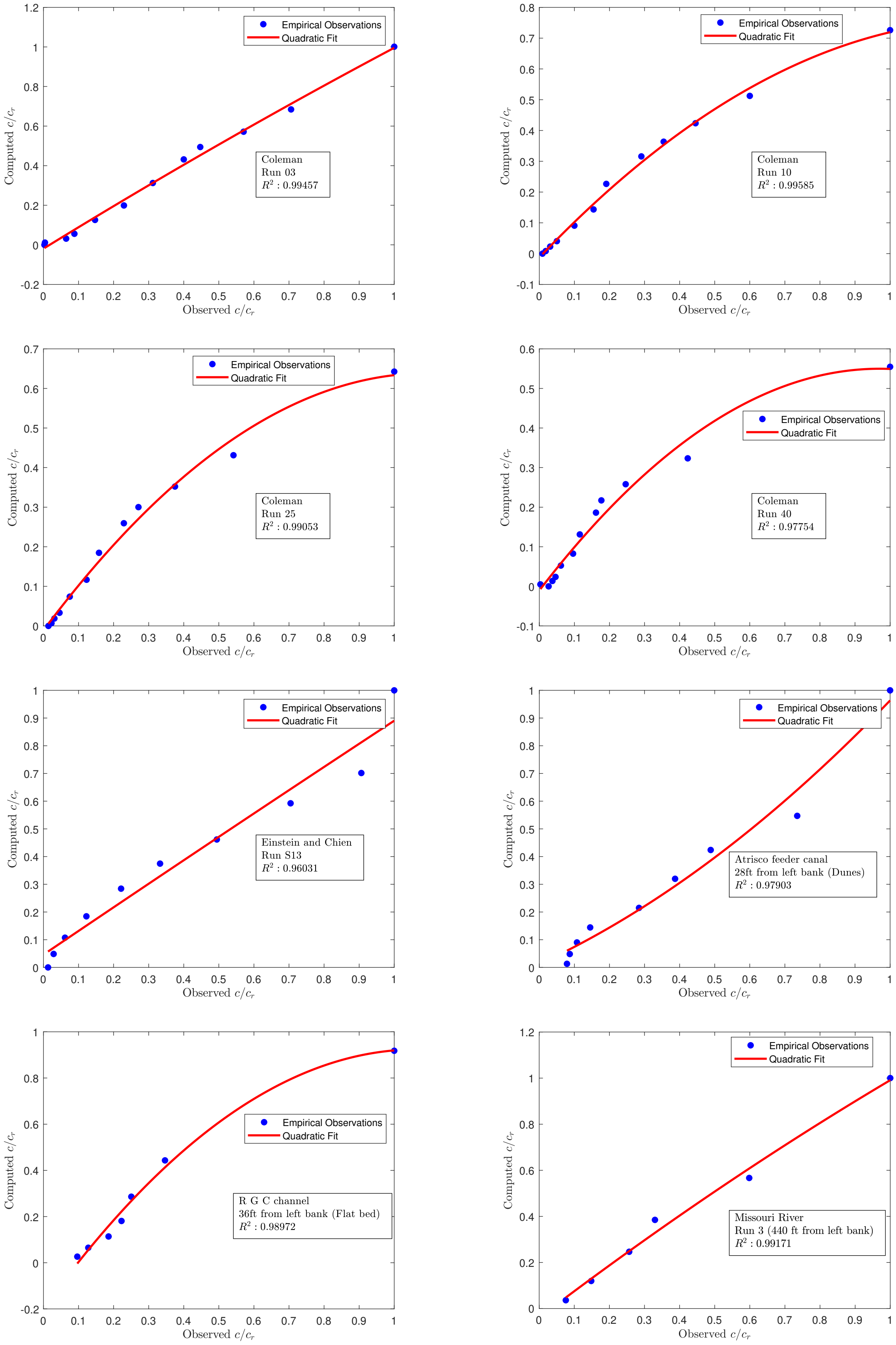

Figure 5.4.3: Regression comparison of computed c/c_r against observed c/c_r for all datasets.

Superiority of the proposed model through error analysis

For comprehensive validation, we compare the proposed FDE-based vertical SSC model, expressed by Eq. (5.4.1), with both classical entropy-based SSC models assuming zero surface concentration (Eqs. (5.2.2) – (5.2.4)), the deterministic Rouse model (Eq. (5.2.1)) and more advanced entropy formulations such as the Rényi model (Ghoshal et. al, 2018) and the fractional Wang (FW) entropy model (Ahamed and Kundu, 2023) that permit non-zero surface concentration.

We evaluate the model performance over a range of flow conditions and sediment particle sizes using multiple accuracy indicators as follows (see Ahamed and Kundu, 2023):

- Relative error $(R_e) = \frac{1}{n}\sum_{k=1}^{n}\frac{|\hat{c}_{k(comp)}-\hat{c}_{k(obs)}|}{\hat{c}_{k(obs)}}$;
- Sum of relative squared error (E1) $= \sum_{k=1}^{n}\frac{(\hat{c}_{k(comp)}-\hat{c}_{k(obs)})^2}{\hat{c}_{k(obs)}^2}$;
- Root-mean-square error (RMSE) $= \sqrt{\frac{1}{n}\sum_{k=1}^{n}(\hat{c}_{k(comp)}-\hat{c}_{k(obs)})^2}$;
- Mean absolute standard error (MASE) $= \frac{1}{n}\sum_{k=1}^{n} M_i$,
  where
  $$M_i = \begin{cases} \frac{\hat{c}_{k(comp)}}{\hat{c}_{k(obs)}} & \text{if } \hat{c}_{k(comp)} > \hat{c}_{k(obs)} \\ \frac{\hat{c}_{k(obs)}}{\hat{c}_{k(comp)}} & \text{if } \hat{c}_{k(comp)} < \hat{c}_{k(obs)} \end{cases};$$
- Sum of logarithmic deviation error (E2) $= \sum_{k=1}^{n}(\log|\hat{c}_{k(comp)}| - \log|\hat{c}_{k(obs)}|)^2$.

Here n refers to the total count of data points in a particular set of data, $\hat{c}_{k(comp)}$ and $\hat{c}_{k(obs)}$ denote the computed and observed dimensionless concentration of sediment at the k^{th} data point, respectively. Now, we compute the above mentioned errors for the proposed normalized SSC model, defined in Eqs. (5.4.1), using the specified experimental and field datasets as shown in Table 5.4.1. Since we have considered zero surface concentration, MASE and E2 error values have been computed by ignoring the data point at the surface to get finite values.

It is observed from Table 5.4.1 that across all the eight chosen datasets (*Einstein and Chien*, *Coleman* and *McQuivey*) spanning a wide range of flow conditions and sediment regimes, the proposed FDE-based SSC model achieves consistently low error statistics. Key observations include:

Table 5.4.1: *Mean error $\mu(\epsilon)$, Standard deviation of error $\sigma(\epsilon)$, Relative error (R_e), Sum of squared relative error (E1), Root-mean-square error (RMSE), Mean-absolute-standard error (MASE) and sum of logarithmic deviation error (E2) for validation of estimated dimensionless concentration $\hat{c}$ with chosen data sets.*

Data set	**Sample size**	$\mu(\epsilon)$ **(g/l)**	$\sigma(\epsilon)$**(g/l)**	**E1**	**RMSE**	$\mathbf{R_e}$	**MASE**	**E2**
Coleman data								
Run 03	12	0.0192	0.0161	4.134	0.0698	0.3346	1.3471	1.7321
Run 10	12	0.0425	0.0764	1.5529	0.0991	0.24337	1.2588	0.9289
Run 25	12	0.0533	0.0999	1.9572	0.1283	0.28894	1.4301	2.1183
Run 40	12	0.0612	0.1236	2.4021	0.1566	0.35531	1.4824	2.2334
Einstein & Chien data								
Run S13	10	0.0595	0.0599	2.4497	0.1347	0.3792	1.3214	2.2396
McQuivey data								
AFC (Dunes)	9	0.0568	0.0570	1.0908	0.1333	0.2498	1.7846	3.8303
RGC (Flat Bed)	7	0.0658	0.0215	1.0596	0.1494	0.3280	1.7138	2.5073
Missouri (Run 3)	6	0.0274	0.0199	0.34097	0.0789	0.1619	1.2651	0.6172

- Mean Prediction Error $\mu(\epsilon)$: Ranges from 0.0192 g/l (Coleman Run 03) to a maximum of only 0.0658 g/l (RGC flat bed), indicating minimal bias for all cases.

- Error Variability $\sigma(\epsilon)$: Standard deviations are generally very small (≤ 0.1236 g/l), reflecting stable predictive performance within each dataset.

- Relative Error R_e: Well below unity in all runs, with especially low values for field data, signifying close agreement with observed SSC profiles.

- E1 and RMSE: Low E1 values ($\leq$ 4.134) and RMSE consistently below 0.16 highlight accurate profile fitting across datasets with varying hydraulic and sediment characteristics.

- MASE: Mostly close to 1, indicating that computed concentrations are, on average, very close in magnitude to measured values.

- Logarithmic Deviation Error E2: Acceptably low values ($\leq$ 3.83 even for the AFC dunes case, which is prone to greater near-bed concentration variation).

Overall, these metrics confirm that the current model predicts SSC profiles with high accuracy, low bias, and strong stability across different bed forms (dunes, flat beds), particle size distributions, and measurement approaches. The consistently low error values provide strong evidence of the model's reliability and robustness in both experimental and field conditions.

Table 5.4.2: *Comparison of the present model with other vertical profile of SSC model.*

SSC models	Current model	Tsallis model	Shannon (Choo) model	Rousian model
Data source	*Missouri River Run 03 of McQuivey data*			
R_e	0.1619*	0.4286	0.4136	0.3103
E1	0.3410*	1.4206	1.4193	1.0278
RMSE	0.0789	0.1849	0.1529	0.0607*
MASE	1.2651*	1.4401	1.4600	2.1839
Data source	*Run 25 of Coleman data*			
R_e	0.2890*	0.5499	0.6317	0.8642
E1	1.9572*	4.6198	5.9007	9.8640
RMSE	0.1283*	0.1439	0.1307	0.1823
MASE	1.4301*	1.5508	1.6116	5.5690
Data source	*Run S13 of Einstein & Chien data*			
R_e	0.3792*	0.5511	1.2769	0.5555
E1	2.4497*	6.1399	31.3755	3.8921
RMSE	0.1347	0.1439	0.1307*	0.1823
MASE	1.3214*	1.9023	2.3154	3.1771

Note: * indicates the minimum values of different types of error for each data source.

Furthermore, from Table 5.4.2, we can observe consistent trends across the field (*Missouri River*) and laboratory (*Coleman; Einstein and Chien*) datasets. *Relative Error* (R_e) is lowest for the current model in all cases, confirming its superior ability to reproduce SSC profiles compared to the Tsallis, Shannon, and Rouse formulations. E1 values also highlight the dominance of current model, with dramatically smaller errors than competing models, especially in the Einstein and Chien dataset where Shannon's error (31.38) was reduced to only 2.45 by current model. For RMSE, the Rouse model occasionally achieves the smallest values, but current model consistently matches or comes very close, demonstrating competitive fit quality. Finally, MASE values are uniformly the lowest for current model, underscoring its ability to capture magnitudes of SSC more reliably than other models.

Overall, the current model most frequently records the lowest R_e, E1, and MASE, while achieving RMSE values that are equal or nearly equal to the best competitor, a pattern that holds across both controlled laboratory datasets and complex field measurements. This confirms the robustness and generality of the FDE formulation for SSC prediction across varied hydraulic and sediment regimes, combining low bias with strong stability.

Additionally, comparisons with the Rényi entropy model (Ghoshal et. al, 2018) and the fractional Wang (FW) entropy model (Ahamed and Kundu, 2023), both of which allow for non-zero surface concentration, as provided in Table 5.4.3, further underline the strengths of the FDE approach. From Table 5.4.3, we have that across selected datasets (Missouri River Run 03, Coleman Runs 10, 25, and 40, and Einstein and Chien

Run S13), the current model consistently achieves the smallest bias $\mu(\epsilon)$, such as 0.0274 in Missouri Run 03 compared with Rényi (0.1486) and FW (0.1215), indicating markedly more accurate central predictions. For variability $\sigma(\epsilon)$, the current model often yields the most stable performance although in some cases Rényi achieves marginally lower values. Even in such cases, the lower bias of the current model ensures that its overall predictive accuracy remains superior.

The improved performance of the proposed FDE-based SSC model in some datasets can be attributed to the flexibility introduced by the fractional order parameter. In suspended sediment transport, concentration is usually high near the bed and decreases toward the free surface. This decrease is often nonlinear and strongly affected by turbulence, settling velocity, and vertical mixing. Therefore, the uncertainty structure of the concentration profile is not uniform over the flow depth.

Compared with Rényi- or Wang-type entropy models, the FDE formulation provides an adjustable sensitivity to the shape of the concentration distribution. This helps the model respond more effectively to sharp near-bed concentration gradients, nonlinear decay, and turbulence-induced heterogeneity. As a result, the proposed model may provide better fitting performance when the observed SSC profile is highly nonuniform or when sediment concentration changes rapidly in the lower part of the flow depth.

It should be noted, however, that the proposed FDE model is not claimed to uniformly dominate all existing entropy-based models for every flow condition. Rather, the numerical results indicate that the model is especially effective for datasets where vertical concentration variation is strong and where an additional sensitivity parameter improves the representation of profile shape.

5.5 Confidence intervals of parameter estimates

In the context of quantifying uncertainties in the fitted parameters- decay parameter a, and Lagrange multipliers λ_0, λ_1 in the FDE-based SSC model, resampling methods such as bootstrap and jackknife empirical likelihood (JEL) replicate the parameter fitting under many different sample compositions, reducing the risk of overfitting our model to peculiarities in one specific dataset. It also provides bias-corrected confidence intervals, enhancing the accuracy of inferential statements about our parameters. Thus, these methods have a significant impact on the stability of the parameter estimates and model predictions by exposing their sensitivity to data variability, enabling more precise uncertainty quantification, detecting outliers, and preventing overconfidence in model outputs. This results

Table 5.4.3: Mean error $\mu(\epsilon)$ and standard deviation of error $\sigma(\epsilon)$ to compare proposed FDE model with Rényi model and fractional Wang (FW) model.

SSC models	**Current model**	**Rényi model**	**FW model**
Data source (Field)			
McQuivey data:			
Missouri River Run 03			
$\mu(\epsilon)$	0.0274*	0.1486	0.1215
$\sigma(\epsilon)$	0.0199*	0.1617	0.1397
Data source (Experimental)			
Coleman data:			
Run 10			
$\mu(\epsilon)$	0.0425*	0.0632	0.0568
$\sigma(\epsilon)$	0.0764	0.0755	0.0564*
Run 25			
$\mu(\epsilon)$	0.0533*	0.1366	0.0728
$\sigma(\epsilon)$	0.0999	0.0700*	0.1100
Run 40			
$\mu(\epsilon)$	0.0612*	0.1281	0.0957
$\sigma(\epsilon)$	0.1236	0.0846*	0.0999

Note: * represents the lowest mean and standard deviation of error across various data sources.

in a robust, credible sediment concentration model that better reflects real-world data complexities.

Bootstrap resampling repeatedly resample our dataset with replacement, fit the model each time, and record parameter estimates. The distribution of these estimates allows estimating confidence intervals and assessing parameter variability. On the other hand, Jackknife resampling iteratively leave out one data point or observation at a time, fit the model to the reduced dataset, and record parameter estimates. JEL estimates assess bias and variance of parameters and their stability to individual data points. If omitting certain points leads to large parameter shifts or prediction changes, those data points can be flagged for further scrutiny, increasing model robustness.

Therefore, in order to improve the robustness and interpretability of the proposed model parameter estimates, we consider the following strategies:

- We begin with numerical nonlinear optimization that aims to minimize residuals between predicted and observed concentrations subject to constraints like normalization and mean concentration. Optimal values of the parameters are obtained from physically and mathematically informed initial values (e.g., from truncated linear solutions of Eqs. (5.3.17) and (5.3.20)). This avoids convergence to unrealistic solutions or local minima and may favor parameter sets different from linear approximations, especially if the data behavior is complex or noisy. For example, the initial guesses ($\lambda_0 \approx 5.96, ; \lambda_1 \approx -7.26, ; a \approx 0.70$) for Coleman Run 25 data come from a truncated linear system approximation, which is a simplified analytical solution serving as a starting point. The final fitted values ($\lambda_0 \approx 3.26; \lambda_1 \approx 0.001, ; a \approx 0.655$) are obtained after optimization of the parameters.

- Next, we use bootstrap and jackknife methods to quantify parameter variability and confidence intervals, which help understand the sensitivity of estimates to data variability and identify unstable parameters.

  The jackknife standard error (SE) is given by:

$$SE_{\text{jack}}(\theta) = \sqrt{\frac{n-1}{n}\sum_{i=1}^{n}\left(\theta_{(i)} - \bar{\theta}\right)^2}$$

  where:

  - $\theta_{(i)}$ = parameter estimate with the i-th observation removed.
  - $\bar{\theta}$ = mean of the jackknife estimates:

$$\bar{\theta} = \frac{1}{n}\sum_{i=1}^{n}\theta_{(i)}.$$

  The adjustment factor $\frac{n-1}{n}$ corrects for the fact that the jackknife uses $n-1$ data points in each subsample.

Results and interpretations

From Table 5.5.1, we get the following results about the influence of the parameters in the proposed FDE-based SSC model:

Parameter a (decay parameter controlling SSC profile steepness): Across all datasets, bootstrap confidence intervals (CI) are reasonably narrow, showing the parameter is identifiable. Jackknife means range from 0.22 to 0.45, with relatively small standard errors (SE), confirming robustness of the estimates. The smallest SE occurs for Coleman Run 40 (0.2233 ± 0.1591), indicating particularly stable estimation.

Parameter λ_0 (multiplier term): Bootstrap CIs are moderate ([0.07, 2.5]) across datasets, showing identifiable but somewhat variable estimates. Jackknife results reveal some spread (SE up to 2.0), but Coleman Run 03 and Run 40 provide stable values with SE below ~ 1.7. Missouri Run 03 shows the widest CI and highest SE, reflecting greater uncertainty, likely due to field variability.

Parameter λ_1 (nonlinearity / scaling parameter): Bootstrap CIs are wider than for a and λ_0, ranging from near-zero (0.001) up to values as large as 11.4. This suggests λ_1 is the most sensitive parameter, strongly affected by dataset conditions and noise. Jackknife results confirm this: Coleman Run 25 yields an extremely stable estimate (0.0010 ± 0.0000), showing the parameter collapsed to its lower bound, while other runs (e.g., Missouri Run 03 and Coleman Run 40) display high SEs (2.8–3.2), implying instability and data-dependence.

Table 5.5.1: Bootstrap 95% Confidence Intervals (CI) and Jackknife mean ± SE for parameters a, λ_0, and λ_1 across datasets.

Dataset	a	λ_0	λ_1
Coleman Run 03	CI: [0.0218, 0.5285] Jack: 0.4450 ± 0.2426	CI: [0.0824, 2.3258] Jack: 1.8168 ± 1.2471	CI: [0.0010, 3.3671] Jack: 0.8160 ± 1.7355
Coleman Run 25	CI: [0.0975, 0.3792] Jack: 0.3442 ± 0.3015	CI: [0.6112, 2.3310] Jack: 2.2971 ± 1.4753	CI: [0.0010, 2.7866] Jack: 0.0010 ± 0.0000
Coleman Run 40	CI: [0.0298, 0.3388] Jack: 0.2233 ± 0.1591	CI: [0.0708, 2.4994] Jack: 2.1052 ± 1.6780	CI: [0.0010, 11.435] Jack: 0.2606 ± 2.8561
Missouri Run 03	CI: [0.0267, 0.4604] Jack: 0.3290 ± 0.3357	CI: [0.1009, 2.3299] Jack: 1.6758 ± 2.0472	CI: [0.0010, 7.7425] Jack: 0.6452 ± 3.2036

Therefore, the results in Table 5.5.1 indicate that the decay parameter a is consistently well estimated across all datasets, with relatively narrow bootstrap confidence intervals and low jackknife standard errors. This suggests that a is the most reliable and stable parameter in the proposed FDE model. The multiplier λ_0 shows moderate uncertainty, with confidence intervals ranging between approximately 0.07 and 2.5, and jackknife errors varying between datasets. This reflects some dataset-specific variability, though the estimates remain interpretable. In contrast, the nonlinearity parameter λ_1 exhibits the greatest sensitivity: its bootstrap intervals are considerably wider (extending up to values of 11.4 in some cases), and jackknife results reveal high variability, with certain runs (e.g., Coleman Run 25) collapsing to the lower bound. This is because the initial values of the Lagrange multipliers λ_0, λ_1 of our simplified SSC model (5.4.1) depends on the assumption identified as $|\lambda_0 + \lambda_1 \hat{c}| < 1$. Overall, the analysis demonstrates that the proposed model provides robust estimates for a and λ_0, while λ_1 requires careful interpretation due to its instability across datasets. These findings highlight that the model structure is sound, but that additional constraints or regularization may be beneficial to improve the reliability of λ_1, particularly in field-scale applications.

Fig. 5.5.1 shows bootstrap histograms for the FDE-based SSC model parameters-decay parameter (a) and Lagrange multipliers (λ_0, λ_1)-for Coleman Runs 25, 40, 03, and Missouri River Run 03. In laboratory datasets, a is sharply peaked and unimodal, confirming strong identifiability of the decay rate, whereas the field dataset (Missouri River Run 03) displays a broader distribution, reflecting environmental variability. The distributions of λ_0 are moderately spread and often right-skewed, stable in experimental data but more sensitive to perturbations in field conditions. In contrast, λ_1 exhibits wide, heavily skewed distributions across all datasets, with many estimates clustering near the lower bound and occasional extreme outliers, indicating weak identifiability and high sensitivity. Overall, the bootstrap analysis confirms that the decay parameter a is robustly estimated in both laboratory and field environments, and that λ_0, while moderately stable, is more susceptible to data-specific effects. In contrast, λ_1 exhibits high uncertainty and weak stability, suggesting its role in SSC profile modeling is secondary and should be interpreted with care, especially in field applications. These insights, drawn from comparative histogram analysis, reinforce both the reliability and the limitations of parameter inference in entropy-based vertical SSC modeling.

Finally, in Fig. 5.5.2, we illustrate the SSC profile sensitivity to parameter uncertainty across four datasets, specifically, Coleman Runs 03, 25, 40 and Missouri River Run 03, showing the observed normalized SSC profile (red points), the median model prediction (solid blue curve), and the bootstrap-derived 95% prediction interval (green shaded region). The shaded green band is obtained by refitting the FDE-based SSC model to 1000 bootstrap resamples of the dataset and propagating the resulting parameter sets into predicted profiles. Here, we find that in the controlled experimental runs (Coleman 25 and 40), the bootstrap-derived 95% confidence intervals (CIs) are narrow, tightly enveloping the median predicted profiles and encompassing nearly all observed data points, highlighting strong parameter identifiability and model precision in these settings. Coleman Run 03 exhibits moderately wider confidence bands, reflecting modestly increased uncertainty yet maintaining good agreement between observations and model predictions. In contrast, the Missouri River field dataset demonstrates substantially wider uncertainty bands, indicative of greater environmental variability and measurement noise influencing parameter estimation. Despite this, the median prediction remains consistent with observed profiles, reflecting the robustness of the current model. Collectively, these results affirm the current model's capacity to produce reliable SSC predictions with quantifiable uncertainty in both experimental and complex natural flow environments.

Physical interpretation of estimated parameters. The estimated parameters should be interpreted not only as numerical fitting quantities, but also in relation to the expected physical behaviour of suspended sediment concentration profiles. In open-channel turbulent flow, sediment concentration is generally higher near the bed and decreases toward the free surface due to the combined effects of settling, turbulent diffusion, and vertical mixing. Therefore, parameters controlling the decay of concentration with height should produce smooth, positive, and bounded concentration profiles with realistic near-bed dominance.

The estimated Lagrange multipliers are considered physically admissible when they generate concentration profiles without negative values, artificial oscillations, or unrealistic surface/near-bed behaviour. The bootstrap confidence intervals and jackknife estimates reported above therefore provide not only statistical information about parameter uncertainty, but also a check on physical consistency. If the confidence intervals preserve realistic monotone or smoothly varying concentration profiles, then the fitted parameters can be regarded as hydraulically meaningful within the range of the observed data.

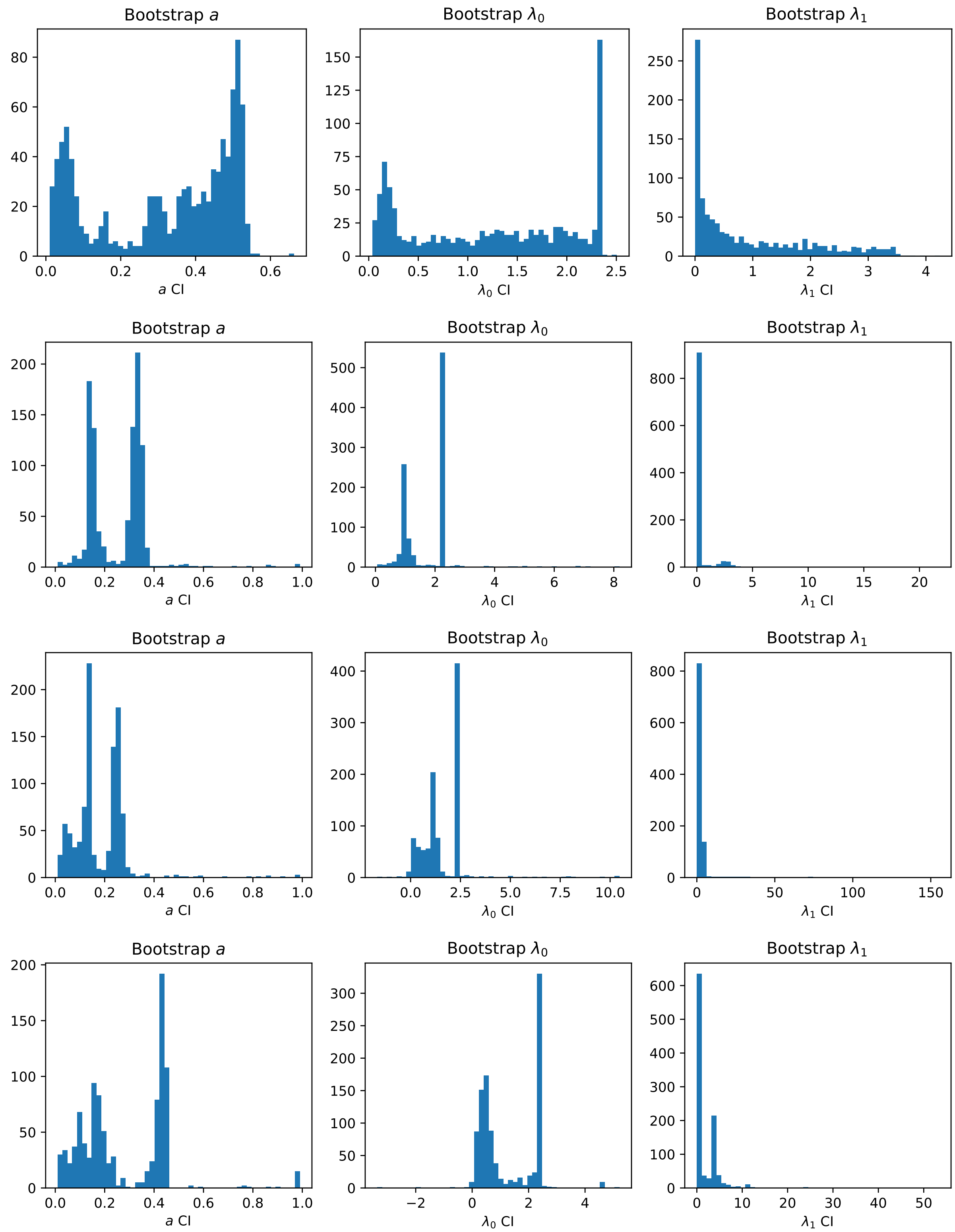

Figure 5.5.1: Parameter histograms of bootstrap samples for Coleman Run 03 (first), Run 25 (second), Run 25 (third) and Missouri river Run 03 (bottom last) data.

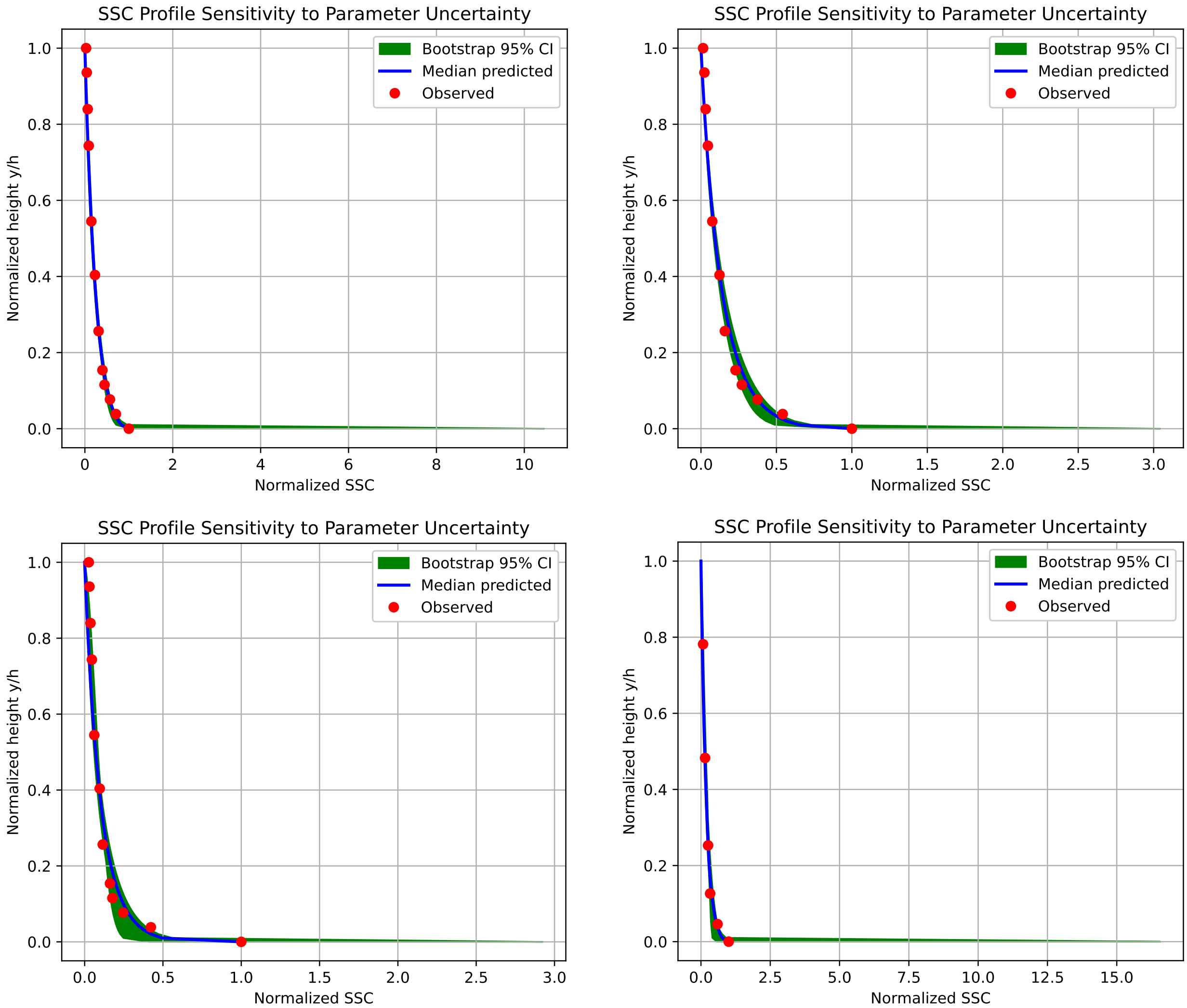

Figure 5.5.2: Sensitivity of normalized concentration c/c_r profiles with y/h for Coleman Run 03 (top left), Run 25 (top right), Run 40 (bottom left) Missouri river Run 03 (bottom right) data.

5.6 Conclusion

FDE has received limited attention in the modeling of uncertainty associated with physical transport processes, particularly in turbulent flow environments. This chapter addresses this gap by developing a simplified yet powerful FDE-based framework for describing the vertical distribution of suspended sediment concentration (SSC) in open-channel flows. By modeling the normalized SSC as a continuous r.v and enforcing the physically realistic condition of vanishing concentration at the free surface, the proposed formulation offers a flexible, data-efficient alternative to conventional deterministic and classical entropy-based approaches. The use of a leading-order approximation enables the derivation of an explicit and analytically tractable SSC profile, making the model both interpretable and computationally efficient.

Extensive validation using laboratory experiments and field measurements demonstrates the strong predictive capability of the FDE approach, with coefficients of determination reaching as high as $R^2 = 0.996$ and consistently lower error metrics compared with existing models. The key advantage of the proposed framework lies in its ability to incorporate fractional non-additivity, which allows it to capture the non-extensive, intermittent, and multiscale characteristics of turbulent sediment transport that are not adequately represented by classical formulations. Sensitivity and resampling analyses further confirm the robustness of the estimated parameters, although the observed sensitivity of the nonlinearity parameter λ_1 highlights opportunities for future refinement and improved physical interpretation.

While the present study focuses on Type I SSC distributions, the FDE framework developed here is readily extensible to Type II and Type III profiles. Such extensions have the potential to provide deeper insight into complex sediment–turbulence interactions across a wider range of flow regimes. Overall, this work establishes FDE as a promising and unifying tool for uncertainty-aware sediment transport modeling, opening new avenues for advancing both theoretical understanding and practical prediction of sediment dynamics in natural and engineered open-channel systems.

Chapter 6

Analytical Formulation of Vertical Concentration Profile for Suspended Sediment in Open Channel Flows using Fractional Entropy[1]

"Nothing takes place in the world whose meaning is not that of some maximum or minimum."

— Leonhard Euler

In continuation of the FDE-based suspended sediment modeling developed in the previous chapter, this chapter presents a generalized probabilistic framework for suspended sediment concentration (SSC) in open channel flows based on the fractional entropy formulation proposed by Machado (2014). By extending the fractional parameter space to the real domain through incorporation of concepts from fractional calculus, the Machado entropy provides increased flexibility for representing non-extensive sediment transport processes. The optimal pdf of the time-averaged normalized SSC is derived through entropy maximization under physically consistent constraints, yielding an implicit analytical form involving the Lambert W function and a corresponding vertical concentration profile under a prescribed convergence condition. To overcome the computational challenges associated with estimating the model parameters, a constrained optimization framework

[1] A manuscript containing the work presented in this chapter has been published in *Stochastic Environmental Research and Risk Assessment*, 40(44), (2026), DOI: https://doi.org/10.1007/s00477-025-03133-7.

embedding the convergence condition is formulated. Regression and error analyses, using laboratory and field datasets, display superior performance of the proposed model relative to existing entropy-based probabilistic and classical deterministic models.

6.1 Introduction

The vertical distribution of velocity and suspended sediment particles in sediment-laden turbulent flows through open channels has been widely studied to mitigate pollutant transport, channel bank erosion, and other potential hazards associated with water bodies. Sediments frequently act as carriers of toxic and non-degradable materials, thereby exerting a significant influence on water quality and aquatic ecosystems. In this context, accurate representation of the vertical distribution of suspended sediment concentration (SSC) in turbulent open channel flows is central to the analysis of sediment transport mechanisms that influence river morphodynamics, pollutant dispersion, and channel stability. Research on sediment transport in rivers, irrigation canals, and other open channel flows has traditionally been classified into studies on bed-load transport and suspended-load transport, as comprehensively discussed by Dey (2012). While both modes contribute to sediment dynamics, suspended-load transport has received particular attention due to its dominant role in controlling channel morphology, sediment fluxes, and pollutant dispersion in turbulent flows. Extensive theoretical, experimental, and field-based investigations addressing suspended sediment dynamics and associated flow-sediment interactions are systematically reviewed in Dey (2014). These studies primarily focus on the estimation of SSC profiles, which form the basis for determining reference concentration levels, suspended-load transport rates, and transport capacity in open channels. Despite the significant progress reported in the literature, accurately representing the vertical distribution of SSC under varying flow and sediment conditions remains challenging, thereby motivating the continued development of improved and physically consistent modeling approaches.

The vertical distribution of suspended sediment concentration (SSC) has been broadly categorized into three types, namely Type I, Type II, and Type III profiles (see Li et al., 2020, and references therein). In Type I distributions, the sediment concentration increases gradually from the channel bed to a certain elevation above the bed and decreases thereafter toward the water surface, resulting in a maximum concentration occurring at an intermediate height. In Type II profiles, the SSC decreases monotonically from the bed to the flow surface, typically exhibiting a hyperbolic, upward concave shape. In contrast, Type III profiles are characterized by a gentle, asymmetric inverse S-shaped distribution extending from the water surface to the channel bed.

The concentration of sediment maintained in suspension is governed by several interacting factors, including particle size, settling velocity, fluid and sediment densities, flow stratification, and turbulent stresses. Depending on how these factors are incorporated, methods for predicting SSC distributions are commonly classified as empirical, hydraulic, or entropy-based approaches. Empirical models are often expressed in exponential or power-law forms (Singh, 1996) or linear formulations (Simons and Senturk, 1992). Among hydraulic approaches, the most widely accepted method for determining the vertical distribution of sediment concentration is based on the diffusion theory originally proposed by Rouse (1937).

Hydraulic diffusion-based models describe suspended sediment transport in turbulent flows as a balance between the upward transport of sediment particles by turbulent velocity fluctuations and their downward motion due to gravitational settling. Under equilibrium conditions and assuming uniform channel geometry, this balance leads to a vertically consistent SSC profile along the flow direction (Sturm, 2010). The governing differential equation for sediment concentration along the vertical axis may therefore be expressed as

$$-\epsilon_s \frac{dc}{dy} = \omega_s c, \tag{6.1}$$

where c denotes the sediment concentration at a vertical level y measured from the channel bed, ϵ_s is the diffusion coefficient for sediment transfer, and ω_s is the settling velocity of sediment particles. The settling velocity plays a crucial role in distinguishing suspended load from bed load and depends on particle size and shape, submerged specific weight, kinematic viscosity of water, and the densities of water and sediment particles. Since sediment concentration generally decreases with height above the bed, it follows that $\frac{dc}{dy} < 0$.

In alluvial channel flows, the diffusion coefficient ϵ_s is not constant, particularly near the bed where turbulence characteristics vary with elevation. Consequently, ϵ_s is commonly expressed as $\epsilon_s = \beta \epsilon_v$, where β is a proportionality coefficient, often referred to as the inverse of the turbulent Schmidt number (see Woo et al., 1988; Tsujimoto, 2010), and ϵ_v is the turbulent eddy viscosity for momentum transfer. The eddy viscosity may be computed as (Chiu et al., 2000):

$$\epsilon_v = v_*^2 \frac{\tau}{\tau_0} \left(\frac{dv}{dy} \right)^{-1}, \tag{6.2}$$

where $\frac{dv}{dy}$ is the vertical velocity gradient, v_* is the shear velocity, and $\frac{\tau}{\tau_0}$ denotes the normalized shear stress, with τ_0 representing the shear stress at the channel bed.

Solving equation (6.1) using (6.2) yields the general expression for sediment concentration distribution:

$$\frac{c}{c_r} = \exp\left[-\frac{\omega_s}{\beta v_*^2}\int_0^y \left(\frac{\tau}{\tau_0}\right)^{-1}\frac{dv}{dy}\,dy\right], \tag{6.3}$$

where c_r is the sediment concentration at a reference level r. Various SSC models have been derived from Eq. (6.3) by adopting different shear stress and velocity distributions. A well-known example is the Rouse equation (Rouse, 1937), obtained by employing the Prandtl-von Kármán logarithmic velocity profile and assuming a linear shear stress distribution, given by

$$\frac{c}{c_r} = \left[\left(\frac{h-y}{y}\right)\left(\frac{r}{h-r}\right)\right]^R, \tag{6.4}$$

where $R = \omega_s/(\beta\kappa v_*)$ is the Rouse number, h is the total flow depth, and κ is the von Kármán constant.

Although the Rouse equation has been validated against experimental and field data for moderate concentrations away from the bed and free surface, significant deviations have been reported under high concentration conditions. Einstein and Chien (1955) observed that the Rouse formulation fails to accurately represent SSC distributions near the channel bed and close to the water surface, primarily due to its neglect of bed-load transport effects (Simons and Senturk, 1992). To address these limitations, Chiu et al. (2000) proposed an alternative entropy-based SSC model derived from Eq. (6.3) using Shannon entropy (Shannon, 1948), which was shown to yield improved predictions, particularly near the channel bed.

$$\frac{C}{C_0} = \left[\frac{1-\frac{y}{h}}{1+(e^M-1)\frac{y}{h}}\right]^{\lambda'}, \tag{6.5}$$

where $C = C(y=0)$, $j = \frac{y}{h}$, $\lambda' = \lambda P$, $\lambda = \frac{\omega_s \bar{u}}{\beta v_*^2}$ and $P = \frac{1-e^{-M}}{M\delta}$, $\delta = \frac{\bar{u}}{u_{max}} = \frac{e^M}{e^M-1} - \frac{1}{M}$. Here, the mean velocity $\bar{u} = \frac{Q}{A}$, where Q is the flow discharge rate and A is the cross-sectional area of the channel under study. The settling velocity ω_s can be calculated from the relation:

$$\frac{\omega_s d}{\nu} = (\sqrt{25+1.2d_*^2}-5)^{1.5},$$

where d = diameter of sediment particle , ν = kinematic viscosity of the fluid; and

$$d_* = \left(\frac{(\rho_s-\rho)g}{\rho\nu^2}\right)d,$$

with ρ_s representing sediment density and ρ denoting fluid density. This model (6.5) was further refined by Chiu et al. (2000) to represent the velocity dip position where maximum velocity is observed below the water surface. Considering the variable

$$j = \frac{y}{h - h_d} exp\left(1 - \frac{y}{h - h_d}\right), \tag{6.6}$$

the refined Chiu model is defined as:

$$\frac{C}{C_0} = exp\left(-\lambda' I\left(\frac{y}{h}, \frac{h_d}{h}, M\right)\right), \tag{6.7}$$

where

$$I\left(\frac{y}{D}, \frac{h}{D}, M\right) = \frac{e^M}{j_{max}} \int_0^y h_j \left[1 + (e^M - 1)\frac{j}{j_{max}}\right] \left(\frac{\tau}{\tau_0}\right)^{-1} dj,$$

$$\frac{\tau}{\tau_0} = \left(\frac{h_d}{h}\right)\left(1 - \frac{y}{h - h_d}\right) + \left(1 - \frac{h_d}{h}\right)\left(1 - \frac{y}{(h - h_d)}\right)^2,$$

and $h_j = \frac{dy}{dj} = \left[\frac{j}{y}(1 - \frac{y}{h - h_d})\right]^{-1}$. In this model, $h_d > 0$ when maximum velocity v_{max} occurs below the fluid surface and $h_d \leq 0$ if v_{max} is observed on the fluid surface. However, the model (6.7) was not much useful and practical due to inclusion of too many parameters and it also required solving the integral $I\left(\frac{y}{D}, \frac{h}{D}, M\right)$, which was not always feasible. In an attempt to simplify the Chiu model (6.7), Choo (2000) developed an alternative model for describing the vertical SSC distribution in terms of Shannon entropy. The Choo SSC formula can be expressed as:

$$\frac{c}{c_0} = \frac{c_0}{R'} \log\left\{exp(R') - \left[exp(R') - exp\left(\frac{R'}{r}\right)\right]\frac{y}{h}\right\}$$

where $R' = \lambda_1 c_0$, λ_1 = Lagrange multiplier, c_0 = maximum sediment concentration at $y = 0$ or at a reference height, $r = c_0/c_h$, with c_h representing the surface concentration. Recently, Mirauda et al. (2018b) derived a new SSC model from eq. (6.7) to increase the practical usefulness of the refined Chiu model by expanding the exponential function in the generalized spatial coordinate j expressed by eq. (6.7) and approximating upto the leading order term. Therefore, using the approximated spatial coordinate $j = \frac{e}{h-h_d}y$ and the linear shear stress distribution $\frac{\tau}{\tau_0} = 1 - \frac{h-h_d}{eh}j = 1 - nj$, the simplified Chiu model as proposed by Mirauda et al. (2018b) is defined as:

$$\frac{C}{C_0} = \left[\frac{1 - \frac{y}{h}}{1 + (e^M - 1)\frac{ey}{h - h_M}}\right]^{\lambda_m}, \tag{6.8}$$

where

$$\lambda_m = \frac{\lambda(e^M - 1)^2}{[Me^M - (e^M - 1)][(e^M - 1) + \frac{h - h_d(M)}{eh}]}$$

with the veocity dip position $h_d = h_d(M)$ chosen as a function of M, defined as (Mirauda et al., 2018a):

$$h_d(M) = h - h\left[\frac{M}{e^M - 1}\left(e^M\left(\frac{1}{M} - \frac{1}{M^2} + \frac{1}{M^2}\right)\right)\right]$$

The parameter M represents channel cross-sectional geometry, coarseness and morphology which interacts with the gradient of vertical velocity and shear stress profiles (Mirauda et al., 2018b). However, these SSC formulas were based on Shannon entropy which failed to provide a holistic representation of the complex non-linear interactions of hydraulic variables affecting the sediment concentration in open channels. To address the limitations of Shannon entropy, Cui and Singh (2014) derived a SSC model in terms of Tsallis entropy, which is a parametric generalization of Shannon entropy. The Cui and Singh SSC formula is defined as:

$$\frac{c}{c_0} = 1 - \frac{1}{N'}\left(1 - \left\{(1-N')^{\frac{m'}{m'-1}} + \left[1 - (1-N')\frac{m'}{m'-1}\right]F(c)\right\}^{\frac{m'-1}{m'}}\right), \tag{6.9}$$

where $F(c)$ is computed from eq. (24) of Cui and Singh (2014) and N is obtained from the expression:

$$\frac{\bar{c}}{c_0} = 0.176 + 0.5083N' - 0.1561N^2,$$

with $\bar{c}$ denoting mean concentration, c_0 representing concentration at channel bed ($y = 0$).

These authors demonstrated that entropy-based equations yield more accurate predictions of SSC than traditional empirical or hydraulics-based models. Following this finding, several other entropy-based approaches emerged, particularly those built upon generalizations of Shannon entropy, such as Rényi entropy (Ghoshal et. al, 2018). Subsequently, some theories were developed to predict SSC using generalized forms of Shannon entropy involving fractional derivatives (Ahamed and Kundu, 2023). More recently, Kumbhakar and Tsai (2023) showed that fractional Machado entropy offers superior predictive accuracy for velocity distribution compared to conventional entropy measures such as Shannon, Tsallis, and Rényi. In light of this, it would be compelling to investigate whether Machado entropy can be applied to derive the vertical SSC profile, and to assess its performance with respect to the extant entropy-based SSC distribution models.

It is useful to clarify the relation between the present chapter and Chapter 5 here. Chapter 5 develops an FDE-based suspended sediment concentration model mainly through an entropy-optimization and parameter-estimation framework. The present chapter advances that development by deriving a more explicit analytical normalized suspended sediment concentration profile. In particular, the optimization framework used here incorporates three constraints, rather than the two-constraint structure commonly used in earlier SSC entropy models. This additional constraint improves the flexibility of the analytical profile and helps represent the vertical variation of concentration more directly.

Thus, Chapter 6 should not be viewed as a repetition of Chapter 5. Instead, it is an analytical extension that provides a closed-form NSSC representation, reduces dependence on repeated numerical fitting, and makes comparison with classical models such as Rouse/Rousian-type formulations more transparent.

Henceforth, the primary objective of this study is to derive the vertical distribution of SSC using the framework of fractional Machado entropyas presented in Section 6.2, and to validate the resulting distribution against experimental and field data by comparing its performance with that of the classical Rouse model and other existing entropy-based formulations (Chiu et al., 2000; Choo, 2000; Cui and Singh, 2014; Mirauda et al., 2018b, models), as discussed in Section 6.3. The proportionality constant β is defined as the ratio of sediment diffusivity, representing the momentum transferred by sediment particles (ϵ_s), to the momentum diffusion coefficient of the flowing water per unit volume, commonly referred to as the eddy viscosity (ϵ_v). This constant can therefore be interpreted as a momentum conservation coefficient governing the vertical SSC distribution. For the sake of simplicity, it is assumed in the present study that the sediment diffusivity is equal to the kinematic eddy viscosity, which is equivalent to momentum diffusion coefficient (ϵ_m), i.e., $\epsilon_s = \epsilon_v = \epsilon_m$, which implies $\beta = 1$. Consequently, the proportionality constant β is considered to be 1 in this study. In addition, it is assumed that the sediment concentration diminishes to zero at the water surface. Finally, Section 6.4 concludes the chapter with a summary of the key findings and a discussion on the implications of the proposed model for future research.

6.2 Derivation of vertical profile of normalized SSC (NSSC)

In this study, we employ Machado fractional entropy defined as (Machado, 2014):

$$H_{M,q}(p) = \sum_i p(i) \left[-\frac{p(i)^{-q}}{\Gamma(q+1)} (\log p(i) + \tilde{\psi}) \right], \; q \in \mathbb{R}, \tag{6.1}$$

which generalizes Shannon entropy by considering the Shannon information gain function $I_S(p(i)) = -\log p(i)$ as a zeroth-order function lying between the integer-order derivative cases $D^{-1}I(p(i)) = p(i)(1 - \log p(i))$ and $D^{1}(p(i)) = -\frac{1}{p(i)}$, and then generalizing the Ubriaco information gain function $I_U(p(i)) = (-\log p(i))^{\alpha}$ by using fractional calculus tools to give his definition for information gain function with real order q as follows:

$$I_M^q(p(i)) = D^q I_S(p(i)) = -\frac{p(i)^{-q}}{\Gamma(q+1)}\left(\log p(i) + \tilde{\psi}\right), \quad q \in \mathbb{R}, \tag{6.2}$$

where D^q is the fractional derivative operator and $\tilde{\psi} = \psi(1) - \psi(1-q)$ involves digamma functions $\psi(\cdot)$. This fractional approach introduces an index q that controls the degree of "fractionality", adding additional flexibility to the entropy function, thereby allowing it to represent both trustworthy information represented by positive values of I_M^q and misleading information in sediment concentration indicated by the negative values. In short, the Machado entropy derives from a fractional calculus extension of the Shannon information gain, offering a flexible parameter q to model uncertainty and information reliability in sediment concentration data.

Definition 6.2.1. ***Fractional entropy:*** *If we consider the normalized suspended sediment concentration (NSSC) $\hat{\mathcal{C}} = \mathcal{C}/c_{max}$, c_{max} being the maximum concentration at a vertical height y of an open channel, as the random variable with $f(\hat{c})$ being the probability density function (pdf), then the Machado entropy for the NSSC is defined as:*

$$H_M^q(\hat{\mathcal{C}}, f) = \int_{\hat{c}_h}^{1} f(\hat{c})\left[-\frac{f(\hat{c})^{-q}}{\Gamma(q+1)}\left(\log f(\hat{c}) + \tilde{\psi}\right)\right] d\hat{c}, q \in \mathcal{R}. \tag{6.3}$$

Here $\hat{c}_h = c_h/c_{max}$ is the normalized sediment concentration at the channel surface height $y = h$, $\tilde{\psi} = \psi(1) - \psi(1-q)$, $\Gamma(\cdot)$ and $\psi(\cdot)$ represent gamma and digamma functions, respectively.

When $q = 0$, we get back the Shannon differential entropy (Shannon, 1948)

$$H_S(\hat{\mathcal{C}}, f) = -\int_{\hat{c}_h}^{1} f(\hat{c}) \log f(\hat{c}) d\hat{c}. \tag{6.4}$$

6.2.1 Derivation of fractional entropy-based NSSC in terms of vertical height

To obtain the pdf along the vertical section of an open channel in terms of the fractional entropy (6.3), one can apply the maximum entropy principle introduced by Jaynes (1957a,b). For that purpose, we need to specify the constraint equations in order to define the optimization problem of maximizing the entropy (6.3). While considering the NSSC distribution in open-channels, the first-order statistical moment constraint representing conservation of mass is the primary condition that needs to be satisfied by any random variable along with the normalization constraint. The normalization constraint can be defined as:

$$\int_{\hat{c}_h}^{1} f(\hat{c})d\hat{c} = 1, \tag{6.5}$$

and the conservation of mass constraint is represented as:

$$\int_{\hat{c}_h}^{1} \hat{c} f(\hat{c})d\hat{c} = \bar{\hat{c}}, \tag{6.6}$$

where $\bar{\hat{c}} = \bar{c}/c_{max}$ is the normalized mean concentration. Other moment constraints which are ignored so as to reduce the complexity of the NSSC distribution model are:

$$\int_{\hat{c}_h}^{1} \hat{c}^2 f(\hat{c})d\hat{c} = \beta \bar{\hat{c}}^2, \tag{6.7}$$

and

$$\int_{\hat{c}_h}^{1} \hat{c}^3 f(\hat{c})d\hat{c} = \alpha \bar{\hat{c}}^3, \tag{6.8}$$

where β and α are the momentum and energy distribution coefficients, respectively.

Therefore, the optimization problem can be constructed as:

$$\max_{f(\hat{c})} \; H_M^q(\hat{\mathcal{C}}, f) \text{ subject to } \int_{\hat{c}_h}^{1} \hat{c}^i f(\hat{c})d\hat{c} = M_i; \; i = 0, 1, \tag{6.9}$$

where $M_0 = 1$, $M_1 = \bar{\hat{c}}$. The optimization problem can be solved for the least biased pdf $f(\hat{c})$ of the normalized random variable $\hat{\mathcal{C}}$ with the help of the method of Lagrange multipliers. The Lagrange function can be developed as:

$$L(f,\hat{c}) = \int_{\hat{c}_h}^{1} f(\hat{c}) \left[-\frac{f(\hat{c})^{-q}}{\Gamma(q+1)} \left(\log f(\hat{c}) + \tilde{\psi} \right) \right] d\hat{c} - \nu_0 \left(\int_{\hat{c}_h}^{1} f(\hat{c})d\hat{c} - 1 \right) - \nu_1 \left(\int_{\hat{c}_h}^{1} \hat{c} f(\hat{c})d\hat{c} - \bar{\hat{c}} \right), \tag{6.10}$$

where ν_0 and ν_1 are the Lagrange multipliers. Then the Euler-Lagrange equation can be expressed as:

$$\frac{\partial L}{\partial f} - \frac{d}{d\hat{c}} \left(\frac{\partial L}{\partial f'} \right) = 0. \tag{6.11}$$

From (6.10) and (6.11), we get

$$\frac{\partial L}{\partial f} = 0. \tag{6.12}$$

Consequently, substituting the value of L from (6.10) in (6.12) and ignoring the integral signs, we obtain

$$f(\hat{c})^{-q}\left[\frac{1}{\Gamma(q+1)}(q-1)\log f(\hat{c})+\frac{\tilde{\psi}}{\Gamma(q+1)}(q-1)-\frac{1}{\Gamma(q+1)}\right]=\nu_0+\nu_1\hat{c}. \tag{6.13}$$

Starting from Eq. (6.13), we introduce the notational constants

$$k=\frac{\tilde{\psi}}{\Gamma(q+1)}, \qquad k_1=\frac{1}{\Gamma(q+1)},$$

so that Eq. (6.13) can be rewritten in the compact form

$$f(\hat{c})^{-q}\Big[k_1(q-1)\log f(\hat{c})+k(q-1)-k_1\Big]=\nu_0+\nu_1\hat{c}. \tag{6.14}$$

Using $k_2=k(q-1)-k_1$, Eq. (6.14) becomes

$$f(\hat{c})^{-q}\Big[k_1(q-1)\log f(\hat{c})+k_2\Big]=\nu_0+\nu_1\hat{c}. \tag{6.15}$$

Next, we set

$$x=\log f(\hat{c}) \quad\Longrightarrow\quad f(\hat{c})^{-q}=e^{-qx}.$$

Substituting into Eq. (6.15) yields

$$e^{-qx}\Big[k_1(q-1)x+k_2\Big]=\nu_0+\nu_1\hat{c}. \tag{6.16}$$

Dividing both sides by $k_1(q-1)$ gives

$$e^{-qx}\left[x+\frac{k_2}{k_1(q-1)}\right]=\frac{\nu_0+\nu_1\hat{c}}{k_1(q-1)}. \tag{6.17}$$

To bring this into a standard Lambert-W form, we write the expression inside the square bracket as $(x-b)$ by defining

$$b=\frac{k_2}{k_1(1-q)}$$

Then Eq. (6.17) becomes

$$e^{qx}=\frac{k_1(q-1)}{\nu_0+\nu_1\hat{c}}\,(x-b). \tag{6.18}$$

This matches the canonical identity: if $e^{-mx}=n(x-b)$, then

$$x=b+\frac{1}{m}W\left(\frac{m\,e^{-mb}}{n}\right).$$

Here we identify

$$m = -q, \qquad n = \frac{k_1(q-1)}{\nu_0 + \nu_1 \hat{c}}, \qquad b = \frac{k_2}{k_1(1-q)}.$$

Therefore,

$$x = \frac{k_2}{k_1(1-q)} - \frac{1}{q} W\left(\frac{q(\nu_0 + \nu_1 \hat{c})}{k_1(1-q)} \exp\left[\frac{q}{1-q}\frac{k_2}{k_1}\right]\right). \tag{6.19}$$

Since $f(\hat{c}) = e^x$, we obtain the pdf in Lambert-W form:

$$f(\hat{c}) = \exp\left[\frac{k_2}{k_1(1-q)} - \frac{1}{q} W\left(\frac{q(\nu_0 + \nu_1 \hat{c})}{k_1(1-q)} \exp\left[\frac{q}{1-q}\frac{k_2}{k_1}\right]\right)\right]. \tag{6.20}$$

For convenience, we define the constants

$$K_1 = \exp\left(\frac{k_2}{k_1(1-q)}\right), \qquad K_2 = \frac{q}{k_1(1-q)} \exp\left(\frac{k_2}{k_1}\frac{q}{1-q}\right), \qquad x_0 = K_2(\nu_0 + \nu_1 \hat{c}).$$

Using the Lambert-W identity: $\exp(-W(x)) = W(x)/x$, Eq. (6.20) can be expressed in the compact form

$$f(\hat{c}) = K_1 \left[\frac{W(x_0)}{x_0}\right]^{\frac{1}{q}}, \tag{6.21}$$

which is the form adopted in the optimization problem represented by Eq. (6.9).

In order to obtain an explicit analytical approximation of the pdf $f(\hat{c})$ in Eq. (6.21), we restrict to the principal branch of the Lambert function, $W_0(\cdot)$, and employ its Taylor expansion about the origin (Corless et al., 1996):

$$W(x_0) = \sum_{i=1}^{\infty} \frac{(-i)^{i-1}}{i!} x_0^i.$$

Since this series converges for $|x_0| < 1/e$, we truncate it to the first two terms, yielding

$$W(x_0) \approx x_0 - x_0^2. \tag{6.22}$$

It is noted that at least two terms are required to obtain an approximation capable of satisfying the two constraints in Eqs. (6.5) and (6.6).

Substituting Eq. (6.22) into Eq. (6.21) and using $x_0 = K_2(\nu_0 + \nu_1 \hat{c})$, the pdf takes the explicit form

$$f(\hat{c}) = K_1 \left[1 - K_2(\nu_0 + \nu_1 \hat{c})\right]^{\frac{1}{q}}. \tag{6.23}$$

Consequently, the validity of Eq. (6.23) is restricted by the convergence condition $|x_0| < 1/e$, i.e.,

$$|K_2(\nu_0 + \nu_1 \hat{c})| < \frac{1}{e}. \tag{6.24}$$

To obtain a constraint that is independent of $\hat{c}$, we use the triangle inequality $|x_1+x_2| \leq |x_1| + |x_2|$ for $x_1, x_2 \in \mathbb{R}$:

$$|\nu_0| = |\nu_0 + \nu_1\hat{c} - \nu_1\hat{c}| \leq |\nu_0 + \nu_1\hat{c}| + |\nu_1\hat{c}|.$$

Since $0 \leq \hat{c} \leq 1$, it follows that $|\nu_1\hat{c}| \leq |\nu_1|$, and hence

$$\begin{aligned} |\nu_0| &\leq |\nu_0 + \nu_1\hat{c}| + |\nu_1| \\ \implies \quad |\nu_0 + \nu_1\hat{c}| &\geq |\nu_0| - |\nu_1|. \end{aligned} \tag{6.25}$$

Combining Eqs. (6.24) and (6.25) and using $|x_1x_2| = |x_1||x_2|$ for $x_1, x_2 \in \mathbb{R}$, we obtain the following sufficient inequality constraint for the proposed pdf:

$$|K_2|\big(|\nu_0| - |\nu_1|\big) \leq \frac{1}{e}. \tag{6.26}$$

To obtain the cumulative distribution function (cdf) of the normalized suspended sediment concentration (NSSC) with respect to the concentration domain, we define

$$\begin{aligned} F(\hat{c}) &= P(\hat{\mathcal{C}} \leq \hat{c}) \\ &= \int_{\hat{c}_h}^{\hat{c}} f(\hat{c})\, d\hat{c}, \end{aligned} \tag{6.27}$$

where $\hat{c}_h$ denotes the normalized sediment concentration at the lower bound of the concentration domain.

Substituting the expression for $f(\hat{c})$ from Eq. (6.23) into Eq. (6.27) and integrating, the cdf is obtained as

$$F(\hat{c}) = \frac{K_1}{\nu_1 K_2}\left(\frac{q}{q+1}\right)\left[(1 - K_2(\nu_0 + \nu_1\hat{c}_h))^{\frac{q+1}{q}} - (1 - K_2(\nu_0 + \nu_1\hat{c}))^{\frac{q+1}{q}}\right]. \tag{6.28}$$

In order to derive an explicit expression for NSSC $\hat{c}$ as a function of the vertical coordinate, the concentration-based cdf in Eq. (6.28) is related to a spatial cdf formulation. Following the hypothesis proposed by Ghoshal et. al (2018), the cdf of $\hat{\mathcal{C}}$ in terms of the vertical height is expressed as

$$F(\hat{c}) = [1 - \mathcal{Y}^a]\exp(-\mathcal{Y}^a), \tag{6.29}$$

where

$$\mathcal{Y} = \frac{y - y_r}{h - y_r},$$

with h denoting the total flow depth, y_r the vertical location at which the maximum sediment concentration occurs, and $y_r \leq y \leq h$. The parameter $a \in (0,1)$ is a fitting parameter that characterizes sediment properties.

Equating the concentration-domain cdf in Eq. (6.28) with the spatial cdf in Eq. (6.29), we obtain

$$\frac{K_1}{\nu_1 K_2}\left(\frac{q}{q+1}\right)\Bigg[(1-K_2(\nu_0+\nu_1\hat{c}_h))^{\frac{q+1}{q}} - (1-K_2(\nu_0+\nu_1\hat{c}))^{\frac{q+1}{q}}\Bigg] = [1-\mathcal{Y}^a]\exp(-\mathcal{Y}^a). \tag{6.30}$$

Multiplying both sides of Eq. (6.30) by

$$\frac{\nu_1 K_2}{K_1}\left(\frac{q+1}{q}\right),$$

we get

$$(1-K_2(\nu_0+\nu_1\hat{c}_h))^{\frac{q+1}{q}} - (1-K_2(\nu_0+\nu_1\hat{c}))^{\frac{q+1}{q}} = \frac{\nu_1 K_2}{K_1}\left(\frac{q+1}{q}\right)[1-\mathcal{Y}^a]\exp(-\mathcal{Y}^a). \tag{6.31}$$

Rearranging Eq. (6.31) gives

$$(1-K_2(\nu_0+\nu_1\hat{c}))^{\frac{q+1}{q}} = (1-K_2(\nu_0+\nu_1\hat{c}_h))^{\frac{q+1}{q}} - \frac{\nu_1 K_2}{K_1}\left(\frac{q+1}{q}\right)[1-\mathcal{Y}^a]\exp(-\mathcal{Y}^a). \tag{6.32}$$

For notational convenience, we define

$$Y = \left[(1-K_2(\nu_0+\nu_1\hat{c}_h))^{\frac{q+1}{q}} - \frac{\nu_1 K_2}{K_1}\left(\frac{q+1}{q}\right)\left(1-\left(\frac{y-y_r}{h-y_r}\right)^a\right)\exp\left(-\left(\frac{y-y_r}{h-y_r}\right)^a\right)\right]. \tag{6.33}$$

Then Eq. (6.32) becomes

$$(1-K_2(\nu_0+\nu_1\hat{c}))^{\frac{q+1}{q}} = Y. \tag{6.34}$$

Raising both sides of Eq. (6.34) to the power $\frac{q}{q+1}$, we obtain

$$1-K_2(\nu_0+\nu_1\hat{c}) = Y^{\frac{q}{q+1}}. \tag{6.35}$$

Hence,

$$K_2(\nu_0+\nu_1\hat{c}) = 1-Y^{\frac{q}{q+1}}. \tag{6.36}$$

Dividing by K_2 gives

$$\nu_0 + \nu_1 \hat{c} = \frac{1}{K_2}\left(1 - Y^{\frac{q}{q+1}}\right). \tag{6.37}$$

Therefore, solving for $\hat{c}$, the normalized suspended sediment concentration profile is obtained as:

$$\hat{c} = \frac{1}{\nu_1}\left[\frac{1}{K_2}\left(1 - Y^{\frac{q}{q+1}}\right) - \nu_0\right]. \tag{6.38}$$

In the special case where the normalized concentration at the lower bound vanishes, i.e. $\hat{c}_h = 0$, Eq. (6.33) simplifies to

$$Y = (1 - K_2\nu_0)^{\frac{q+1}{q}} - \frac{\nu_1 K_2}{K_1}\left(\frac{q+1}{q}\right)\left(1 - \left(\frac{y - y_r}{h - y_r}\right)^a\right)\exp\left(-\left(\frac{y - y_r}{h - y_r}\right)^a\right), \tag{6.39}$$

which is adopted in the subsequent analysis.

For the profile to remain real-valued, the quantity Y must be nonnegative and the powers appearing in Eqs. (6.38)–(6.39) must be well-defined. These admissibility requirements are imposed during parameter estimation through the convergence and feasibility constraints discussed below.

6.2.2 Determination of variable parameters

The proposed fractional entropy-based concentration distribution defined by Eqs. (6.38) and (6.39) depends on three unknown parameters, namely the Lagrange multipliers ν_0 and ν_1, and the fractional entropy index $q \in \mathbb{R}$. Determination of these parameters requires three independent constraint equations. However, introducing additional constraints generally increases the computational complexity of the model, while prescribing a fixed value of q would restrict the physical generality of the formulation. To address this issue, the second-order moment constraint given by Eq. (6.7) is employed together with the two primary constraints defined by Eqs. (6.5) and (6.6). In order to further reduce computational complexity, the momentum conservation coefficient β is assumed to be unity. Moreover, the original entropy maximization problem is reformulated as a minimization problem to accommodate the inequality constraint (6.26), allowing the simultaneous determination of the Lagrange multipliers and the fractional entropy parameter q.

Substituting the probability density function given by Eq. (6.23) into the constraint equations (6.5), (6.6), and (6.7), and introducing the change of variables

$$u = \nu_0 + \nu_1 \hat{c},$$

the resulting integrals are evaluated by parts over the interval $\hat{c} \in [0, 1]$. This procedure yields the following system of nonlinear algebraic equations.

Normalization constraint

$$-\frac{K_1}{K_2\nu_1}\left(\frac{q}{q+1}\right)\left[(1-K_2(\nu_0+\nu_1))^{\frac{q+1}{q}} - (1-K_2\nu_0)^{\frac{q+1}{q}}\right] = 1. \tag{6.40}$$

Derivation of the normalization constraint (6.40): The normalization condition for $\hat{c}_h = 0$ is

$$\int_0^1 f(\hat{c})\, d\hat{c} = 1, \tag{6.41}$$

where the proposed pdf is given by Eq. (6.23). Substituting (6.23) into (6.41) yields

$$K_1 \int_0^1 [1 - K_2(\nu_0 + \nu_1\hat{c})]^{\frac{1}{q}}\, d\hat{c} = 1. \tag{6.42}$$

Introducing the change of variables $u = \nu_0 + \nu_1\hat{c}$, under which the limits $\hat{c} \in [0, 1]$ map to $u \in [\nu_0, \nu_0 + \nu_1]$. Then we get

$$K_1 \frac{1}{\nu_1} \int_{\nu_0}^{\nu_0+\nu_1} [1 - K_2 u]^{\frac{1}{q}}\, du = 1. \tag{6.43}$$

Next, we set $z = 1 - K_2 u$, so that $dz = -K_2\, du$ and $du = -\frac{1}{K_2} dz$. The integration limits become

$$u = \nu_0 \;\Rightarrow\; z_0 = 1 - K_2\nu_0, \qquad u = \nu_0 + \nu_1 \;\Rightarrow\; z_1 = 1 - K_2(\nu_0 + \nu_1).$$

Hence, (6.43) becomes

$$K_1 \frac{1}{\nu_1}\left(-\frac{1}{K_2}\right) \int_{z_0}^{z_1} z^{\frac{1}{q}}\, dz = 1. \tag{6.44}$$

Evaluating the power integral,

$$\int z^{\frac{1}{q}}\, dz = \frac{q}{q+1}\, z^{\frac{q+1}{q}},$$

and substituting into (6.44) gives

$$-\frac{K_1}{K_2\nu_1}\left(\frac{q}{q+1}\right)\left[z_1^{\frac{q+1}{q}} - z_0^{\frac{q+1}{q}}\right] = 1. \tag{6.45}$$

Finally, replacing z_0 and z_1 by their definitions yields the normalization constraint (6.40)

First-moment constraint

$$-\frac{K_1}{(K_2\nu_1)^2}\Bigg[(1-K_2\nu_0)\frac{q}{q+1}\left((1-K_2(\nu_0+\nu_1))^{\frac{q+1}{q}}-(1-K_2\nu_0)^{\frac{q+1}{q}}\right)$$
$$-\frac{q}{1+2q}\left((1-K_2(\nu_0+\nu_1))^{\frac{1+2q}{q}}-(1-K_2\nu_0)^{\frac{1+2q}{q}}\right)\Bigg]=\bar{\hat{c}}. \tag{6.46}$$

Derivation of the first-moment constraint (6.46): The first-moment constraint for $\hat{c}_h = 0$ is

$$\int_0^1 \hat{c}\, f(\hat{c})\, d\hat{c} = \bar{\hat{c}}, \tag{6.47}$$

where the proposed pdf is given by Eq. (6.23). Substituting (6.23) into (6.47) gives

$$K_1\int_0^1 \hat{c}\,[1-K_2(\nu_0+\nu_1\hat{c})]^{\frac{1}{q}}\; d\hat{c}=\bar{\hat{c}}. \tag{6.48}$$

Using the substitution $u=\nu_0+\nu_1\hat{c}$ in (6.48), such that the limits $\hat{c}\in[0,1]$ map to $u\in[\nu_0,\nu_0+\nu_1]$. This yields

$$\frac{K_1}{\nu_1^2}\int_{\nu_0}^{\nu_0+\nu_1}(u-\nu_0)\,(1-K_2u)^{\frac{1}{q}}\; du=\bar{\hat{c}}. \tag{6.49}$$

Next, if we set $z=1-K_2u$, then

$$u=\nu_0\Rightarrow z_0=1-K_2\nu_0, \qquad u=\nu_0+\nu_1\Rightarrow z_1=1-K_2(\nu_0+\nu_1),$$

and

$$u-\nu_0=\frac{1-z}{K_2}-\nu_0=\frac{(1-K_2\nu_0)-z}{K_2}.$$

Substituting into (6.49) gives

$$-\frac{K_1}{(K_2\nu_1)^2}\int_{z_0}^{z_1}\Big((1-K_2\nu_0)-z\Big)\,z^{\frac{1}{q}}\,dz=\bar{\hat{c}}. \tag{6.50}$$

Splitting the integral and using the standard power integrals

$$\int z^{\frac{1}{q}}\,dz=\frac{q}{q+1}\,z^{\frac{q+1}{q}}, \qquad \int z^{1+\frac{1}{q}}\,dz=\frac{q}{1+2q}\,z^{\frac{1+2q}{q}},$$

we obtain

$$-\frac{K_1}{(K_2\nu_1)^2}\left[(1-K_2\nu_0)\frac{q}{q+1}\left(z_1^{\frac{q+1}{q}}-z_0^{\frac{q+1}{q}}\right)-\frac{q}{1+2q}\left(z_1^{\frac{1+2q}{q}}-z_0^{\frac{1+2q}{q}}\right)\right]\quad=\bar{\hat{c}}. \tag{6.51}$$

Finally, substituting $z_0=1-K_2\nu_0$ and $z_1=1-K_2(\nu_0+\nu_1)$ yields Eq. (6.46).

Second-moment constraint

$$
\begin{aligned}
-\frac{K_1}{(K_2\nu_1)^3}\Bigg[&(1-K_2\nu_0)^2\frac{q}{q+1}\left((1-K_2(\nu_0+\nu_1))^{\frac{q+1}{q}}-(1-K_2\nu_0)^{\frac{q+1}{q}}\right)\\
&-2(1-K_2\nu_0)\frac{q}{1+2q}\left((1-K_2(\nu_0+\nu_1))^{\frac{1+2q}{q}}-(1-K_2\nu_0)^{\frac{1+2q}{q}}\right)\\
&+\frac{q}{1+3q}\left((1-K_2(\nu_0+\nu_1))^{\frac{1+3q}{q}}-(1-K_2\nu_0)^{\frac{1+3q}{q}}\right)\Bigg]=\bar{\hat{c}}^2. \qquad (6.52)
\end{aligned}
$$

Derivation of the second-moment constraint (6.52): The second-order moment constraint for $\hat{c}_h = 0$ is

$$\int_0^1 \hat{c}^2\, f(\hat{c})\, d\hat{c} = \bar{\hat{c}}^2, \qquad (6.53)$$

where, the pdf is given by Eq. (6.23). Substituting (6.23) into (6.53) yields

$$K_1 \int_0^1 \hat{c}^2\, [1 - K_2(\nu_0 + \nu_1\hat{c})]^{\frac{1}{q}}\; d\hat{c} = \bar{\hat{c}}^2. \qquad (6.54)$$

Introducing the change of variables $u = \nu_0 + \nu_1\hat{c}$, such that

$$\hat{c} = \frac{u-\nu_0}{\nu_1}, \qquad d\hat{c} = \frac{1}{\nu_1}\, du,$$

and the limits $\hat{c} \in [0, 1]$ map to $u \in [\nu_0, \nu_0 + \nu_1]$. Then (6.54) becomes

$$\frac{K_1}{\nu_1^3}\int_{\nu_0}^{\nu_0+\nu_1} (u-\nu_0)^2\,(1-K_2u)^{\frac{1}{q}}\; du = \bar{\hat{c}}^2. \qquad (6.55)$$

Next, we set $z = 1 - K_2u$, such that the integration limits become

$$u = \nu_0 \Rightarrow z_0 = 1 - K_2\nu_0, \qquad u = \nu_0 + \nu_1 \Rightarrow z_1 = 1 - K_2(\nu_0 + \nu_1),$$

and

$$u - \nu_0 = \frac{1-z}{K_2} - \nu_0 = \frac{(1-K_2\nu_0)-z}{K_2}.$$

Substituting these values into (6.55) gives

$$-\frac{K_1}{(K_2\nu_1)^3}\int_{z_0}^{z_1}\Big((1-K_2\nu_0)-z\Big)^2 z^{\frac{1}{q}}\, dz = \bar{\hat{c}}^2. \qquad (6.56)$$

Expanding the square term, we get

$$\Big((1-K_2\nu_0)-z\Big)^2 = (1-K_2\nu_0)^2 - 2(1-K_2\nu_0)z + z^2,$$

and splitting the integral accordingly, we use the power integrals

$$\int z^{\frac{1}{q}}\,dz = \frac{q}{q+1}\,z^{\frac{q+1}{q}}, \qquad \int z^{1+\frac{1}{q}}\,dz = \frac{q}{1+2q}\,z^{\frac{1+2q}{q}}, \qquad \int z^{2+\frac{1}{q}}\,dz = \frac{q}{1+3q}\,z^{\frac{1+3q}{q}}.$$

Therefore, Eq. (6.56) yields

$$-\frac{K_1}{(K_2\nu_1)^3}\Bigg[(1-K_2\nu_0)^2\frac{q}{q+1}\left(z_1^{\frac{q+1}{q}}-z_0^{\frac{q+1}{q}}\right)-2(1-K_2\nu_0)\frac{q}{1+2q}\left(z_1^{\frac{1+2q}{q}}-z_0^{\frac{1+2q}{q}}\right) + \frac{q}{1+3q}\left(z_1^{\frac{1+3q}{q}}-z_0^{\frac{1+3q}{q}}\right)\Bigg] = \bar{\hat{c}}^2. \tag{6.57}$$

Finally, substituting $z_0 = 1-K_2\nu_0$ and $z_1 = 1-K_2(\nu_0+\nu_1)$ into (6.57) gives Eq. (6.52).

The system of eqs. (6.40), (6.46) and (6.52) can be solved numerically for each data set. To reduce the complexity we have framed a minimization problem with the help of least square method using the above three equations subject to the inequality constraint (6.26) and used the fmincon function of Matlab along with some mathematical adjustments to get finite solution of the problem. Therefore, the objective function to be minimized is framed as:

$$f_1^2+f_2^2+f_3^2$$

where

$$\begin{aligned}
f_1 &= -\frac{K_1}{K_2\nu_1}\left(\frac{q}{q+1}\right)\left[(1-K_2(\nu_0+\nu_1))^{\frac{1+q}{q}}-(1-K_2\nu_0)^{\frac{1+q}{q}}\right]-1,\\
f_2 &= -\frac{K_1}{(K_2\nu_1)^2}\left((1-K_2\nu_0)\frac{q}{1+q}\left((1-K_2(\nu_0+\nu_1))^{\frac{1+q}{q}}\right)\right)\\
&\quad -(1-K_2\nu_0)^{\frac{1+q}{q}}-\frac{q}{1+2q}\left((1-K_2(\nu_0+\nu_1))^{\frac{1+2q}{q}}-(1-K_2\nu_0)^{\frac{1+2q}{q}}\right)-\bar{\hat{c}} \text{ and}\\
f_3 &= -\frac{K_1}{(K_2\nu_1)^3}\left((1-K_2\nu_0)^2\frac{q}{1+q}\left((1-K_2(\nu_0+\nu_1))^{\frac{1+q}{q}}\right)\right)-(1-K_2\nu_0)^{\frac{1+q}{q}}\\
&\quad -2(1-K_2\nu_0)\frac{q}{1+2q}\left((1-K_2(\nu_0+\nu_1))^{\frac{1+2q}{q}}-(1-K_2\nu_0)^{\frac{1+2q}{q}}\right)\\
&\quad +\frac{q}{1+3q}\left((1-K_2(\nu_0+\nu_1))^{\frac{1+3q}{q}}-(1-K_2\nu_0)^{\frac{1+3q}{q}}\right)-\bar{\hat{c}}^2
\end{aligned}$$

6.3 Validation and performance comparison with experimental and field data

The validity of the NSSC distribution derived using fractional Machado entropy is examined in this section using some experimental and field data sets of wide open channel flows, where the concentration decreases from a reference height above the channel bed to the flow surface, representing type I vertical SSC distribution. A sensitivity analysis is also conducted to investigate the influence of the parameters on the normalized concentration distribution. Further, error analysis is performed for the selected data sets to compare the functioning of the proposed NSSC model with that of the existing entropy-based and deterministic NSSC models with zero surface concentration assumption.

6.3.1 Experimental and field data

The accuracy of the proposed model is evaluated using both experimental and field data sets. Specifically, we selected experimental data from Coleman (1986) and Einstein and Chien (1955), as well as field data from McQuivey (1973). For each data set, the reference height, y_r is set as the lowest recorded height with available concentration details so as to avoid overestimation or underestimation of the reference height derived from deterministic methods (Mazumder and Ghoshal, 2002, 2006). Einstein and Chien's experiments were conducted in a 40 ft-long, 1.006 ft-wide, and 1.17 ft-deep painted steel flume. They carried out 29 runs—13 with clear water and 16 with sediment-laden water, maintaining average flow discharges between 2.6 and 3.0 cfs and water depths from 0.36 to 0.49 ft. Sediment particle sizes included coarse ($d = 1.3$ mm), medium ($d = 0.94$ mm), and fine ($d = 1.14$ mm). For further details on these experimental conditions, one may refer to Ahamed and Kundu (2023) and Cui (2011). Similarly, Coleman (1986) performed his experiments in a 0.356 m-wide and 15 m-long plexiglas channel, completing 40 runs with an average discharge of 0.064 m^3/s and an average flow depth of 0.169 m. Experiments were conducted using sand particles with diameters of 0.105 mm, 0.210 mm, and 0.420 mm. Comprehensive descriptions of these experiments can be found in Coleman (1986, 1981), while details on the field data are available in McQuivey (1973).

For model validation, Run 03 and Run 25 from the Coleman experimental data, Run S13 from the Einstein and Chien data, and Run 03 from the Missouri river field data reported by McQuivey (1973) were selected, as shown in Fig. 6.3.1. For each dataset, the model parameters were determined following the procedure outlined in the previous section. The hypothetical cumulative distribution function (CDF) given by Eq. (6.29) was then fitted to the estimated CDF in Eq. (6.28) using a nonlinear least-squares approach to determine the curve-fitting parameter a, as depicted in Fig. 6.3.1. As illustrated in Fig. 6.3.1, the CDF decreases monotonically with increasing normalized height (y/h), attaining a maximum value of unity at the reference height ($y/h = y_r/h$) and a minimum

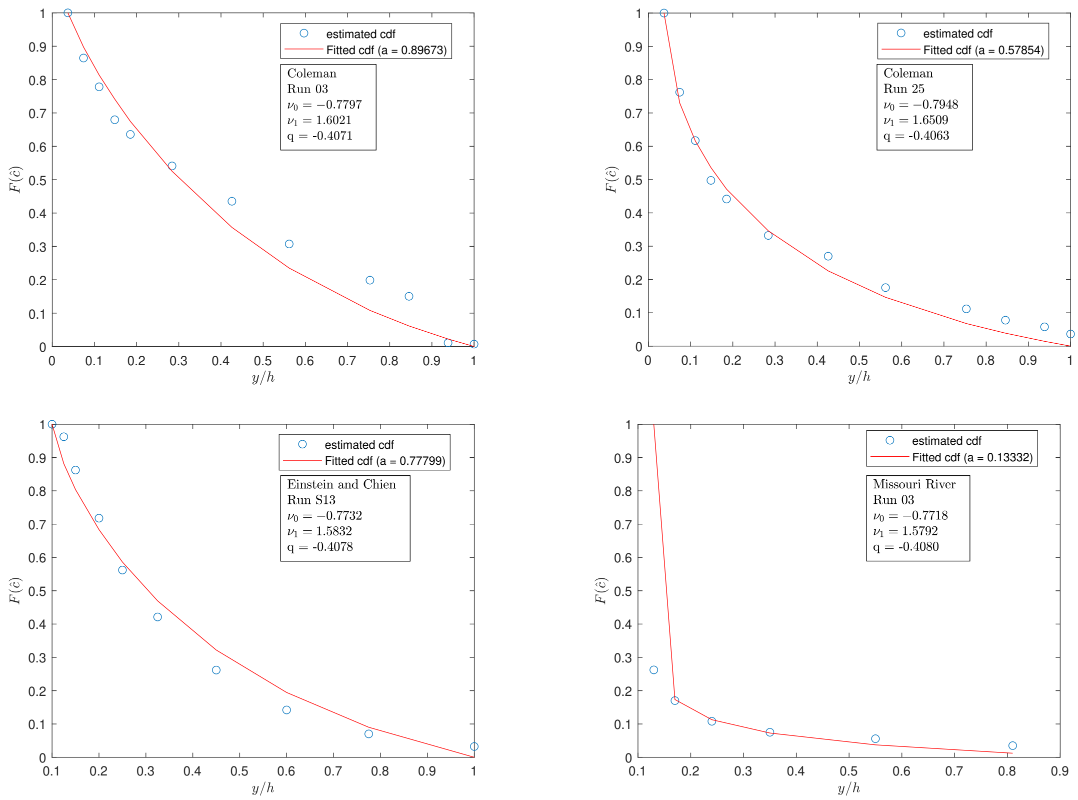

Figure 6.3.1: Fitting of the hypothetical cdf (6.29) with the computed cdf (6.28) for the chosen data sets to determine a

at the water surface ($y/h = 1$). The estimated value of a was subsequently employed to validate the proposed model by examining the variation of the normalized suspended sediment concentration (NSSC), $\hat{c}$, with normalized height y/h for the selected datasets.

From Fig. 6.3.2, one can conclude that the derived fractional entropy-based NSSC formulation (6.38) closely predicts the observed data for the experimental data. However, the computed results shows deviations from the observed results for the field data set of Missouri river Run 03, showing erroneous predictions. This can be attributed to the turbulence and shear stress effects on the suspended sediment particles. It can be resolved through making changes in the value of the proportionality constant β which was taken as 1 in our study for reducing computational complexity. Apart from this, to quantify the accuracy of predictions of the current model, regression analysis is done. The prediction accuracy is highlighted by the high values of the regression coefficient R^2 as can be seen clearly through Fig. 6.3.3. The R^2 values varies from 0.97493 to 0.99002 for the chosen data sets, which are pretty close to 1. Precisely, it can be stated that the estimated NSSC

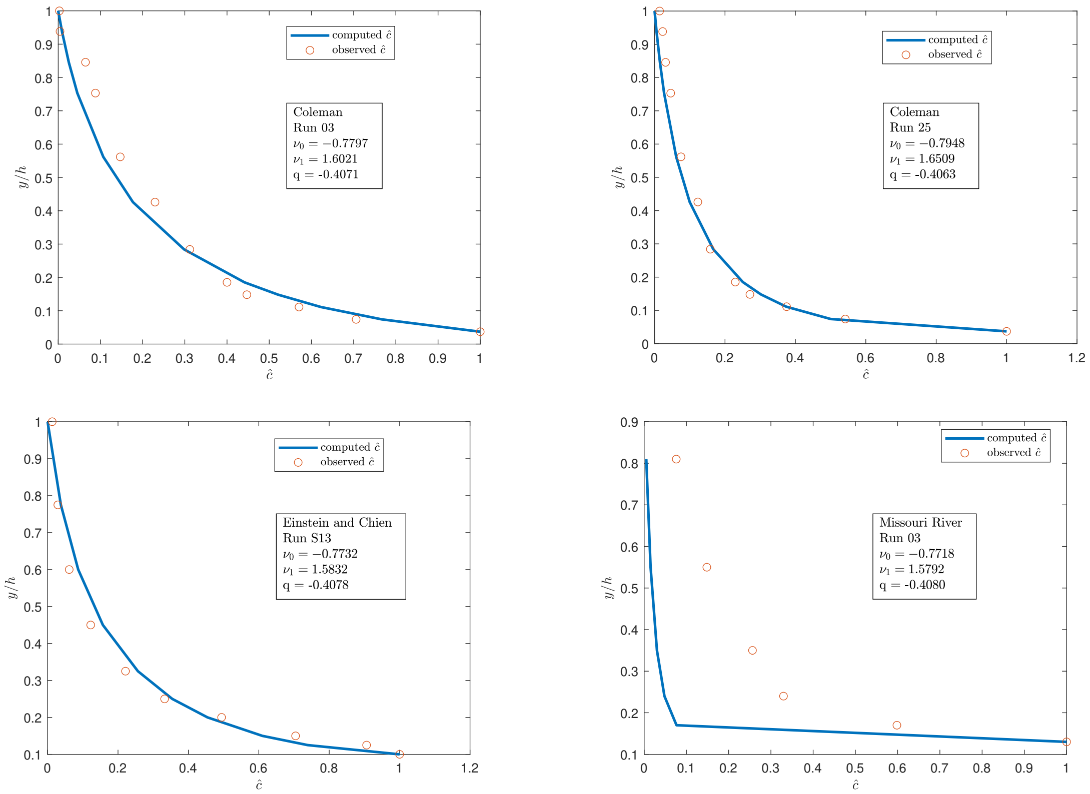

Figure 6.3.2: NSSC, $\hat{c}$ with respect to normalized height, y/h

distribution describe the real data sets quite accurately, especially for the experimental data sets. Since the vertical profile of concentration depends on the Lagrange multipliers, exploring the effect of the Lagrange multipliers on the NSSC profile (6.38) may prove to be an important aspect to be explored. For that purpose, one of the Lagrange multipliers is kept fixed and the effect of the variations of NSSC is shown by varying the other for Run 03 data of Coleman. The results are displayed in Fig. 6.3.4. It can be seen from Fig. 6.3.4 that the vertical concentration profile is more sensitive towards changes in the Lagrange multiplier ν_0 which corresponds to the normalization constraint. In other words, the concentration $\hat{c}$ increases more gradually with decrease in height y/h at high ν_0 values whereas the slope of $\hat{c}$ with respect to y/h is steeper at lower ν_0 values. The NSSC distribution is less responsive towards variations in ν_1 corresponding to the mass conservation constraint. This implies that the rate of decrease in concentration with increase in height does not show much changes with variations in the values of ν_1. Thus we can deduce that the Lagrange multipliers significantly impact the shape of the concentration curve.

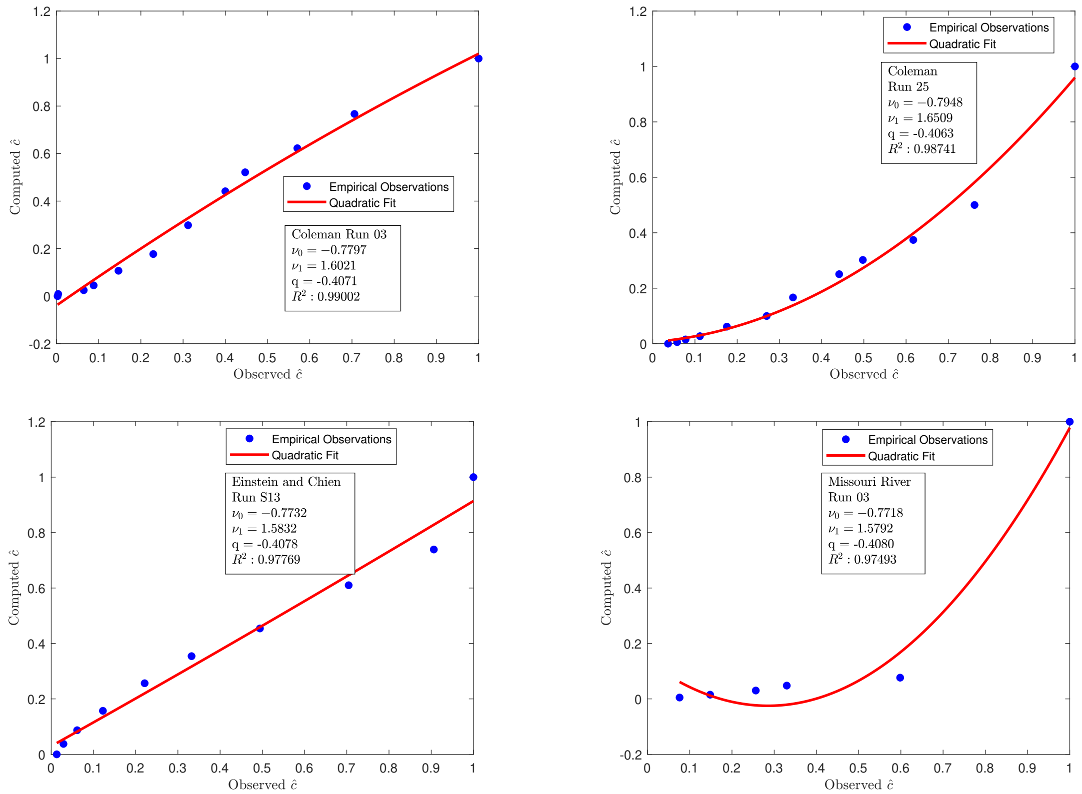

Figure 6.3.3: Regression analysis for computed $\hat{c}$ with respect to observed $\hat{c}$

6.3.2 Comparison of the current NSSC model with the extant entropy-based and Rousian models

For further validation, we have compared the current fractional Machado entropy-based NSSC distribution model (6.38) with the existing entropy-based models with zero surface concentration assumption referred to as the Choo (Shannon entropy), CS (Tsallis entropy) and Rousian models defined in Choo (2000), Cui and Singh (2014) and Rouse (1937), respectively. For this purpose, we have done error analysis for the normalized concentration $\hat{c}$. The types of errors considered in this study for comparison purpose have been defined in Kumbhakar and Tsai (2023). The errors can be described as follows:

- Mean relative absolute error (MRAE or R_e) $= \frac{1}{n}\sum_{k=1}^{n} \frac{\left|\hat{c}_{k(comp)} - \hat{c}_{k(obs)}\right|}{\hat{c}_{k(obs)}}$

- Root-mean-square error (RMSE) $= \sqrt{\dfrac{1}{n}\displaystyle\sum_{k=1}^{n}(\hat{c}_{k(comp)} - \hat{c}_{k(obs)})^2}$

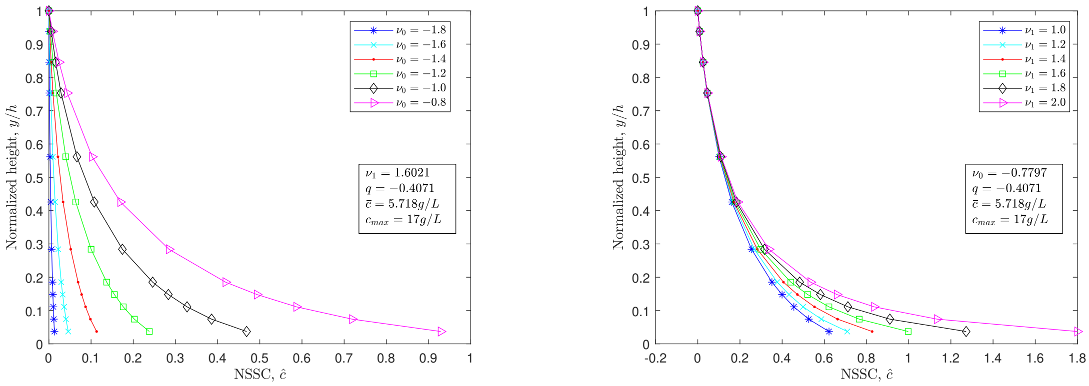

Figure 6.3.4: Variation of NSSC with Lagrange multipliers for Run 03 data of Coleman

- Sum of squared relative error (E1) $= \sum_{k=1}^{n} \frac{(\hat{c}_{k(comp)} - \hat{c}_{k(obs)})^2}{\hat{c}^2_{k(obs)}}$

where n is the total number of data points in a particular data set, $\hat{c}_{k(comp)}$ and $\hat{c}_{k(obs)}$ denote the computed and observed concentration of sediment at the k^{th} data point. The results for Coleman Run 25, Run 13 of Einstein and Chien and field data of Missouri river are presented in Table 6.3.1 .

Table 6.3.1: Comparison of the present model with other vertical profile of SSC models

SSC models	Rousian model	Choo model	CS model	Proposed model
Run 25 of Coleman				
MRAE	0.8642	0.6317	0.5499*	0.5674
RMSE	0.1823	0.1307*	0.1439	0.1546
E1	9.8640	5.9007	4.6198*	4.7234
Run S13 of Einstein and Chien data				
MRAE	0.5555	1.2769	0.5511	0.2624*
RMSE	0.1823	0.1307	0.1439	0.0650*
E1	3.8921	31.3755	6.1399	1.4316*
Missouri River Run 03 of McQuivey data				
MRAE	0.3103*	0.4136	0.4286	0.7403
RMSE	0.0607*	0.1529	0.1849	0.2663
E1	1.0278*	1.4193	1.4206	3.9495

Note: * indicates the minimum values of each of the errors for a given data source.

We show that our model has tolerable errors for most of the data sets provided in Table 6.3.1 and some of its values are the least among all other models for some of the chosen data sets, especially for the experimental data set. Furthermore, in order to provide stronger justification for the physical advantages of the proposed SSC model, we have considered a wide range of experimental data sets under diverse flow and sediment conditions. These include Runs 16, 25, 29 and 40, representing different classes of sediment particles having diameters equal to 0.105 mm, 0.210 mm and 0.420 mm, respectively, from Coleman (1986).

The previously defined errors are then computed for the Chiu et al. (2000) model, Miraud a et al. (2018b) model, Cui and Singh (2014) model and Rouse Rouse (1937) model using these data sets and displayed in Table 6.3.2. The proposed model's consistently lower RMSE and error sums imply it captures the vertical SSC profiles more accurately across a range of sediment sizes and flow conditions tested. The advantage is most pronounced in Runs 16 and 29, which might correspond to finer sediments or flow conditions where more complex turbulence-sediment interactions exist. The reduced advantage in Run 40 suggests the model may perform less distinctively in coarser sediment or lower turbulence regimes, or where profile shapes differ significantly. The results also claim that the Tsallis entropy-based CS model and the simplified Chiu model performs better under coarser sediment particle and low turbulence conditions for the specified parameters described previously. In conclusion, our proposed model yields better results over other concentration models for most of the considered data sets.

Table 6.3.2: Comparison of the proposed model with other vertical SSC models using Coleman (1986) data

SSC models	Rouse model	Chiu model	Simplified Chiu model	CS model	Proposed model
Run 16 of Coleman data					
RMSE	0.0991	0.0550	0.0569	0.2075	0.0226*
MRAE	0.9886	0.4271	0.4337	0.3204	0.2437*
E1	20.9343	3.0780	3.1399	2.0330	1.5777*
Run 29 of Coleman data					
RMSE	0.1246	0.0509	0.0511	0.1934	0.0207*
MRAE	1.0716	0.4807	0.4816	0.2836	0.2531*
E1	19.3467	3.9082	3.9164	1.9229	1.7859*
Run 40 of Coleman					
RMSE	0.1573	0.0324*	0.0324*	0.1818	0.0612
MRAE	0.9355	0.4715	0.4716	0.4155*	0.4291
E1	12.9471	4.3861	4.3909	2.7806*	3.38354

Note: * indicates the minimum values of each of the errors for a given data source.

Additionally, we have conducted a thourough comparison between our proposed fractional entropy-based SSC distribution model and the simplified Chiu model proposed by Miraud a et al. (2018b) employing the Coleman measurements through graphical illustrations. The results are displayed in Fig. 6.3.5, which presents the NSSC profiles represented by Eqs. (6.4), (6.8), (6.9) and (6.38) in relation to the observed NSSC data.

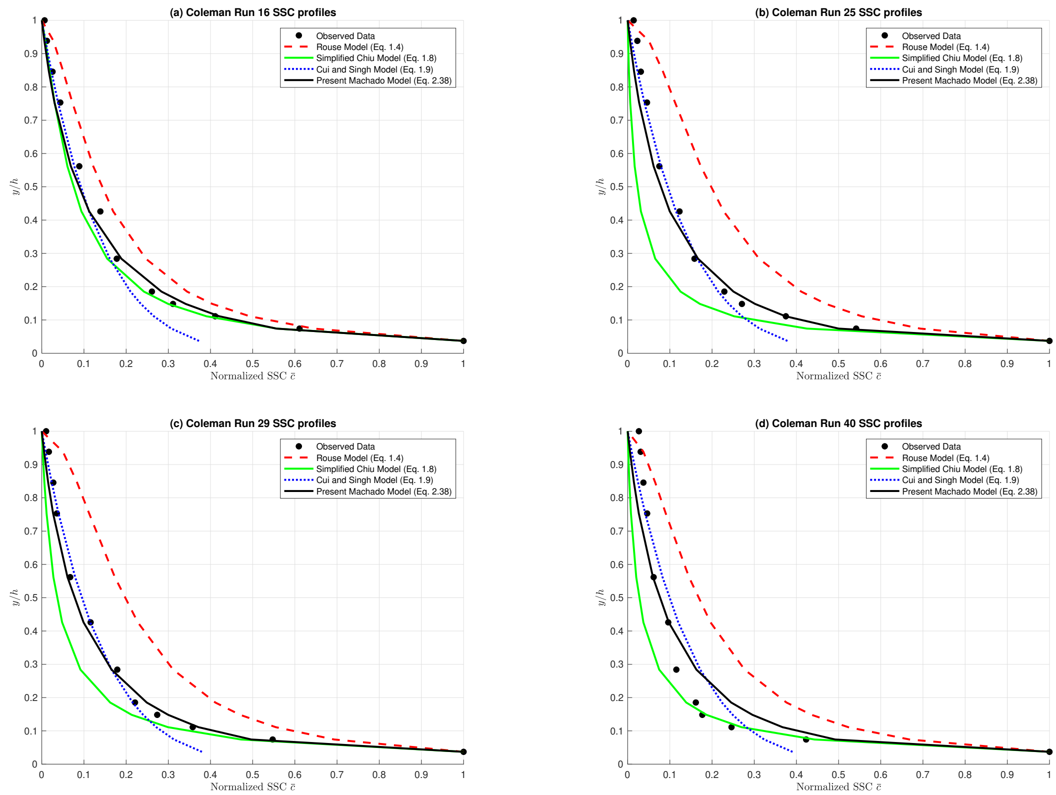

Figure 6.3.5: Comparison of SSC models with Coleman data (Runs 16, 25, 29 and 40)

It clearly portrays better alignment of our proposed Machado entropy-based model as compared to the other considered models, especially the Shannon entropy-based simplified Chiu model (Mirauda et al., 2018b) and the Tsallis entropy-based model (Cui and Singh, 2014) for almost all the data sets except for Run 40 with coarser sediments. This indicates that the proposed model works better with fine and medium sized sediment particles under the experimental channel conditions of Coleman data. The experimental conditions considered in this comparitive study were similar to the ones used in Chiu et al. (2000) model defined by Eq. (6.5) and the Mirauda et al. (2018b) model represented by eq. (6.8). These studies revealed that the parameters greatly shape the concentration distribution. Therefore, the fitting of the parameters are crucial for getting the best fit with respect to the observations. In our study, for Run 16, the parameter values taken for Rouse model are $z = 0.7, C_r = 1.36 * 10^{-2}; M = 7, \lambda = 5.6$ for simplified Chiu model and $N = 0.17, \eta = 0.154, m = 1/8$ for the Tsallis entropy-based Cui and Singh (2014) model. For Run 29 data, $z = 0.55, C_r = 7.995 * 10^{-3}$ for Rouse model, $M = 8, \lambda = 8.2$ for simplified Chiu model and $N = 0.1263, \eta = 0.154, m = 1/8$ for Tsallis model. Finally, in case of Run 40, the parameter values are: $z = 0.5, C_r = 2.075 * 10^{-3}$ for Rouse model,

$M = 9, \lambda = 8.9$ for the simplified Chiu model and $N = 0.0516, \eta = 0.154, m = 1/8$ for the Tsallis model. The optimized parameters (q, η_0, η_1, a) for our proposed fractional Machado entropy-based SSC model for each data set were directly calculated by the optimization technique introduced in this study. The results portrayed by Fig. 6.3.5 highlight the importance and robustness of our study across all flow regimes of the verical section of open channels as we can derive optimized parameters for each data set, unlike the other models where no such optimization technique was introduced nor the momentum conservation constraint was considered for determining the parameters. This makes the other SSC models more parameter sensitive and less consistent, leading to restricted applicabilities in studying the randomness of physical processes.

6.3.3 Results and discussion

From Tables 6.3.1 and 6.3.2 and Fig. 6.3.5, it is clealy seen that physically, our model incorporates a more flexible entropy framework that better captures the complex interactions governing suspended sediment distributions, especially under varying flow regimes and sediment characteristics. The improved performance is primarily due to:

- Adaptive Representation of Turbulence and Mixing: The fractional entropy formulation enables the model to account for variations in turbulent mixing and sediment diffusivity more precisely, which are critical in shaping vertical SSC profiles under real-world channel conditions.

- Optimized Parameter Determination: While the method involves optimization of both the entropy index and Lagrange multipliers, these parameters are not arbitrarily introduced for curve-fitting; rather, they are systematically derived from the data and linked to the underlying statistics of sediment transport. This allows the model to adapt its shape across different scenarios without excessive complexity.

- Physical Consistency across Regimes: The approach maintains consistency with fundamental principles such as mass conservation and momentum diffusion, but with added flexibility to capture nonlinearities and departures from idealized conditions (e.g., non-uniform turbulence, stratification).

- Broader Applicability: The model's adaptability is especially beneficial for data sets with higher sediment concentrations, finer particles, or departures from classic exponential or logarithmic SSC profiles. Conventional models like the Tsallis entropy-based solution (Cui and Singh, 2014) tend to lose accuracy in such scenarios.

Moreover, we have also considered the momentum conservation constraint for the first time in our concentration model which also demonstrates its higher physical significance among all other models. Additionally, the derived NSSC distribution offers a simplified approach of computing the Lagrange multipliers ν_0 and ν_1 and the entropy index q by converting the maximization problem into the minimization problem, with the aid of some mathematical arrangements to avoid getting infinite values in the final optimal solution.

6.4 Conclusion and future scope

This study applies Machado's fractional entropy to derive an entropy-based vertical concentration profile for open channel flows. The model integrates momentum, mass, and normalization constraints to determine the Lagrange multipliers and entropy index, increasing its physical relevance. The concentration profile is obtained by approximating the probability density function using the Lambert function based on a convergence criterion. A corresponding minimization problem is solved to determine the model parameters for the chosen data sets. The fractional index provides added flexibility, influencing the shape of the concentration curve. Model validation with experimental and field data shows higher accuracy for experimental data, likely due to the assumption that sediment diffusivity equals turbulent eddy viscosity, which may not hold for turbulent, wide rivers. Future improvements in estimating the momentum conservation constant (β) may enhance field predictions. The results demonstrate that the proposed fractional entropy-based model yields lower errors than existing models for selected data sets and demonstrates a strong correlation with observed values, as shown by regression coefficients close to one.

Additionally, a comparitive study with a broader data set of Coleman confirms the reliability and high prediction accuracy of the current model. The results indicate that:

- The proposed method provides superior accuracy in scenarios with higher sediment concentrations and finer particles, where complex suspended sediment dynamics are more pronounced.

- In moderate flow and sediment conditions, our model performs comparably or slightly better than the Cui and Singh model, offering improved flexibility through optimized entropy parameters.

- For coarser sediments and lower turbulence flows, both models perform almost similarly, though our approach maintains consistent robustness.

Overall, the superior performance arises from the method's ability to reflect the real physical variability in sediment transport with an entropy structure that naturally accommodates different flow and sediment regimes. It achieves this with a minimal, purpose-driven parameter set, not simply by introducing more parameters for fitting, but by employing parameters that are physically meaningful and data-informed.

Chapter 7

Quantile-Based Fractional Generalized Cumulative Past Entropy and its Role in Analyzing Human Mortality Uncertainty [1]

"Statistical methods are a way of thinking, not a collection of techniques."
— David R. Cox

Understanding uncertainty in human mortality is a central problem in survival analysis, particularly for life-threatening diseases such as lung cancer. Classical survival analysis tools, including survival and hazard functions, primarily provide pointwise or instantaneous descriptions of mortality risk and therefore offer limited insight into the evolving uncertainty associated with survival times at the population level. Information-theoretic measures provide a natural complementary framework by quantifying the dispersion and unpredictability of lifetimes in a distributional sense. In this context, in this chapter, a *quantile-based fractional generalized cumulative past entropy* (QFGCPE), along with its dynamic extension (DQFGCPE), is proposed to analyze uncertainty in mortality using life-table data and to study the temporal evolution of uncertainty in lung cancer survival. By integrating quantile-based representations with fractional-order entropy, the proposed framework enables tunable sensitivity across survival horizons while avoiding

[1] The results discussed in this chapter is to be submitted and is also archived with the DOI: *https://doi.org/10.48550/arXiv.2509.09182*

distributional assumptions. Key analytical properties, including bounds, monotonicity, and stochastic ordering relations, are established, and nonparametric estimators based on empirical and Kaplan–Meier methods are developed to accommodate both uncensored and right-censored data. Overall, the proposed approach offers a unified and interpretable measure of mortality uncertainty that complements classical survival analysis tools.

To prevent notational ambiguity, the fractional parameter associated with the entropy measure is represented by η instead of α.

7.1 Introduction

Understanding uncertainty in the timing of death is a central problem in survival analysis, particularly in the study of chronic and degenerative diseases such as lung cancer, where patient outcomes exhibit substantial heterogeneity over time since diagnosis. Beyond estimating survival probabilities or instantaneous risks, it is essential to quantify how uncertainty in survival outcomes accumulates and evolves across different time horizons. Such assessments are fundamental for understanding disease progression, informing prognosis and treatment strategies, and interpreting mortality patterns derived from both complete lifespan data and disease-specific survival studies.

Classical survival analysis tools, including survival functions and hazard rates, primarily provide pointwise or instantaneous descriptions of mortality risk. While these measures are indispensable, they focus on local aspects of the survival process and offer limited insight into the dispersion and unpredictability of survival times experienced by individuals or populations over time. In contrast, uncertainty measures aim to characterize the variability and heterogeneity inherent in the entire survival distribution, thereby complementing traditional risk-based summaries used in biostatistics, reliability theory, medical survival analysis and demographic transition studies.

Information-theoretic measures, beginning with Shannon's seminal work (Shannon, 1948), provide a natural framework for quantifying distributional uncertainty. Shannon entropy and its fractional generalizations have been widely applied across diverse fields, including reliability engineering, financial decision-making, and hydraulic studies. However, in medical survival analysis, particularly in cancer studies, lifetime distributions are often highly skewed, heavy-tailed, and subject to censoring. As a result, density-based entropy measures such as Shannon differential entropy or fractional differential entropy may be difficult to estimate reliably and may lack direct interpretability for clinical and health policy-oriented decision-making.

These limitations have motivated the development of *cumulative entropy measures*, which operate directly on cumulative distribution or survival functions and therefore avoid explicit density estimation. Such measures are especially attractive in survival analysis, where life-table data and censored observations naturally provide cumulative information. Prominent examples include the cumulative residual entropy (CRE) introduced by (Rao et al., 2004) and the cumulative past entropy (CPE) proposed by (Di Crescenzo and Longobardi, 2009). These measures remain well-defined even when the underlying probability density function (pdf) is irregular or unavailable (see Di Crescenzo and Longobardi, 2009; Di Crescenzo and Toomaj, 2017; Navarro et al., 2010; Rao et al., 2004, and references therein).

In the context of mortality studies, cumulative past entropy is particularly relevant because it aggregates uncertainty associated with deaths occurring prior to a given time horizon. Its dynamic extension enables the assessment of uncertainty accumulated up to a specified age or follow-up time, aligning naturally with both life-table-based mortality analysis over the full human lifespan and disease-specific survival studies with finite observation windows. To further enhance flexibility and capture long-range dependence in lifetime behavior, fractional generalizations of cumulative entropy have been proposed using tools from fractional calculus, including the fractional cumulative residual entropy (FCRE) (Xiong et al., 2019) and the fractional generalized cumulative past entropy (FGCPE) (Di Crescenzo et al., 2021).

Despite these advances, two important challenges remain. First, classical and fractional cumulative entropy measures are inherently distribution-based and therefore inherit difficulties associated with estimating distribution or density functions from grouped, censored, or incomplete survival data. Second, fixed weighting across the support of the distribution limits their ability to distinguish uncertainty arising from early mortality versus long-term survival heterogeneity, an issue of particular importance in diseases such as lung cancer, where early and late risks differ markedly.

These challenges motivate the use of *quantile-based methods* in survival analysis. Quantile functions provide a robust and flexible alternative for characterizing survival behavior by working directly with the inverse cumulative distribution function, thereby avoiding explicit assumptions on the underlying distribution (Sankaran and Sunoj, 2016; Sunoj and Sankaran, 2012). Quantile-based approaches assign equal importance across the entire support of the data, including extreme survival times, making them especially suitable for heavy-tailed distributions, heterogeneous populations, and settings where closed-form distribution functions are unavailable (see Nair et al., 2013; Nair and Sankaran, 2009). Consequently, quantile-based techniques have gained increasing attention in survival and reliability analysis due to their robustness, interpretability, and suitability for complex lifetime models (see Gilchrist, 2000; Nair and Vineshkumar, 2011; Nair et al., 2012; Vineshkumar et al., 2015; Aswin et al., 2023; Varkey and Haridas, 2023; Kayal and Balakrishnan, 2024, and references therein).

Building on these ideas, quantile-based entropy formulations offer a powerful framework for capturing uncertainty in survival data while preserving robustness under censoring and distributional complexity. In particular, the quantile-based fractional cumulative residual entropy (QFCRE), recently proposed by (Sunoj and Sebastian, 2025), is given by

$$\mathcal{C}R\xi_Q^{\eta}(X) = \int_0^1 (1-p)\,[-\ln(1-p)]^{\eta}\,q(p)\,dp, \qquad 0 \le \eta \le 1, \tag{7.1.1}$$

where X denotes a non-negative absolutely continuous random variable representing survival time, $Q(p)$ is the associated quantile function (QF), and $q(p)$ denotes the quantile density function (qdf). The fractional parameter η enables differential weighting of early and late portions of the survival distribution, thereby providing a principled mechanism to study the *temporal evolution of mortality uncertainty.* This feature is particularly valuable in lung cancer survival analysis, where early mortality risk, treatment response, and long-term survivor heterogeneity play distinct and clinically meaningful roles.

Motivated by the need for flexible and robust uncertainty measures in survival analysis, this chapter develops a *quantile-based fractional generalized cumulative past entropy* (QFGCPE) framework, together with its dynamic extension (DQFGCPE), to study uncertainty in complete lifespan mortality derived from life-table data and the temporal evolution of uncertainty in disease-specific lung cancer survival. By integrating cumulative entropy formulations with quantile-based representations and fractional weighting, the proposed framework provides a nonparametric and interpretable characterization of survival-time uncertainty that is well suited to life-table and right-censored survival data across diverse mortality settings. The remainder of the chapter is organized as follows. Section 7.2 outlines the survival analysis framework and data structures relevant to this study. Here, we introduce the concept of temporal evolution of mortality risk. In Section 7.3, we define QFGCPE and investigate its theoretical properties and ordering relationships. Section 7.4 extends the QFGCPE framework to a dynamic setting. In

Section 7.5, we develop a non-parametric estimator and evaluate its performance through simulations. In Section 7.6, we validate the non-parametric estimator and analyze the sensitivity of the proposed QFGCPE measure to survival quantiles through logistic maps. Section 7.7 applies the methodology to lung cancer survival data and develop a censoring-adjusted Kaplan-Meier estimator, demonstrating insights beyond hazard-based analysis. Section 7.8 concludes the chapter.

7.2 Survival analysis framework and life-table data

In survival analysis, mortality risk is inherently time-dependent. Let T denote the survival time of an individual following diagnosis of a life-threatening disease such as lung cancer. The probabilistic behavior of T is described by the cumulative distribution function (cdf) $F(t)$ and the survival function (sf) $S(t) = 1-F(t)$. In clinical and epidemiological studies, survival outcomes are frequently subject to censoring, most commonly right censoring, where the event of interest has not occurred for some individuals by the end of follow-up. Consequently, the complete distribution of T is rarely observed directly.

Classical survival analysis primarily relies on the hazard function $h(t) = f(t)/S(t)$ to characterize instantaneous mortality risk. While indispensable, the hazard function provides a local description of the survival process and does not capture the accumulated uncertainty in the timing of death up to a given time point. Moreover, hazard-based inference is highly sensitive to censoring and sparse observations at late follow-up times, which are common in cancer survival studies. As a result, populations with similar hazard rates at specific time points may exhibit substantially different dispersion and predictability of survival times.

In large-scale cancer registries and demographic studies, survival information is commonly reported using life tables, which characterize mortality over discrete age or time intervals via the number of survivors (l_x), the number of deaths (d_x), the conditional probabilities of death and survival (q_x, p_x), and the remaining life expectancy at age x (e_x). While life tables yield direct estimates of $S(t)$ and $F(t)$, they do not support reliable estimation of density or hazard functions without additional modeling or smoothing assumptions. These practical limitations further motivate the use of cumulative, distribution-level measures of uncertainty (see Mariotto et al., 2018, and references therein).

The notion of *temporal evolution of mortality risk* refers to systematic changes in mortality-related uncertainty as survival time since diagnosis progresses. In lung cancer survival, early post-diagnosis periods are typically characterized by substantial heterogeneity in patient outcomes, resulting in elevated uncertainty in survival times. As time advances, survivor selection leads to a more homogeneous population of long-term survivors, and uncertainty may stabilize or decline. Capturing such dynamics requires measures that integrate information over the entire survival history rather than focusing solely on instantaneous behavior.

Entropy-based measures provide a natural framework for quantifying uncertainty in survival data. Unlike hazard functions, which describe instantaneous risk, cumulative entropy measures summarize the dispersion and unpredictability of survival times accumulated up to a given time point. In particular, cumulative past entropy focuses on uncertainty associated with deaths occurring prior to time t, making it especially suitable for mortality analysis based on life-table and censored survival data. Tracking entropy as a function of time or survival quantiles therefore yields an entropy trajectory that directly reflects the temporal evolution of mortality uncertainty.

A quantile-based perspective further enhances this interpretation by associating uncertainty with specific survival horizons, distinguishing early mortality, typical survival, and long-term outcomes. This perspective is particularly valuable in life-table analysis, where survival probabilities are reported at discrete time points and quantiles are often more stable than local density or hazard estimates. Incorporating fractional entropy introduces a tunable parameter that differentially weights early and late survival behavior, providing additional flexibility for studying evolving mortality patterns across time scales.

Together, quantile-based formulations and fractional cumulative entropy measures provide a flexible and robust framework for characterizing the temporal evolution of survival uncertainty. This perspective naturally motivates the quantile-based fractional generalized cumulative past entropy introduced in the next section, which constitutes the central methodological contribution of this chapter.

7.3 Quantile-based fractional generalized cumulative past entropy

Classical density-based entropy measures uncertainty through the probability density function of a random variable. Such measures are useful when the density is known or can be estimated reliably. However, in survival analysis, direct density estimation may be difficult because lifetime data are often skewed, incomplete, or right-censored. In such cases, the estimated density may become unstable and may not represent the uncertainty structure accurately.

Quantile-based entropy takes a different approach. Instead of describing uncertainty through the density, it uses the quantile function, which represents ordered lifetime values corresponding to probability levels. This makes the measure more directly connected with percentiles, survival probabilities, and Kaplan–Meier-type estimation. Therefore, quantile-based entropy is particularly useful for survival data because it can describe uncertainty in lifetime distributions without relying strongly on direct density estimation. Motivated by the need to quantify the evolving uncertainty in mortality timing using cumulative and quantile-based information, we now introduce the *quantile-based fractional generalized cumulative past entropy* (QFGCPE).

Let X denote a non-negative continuous random variable representing survival time since diagnosis, with cdf F, sf S, and QF $Q(v)$ defined in (1.2.11). We recall that the quantile function provides the survival time corresponding to the v-th proportion of deaths in the population, thereby offering a natural interpretation in terms of survival horizons.

Definition 7.3.1. *If X is a non-negative continuous random variable with QF $Q(v)$, then the* quantile-based fractional generalized cumulative past entropy *(QFGCPE) of X is defined as*

$$\begin{aligned}\mathcal{CP}\xi_Q^{\eta} &= \frac{1}{\Gamma(\eta+1)}\int_0^1 p\,(-\ln p)^{\eta}\, dQ(p)\\ &= \frac{1}{\Gamma(\eta+1)}\int_0^1 p\,(-\ln p)^{\eta}\, q(p)\, dp, \qquad \eta>0, \end{aligned} \tag{7.3.1}$$

where $q(p)=\frac{d}{dp}Q(p)$ denotes the quantile density function (qdf).

From a survival analysis perspective, the integrand $p(-\ln p)^{\eta}$ weights uncertainty contributions according to survival quantiles. Lower values of p correspond to early deaths, while larger values represent later survival times. The fractional order η modulates the relative emphasis placed on different regions of the survival distribution, allowing enhanced sensitivity to early or late mortality uncertainty.

In the QFGCPE measure, the fractional parameter η acts as an uncertainty-sensitivity parameter. It controls how strongly the entropy measure responds to uncertainty across different parts of the lifetime distribution. In demographic and medical survival data, this means that different values of η may emphasize different patterns of death-time uncertainty, such as uncertainty among short-survival, middle-survival, or long-survival individuals.

It should be noted that η is not a direct biological or clinical parameter such as age, hazard rate, treatment effect, or mortality rate. Rather, it is an effective sensitivity parameter that helps quantify how dispersed or concentrated the lifetime distribution is across quantile levels. For medical datasets, such as lung cancer survival data, variation in η may help indicate whether survival uncertainty is concentrated among short-survival patients, long-survival patients, or distributed across the overall lifetime range.

7.3.1 Representation via reversed hazard quantile function

For a continuous survival time random variable X with density $f(x)$ and distribution function $F(x)$, the reversed hazard rate function is defined as

$$r(x) = \frac{f(x)}{F(x)},$$

which describes the instantaneous rate of death occurrence prior to time x. The quantile analogue of the reversed hazard rate, known as the reversed hazard quantile function (RHQF), is given by (Sunoj et al., 2013; Nair et al., 2019; Qiu, 2019)

$$\mathcal{R}(v) = r(Q(v)) = \frac{f(Q(v))}{v} = [vq(v)]^{-1}. \tag{7.3.2}$$

Using (7.3.2), the QFGCPE defined in (7.3.1) can be expressed equivalently as

$$\mathcal{C}P\xi_Q^{\eta} = \int_0^1 [\mathcal{R}(p)]^{-1} (-\ln p)^{\eta}\, dp, \tag{7.3.3}$$

highlighting the close relationship between QFGCPE and quantile-based reversed hazard behavior. This representation underscores the interpretation of QFGCPE as an accumulated measure of mortality intensity across survival quantiles.

7.3.2 Closed-form expressions for standard lifetime models

To illustrate the behavior and interpretability of QFGCPE, closed-form expressions are derived for several commonly used lifetime distributions. These models are frequently employed in survival and reliability analysis to represent diverse mortality patterns, including early high-risk, long-tailed survival, and heterogeneous hazard structures. Table 7.3.1 summarizes the corresponding quantile functions, quantile densities, and QFGCPE expressions.

Table 7.3.1: Quantile functions and QFGCPE for selected lifetime distributions.

Distribution	**Parameters**	$q(v)$	$Q(v)$	$\mathcal{C}P\xi_Q^\eta$
Uniform	$[0, b],\ b > 0$	b	bv	$\frac{1}{2^{\eta+1}}$
Exponential	$\lambda > 0$	$\frac{1}{\lambda(1-v)}$	$-\frac{1}{\lambda}\ln(1-v)$	$\frac{1}{\lambda}\left[\zeta(\eta+1)-1\right]$
Power	$0 < v < a,\ a, b > 0$	$\frac{a}{b}v^{\frac{1}{b}-1}$	$av^{1/b}$	ab^η
Half-logistic	$k \geq 0$	$\frac{2k}{1-v^2}$	$k\ln\left(\frac{1+v}{1-v}\right)$	$2^{-\eta}k\zeta(\eta+1)$
Fréchet	$a, b > 0$	$\frac{b^{1/a}}{av}(-\ln v)^{-(1+\frac{1}{a})}$	$\left(-\frac{b}{\ln v}\right)^{1/a}$	$\frac{b^{1/a}}{a\Gamma(\eta+1)}\Gamma\left(\eta-\frac{1}{a}\right)$

Note: $\zeta(s) = \sum_{k=1}^{\infty} k^{-s}$, $s > 1$, denotes the Riemann zeta function.

These explicit forms demonstrate how QFGCPE responds to different survival structures and allow direct comparison of mortality uncertainty across models with distinct hazard and tail behaviors.

7.3.3 Models with intractable distribution functions

An important advantage of the quantile-based framework is its applicability to lifetime models that lack closed-form distribution functions. Consider a survival time random variable with quantile density function

$$q(v) = Kv^b(1-v)^{-(a+b)}, \tag{7.3.4}$$

where $a, b \in \mathbb{R}$ and K is a scaling constant related to distributional shape (Nair et al., 2012). Such models arise naturally in survival analysis when mortality exhibits strong skewness, heavy tails, or non-monotone hazard behavior.

Substituting (7.3.4) into (7.3.1), the corresponding QFGCPE is obtained as

$$\mathcal{C}P\xi_Q^\eta = \begin{cases} \dfrac{K}{(b+2)^{\eta+1}}, & a+b=0, \\ K\left(\zeta(\eta+1) - \sum_{m=1}^{b+1} m^{-(\eta+1)}\right), & a+b=1, \\ K\left[\dfrac{1}{(b+2)^{\eta+1}} - \dfrac{1}{(b+3)^{\eta+1}}\right], & a+b=-1. \end{cases}$$

Random variables with quantile density functions of the form (7.3.4) encompass several important survival models, including exponential, generalized Pareto, rescaled beta, log-logistic, and the Govindarajulu lifetime distribution (Govindarajulu, 1977). These models

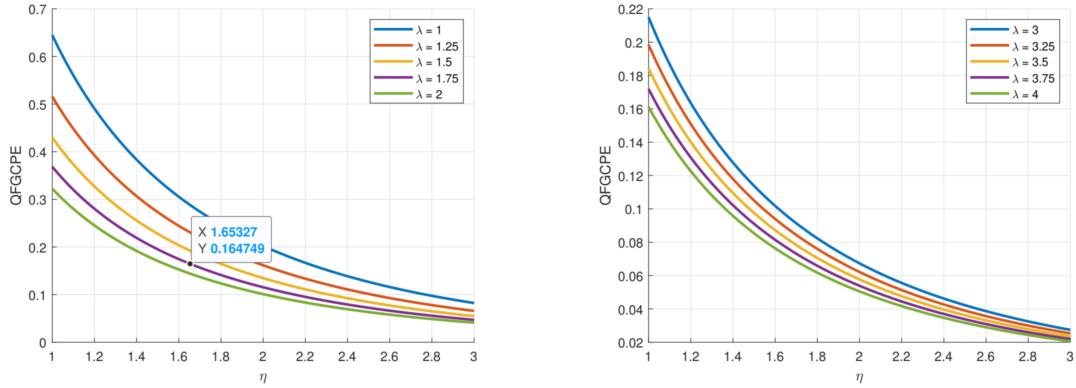

Figure 7.3.1: Variation of QFGCPE for exponential distribution for $\lambda = 1, 1.25, 1.5, 1.75, 2$ (left) and $\lambda = 3, 3.25, 3.5, 3.75, 4(right)$.

allow for monotone or non-monotone reversed hazard quantile functions, making them particularly relevant for diseases such as lung cancer, where mortality risk may evolve nonlinearly over time.

The sensitivity of the QFGCPE measure with respect to its governing parameters is illustrated in Figs. 7.3.1–7.3.3. Figs. 7.3.1 and 7.3.2 demonstrate the monotonic behavior of QFGCPE with respect to key model parameters for representative lifetime distributions with tractable distribution functions, namely the exponential and half-logistic models. For the exponential distribution, Fig. 7.3.1 indicates that QFGCPE is more sensitive to changes in the rate parameter for lower values of $\lambda < 2$, corresponding to higher early mortality variability, whereas sensitivity diminishes for larger values $\lambda > 3$. This behavior reflects the stronger influence of early-time uncertainty in rapidly decaying survival distributions. Fig. 7.3.2 shows that, for the half-logistic distribution, QFGCPE exhibits

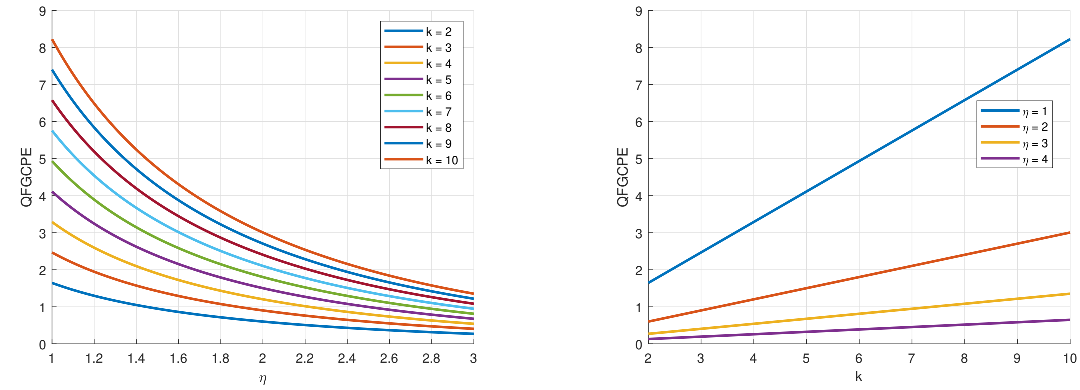

Figure 7.3.2: Variation of QFGCPE for half-logistic distribution w.r.t η(left) and k(right).

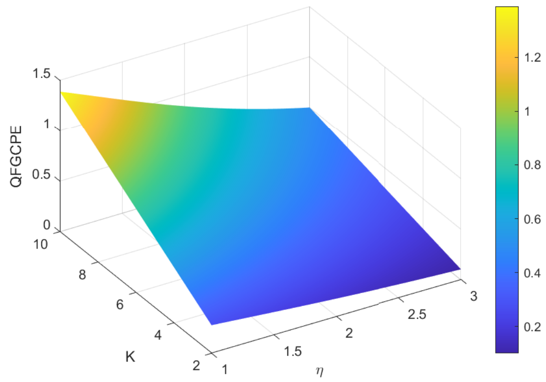

Figure 7.3.3: Monotonic behaviour of QFGCPE for a random variable having $q(v) = Kv^b(1-v)^{-(a+b)}$ w.r.t changes in its parameters for $a = -1,\ b = 0$.

greater sensitivity to the scale parameter k than to the fractional order parameter η, highlighting the dominant role of distributional scale in shaping accumulated survival uncertainty. In addition, Fig. 7.3.3 provides a visual illustration of the variation of QFGCPE with respect to the parameters η and K for a lifetime model with an intractable distribution function but a closed-form quantile density function given by (7.3.4) for the case $a + b = -1$. These illustrations emphasize the practical relevance of quantile-based entropy measures for studying survival variability even when explicit distributional forms are unavailable.

We now consider a transformation relevant to comparative survival analysis. Let X and Y be two non-negative continuous random variables representing survival times, with quantile functions $Q_X(v)$ and $Q_Y(v)$, respectively. The random variable Y is said to follow a proportional reversed hazard quantile model (PRHQM) with respect to X if

$$Q_Y(v) = Q_X(v^{1/\theta}), \qquad \theta > 0,$$

which implies that the corresponding quantile density function of Y is given by

$$q_Y(v) = \frac{1}{\theta}\, q_X(v^{1/\theta})\, v^{1/\theta - 1}, \qquad 0 < v < 1,$$

see (see Nair et al., 2019). Under this transformation, the QFGCPE of Y takes the form

$$\mathcal{C}P\xi_Q^{\eta}(Y) = \frac{1}{\theta\,\Gamma(\eta+1)} \int_0^1 p^{1/\theta}(-\ln p)^{\eta}\, q_X(p^{1/\theta})\, dp. \tag{7.3.5}$$

Example 7.3.1. *Let X follow a power lifetime distribution with quantile density function $q_X(v) = \frac{a}{b}v^{\frac{1}{b}-1}$, and let Y denote its proportional reversed hazard quantile counterpart with*

$q_Y(v) = \frac{a}{b\theta} v^{\frac{1}{b\theta}-1}$, where $a, b > 0$ and $0 < v < a < 1$. In this case, the QFGCPE of Y is given by

$$\mathcal{C}P\xi_Q^{\eta}(Y) = \frac{a(b\theta)^{\eta}}{(1+b\theta)^{\eta+1}}, \qquad \eta > 0.$$

This example illustrates that, although the underlying reversed hazard rates may be proportional, the corresponding reversed hazard *quantile* functions need not preserve this proportionality except in the trivial case $\theta = 1$, where X and Y are identically distributed. Specifically,

$$R_Y(v) = b\theta v^{-1/(b\theta)} \neq \theta R_X(v) = \theta b v^{-1/b}.$$

From a survival analysis perspective, this highlights the ability of QFGCPE to distinguish differences in accumulated mortality uncertainty across populations that may appear similar under traditional hazard-based comparisons.

7.3.4 Some properties and bounds of QFGCPE

We summarize below several fundamental properties of QFGCPE, which are relevant for characterizing accumulated mortality uncertainty in survival analysis.

1. **Non-negativity.** The QFGCPE is always non-negative, that is,

   $$\mathcal{C}P\xi_Q^{\eta}(X) \geq 0,$$

   which follows directly from the non-negativity of the integrand in its definition.

2. **Scale dependence and shift invariance.** The QFGCPE is scale-dependent but invariant under location shifts. Let $a > 0$ and $b \geq 0$, and consider the affine transformation $Y = aX + b$. Then,

   $$\mathcal{C}P\xi_Q^{\eta}(Y) = a\,\mathcal{C}P\xi_Q^{\eta}(X).$$

   Proof. From the definition of FGCPE,

   $$\begin{aligned}\mathcal{C}P\xi^{\eta}(Y) &= \frac{1}{\Gamma(\eta+1)} \int_0^{\infty} F_Y(y)\big[-\ln F_Y(y)\big]^{\eta} dy \\ &= \frac{1}{\Gamma(\eta+1)} \int_b^{\infty} F_X\left(\frac{x-b}{a}\right)\left[-\ln F_X\left(\frac{x-b}{a}\right)\right]^{\eta} dx. \qquad (7.3.6)\end{aligned}$$

   Substituting $u = (x-b)/a$ in (7.3.6) yields

   $$\mathcal{C}P\xi^{\eta}(Y) = a\,\mathcal{C}P\xi^{\eta}(X). \qquad (7.3.7)$$

From (7.3.7), we obtain

$$\mathcal{CP}\xi_Q^\eta(Y) = a\,\mathcal{CP}\xi_Q^\eta(X),$$

which gives the stated result. □

3. **Additivity under quantile decomposition.** If the QF of X can be expressed as $Q(v) = Q_1(v) + Q_2(v)$, where Q_1 and Q_2 are valid QFs, then

$$\mathcal{CP}\xi_Q^\eta(X) = \mathcal{CP}\xi_{Q_1}^\eta(X) + \mathcal{CP}\xi_{Q_2}^\eta(X).$$

This follows from the linearity of the integral in the definition of QFGCPE.

For illustration, choosing Q_1 and Q_2 as quantile functions of two uniform distributions with parameters $\alpha = 0.5$ and $\lambda = 2$, respectively, yields

$$\mathcal{CP}\xi_Q^\eta(X) = 1.159730, \quad \mathcal{CP}\xi_{Q_1}^\eta(X) = 0.353553, \quad \mathcal{CP}\xi_{Q_2}^\eta(X) = 0.806176,$$

confirming the additivity property.

4. **Lower bound under quantile summation.** If $Q(v) = Q_1(v) + Q_2(v)$, then

$$\mathcal{CP}\xi_{Q_1+Q_2}^\eta \geq \max\{\mathcal{CP}\xi_{Q_1}^\eta, \mathcal{CP}\xi_{Q_2}^\eta\}.$$

Proof. This result follows directly from Properties 1 and 3. □

5. **Product of quantile functions.** If $Q(v) = Q_1(v)Q_2(v)$, where Q_1 and Q_2 are positive QFs, then

$$\mathcal{CP}\xi_Q^\eta(X) = \frac{1}{\Gamma(\eta+1)} \int_0^1 p(-\ln p)^\eta \big[Q_2(p)q_1(p) + Q_1(p)q_2(p)\big]\, dp.$$

Proof. The result follows immediately from the definition of QFGCPE. □

6. **Reciprocal transformation.** Let $Q_X(v)$ denote the quantile function of X. Then, for $Y = 1/X$, the QF is

$$Q_Y(v) = \frac{1}{Q_X(1-v)},$$

and the corresponding QFGCPE is given by

$$\mathcal{CP}\xi_Q^\eta(Y) = \frac{1}{\Gamma(\eta+1)} \int_0^1 p(-\ln p)^\eta \frac{q(1-p)}{Q^2(1-p)}\, dp.$$

As an example, if X follows a power distribution with $Q_X(v) = v^b$, then $Y = 1/X$ follows a Pareto distribution with $Q_Y(v) = (1-v)^{-b}$. For $b = 1$, the QFGCPE reduces to

$$\mathcal{CP}\xi_Q^\eta(Y) = \zeta(\eta) - 3\zeta(\eta+1) - \sum_{m=1}^{3} \left(\frac{1}{m^\eta} - \frac{3}{m^{\eta+1}} \right).$$

7. **Bounds via quantile-based Shannon entropy.** For $0 \leq \eta \leq 1$, the QFGCPE satisfies

$$\mathcal{C}P\xi_Q^{\eta}(X) \leq \left[\mathcal{C}P\xi_Q(X)\right]^{\eta},$$

where $\mathcal{C}P\xi_Q(X)$ denotes the quantile-based cumulative past entropy.

Proof. Using $p \leq p^{\eta}$ for $0 \leq p, \eta \leq 1$ and Jensen's inequality,

$$\mathcal{C}P\xi_Q^{\eta}(X) \leq \left[\int_0^1 (-p\ln p)\, q(p)\, dp\right]^{\eta} = \left[\mathcal{C}P\xi_Q(X)\right]^{\eta}.$$

This gives the required bound. □

Furthermore, the following lower bound holds:

$$\mathcal{C}P\xi_Q^{\eta}(X) \geq D(q)\exp\left[\xi_Q^{\eta}(X)\right],$$

where

$$\xi_Q^{\eta}(X) = -\int_0^1 \ln q(p)\, dp$$

is the quantile-based Shannon differential entropy and

$$D(q) = \exp\left[\int_0^1 \ln\left(p(-\ln p)^{\eta}\right) dp\right].$$

Theorem 7.3.1. *Let Q_X and q_X denote the QF and qdf of a random variable X. If Ψ is a positive increasing transformation and $Y = \Psi(X)$, then*

$$\mathcal{C}P\xi_Q^{\eta}(\Psi(X)) = \int_0^1 p(-\ln p)^{\eta} q_X(p)\Psi'(Q_X(p))\, dp.$$

Proof. Since $G_Y(y) = G_X(\Psi^{-1}(y))$, it follows that $Q_Y(v) = \Psi(Q_X(v))$ and $q_Y(v) = q_X(v)\Psi'(Q_X(v))$, which yields the stated result. □

Example 7.3.2. *Let $X \sim Unif(0,1)$ and define $Y = X^{\beta}$, $\beta > 0$. Then Y follows a power distribution with $Q_Y(v) = v^{1/\beta}$. The corresponding QFGCPE is*

$$\mathcal{C}P\xi_Q^{\eta}(Y) = \frac{\beta}{(\beta+1)^{\eta+1}}.$$

The properties established above are particularly relevant in survival analysis because they ensure that QFGCPE behaves consistently under common data transformations and modeling assumptions encountered in practice. Scale dependence reflects sensitivity to changes in the time scale of survival (e.g., months versus years), while shift invariance ensures robustness to baseline time offsets. Additivity and bounding properties provide insight into how uncertainty aggregates across heterogeneous survival components, which is essential when comparing subpopulations or treatment groups. Moreover, the transformation results demonstrate that QFGCPE remains tractable under monotone changes of the survival variable, a key requirement for analyzing censored and grouped data. Collectively, these properties support the use of QFGCPE as a stable and interpretable measure of accumulated mortality uncertainty in life-table-based survival studies, such as those arising in lung cancer research.

7.3.5 Orderings of QFGCPE

Stochastic orderings provide a systematic framework for comparing the uncertainty and risk associated with different lifetime distributions and are widely used in survival and risk analysis (see Wang et al., 2021, and references therein). Traditionally, such comparisons are formulated in terms of distribution or survival functions (Shaked and Shanthikumar, 2007). For completeness, we recall some commonly used stochastic orderings.

Definition 7.3.2. *A random variable X is said to be smaller than another random variable Y in the*

(i) hazard rate order, denoted by $X \leq_{hr} Y$, if $h_X(t) \geq h_Y(t)$ for all t, where $h_X(t) = \frac{f_X(t)}{\bar{F}_X(t)}$;

(ii) reversed hazard rate order, denoted by $X \leq_{rhr} Y$, if $r_X(t) \leq r_Y(t)$ for all t;

(iii) dispersive order, denoted by $X \leq_{disp} Y$, if $F_Y^{-1}(F_X(t)) - t$ is non-decreasing in $t \geq 0$.

Since QFGCPE is formulated in terms of QFs, it is natural to consider quantile-based analogues of these orderings.

Definition 7.3.3. *A random variable X is said to be smaller than another random variable Y in the*

(iv) hazard quantile order, denoted by $X \leq_{HQ} Y$, if $H_X(v) \geq H_Y(v)$ for all $v \in (0,1)$, where

$$H_X(v) = h(Q_X(v)) = \frac{g(Q_X(v))}{1-v} = [(1-v)q_X(v)]^{-1};$$

(v) reversed hazard quantile order, denoted by $X \leq_{RHQ} Y$*, if* $R_X(v) \leq R_Y(v)$ *for all* $v \in (0,1)$*;*

(vi) quantile dispersive order, denoted by $X \leq_{disp} Y$*, if* $Q_Y(v) - Q_X(v) \geq 0$ *for all* $v \in (0,1)$*.*

Based on these quantile-based orderings, we now introduce an ordering induced by QFGCPE.

Definition 7.3.4. *A random variable* X *is said to be smaller than another random variable* Y *in the QFGCPE order, denoted by* $X \leq_{QFGCPE} Y$*, if*

$$\mathcal{C}P\xi_Q^\eta(X) \leq \mathcal{C}P\xi_Q^\eta(Y).$$

This ordering allows direct comparison of accumulated survival uncertainty between populations.

Theorem 7.3.2. *If* $X \leq_{HQ} Y$ *or equivalently* $X \geq_{RHQ} Y$*, then* $X \leq_{QFGCPE} Y$*.*

Proof. Since $X \leq_{HQ} Y \iff X \geq_{RHQ} Y$ (Kundu, 2015), using the definition of the reversed hazard quantile function,

$$X \leq_{HQ} Y \;\Rightarrow\; vq_X(v) \leq vq_Y(v), \quad \forall v \in (0,1).$$

Multiplying both sides by $(-\ln v)^\eta$ and integrating over $(0,1)$ yields

$$\int_0^1 v(-\ln v)^\eta q_X(v)\,dv \leq \int_0^1 v(-\ln v)^\eta q_Y(v)\,dv,$$

which implies $\mathcal{C}P\xi_Q^\eta(X) \leq \mathcal{C}P\xi_Q^\eta(Y)$. □

Theorem 7.3.3. *Let* $X \leq_{RHQ} Y$ *and let* Ψ *be an increasing concave function. If* $X \leq_{disp} Y$*, then*

$$\Psi(X) \geq_{QFGCPE} \Psi(Y).$$

Similarly, if $X \leq_{HQ} Y$ *and* Ψ *is increasing and convex, then* $X \leq_{disp} Y$ *implies*

$$\Psi(X) \leq_{QFGCPE} \Psi(Y).$$

Proof. If $X \leq_{disp} Y$, then $Q_X(v) \leq Q_Y(v)$ for all $v \in (0,1)$. For an increasing concave function Ψ, this implies

$$\Psi'(Q_X(v)) \geq \Psi'(Q_Y(v)), \tag{7.3.8}$$

and hence

$$\frac{1}{vq_X(v)} \leq \frac{1}{vq_Y(v)}. \tag{7.3.9}$$

Combining (7.3.8) and (7.3.9) yields

$$\int_0^1 p(-\ln p)^\eta q_X(v)\Psi'(Q_X(v))\, dp \geq \int_0^1 p(-\ln p)^\eta q_Y(v)\Psi'(Q_Y(v))\, dp,$$

which implies

$$\mathcal{C}P\xi_Q^\eta(\Psi(X)) \geq \mathcal{C}P\xi_Q^\eta(\Psi(Y)).$$

The convex case follows analogously. $\square$

These ordering results demonstrate that QFGCPE is consistent with established hazard- and quantile-based comparisons while providing a direct ranking of populations in terms of accumulated mortality uncertainty.

Overall, the QFGCPE framework provides a flexible and interpretable measure of accumulated mortality uncertainty that naturally integrates quantile-based survival information with fractional weighting. In the next section, we extend this framework dynamically to study how mortality uncertainty evolves across survival quantiles and time horizons.

7.4 Dynamic quantile-based FGCPE

In survival analysis, it is often of interest to assess how mortality uncertainty evolves as survival time progresses. Static entropy measures summarize uncertainty over the entire lifetime distribution, whereas dynamic measures quantify uncertainty accumulated up to a given survival horizon. Motivated by this perspective, we introduce a time-dependent, or dynamic, version of the quantile-based fractional generalized cumulative past entropy.

Definition 7.4.1. *The dynamic quantile-based fractional generalized cumulative past entropy (DQFGCPE) of a non-negative random variable X is defined as*

$$\mathcal{C}P\xi_Q^\eta(X,v) = \frac{1}{v\,\Gamma(\eta+1)} \int_0^v p\big(\ln v - \ln p\big)^\eta q(p)\, dp, \qquad \eta > 0,\ 0 < v < 1, \tag{7.4.1}$$

where v denotes a survival quantile representing a time horizon in the distribution of X.

For $0 \leq \eta \leq 1$, $\mathcal{C}P\xi_Q^{\eta}(X,v)$ quantifies fractional information associated with mortality occurring up to the $100v\%$ point of the survival distribution. In a clinical context, this measure captures uncertainty accumulated among individuals who experience the event prior to a given survival quantile, making it particularly suitable for early- and mid-term survival analysis.

Closed-form expressions of DQFGCPE for selected lifetime distributions are summarized in Table 7.4.1. These examples illustrate the analytical tractability of the proposed measure for common survival models.

Table 7.4.1: Quantile-based DFGCPE for selected lifetime distributions.

Distribution	**Parameters**	$\mathbf{F(x)}$	$\mathcal{CP}\xi_{\mathbf{Q}}^{\eta}(\mathbf{X},\mathbf{v})$
Exponential	$\lambda > 0$	$1-e^{-\lambda x},\ x \geq 0$	$\Gamma(\eta+1)\Phi(v,\eta+1,2) = \frac{1}{\lambda v}\big(Li_{\eta+1}(v) - v\big)$
Power	$0 < v < 1,\ b > 0$	$x^b,\ 0 \leq x \leq l$	$vb^{\eta}/(b+1)^{\eta}$
Fréchet	$a, b > 0$	$e^{-bx^{-a}},\ x > 0$	$\frac{b^{1/a}}{a}(-\ln v)^{\eta-\frac{1}{a}}\, U\big(\eta+1, \eta+1-\frac{1}{a}, -\ln v\big)$

Note:

1. $\Phi(z,s,a) = \sum_{k=0}^{\infty}\frac{z^k}{(a+k)^s}$ is the Lerch transcendent function, which gives the polylogarithm function for $a=1$, expressed as $Li_s(v) = \sum_{k=1}^{\infty}\frac{v^k}{k^s}$;
2. $\mathrm{U}(A,B,z) = = \frac{1}{\Gamma(A)}\int_0^{\infty} e^{-zt}\, t^{\,A-1}(1+t)^{\,B-A-1}\, dt$, represents the Tricomi confluent hypergeometric function, which can also be expressed in terms of Kummer's confluent hypergeometric function ${}_1F_1$ as

$$U(a,b,z) \;=\; \frac{\pi}{\sin(\pi b)}\left(\frac{{}_1F_1(a,b,z)}{\Gamma(1+a-b)\Gamma(b)} - \frac{z^{\,1-b}\,{}_1F_1(1+a-b,2-b,z)}{\Gamma(a)\Gamma(2-b)}\right).$$

Fig. 7.4.1 illustrates the behavior of DQFGCPE for the power distribution. The measure increases monotonically with respect to the quantile level v for all admissible values of the distribution parameter $b > 0$ and entropy order $\eta > 0$. Larger values of η amplify sensitivity to accumulated early-time uncertainty, highlighting the role of fractional weighting in emphasizing different phases of the survival process.

We next examine the behavior of DQFGCPE under monotone transformations of survival time.

Theorem 7.4.1. *Let X be a non-negative random variable with quantile function Q_X and quantile density function q_X. If $Y = \Psi(X)$, where Ψ is a positive increasing function,*

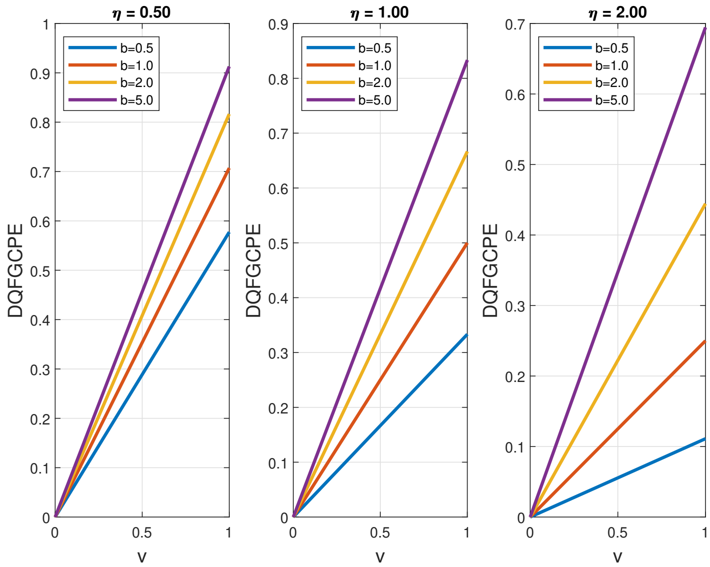

Figure 7.4.1: Monotonic behaviour of DQFGCPE for power distribution w.r.t v.

then

$$\mathcal{CP}\xi_Q^{\eta}(\Psi(X), v) = \frac{1}{v\,\Gamma(\eta+1)} \int_0^v p(\ln v - \ln p)^{\eta} q_X(p) \Psi'(Q_X(p))\, dp.$$

Proof. The result follows directly from the transformation property of QFGCPE established in Theorem 7.3.1. □

Based on DQFGCPE, we define dynamic classes of lifetime distributions.

Definition 7.4.2. *A random variable X is said to have*

- *increasing DQFGCPE (IDQFGCPE) if $\mathcal{CP}\xi_Q^{\eta}(X, v)$ is increasing in v,*
- *decreasing DQFGCPE (DDQFGCPE) if $\mathcal{CP}\xi_Q^{\eta}(X, v)$ is decreasing in v.*

These classes characterize whether accumulated mortality uncertainty increases or decreases as progressively larger survival quantiles are considered. In survival studies, IDQFGCPE behavior is typically associated with increasing heterogeneity among early failures, while DDQFGCPE reflects stabilization of survival outcomes among longer-term survivors.

Definition 7.4.3. *For two random variables X and Y, if*

$$\mathcal{CP}\xi_Q^{\eta}(X, v) \le \mathcal{CP}\xi_Q^{\eta}(Y, v) \quad \forall\, v \in (0, 1),$$

then X is said to have smaller dynamic QFGCPE than Y, denoted by $X \leq_{DQFGCPE} Y$.

This ordering allows comparison of populations in terms of accumulated mortality uncertainty up to any survival quantile. For example, if X and Y follow exponential distributions with rates λ_1 and λ_2, respectively, then $\lambda_1 \geq \lambda_2$ implies $X \leq_{DQFGCPE} Y$, reflecting greater early mortality concentration in X.

Theorem 7.4.2. *Let $Y = \Psi(X)$, where Ψ is an increasing, non-negative, convex (or concave) function. If X is IDQFGCPE (or DDQFGCPE), then Y is also IDQFGCPE (or DDQFGCPE).*

Proof. From the definition of the dynamic QFGCPE in (7.4.1), we have

$$\mathcal{C}P\xi_Q^\eta(Y,v) = \frac{1}{v\,\Gamma(\eta+1)} \int_0^v p\big(\ln v - \ln p\big)^\eta q_Y(p)\,dp, \qquad \eta > 0,\ 0 < v < 1.$$

Since $Y = \Psi(X)$ with Ψ increasing, the quantile density of Y is $q_Y(p) = q_X(p)\Psi'(Q_X(p))$. Hence,

$$\mathcal{C}P\xi_Q^\eta(Y,v) = \frac{1}{v\,\Gamma(\eta+1)} \int_0^v p\big(\ln v - \ln p\big)^\eta q_X(p)\Psi'(Q_X(p))\,dp. \tag{7.4.2}$$

Because Ψ is increasing and non-negative, $\Psi'(Q_X(p)) \geq 0$. Moreover, if Ψ is convex (respectively, concave), then Ψ' is increasing (respectively, decreasing). Since $Q_X(p)$ is increasing in p, it follows that $\Psi'(Q_X(p))$ is increasing (respectively, decreasing) in p.

Now observe that, for fixed $\eta > 0$, the kernel

$$K(v,p) = \frac{1}{v\,\Gamma(\eta+1)} p\big(\ln v - \ln p\big)^\eta, \qquad 0 < p < v,$$

is non-negative and increasing in v for each fixed $p \in (0,1)$. Hence, if X is IDQFGCPE, the integral

$$\int_0^v K(v,p)\,q_X(p)\,dp = \mathcal{C}P\xi_Q^\eta(X,v)$$

is increasing in v.

Multiplying the integrand by the non-negative and increasing function $\Psi'(Q_X(p))$ preserves this monotonicity, so the right-hand side of (7.4.2) is also increasing in v. Therefore, $\mathcal{C}P\xi_Q^\eta(Y,v)$ is increasing in v, and Y is IDQFGCPE.

The argument is analogous when Ψ is concave. In that case, $\Psi'(Q_X(p))$ is non-negative and decreasing in p, and multiplication by a decreasing weight preserves the decreasing behavior of $\mathcal{C}P\xi_Q^\eta(X,v)$. Hence, if X is DDQFGCPE, then $\mathcal{C}P\xi_Q^\eta(Y,v)$ is decreasing in v, and Y is also DDQFGCPE. □

Theorem 7.4.3. *If $X \leq_{disp} Y$, then $X \leq_{DQFGCPE} Y$.*

Proof. Since $X \leq_{disp} Y$ implies $q_X(v) \leq q_Y(v)$ for all $v \in (0,1)$, substitution into (7.4.1) yields

$$\mathcal{CP}\xi_Q^{\eta}(X,v) \leq \mathcal{CP}\xi_Q^{\eta}(Y,v),$$

which establishes the result. □

The dynamic formulation of QFGCPE provides a principled tool for examining how mortality uncertainty accumulates across survival horizons. Unlike hazard-based dynamic measures, DQFGCPE integrates information over quantiles and directly reflects heterogeneity among early and late failures. This makes it particularly suitable for life-table and cancer survival data, where early mortality is prominent and long-term survivor behavior differs substantially across populations.

7.5 Non-parametric estimation of QFGCPE

In survival analysis, non-parametric estimation is particularly attractive when the underlying lifetime distribution is unknown or difficult to model, as is often the case with life-table or registry-based data. In this section, we develop a non-parametric estimator for the quantile-based fractional generalized cumulative past entropy (QFGCPE) that is constructed directly from sample quantiles and therefore avoids parametric assumptions.

Let $X_1, X_2, \ldots, X_n$ be a random sample of independent and identically distributed non-negative random variables representing observed survival times, with cumulative distribution function (cdf) $F(x)$ and corresponding quantile function $Q(v)$. Denote the associated order statistics by

$$X_{1:n} \leq X_{2:n} \leq \cdots \leq X_{n:n},$$

where $X_{k:n}$ represents the kth smallest observed survival time.

The empirical distribution function (edf),

$$F_n(x) = \frac{1}{n}\sum_{i=1}^{n} \mathbf{1}_{\{X_i \leq x\}}, \qquad x \in \mathbb{R},$$

serves as a non-parametric estimator of $F(x)$. The corresponding empirical quantile function (EQF) is defined by

$$Q_n(v) = \inf\{x \in \mathbb{R} : F_n(x) \geq v\}, \qquad 0 < v < 1.$$

For $v \in \left(\frac{k-1}{n}, \frac{k}{n}\right]$, the EQF coincides with the order statistic $X_{k:n}$ (Philippatos and Wilson, 1972), establishing a direct link between quantiles and observed survival times.

To obtain a smooth approximation of the EQF, we employ the linear interpolation estimator (Sunoj and Sebastian, 2025)

$$\overline{Q}_n(v) = n\Big(\tfrac{k}{n} - v\Big)X_{k-1:n} + n\Big(v - \tfrac{k-1}{n}\Big)X_{k:n}, \qquad v \in \Big(\tfrac{k-1}{n}, \tfrac{k}{n}\Big),$$

which leads to the empirical quantile density function (eqdf)

$$\overline{q}_n(v) = n\big(X_{k:n} - X_{k-1:n}\big), \tag{7.5.1}$$

for $v \in \left(\frac{k-1}{n}, \frac{k}{n}\right)$.

Substituting the eqdf into the definition of QFGCPE in (7.3.1), we obtain the non-parametric estimator

$$\widehat{\mathcal{C}P\xi}^{\eta}_{Q}(X) = \frac{1}{\Gamma(\eta+1)} \int_0^1 p(-\ln p)^{\eta}\overline{q}_n(p)\,dp, \qquad \eta > 0. \tag{7.5.2}$$

Approximating the integral in (7.5.2) by a Riemann sum over the n quantile intervals yields

$$\widehat{\mathcal{C}P\xi}^{\eta}_{Q}(X) = \frac{1}{\Gamma(\eta+1)} \sum_{k=1}^{n-1} \frac{k}{n}\Big(-\ln \tfrac{k}{n}\Big)^{\eta}\big(X_{k:n} - X_{k-1:n}\big). \tag{7.5.3}$$

The estimator in (7.5.3) depends only on observed order statistics and empirical quantile levels, making it particularly well suited for survival data with limited distributional information. In a clinical context, this estimator captures accumulated mortality uncertainty by weighting inter-quantile spacings according to their position in the survival distribution, thereby emphasizing early versus late survival behavior through the fractional parameter η.

7.5.1 Simulation study

To assess the finite-sample performance of the proposed non-parametric estimator of QFGCPE defined in (7.5.3), we conducted a Monte Carlo simulation study under both the standard exponential distribution and the Govindarajalu distribution. The exponential model serves as a baseline lifetime distribution with a tractable form, while the Govindarajalu distribution is included to demonstrate the effectiveness of the quantile-based framework for models with intractable distribution functions.

Independent random samples of sizes $n = 50, 100, 500, 1000$, and 5000 were generated for each distributional setting, with $N_{\text{sim}} = 500$ Monte Carlo replications. For each simulated sample, the QFGCPE was estimated using the proposed non-parametric estimator, and its empirical bias and mean squared error (MSE) were evaluated against the corresponding theoretical values derived from (7.3.1). The results are summarized in Tables 7.5.1–7.5.4.

The Govindarajalu distribution (Sunoj and Sebastian, 2025) is particularly relevant in this context, as it admits a closed-form quantile function but lacks a tractable distribution function. This feature highlights the practical advantage of quantile-based entropy measures in survival analysis, especially for lifetime models exhibiting non-standard hazard shapes such as bathtub-type behavior (Nair et al., 2013). The quantile function of the Govindarajalu distribution is given by

$$Q(v) = \alpha + \beta\big[(\gamma+1)v^{\gamma} - \gamma v^{\gamma+1}\big], \qquad \alpha \in (-\infty, \infty),\ \beta, \gamma > 0,\ v \in (0,1).$$

Tables 7.5.1–7.5.4 report the empirical mean of the estimator, bias, MSE, RMSE, and the corresponding theoretical values for different choices of the fractional order parameter η. Across all distributions and parameter settings, the estimator exhibits clear consistency: both bias and MSE decrease systematically as the sample size increases, and the empirical mean converges toward the theoretical benchmark. As expected, finite-sample bias and variability are more pronounced for small samples ($n = 50, 100$), but diminish rapidly for moderate and large samples. For $n = 5000$, the bias is negligible and the RMSE is very small, indicating high estimation accuracy.

Table 7.5.1: Comparison of empirical vs theoretical QFGCPE ($\eta = 0.5$) for exponential ($\lambda = 1$) distribution.

n	Mean Empirical	Bias	MSE	RMSE	Theoretical Value
50	1.3861	−0.2262	0.1364	0.3694	1.6124
100	1.4610	−0.1514	0.0761	0.2759	1.6124
500	1.5326	−0.0797	0.0222	0.1490	1.6124
1000	1.5573	−0.0550	0.0120	0.1094	1.6124
5000	1.5883	−0.0241	0.0025	0.0499	1.6124

Table 7.5.2: Comparison of empirical vs theoretical QFGCPE ($\eta = 0.75$) for exponential ($\lambda = 1$) distribution.

n	Mean Empirical	Bias	MSE	RMSE	Theoretical Value
50	0.91716	−0.04516	0.02760	0.1661	0.96232
100	0.94243	−0.01989	0.01356	0.1164	0.96232
500	0.95234	−0.00998	0.00330	0.0574	0.96232
1000	0.95623	−0.00609	0.00164	0.0406	0.96232
5000	0.96123	−0.00109	0.00028	0.0169	0.96232

Table 7.5.3: Comparison of empirical vs theoretical QFGCPE for Govindarajalu(α, β, γ) distribution with $(\alpha, \beta, \gamma) = (1, 2, 2)$ and $\eta = 0.25$.

n	Mean Empirical	Bias	MSE	RMSE	Theoretical Value
50	0.9045	-1.35×10^{-2}	3.80×10^{-3}	6.16×10^{-2}	0.91802
100	0.9148	-3.20×10^{-3}	1.84×10^{-3}	4.29×10^{-2}	0.91802
500	0.9171	-9.40×10^{-4}	3.78×10^{-4}	1.94×10^{-2}	0.91802
1000	0.9176	-4.20×10^{-4}	1.84×10^{-4}	1.36×10^{-2}	0.91802
5000	0.9182	1.53×10^{-4}	3.55×10^{-5}	5.96×10^{-3}	0.91802

In addition to point estimation, we evaluated the interval estimation performance of the proposed estimator using bootstrap-based confidence intervals. For each Monte Carlo replication, $B_{\text{boot}} = 500$ bootstrap samples were generated, and 95% percentile confidence intervals were constructed. Empirical coverage probabilities and Monte Carlo standard errors (MCSE) were then computed across replications. The results for the exponential and Govindarajalu$(1, 2, 2)$ distributions with $\eta = 0.75$ are presented in Tables 7.5.5 and 7.5.6, respectively.

For the exponential distribution, Table 7.5.5 shows that coverage probabilities increase with sample size, rising from approximately 76% at $n = 50$ to over 90% for $n \geq 500$. Similar behavior is observed for the Govindarajalu distribution in Table 7.5.6, where

Table 7.5.4: Comparison of empirical vs theoretical QFGCPE for Govindarajalu(α, β, γ) distribution with $(\alpha, \beta, \gamma) = (1, 2, 2)$ and $\eta = 0.75$.

n	Mean Empirical	Bias	MSE	RMSE	Theoretical Value
50	0.68147	-1.26×10^{-2}	9.35×10^{-4}	3.06×10^{-2}	0.69411
100	0.68875	-5.35×10^{-3}	3.87×10^{-4}	1.97×10^{-2}	0.69411
500	0.69315	-9.53×10^{-4}	7.51×10^{-5}	8.67×10^{-3}	0.69411
1000	0.69320	-9.06×10^{-4}	3.83×10^{-5}	6.19×10^{-3}	0.69411
5000	0.69407	-3.03×10^{-5}	6.45×10^{-6}	2.54×10^{-3}	0.69411

coverage approaches the nominal 95% level for moderate to large samples. The associated MCSE values decrease with increasing n, indicating improved precision and stability of the coverage estimates.

Overall, the simulation results confirm that the proposed non-parametric estimator of QFGCPE is consistent and exhibits favorable finite-sample properties. Bootstrap confidence intervals provide reliable uncertainty quantification in moderate to large samples, while slight under-coverage for small samples reflects finite-sample bias rather than structural deficiencies of the estimator. These findings support the applicability of the proposed methodology for practical survival analysis settings, including those involving complex or intractable lifetime distributions.

Table 7.5.5: Bootstrap coverage probabilities and Monte Carlo standard errors (MCSE) for 95% percentile confidence intervals of QFGCPE for Exponential($\lambda = 1$) distribution with $\eta = 0.75$.

n	Coverage Probability	MCSE
50	0.758	0.019
100	0.846	0.016
500	0.912	0.013
1000	0.924	0.013

Table 7.5.6: Bootstrap coverage probabilities and Monte Carlo standard errors (MCSE) for 95% percentile confidence intervals of QFGCPE for Govindarajalu(1,2,2) distribution with $\eta = 0.75$.

n	Coverage Probability	MCSE
50	0.892	0.0139
100	0.924	0.0119
500	0.958	0.0090
1000	0.942	0.0105

7.6 Validity and sensitivity of QFGCPE using logistic maps

To further assess the validity and sensitivity of the proposed QFGCPE measure, we investigate its behavior under controlled dynamical regimes generated by a canonical logistic map, a well-known deterministic model exhibiting transitions from stability to chaos. The logistic map is defined by the recurrence relation

$$x_{n+1} = cx_n(1 - x_n), \qquad x_n \in [0, 1], \tag{7.6.1}$$

where the control parameter $c \in [0, 4]$ governs the qualitative nature of the dynamics. Depending on the value of c, the system exhibits stable fixed points, periodic oscillations, or fully developed chaotic behavior. In particular, for $c \lesssim 3$ the dynamics are stable or periodic, while for $c > 3$ the system undergoes successive bifurcations leading to chaos.

For the simulation study, we fix the initial condition at $x_0 = 0.1$ and generate time series for selected values of the control parameter $c = 1, 1.5, 2, 2.5, 3, 3.5$, and 4. These sequences are then treated as realizations of stochastic-like processes with varying degrees of intrinsic uncertainty, allowing us to examine whether QFGCPE appropriately reflects transitions in dynamical complexity.

Figure 7.6.1 displays QFGCPE as a function of the control parameter c for different fractional orders η, alongside the corresponding bifurcation structure of the logistic map. In the stable and low-period regimes ($c \lesssim 3$), QFGCPE remains close to zero, consistent with the highly predictable nature of the dynamics. As c increases beyond the

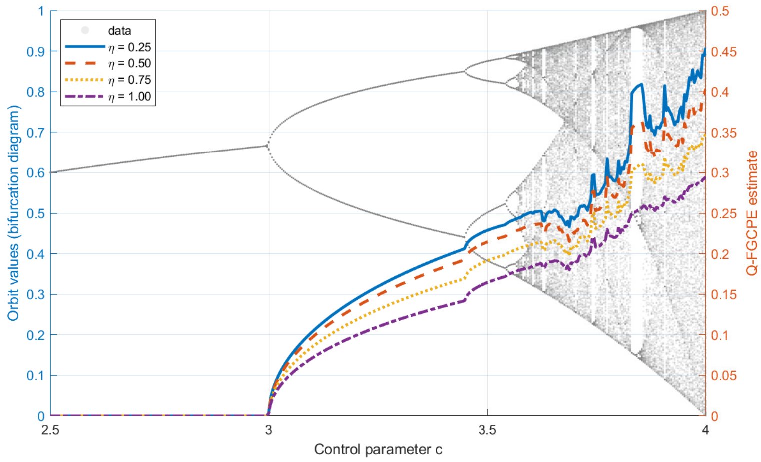

Figure 7.6.1: Logistic map: bifurcation vs QFGCPE w.r.t c for different η values.

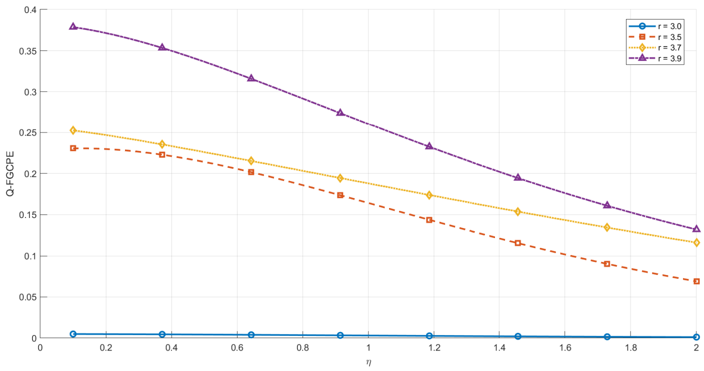

Figure 7.6.2: Logistic map: QFGCPE w.r.t η for different c values.

bifurcation threshold, QFGCPE rises sharply, capturing the onset of irregular and chaotic behavior. The overall pattern closely mirrors the bifurcation diagram, thereby validating that QFGCPE effectively quantifies the degree of dynamical uncertainty inherent in the system.

Different values of the fractional order parameter η produce qualitatively similar trends but operate at different sensitivity levels. Smaller values of η emphasize fine-scale fluctuations and yield sharper responses near transition points, whereas larger values of η smooth local variability and reflect broader uncertainty patterns.

To further examine sensitivity with respect to η, Fig. 7.6.2 illustrates QFGCPE as a function of η for representative values of c, including a periodic regime ($c = 3.2$) and a chaotic regime ($c = 3.7$). In periodic regimes, QFGCPE exhibits weak dependence on η, consistent with low dynamical complexity. In contrast, for chaotic regimes, QFGCPE increases more rapidly with η, indicating enhanced responsiveness of the measure to changes in fractional weighting under high-uncertainty dynamics.

Taken together, these results demonstrate that QFGCPE is both valid and sensitive: it reliably distinguishes between regular and chaotic regimes and adapts smoothly across different levels of dynamical complexity through the fractional parameter η. This validation supports the broader applicability of QFGCPE as a flexible entropy-based measure capable of capturing uncertainty patterns in complex systems, including those arising in survival and reliability analyses.

7.7 Application to lung cancer life-table data

Entropy-based measures provide a powerful framework for analyzing survival data by quantifying heterogeneity and uncertainty beyond classical summaries such as mean survival or hazard rates. In particular, quantile-based entropy measures can reveal structural differences in survival distributions without relying on density estimation or restrictive parametric assumptions. To demonstrate the practical utility of the proposed quantile-based fractional generalized cumulative past entropy (QFGCPE), we analyze the well-known `lung` cancer dataset from the North Central Cancer Treatment Group, available through the `survival` package and re-exported via the `lifelines` library.

The dataset consists of 228 patients diagnosed with advanced lung cancer and includes survival times along with covariates such as age, sex, ECOG performance score, and treatment information. Approximately 63% of observations correspond to observed events, with the remainder subject to right censoring. Because censoring prevents direct application of the empirical estimator in Eq. (7.5.3), we employ a Kaplan-Meier (KM)-adjusted estimator of QFGCPE that constructs empirical quantiles from the KM survival function. To illustrate clinically relevant heterogeneity, the analysis is stratified by sex, yielding male and female subgroups.

7.7.1 Kaplan-Meier (KM)-based estimation of QFGCPE under right censoring

In many survival studies, including lung cancer registries, failure times are subject to right censoring or available only in grouped form through life tables. The estimator in (7.5.3) adapts naturally to these settings by replacing the empirical distribution function with the Kaplan-Meier(KM) estimator for censored data or life-table survival estimates for grouped data. Empirical quantiles are then obtained by inversion, and inter-quantile spacings computed accordingly. This preserves the non-parametric structure of the estimator and ensures robust QFGCPE estimation under practical data limitations common in population-based survival analysis.

Let (T_i, δ_i) denote the observed survival time and censoring indicator for the ith patient, where $\delta_i = 1$ indicates death and $\delta_i = 0$ indicates right censoring. The Kaplan–Meier estimator of the survival function,

$$\widehat{S}(t) = \prod_{T_j \leq t} \left(1 - \frac{d_j}{r_j}\right),$$

provides a nonparametric estimate of survival in the presence of censoring. Inverting $\widehat{S}(t)$ yields the KM-based empirical quantile function

$$\widehat{Q}(p) = \inf\{t : 1 - \widehat{S}(t) \geq p\}, \qquad 0 < p < 1.$$

Since $\widehat{Q}(p)$ is piecewise constant, the quantile density function is approximated using finite differences over a grid of probability levels $\{p_k\}$, leading to the KM-adjusted estimator

$$\widehat{CP}_{\xi,\eta}^{Q,KM}(X) = \frac{1}{\Gamma(\eta+1)} \sum_{k=1}^{m-1} p_k(-\ln p_k)^{\eta} \big(\widehat{Q}(p_{k+1}) - \widehat{Q}(p_k)\big). \tag{7.7.1}$$

This estimator reduces to the uncensored version in Eq. (7.5.3) when no censoring is present and remains stable in moderately censored settings.

Table 7.7.1: KM-based QFGCPE estimates for male and female lung cancer patients for selected fractional orders η.

Fractional Order η	**Male**	**Female**
0.25	489.921	414.551
0.50	346.483	334.217
1.00	185.480	219.085
2.00	71.749	103.833

Table 7.7.1 reports KM-based QFGCPE estimates for male and female patients across four representative fractional orders η. For smaller values of η (0.25 and 0.50), male patients exhibit higher QFGCPE, indicating greater uncertainty across the early-to-mid

survival region. For larger values ($\eta = 1.00$ and 2.00), the ordering reverses, with females showing higher QFGCPE, reflecting greater instability in the extreme early-failure tail. These scale-dependent reversals highlight survival heterogeneity that is not apparent from standard summaries.

Table 7.7.2: Uncensored empirical QFGCPE values based on observed event times only.

η	**Male(emp.)**	**Female(emp.)**
0.25	377.861	336.126
0.50	263.687	261.745
1.00	143.384	160.340
2.00	57.780	72.224

For comparison, Table 7.7.2 presents QFGCPE values computed using uncensored event times only. Although qualitative patterns are similar, the magnitudes are uniformly smaller, underscoring the loss of information when censoring is ignored and emphasizing the importance of KM adjustment in clinical data.

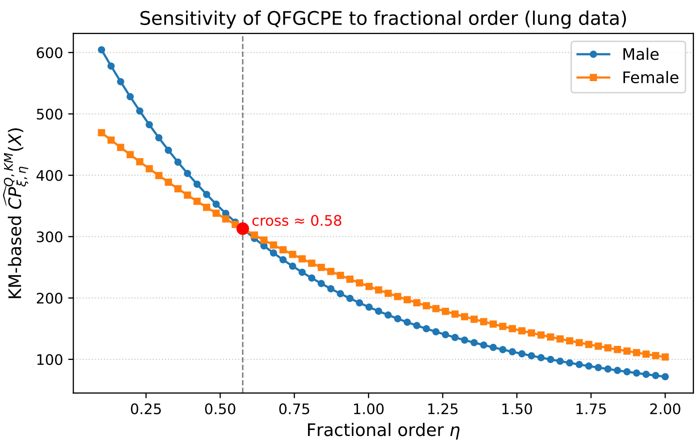

Figure 7.7.1: Sensitivity of the Kaplan–Meier based QFGCPE to η for male and female lung cancer patients.

To further examine sensitivity to the fractional parameter, Fig. 7.7.1 displays KM-based QFGCPE as a function of $\eta \in [0.1, 2.0]$ for both subgroups. The curves decrease monotonically with η and intersect near $\eta \approx 0.58$, marking a transition in which uncertainty shifts from broader early-survival variability (smaller η) to instability concentrated in the extreme lower tail (larger η). This tunability allows analysts to focus on clinically relevant regions of the survival distribution, from overall dispersion to high-risk early deterioration.

Overall, the lung cancer application demonstrates that QFGCPE provides a flexible and informative summary of survival-time uncertainty. By combining quantile-based inference, fractional weighting, and KM adjustment for censoring, the proposed framework uncovers subgroup differences and scale-dependent survival patterns that are not captured by traditional hazard-based or single-scale entropy measures.

7.8 Conclusion

This chapter introduced the quantile-based fractional generalized cumulative past entropy (QFGCPE) as a flexible and non-parametric framework for quantifying mortality uncertainty and its temporal evolution in survival data. By integrating quantile representations with fractional entropy weighting, the proposed measure captures cumulative uncertainty in survival times without relying on density estimation or restrictive parametric assumptions, and is naturally suited to censored and life-table data. Key theoretical properties, stochastic orderings, and dynamic extensions were established to ensure interpretability and consistency within a survival analysis setting. Non-parametric and Kaplan-Meier-adjusted estimators were developed for practical implementation under complete, censored, and grouped data structures, and simulation studies confirmed favorable finite-sample performance. Application to lung cancer survival data demonstrated that QFGCPE reveals scale-dependent survival heterogeneity and subgroup differences that are not detectable using conventional hazard-based summaries.

Beyond the analyses presented here, this chapter establishes the methodological foundation for ongoing and future work focused on large-scale mortality datasets. In particular, planned extensions include comparative analyses of mortality uncertainty across sex, age groups, and countries using life-table data, with explicit examination of low and high mortality quantiles. Additionally, dynamic QFGCPE will be employed to study temporal changes in mortality uncertainty across historical periods and cohorts, providing insight into long-term population-level risk evolution. For disease-specific survival, further applications using some published cancer registries will be conducted to examine how mortality uncertainty evolves over time and differs across demographic and clinical subgroups.

Overall, this chapter positions QFGCPE as a unifying and extensible framework for quantifying mortality uncertainty in both population and disease-specific survival analysis. By using quantile-based cumulative entropy measures, the proposed methodology opens new avenues for understanding heterogeneity, temporal evolution, and structural differences in survival outcomes across diverse real-world settings.

Chapter 8

Conclusion and Future Scope

"Information is the resolution of uncertainty."
— Claude E. Shannon

This chapter summarizes and concludes the key findings of the research presented in this thesis. The originality of this work is attributed to the exploration of the practical relevance of information-theoretic components and the associated theoretical frameworks developed throughout the study, representing, to the best of our knowledge, the first attempt within the fields under consideration. The results obtained reveal several promising avenues for further investigation. Accordingly, this chapter also outlines potential directions for future research that may be pursued based on the insights and outcomes of the present work.

Overall summary and significance of the present work

The present thesis develops fractional order entropy-based frameworks for modeling uncertainty in non-extensive systems. Starting from the limitations of Shannon entropy in systems with heterogeneity, memory effects, long-range dependence, and nonlinear behaviour, the work focuses on Ubriaco entropy and its generalizations as flexible tools for uncertainty quantification. The main contributions of the thesis may be grouped into theoretical and applied contributions as follows.

Theoretical contributions

First, the thesis provides a systematic interpretation of the fractional order parameter in Ubriaco entropy. The parameter α is interpreted as a sensitivity parameter that controls the response of entropy to uncertainty. In financial decision-making, this parameter is further interpreted in behavioral terms, where different values of α represent different levels of investor risk sensitivity. Second, two fractional entropy-based risk measures, namely EU-FE and EU-FEV, are developed by combining fractional entropy with expected utility and variance. These measures extend classical utility- and variance-based decision-making models by incorporating entropy-based uncertainty and investor-specific sensitivity through the parameter α (Chapter 2).

Third, the thesis introduces normalized fractional order entropy-based risk measures, namely NEU-FE and NEU-FEV. The normalization removes scale dependence, improves comparability across assets and datasets, and enhances numerical stability while preserving the basic fractional entropy structure (Chapter 3).

Fourth, the thesis extends Ubriaco entropy to continuous settings through fractional differential entropy (FDE). This provides a theoretical basis for using fractional order entropy in continuous physical profile modeling, especially for hydraulic velocity and suspended sediment concentration distributions (Chapter 4).

Fifth, the thesis further extends the sediment concentration framework using Machado's fractional entropy, where the fractional parameter is allowed to vary over a broader real-order setting. This shows that the modeling philosophy is not restricted to a single entropy form, but is based on a broader fractional entropy principle (Chapter 5 – 6).

Finally, the thesis develops a quantile-based fractional generalized cumulative past entropy framework for survival analysis. This quantile-based formulation does not rely directly on density estimation and is therefore suitable for lifetime data, censored observations, and situations where density-based entropy measures may be unstable (Chapter 7).

Applied contributions

In financial decision-making, the proposed EU-FE and EU-FEV models are applied to portfolio selection and risk assessment using machine learning techniques for parameter estimation and predictive validation. Empirical studies using PSI20 data demonstrate that fractional order entropy effectively incorporates investor risk sensitivity into decision-making under uncertainty. The robustness of the proposed models is further supported through simulation studies under representative probability distributions and comparative machine learning analyses involving Linear Regression, Lasso Regression, Sinusoidal Regression and ANN. The normalized counterparts, NEU-FE and NEU-FEV, are subsequently validated using NIFTY50 data, demonstrating improved comparability, numerical stability and robust stock-selection performance (Chapters 2–3).

In hydraulic flow modeling, the FDE-based framework is applied to the one-dimensional vertical velocity distribution in open-channel flows. The model is validated using experimental and field datasets and is shown to provide a flexible entropy-based alternative to classical velocity-profile models (Chapter 4).

In suspended sediment concentration modelling, FDE-based and Machado entropy-based formulations are used to model the vertical distribution of SSC in open-channel turbulent flows. The proposed models capture nonlinear vertical variation, near-bed concentration dominance, and sediment-profile heterogeneity. Bootstrap and jackknife analyses further support the reliability of the estimated parameters (Chapter 5 – 6).

In survival analysis, the proposed QFGCPE and its dynamic extension are applied to lifetime uncertainty modeling. Simulation studies, logistic map analysis, Kaplan–Meier estimation, and real lung cancer data demonstrate that the quantile-based framework is useful for analysing mortality uncertainty, especially when censoring or density-estimation difficulties are present (Chapter 7).

Overall, the thesis transforms Ubriaco entropy from a largely theoretical fractional order entropy measure into an interpretable and application-oriented framework for uncertainty quantification. The unity of the thesis lies not in using one identical entropy formula for all datasets, but in using fractional entropy as a flexible principle adapted to the structure of the data: probability-based measures for financial decision-making, differential entropy for continuous hydraulic profiles, and quantile-based entropy for survival data.

Future scope of the present work

A natural extension of the present work is to develop fractional entropy-based decision models under more realistic market features. The current financial chapters focus on entropy-based risk ranking and stock selection using empirical return data. Future studies may incorporate additional market characteristics such as transaction costs, liquidity risk, short-selling constraints, regime switching, volatility clustering, heavy-tailed returns, and investor-specific risk preferences. Such extensions would make the proposed entropy-based decision framework more suitable for realistic portfolio construction and financial risk management.

Another important direction is entropy-based portfolio optimization. The fractional order entropy measures developed in this thesis may be combined with classical mean–variance optimization, downside-risk measures, conditional value-at-risk, and robust portfolio selection models. In this setting, the fractional parameter may be treated as an adaptive risk-sensitivity parameter, allowing the portfolio strategy to change according to market uncertainty, investor behaviour, or regime conditions.

Advanced machine learning can also be integrated with the proposed framework. For example, deep neural networks, recurrent networks, LSTM/GRU models, attention-based models, graph neural networks, and reinforcement learning may be used to estimate time-varying entropy-based risk scores, detect market regimes, or construct adaptive portfolios. However, such models should be used with suitable safeguards against overfitting, including cross-validation, regularization, out-of-sample testing, and robust statistical comparison.

Future work may also consider multivariate and adaptive entropy systems. Multivariate fractional entropy measures could capture dependence among assets, sectoral co-movement, and systemic risk, while adaptive entropy models could allow the fractional order parameter to vary over time according to market conditions. Such extensions would move the present static entropy-based framework toward dynamic, data-driven, and market-adaptive uncertainty modeling.

Bibliography

Abe, S. (1997), A note on the q-deformation-theoretic aspect of the generalized entropies in nonextensive physics. *Physics Letters A*, *224*(326).

Ahamed, N. and Kundu, S. (2023), Fractional entropy-based modeling of suspended concentration distribution of type I and type II and sediment discharge in pipe and open-channel turbulent flows. *Journal of Applied Mathematics and Physics*, *74*, 101.

Ahamed, N. and Kundu, S. (2024), Fractional entropy-based models for S-type velocity distributions in turbulent open-channel flows and turbulent Couette flows. *Stochastic Environmental Research and Risk Assessment*, *38*, 3345–3361.

Afzalmehr, L. (2008), Iran open channel flow velocity data. *Personal Communication.*

Aksarayli, M. and Pala, O. (2018), A polynomial goal programming model for portfolio optimization based on entropy and higher moments. *Expert Systems with Applications*, *94*, 185–192.

Aggarwal, M. (2021a), Human decision-making through an entropic framework. *Expert Systems with Applications*, *183*.

Aggarwal, M. (2021b), Attitude-based entropy function and applications in decision-making. *Engineering Applications of Artificial Intelligence*, *104*, 104290.

Allais, M. (1953), The behavior of the rational man in the face of risk, critique of the postulates and axioms of the American school. *Econometrica*, *21*, 503–546.

Aswin, I.C., Sankaran, P.G. and Sunoj, S.M. (2023), Reliability aspects of quantile-based residual coefficient of variation. *International Journal of Reliability, Quality and Safety Engineering*, *30*(02), 2250021.

Bhattacharyya, R., Chatterjee, A. and Kar, S. (2013), Uncertainty theory based multiple objective mean-entropy-skewness stock portfolio selection model with transaction costs. *Journal of Uncertainty Analysis and Applications*, *1*(16).

Bickel, P.J. and Lehmann, E.L. (1976), Descriptive statistics for nonparametric models IV. Spread. *In:* Lehmann, E.L. (ed.), *Selected Works of E.L. Lehmann in Probability and Statistics, Springer, Boston, MA,* 519–526.

Bonami, P. and Lejeune, M.A. (2009), An exact solution approach for portfolio optimization problems under stochastic and integer constraints. *Operations Research*, *57*(3), 650–670.

Bonanno, G., Lillo, F. and Mantegna, R.N. (2001), High-frequency cross-correlation in a set of stocks. *Physica A: Statistical Mechanics and its Applications*, *299*(1–2), 16–27.

Brachinger, H.W. and Weber, M. (1997), Risk as a primitive: A survey of measures of perceived risk. *OR Spektrum 19*, 235–250.

Brito, I. (2020), A decision model based on expected utility, entropy and variance. *Applied Mathematics and Computation*, *379*, 125285.

Brito, I. (2022), The normalized expected utility, entropy and variance model for decisions under risk, *International Journal of Approximate Reasoning*, *148*, 174–201.

Brito, I. (2023), A portfolio stock selection model based on expected utility, entropy and variance. *Expert Systems with Applications*, *213,Part A*, 118896.

Buchen, P.W. and Kelly, M. (1996), The maximum entropy distribution of an asset inferred from option prices. *Journal of Financial and Quantitative Analysis*, *31*(1), 143–159.

Butzer, P. L. and Wesphal, U. (2000), An introduction to fractional calculus. *Applications of Fractional Calculus in Physics*, 1–85.

Chang, T.P., Meade, N., Beasley, J.E. and Sharaiha, Y.M. (2000), Heuristics for cardinality constrained portfolio optimisation, *Computers & Operations Research*, *27*(13), 1271–1302.

Chanson, H. (2004), *The Hydraulics of Open Channel Flow: An Introduction.* 2nd edn, Elsevier, Kidlington.

Chen, W., Zhang, H., Mehlawat, M.K. and Jia, L. (2021), Mean-variance portfolio optimization using machine learning-based stock price prediction. *Applied Soft Computing*, *100*, 106943.

Chiu, C.L. (1987), Entropy and probability concepts in hydraulics. *Journal of Hydrologic Engineering*, *113*(5), 583–599.

Chiu, C.L., Jin, W. and Chen, Y.C. (2000), Mathematical models of distribution of sediment concentration. *Journal of Hydrologic Engineering*, *1*(16), 576–594.

Choo, T.H. (2000), An efficient method of the suspended sediment-discharge measurement using entropy concept. *Water Engineering Research*, *1*(2), 95–105.

Chow, V.T. (1959), *Open-Channel Hydraulics*. McGraw-Hill, New York.

Clausius, R. (1865), On various forms of the fundamental equations of the mechanical theory of heat that are convenient for applications. *Annals of Physics and Chemistry*, *125*, 353–400.

Coleman, N. (1986), Effects of suspended sediment on the open-channel velocity distribution. *Water Resources Research*, *22*(10), 1377–1384.

Coles, D. (1956), The law of the wake in the turbulent boundary layer. *Journal of Fluid Mechanics*, *1*, 191–226.

Corless, R.M, Gonnet, G.H., Hare, D.E., Jeffrey D.J. and Knuth D.E. (1996), On the Lambert W function. *Advances in Computational Mathematics*, *5*(1), 329–59.

Cover, T.M. and Thomas, J.A. (2006), *Elements of Information Theory*. 2nd ed., John Wiley and Sons, Hoboken, New Jersey.

Cox, D.R. (1972), Regression models and life-tables. *Journal of the Royal Statistical Society Series B*, *34*, 187–220.

Cui, H. (2011), *Estimation of Velocity Distribution and Suspended Sediment Discharge in Open Channels using Entropy*. M.Sc. Thesis, A&M University, Texas.

Cui, H. and Singh, V.P. (2012), On the cumulative distribution function for entropy-based hydrologic modeling. *Transactions of the American Society of Agricultural and Biological Engineers (ASABE)*, *55*(2), 429–438.

Cui, H. and Singh, V.P. (2014), Suspended sediment concentration in open channels using Tsallis entropy. *Journal of Hydrologic Engineering*, *19*(5), 966–977.

Dalir, M. and Bashour, M. (2010), Applications of fractional calculus. *Applied Mathematical Sciences*, *4*(21), 1021–1032.

Debnath, L. (2004), A brief historical introduction to fractional calculus. *International Journal of Mathematical Education in Science and Technology*, *35*(4), 487–501.

Demetrius, L. (1974), Demographic parameters and natural selection. *Proceedings of the National Academy of Sciences*, *71*, 4645–4647.

Demetrius, L. (1975), Reproductive strategies and natural selection. *American Naturalist*, *109*, 243–249.

Demetrius, L. (1976), Measures of variability in age-structured populations. *Journal of Theoretical Biology, 63*, 397–404.

Dey, S. (2012), *Fluvial Hydrodynamics: Sediment Transport and Scour Phenomena*. Springer, Berlin.

Dey, S. (2014), *Fluvial Hydrodynamics: Hydrodynamic and Sediment Transport Phenomena*. Springer, Berlin.

Dey, S. (2024), Turbulence in open-channel flows. *In: Fluvial Hydrodynamics. GeoPlanet: Earth and Planetary Sciences. Springer, Cham.*

Di Crescenzo A. and Longobardi M. (2002), Entropy-based measure of uncertainty in past lifetime distributions. *Journal of Applied Probability 39*, 434–440.

Di Crescenzo, A., Kayal, S. and Meoli, A. (2021), Fractional generalized cumulative entropy and its dynamic version. *Communications in Nonlinear Science and Numerical Simulation*, *102*, 105899.

Di Crescenzo, A. and Longobardi, M. (2009), On cumulative entropies. *Journal of Statistical Planning and Inference*, *139*(12), 4072–4087.

Di Crescenzo, A. and Toomaj, A. (2017), Further results on the generalized cumulative entropy. *Kybernetika*, *53*(5), 959–982.

Dionisio, A., Menezes, R. and Mendes, D. (2006), An econophysics approach to analyse uncertainty in financial markets: an application to the Portuguese stock market. *The European Physical Journal B - Condensed Matter and Complex Systems*, *50*, 161–164.

Dionisio, A., Menezes, R. and Mendes, D. (2007), Entropy and uncertainty analysis in financial markets. *arXiv:0709.0668*.

Dong, X., Lu, H., Xia, Y. and Xiong, Z. (2016), Decision-making model under risk assessment based on entropy. *Entropy*, *18*, 404.

Ebrahimi, N. (1996), How to measure uncertainty in the residual life distributions. *Sankhya: Series A*, *58*, 48–57.

Einstein, H. and Chien, N. (1955), Effects of heavy sediment concentration near the bed on velocity and sediment distribution. *US Army Corps of Engineers, Missouri River Division*, report no *8*.

Ebrahimi, N., Soofi, E. S. and Soyer, R. (1999), Information measures in perspective. *International Statistical Review*, *67*(3), 383–412.

Fieldsend, J.E., Matatko, J. and Peng, M. (2004), Cardinality constrained portfolio optimisation. *In: Yang, Z.R., Yin, H., Everson, R.M. (eds) Intelligent Data Engineering and Automated Learning – IDEAL 2004, Lecture Notes in Computer Science, vol 3177. Springer, Berlin, Heidelberg.*

Fischer, K. and Kleine, A. (2007), Remarks on "a measure of risk and a decision-making model based on expected utility and entropy" by Jipang Yang and Wanhua Qiu (EJOR 164 (2005), 792-799). *European Journal of Operational Research*, *182*, 469–474.

Foroghi, F., Tahmasebi, S., Afshari, M. and Lak, F. (2022), Extensions of fractional cumulative residual entropy with applications. *Communications in Statistics - Theory and Methods*, 1–20.

Galankashi, R.M., Mokhatab, R.F. and Ghezelbash, M. (2020), Portfolio selection: a fuzzy-ANP approach. *Financial Innovation*, *6*, 17.

Gao, J. and Li, D. (2013), Optimal cardinality constrained portfolio selection. *Operations Research*, *61*, 745–761.

Ghoshal, K., Kumbhakar, M., Singh, V.P. (2018), Suspended sediment concentration and discharge in open channels using Rényi entropy. *Journal of Hydrologic Engineering*, *23*(9), 04018038.

Gilchrist, W. (2000), *Statistical Modelling with Quantile Functions*. Chapman and Hall/CRC, Boca Raton, FLorida.

Goel, M.K., Khanna, P. and Kishore, J. (2010), Understanding survival analysis: Kaplan-Meier estimate. *International Journal of Ayurveda Research*, *1*(4), 274-278.

Govindarajulu, Z. (1977), A class of distributions useful in lifetesting and reliability with applications to nonparametric testing, *In: C.P. Tsokos, I.N. Shimi (eds.) Theory and Applications of Reliability, Acad. Press, New York*, *1*, 109–130.

Hankin, R. K. S. and Lee, A. (2006), A new family of nonnegative distributions, *Australian and New Zealand Journal of Statistics*, *48*, 67–78.

Huang, X. (2007), Portfolio selection with fuzzy returns. *Journal of Intelligent and Fuzzy Systems*, *18*(4), 383–390.

Huang, X. (2008), Mean-entropy models for fuzzy portfolio selection. *IEEE Transactions on Fuzzy Systems*, *16*(1), 1096–1101.

Huang, X. (2008), Mean-semivariance models for fuzzy portfolio selection. *Journal of Computational and Applied Mathematics*, *217*(1), 1–8.

Huang, C.F. (2012), A hybrid stock selection model using genetic algorithms and support vector regression. *Applied Soft Computing*, *12*, 807–818.

Jackson, F. (1910), Quart. *Journal of Pure and Applied Mathematics*, *193*.

Jana, P., Roy, T.K. and Mazumder, S.K. (2021), Multi-objective possibilistic model for portfolio selection with transaction cost. *Journal of Computational and Applied Mathematics*, *228*(1), 188–196.

Jaynes, E. (1957a), Information theory and statistical meachanics: I. *The Physical Review*, *106*(4), 620–630.

Jaynes, E. (1957b), Information theory and statistical meachanics: II. *The Physical Review*, *108*, 171–190.

Kahneman, D. and Tversky, A. (1979), Prospect theory: An analysis of decision under risk. *Econometrica*, *47*(2), 263–292.

Kalbfleisch, J.D. and Schaubel, D.E. (2023), Fifty years of the Cox model. *Annual Review of Statistics and its Application*, *10*, 1–23.

Kaplan, E. L. and Meier, P. (1958), Nonparametric estimation from incomplete observations. *Journal of American Statistical Association*, *53*(282), 457–481.

Karci, A. (2016), Fractional order entropy: New perspectives. *Optik*, *127*(20), 9172–9177.

Kartsonaki, C. (2016), Survival analysis. *Diagnostic Histopathology*, *22*(7), 263–270.

Kayal, S. and Balakrishnan, N. (2023), Weighted fractional generalized cumulative past entropy and its properties. *Methodology and Computing in Applied Probability*, *25*, 61.

Kayal, S. and Balakrishnan, N. (2024), Quantile-based information generating functions and their properties and uses. *Probability in the Engineering and Informational Sciences*, *38*(4), 733–751.

Kayid, M. and Shrahili, M. (2022), Some further results on the fractional cumulative entropy. *Entropy*, *24*, 1037.

Keyfitz, N. (1977), *Applied Mathematical Demography.* John Wiley and Sons, New York.

Krishnan, A. S., Sunoj, S. M. and Nair, N.U. (2020), Some reliability properties of extropy for residual and past lifetime random variables. *Journal of the Korean Statistical Society*, *49*, 457–474.

Kullback, S. (1959), *Information Theory and Statistics. Wiley, New York.*

Kumbhakar M. and Ghoshal, K. (2016), One-dimensional velocity distribution in open channels using Renyi entropy. *Stochastic Environmental Research and Risk Assessment*, *31*, 949–959.

Kumbhakar, M. and Tsai, C.W. (2023), Analytical modeling of vertical distribution of streamwise velocity in open channels using fractional entropy. *Chaos, Solitons and Fractals*, *169*, 113285.

Kundu, S. (2015), *Theoretical Study on Velocity and Suspension Concentration in Turbulent Flow.* Ph.D. Thesis, Indian Institute of Technology, Kharagpur, India.

Kundu, S. and Ghoshal, K. (2014), Effects of secondary current and stratification on suspension concentration in an open channel flow. *Environmental Fluid Mechanics*, *14*(6), 1357–1380.

Lévy, H. (1992), Stochastic dominance and expected utility: Survey and analysis. *Management Science*, *38*(4), 555–593.

Li, D., Yang, Z., Zhu, Z., Guo, M., Gao, W. and Sun, Z. (2020), Estimating the distribution of suspended sediment concentration in submerged vegetation flow based on gravitational theory. *Journal of Hydrology*, *587*, 124921.

Li, B., Sun, Y., Aw, G. and Teo, K.L. (2019), Uncertain portfolio optimization problem under a minimax risk measure. *Applied Mathematical Modelling*, *76*, 274–281.

Li and Zhang (2021), A new mean-variance-entropy model for uncertain portfolio optimization with liquidity and diversification. *Chaos, Solitons & Fractals*, *146*, 110842.

Liu, Y.C. and Yeh, I.C. (2017), Using mixture design and neural networks to build stock selection. *Neural Computing and Applications*, *28*, 521–535.

London, M.D., Evans, A.K. and Turner, M.J. (2001), Conditional entropy and randomness in financial time series. *Quantitative Finance*, *1*, 414.

Lopes, A. M. and Machado, J.A.T. (2020), A review of fractional order entropies. *Entropy*, *22*(12), 1374.

Luce, R.D., Ng., C.T., Marley, A.A.J. and Aczél (2005), Independence properties vis-a-vis several utility representations.. *Risk and Decision Analysis*, *58*, 77–143.

Luo, H. (2009), *Tsallis Entropy Based Velocity Distributions in Open Channel Flows.* Ph.D. Thesis, A&M University, Texas.

Maasoumi, E. (1993), A compendium to information theory in economics and econometrics. *Econometric Reviews*, *12*(2), 137–181.

Machado, J.A.T., Kiryakova, V. and Mainardi, F. (2011), Recent history of fractional calculus. *Communications in Nonlinear Science and Numerical Simulation*, *16*, 1140–1153.

Machado, J.A.T. (2014), Fractional order generalized information. *Entropy*, *16*(4), 2350–2361.

Machado, J.A.T. and Lopes, A.M. (2021), Entropy analysis of human death uncertainty. *Nonlinear Dynamics*, *104*, 3897–3911.

Machina, M.J. (1987), Choice under uncertainty: Problems solved and unsolved. *Journal of Economic Perspectives*, *1*, 121–154.

Kumbhakar, M., Ray, R.K., Ghoshal, K. and Singh, V.P. (2020), On the role of Tsallis entropy index for velocity modelling in open channels, *Physica A: Statistical Mechanics and its Applications*, *557*, 124901.

Mariotto, A.B, Zou, Z., Johnson, C.J., Scoppa, S., Weir, H.K., and Huang, B. (2018), Geographical, racial and socio-economic variation in life expectancy in the US and their impact on cancer relative survival. *PLoS ONE, 13*(7), e0201034.

Markowitz, H. (1952), Portfolio selection. *The Journal of Finance*, *7*(1), 77–91.

Markowitz, H. (1959), *Portfolio Selection: Efficient Diversification of Investments*. Wiley, New York.

Markowitz, H. (2000), *Mean-Variance Analysis in Portfolio Choice and Capital Markets*. Wiley, New York.

Marley, A.A.J. and Luce, R.D. (2008), Utility of gambling II: Risk, paradoxes, and data. *Economic Theory*, *36*, 165–187.

Mazumder, B.S. and Ghoshal, K. (2002), Velocity and suspension concentration in sediment-mixed fluid. *International Journal of Sediment Research*, *17*(3), 220–232.

Mazumder, B.S. and Ghoshal, K. (2006), Velocity and concentration profiles in uniform sediment laden flow. *Applied Mathematical Modelling*, *30*(2), 164–176.

McCauley, J.L. (2003), Thermodynamic analogies in economics and finance: Instability of markets. *Physica A: Statistical Mechanics and its Applications*, *329*(1), 199–212.

McQuivey, R.S. (1973), Summary of turbulence data from rivers, conveyance channels, and laboratory flumes. *USGS Professional Paper 802B. Washington, DC: Government Printing Office.*

Mehralizade, R., Amini, M., Gildeh, B.S. and Ahmadzade, H. (2020), Uncertain random portfolio selection based on risk curve. *Soft Computing*, *24*, 13331–13345.

Mercurio, P.J., Wu, Y. and Xie, H. (2020), An entropy-based approach to portfolio optimization. *Entropy*, *22*(3), 332.

Mirauda, D., Pannone, M. and De Vincenzo, A. (2018a), An entropic model for the assessment of stream-wise velocity dip in wide open channels. *Entropy*, *20*, 69.

Mirauda, De Vincenzo, A. and D., Pannone, M. (2018b), Simplified entropic model for the evaluation of suspended load concentration. *Water*, *10*, 378.

Misra, R.D. (1940), On the stability of crystal lattices II. *In: Mathematical Proceedings of the Cambridge Philosophical Society, Cambridge University Press*, *36*(2), 173–182.

Molgedey, L. and Ebeling, W. (2000), Local order, entropy and predictability of financial time series. *European Physical Journal B*, *15*, 733–737 .

Nadarajah, S. and Zografos, K. (2003), Formulas for Rényi information and related measures for univariate distributions. *Information Sciences*, *155*, 118–119.

Nakagawa, H. (1993), *Turbulence in Open Channel Flows.* 1st ed., Routledge, London.

Nagnur, D. (1986), Rectangularization of the survival curve and entropy: Canadian experience, 1921-1981. *Canadian Studies in Population*, *13*, 83–102 .

Nair, N.U., Sankaran, P.G. and Kumar, B.V. (2012), Modelling lifetimes by quantile functions using Parzen's score function. *Journal of Theoretical and Applied Statistics*, *46*(6), 799–811.

Nair, N.U., Sankaran, P.G. and Balakrishnan, N. (2013). *Quantile-based Reliability Analysis.* Birkhäuser, New York.

Nair, N.U., Sankaran, P.G. and Sunoj, S.M. (2019), Some properties of proportional reversed hazards model based on quantile functions. *International Journal of Reliability, Quality and Safety Engineering*, *26*(1), 1950011.

Nair, N.U., Sunoj, S.M. and Rajesh, G. (2022), *Reliability Modelling with Information Measures.* CRC Press, Boca Raton, Florida.

Nair, N.U. and Sankaran, P.G. (2009), Quantile-based reliability analysis. *Communications in Statistics - Theory and Methods*, *38*(2), 222–232.

Nair, N.U. and Vineshkumar, B. (2011), Ageing concepts: An approach based on quantile function. *Statistics and Probability Letters*, *81*(12), 2016–2025.

Nanda, A.K. and Maiti, S.S. (2007, Rényi information measure for a used item. *Information Sciences*, *177*, 4161–4175.

Navarro, J., del Aguila, Y. and Asadi, M. (2010), Some new results on the cumulative residual entropy. *Journal of Statistical Planning and Inference*, *140*, 310–322.

Nawrocki, D. and Harding, W. (1986), State-value weighted entropy as a measure of investment risk. *Applied Economics*, *18*(4), 411-419.

Nezu, I. and Nakagawa, H. (1995), Turbulence measurements in unsteady free-surface flows, *Flow Measurement and Instrumentation*, *6*(1), 49–59.

Oliveira, E.C. and Machado, J.A.T. (2014), A Review of definitions for fractional derivatives and integral. *Mathematical Problems in Engineering*, *2014*, 238459.

Paiva, F.P., Cardoso, R.T.M., Hanaoka, G.P. and Duarte, W.M. (2019), Decision-making for financial trading: A fusion approach of machine learning and portfolio selection. *Expert Systems with Applications*, *115*, 635–655.

Parzen, E. (1979), Non parametric statistical data modeling, *Journal of American Statistical Association*, *74*, 105–122.

Paul P. and Kundu, C. (2026), Fractional order entropy-based decision-making models under risk. *Communications in Nonlinear Science and Numerical Simulation*, *152*, 109106.

Philippatos, G.C. and Gressis, N. (1975), Conditions of equivalence among E-V, SSD and E-H portfolio selection criteria: The case for uniform, normal and lognormal Distributions. *Management Science*, *21*, 617–625.

Philippatos, G.C., and Wilson, C.J. (1972), Entropy, market risk, and the selection of efficient portfolios. *Applied Economics*, *4*(3), 209–220.

Philippe, J. (1996), *Value at Risk: The New Benchmark for Controlling Market Risk.* Irwin Professional, Chicago.

Pollatsek, A. and Tversky, A. (1970), A theory of risk. *Journal of Mathematical Psychology*, *7*(3), 540–553.

Prandtl, L. (1925), Report on investigations into fully developed turbulence. *Journal of Applied Mathematics and Mechanics*, *5*(2), 136–139.

Qin, Z., Li, X. and Ji, X. (2009), Portfolio selection based on fuzzy cross-entropy. *Journal of Computational and Applied Mathematics*, *228*, 188–196.

Qu, B.Y., Zhou, Q., Xiao, J.M., Liang, J.J. and Suganthan, P.N. (2017), Large-scale portfolio optimization using multiobjective evolutionary algorithms and preselection methods. *Mathematical Problems in Engineering* , 4197914.

Qiu, G. (2019), Further results on quantile entropy in the past lifetime. *Probability in the Engineering and Informational Sciences*, *33*(1), 146–159.

Raghavendran, P., Gunasekar, T. and Gochhait, S. (2024), Application of artificial neural networks for existence and controllability in impulsive fractional Volterra-Fredholm integro-differential equations. *Applied Mathematics in Science and Engineering*, *32*(1), 2436440.

Rényi, A. (1961), On measures of entropy and information. *In: Neyman, J., Ed., 4th Berkeley Symposium on Mathematical Statistics and Probability, Berkeley*, *1*, 547–561.

Rao, M., Chen, Y., Vemuri, B.C. and Wang, F. (2004), Cumulative residual entropy: A new measure of information. *IEEE Transactions on Information Theory*, *50*(6), 1220–1228.

Rouse, H. (1937), Modern conceptions of the mechanics of turbulence. *Transactions of the American Civil Engineers* *102*(1), 463–543.

Sankaran, P.G. and Nair, N. U. (2009), Nonparametric estimation of the hazard quantile function. *Journal of Nonparametric Statistics*, *21*, 757–767.

Sankaran, P.G. and Sunoj, S.M. (2016), Quantile based cumulative entropies. *Communications in Statistics - Theory and Methods*, *46*(2), 805–814.

Sarma, K., Lakshminarayana, P. and Rao, N. (1983), Velocity distribution in smooth rectangular open channels. *Journal of Hydraulic Engineering*, *109*, 270–289.

Shaked, M. and Shanthikumar, J.G. (2007), *Stochastic Orders*. Springer, New York.

Shannon, C.E. (1948), A mathematical theory of communication. *The Bell System Technical Journal*, *27*, 379–423, 623–656.

Simons, D.B. and Senturk, F. (1992), *Sediment Transport Technology.* Water Resources, Littleton, Colorado.

Singh, V.P. (1996), *Kinematic Wave Modeling in Water Resources: Environmental Hydrology*, Wiley, New York.

Singh,V.P. (2014), *Entropy Theory in Hydraulic Engineering: An Introduction.* American Society of Civil Engineers (ASCE), U.S.A.

Singh, V.P. and Luo, H. (2011), Entropy theory for distribution of one-dimensional velocity in open channels. *Journal of Hydrologic Engineering*, *16*(9), 725–735.

Song, K.S. (2001), Rényi information, loglikelihood and an intrinsic distribution measure. *Journal of Statistical Planning and Inference*, *93*, 51-–69.

Soofi, E. (1997), Information theoretic regression methods. *In: Advances in Econometrics - Applying Maximum Entropy to Econometric Problems, Fomby, T. and R. Carter Hill eds. Vol. 12. Jai Press Inc., London.*

Sun, H.G., Zhang, Y., Baleanu, D., Chen, W. and Chen, Y.Q. (2018), A new collection of real world applications of fractional calculus in science and engineering. *Communications in Nonlinear Science and Numerical Simulation*, *64*, 213–231.

Sunoj, S.M., Sankaran, P.G. and Nanda, A.K. (2013), Quantile based entropy function in past lifetime. *Statistics and Probability Letters*, *83*, 366–372.

Sunoj, S.M. and Sankaran, P.G. (2012), Quantile based entropy function. *Statistics and Probability Letters*, *82*, 1049–1053.

Sunoj, S.M. and Sebastian, I.A. (2025), Fractional cumulative residual entropy in the quantile framework and its applications in the financial data. *Communications in Statistics - Theory and Methods*, 1–21.

Sturm, T.W. (2010), *Open Channel Hydraulics.* McGraw-Hill, New York.

Stutzer, M.J. (2000), Simple entropic derivation of a generalized Black-Scholes option pricing model. *Entropy*, *2*(2), 70–77.

Tsallis, C. (1988), Possible generalization of Boltzmann-Gibbs statistics. *Journal of Statistical Physics*, *52*, 479–487.

Tsujimoto, T. (2010), Diffusion coefficient of suspended sediment and kinematic eddy viscosity of flow containing suspended load. *River Flow*, *3*, 801–806.

Ubriaco, M.R. (2009), Entropies based on fractional calculus. *Physics Letters A*, *373*(30), 2516–2519.

Usta, I. and Kantar, Y.M. (2011), Mean-variance-skewness-entropy measures: A multi-objective approach for portfolio selection. *Entropy*, *13*, 117–133.

Valério, D., Trujillo, J.J., Rivero, M., Machado, J.A.T. and Baleanu, D. (2013), Fractional calculus: A survey of useful formulas. *European Physical Journal Special Topics*, *222*, 1827–1846.

van Staden, P.J. and Loots, M.R. (2009), L-moment estimation for the generalized lambda distribution. *Proceedings of the Third Annual ASEARC Conference, New Castle, Australia.*

Varkey, A. and Haridas, H.N. (2023), A review on quantile functions, income distributions, and income inequality measures. *Reliability: Theory and Applications*, *18*, 50–62.

Vineshkumar, B., Nair, N.U. and Sankaran, P. G. (2015), Stochastic orders using quantile-based reliability functions. *Journal of the Korean Statistical Society*, *44*(2), 221–231.

von Kármán, T. (1930), Mechanical similarity and turbulence. *In: Proceedings of the 3rd International Congress on Applied Mechanics. Stockholm, Sweden*, 85–93.

von Neumann, J. and Morgenstern, O. (1947), *The Theory of Games and Economic Behavior*. Princeton University Press, New Jersey, USA.

Wang, W., Li, W., Zhang, N. and Liu, K. (2020), On the dynamic cumulative past quantile entropy ordering. *Symmetry*, *13*, 2001.

Wang, H., Kang, D. and Yan, L. (2021), Portfolio formation with preselection using deep learning from long-term financial data. *Expert Systems with Applications*, *143*, 113042.

Woo, H.S., Julien, P.Y. and Richardson, E.V. (1988), Suspension of large concentrations of sands. *Journal of Hydraulic Engineering*, *114*(8).

Xiong, H., Shang, P. and Zhang, Y. (2019), Fractional cumulative residual entropy. *Communications in Nonlinear Science and Numerical Simulation*, *78*, 104879.

Yam, S.C.P., Yang, H. and Yuen, F.L. (2016), Optimal asset allocation: Risk and information uncertainty. *European Journal of Operational Research*, *251*(2), 554–561.

Yang, J., Feng, Y. and Qiu, W. (2017), Stock selection for portfolios using expected utility-entropy decision model. *Entropy*, *19*(10), 508.

Yang, J. and Qiu, W. (2005), A measure of risk and a decision-making model based on expected utility and entropy. *European Journal of Operational Research*, *164*(3), 792–799.

Yang, J. and Qiu, W. (2014), Normalized expected utility-entropy measure of risk. *Entropy*, *16*(7), 3590–3604.

Zellner, A. (1996), Models, prior information, and Bayesian analysis. *Journal of Econometrics*, *75*(1), 51–68.

Zhou, R., Cai, R. and Tong, G. (2013), Applications of entropy in finance: A review. *Entropy*, *15*(11), 4909-4931.

Zhu, D.M., Lu, J., Ching, W.K. and Siu, T.K. (2017), Discrete-time optimal asset allocation under higher-order hidden Markov model. *Economic Modelling*, *66*(C), 223–232.

List of Publications from the Thesis

Published and Accepted Works

- **Paul, P.** and Kundu, C. (2026), Fractional order entropy-based decision-making models under risk. *Communications in Nonlinear Science and Numerical Simulation*, ***152***, 109106. Elsevier.
DOI: https://doi.org/10.1016/j.cnsns.2025.109106

- **Paul, P.** and Kundu, C. (2026), Analytical formulation of vertical concentration profile for suspended sediment in open channel flows using fractional entropy. *Stochastic Environmental Research and Risk Assessment*, ***40***(44). Springer.
DOI: https://doi.org/10.1007/s00477-025-03133-7

Communicated Works

- **Paul, P.** and Kundu, C. (2026), Modeling of vertical distribution of suspended sediment concentration in open channel turbulent flows using fractional differential entropy, *Journal of Hydraulic Engineering.* (Major revision submitted)

- **Paul, P.** and Kundu, C. (2025), Fractional differential entropy and its application in modeling one-dimensional flow velocity. (*Manuscript under review*)

- **Paul, P.** and Kundu, C. (2025), Normalized fractional order entropy-based decision-making models under risk. (*Manuscript under review*)

- **Paul, P.** and Kundu, C, (2026), Quantile-based fractional generalized cumulative past entropy and its role in analyzing human mortality uncertainty. (*To be submitted*)